COMPOSITE SYSTEMS AND THERMODYNAMIC TOOLS FOR LONG-TERM SORPTION ENERGY STORAGE

Hao Wu

THÈSE POUR OBTENIR LE GRADE DE DOCTEUR DE L'UNIVERSITÉ DE MONTPELLIER

En Chimie des matériaux

École doctorale : Sciences Chimiques Balard

Unité de recherche : Institut Charles Gerhardt de Montpellier UMR 5253

SYSTÈME COMPOSITES ET ANALYSE THERMODYNAMIQUE POUR LE STOCKAGE THERMOCHIMIQUE DE L'ÉNERGIE PAR SORPTION

Présentée par

Hao WU

Le 02 décembre 2019

Devant le jury composé de

Mme A. GIROIR-FENDLER, Professeure, Université Lyon 1, IRCELYON	**Rapportrice**
Mme S. BENNICI, Chargée de recherche, CNRS, IS2M	**Rapportrice**
M. D. BERGE-LEFRANC, Professeur, Aix-Marseille Université, IMBE	**Examinateur**
M. P. TRENS, Professeur, ENSCM, ICGM	**Président du jury**
M. J. ZAJAC, Professeur, Université de Montpellier, ICGM	**Directeur de thèse**
M. F. SALLES, Chargé de recherche, CNRS, ICGM	**Co-directeur de thèse**

UNIVERSITÉ DE MONTPELLIER

THÈSE POUR OBTENIR LE GRADE DE DOCTEUR DE L'UNIVERSITÉ DE MONTPELLIER

En Chimie des matériaux

École doctorale : Sciences Chimiques Balard

Unité de recherche : Institut Charles Gerhardt de Montpellier UMR 5253

SYSTÈME COMPOSITES ET ANALYSE THERMODYNAMIQUE POUR LE STOCKAGE THERMOCHIMIQUE DE L'ÉNERGIE PAR SORPTION

Présentée par

Hao WU

Le 02 décembre 2019

Devant le jury composé de

Mme A. GIROIR-FENDLER, Professeure, Université Lyon 1, IRCELYON	**Rapportrice**
Mme S. BENNICI, Chargée de recherche, CNRS, IS2M	**Rapportrice**
M. D. BERGE-LEFRANC, Professeur, Aix-Marseille Université, IMBE	**Examinateur**
M. P. TRENS, Professeur, ENSCM, ICGM	**Président du jury**
M. J. ZAJAC, Professeur, Université de Montpellier, ICGM	**Directeur de thèse**
M. F. SALLES, Chargé de recherche, CNRS, ICGM	**Co-directeur de thèse**

UNIVERSITÉ DE MONTPELLIER

Table of contents

List of figures

List of tables

General Introduction

Global energetic context

With the prospect of greatly increasing global energy demand along with the scarcity of fossil energy resources and climate change, the need for greater energy efficiency and the diversification of energy sources are becoming urgent. The European Community has launched the "Europe 2020 strategy" including ambitious targets such as 20% reductions of greenhouse gas emissions than 1990 levels, 20% of energy use from renewables, and 20% increase in energy efficiency by 2020 [1].

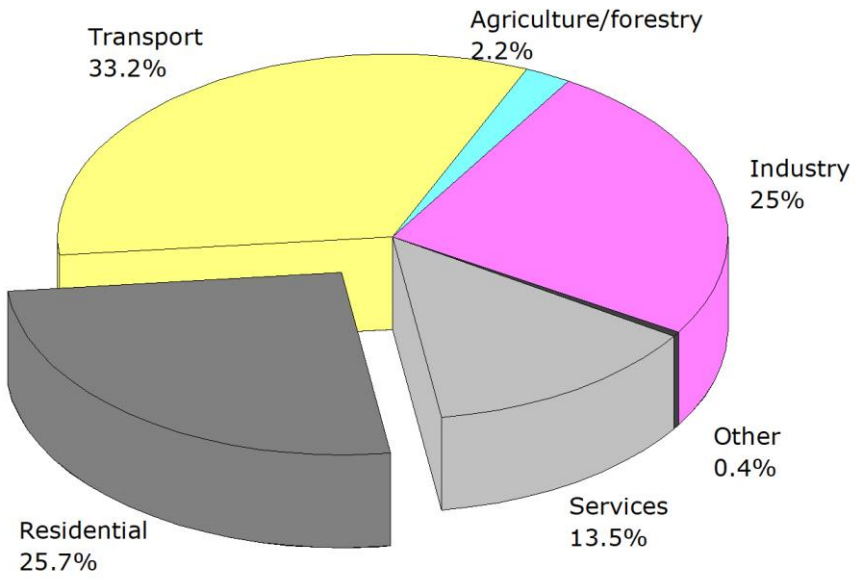

Figure GI. 1*: Global energy consumption by sector in EU-28, 2016. Data source: Eurostat (the last update: 31-05-2018) [2]*

One of the most dominant energy-consuming categories is the residential sector. As shown in Figure GI.1, the 2016 energy consumption of the residential sector accounted for 25.7 % of the total energy use in Europe, making it amongst three prominent energy-consuming categories besides the transport (33 %) and industry (25 %) [2]. Furthermore, the greatest part of this energy consumption is related with the space heating (e.g., 62 % in 2017 according to the French electricity provider EDF; c.f., Figure GI.2)

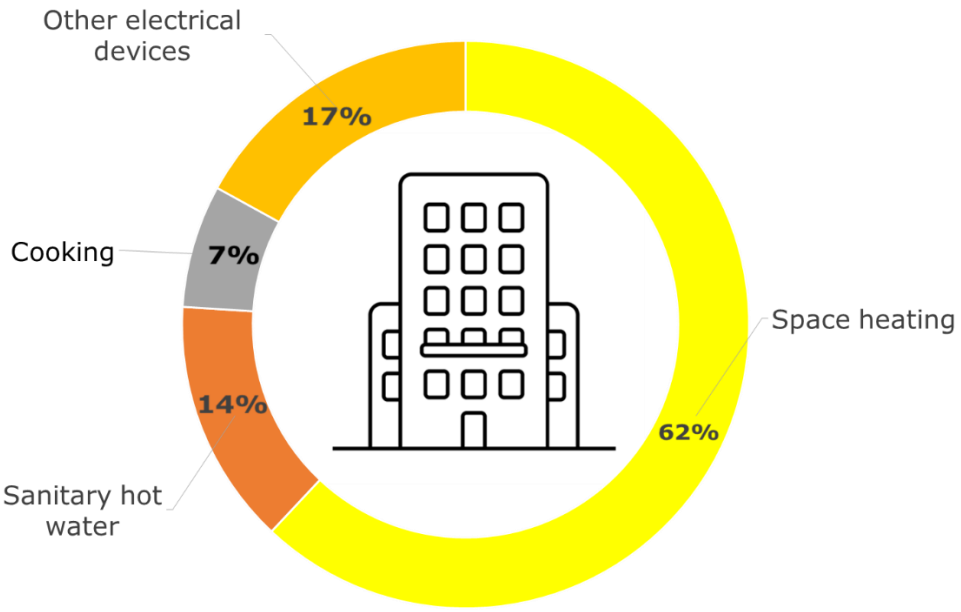

***Figure GI. 2** : Breakdown of energy consumption in an apartment in France, data source: French electricity provider EDF, 2017 [3]*

Under this context, developing clean and renewable energies has become imperative for the sustainable development strategy including better energy efficiency and the reduction of greenhouse gases. Indeed, researches have been more and more focused on such renewable energy sources as solar, wind and hydraulic. Among these renewable energies, solar energy is currently seen as one of the most promising alternatives to the conventional energy production [4]. However its main drawback is due to the intermittence between the supply and the demand of solar energy, as illustrated in Figure GI.3. Therefore, much hope has been put into the Energy Storage System (ESS) capable of capturing and storing the available thermal energy during the periods of sunshine and restoring it in response to the system needs, in order to match heat supply and demand over time.

Currently, different types of the ESS are in various phases of development. The most promising ones are illustrated in Figure GI.4. They are based on such energy forms as

electrochemical (i.e., conventional rechargeable batteries), mechanical (i.e., pumped hydroelectric storage), electrical (i.e., supercapacitors), chemical (i.e., hydrogen fuel cells), and thermal energy (i.e. sensible or latent heat storage) [5,6].

Amongst the existing technologies, Thermal Energy Storage (TES) is now gaining credibility as a promising option for solar energy storage with the purpose of overcoming the existing mismatch between energy supply and demand in the field of domestic heating.

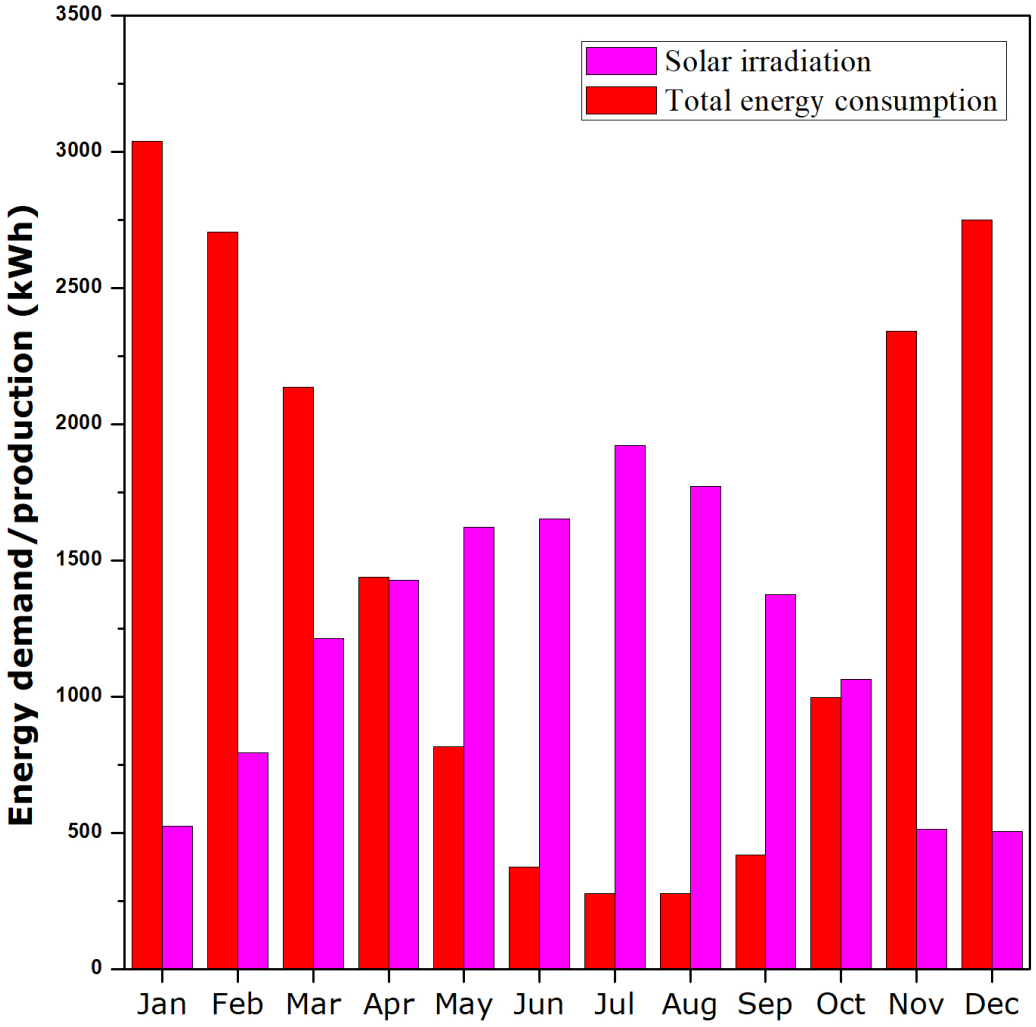

***Figure GI. 3**: Seasonal shift of household energy consumption and solar irradiation over a year in a typical European house. Data adapted from [7].*

Concerning the short-term thermal energy storage in building applications, two main existing technologies, namely sensible and latent heat storage, have already been implemented

industrially on large scale [8]. The sensible heat storage is achieved by the thermal capacity of the storage materials and the latent heat storage involves heat interactions associated with a phase change of a material. Nevertheless, they may be accompanied by a non-negligible energy loss, thermal instability and highly cost investment in thermal insulation, which will be a huge issue when it comes to a seasonal storage system. More recently, thermochemical storage using chemical potential changes from suitable reversible chemical reactions or sorption phenomena is considered as a promising alternative for long-term heat storage since the solar energy can be theoretically stored by separating reacting couple for an arbitrary time without much heat loss. However, in spite of the advantages presented by the thermochemical storage system, some restrictions in operating thermochemical reactors, such as high regeneration temperature or complex storage cycle, may contribute to a high cost and complexity of the material design.

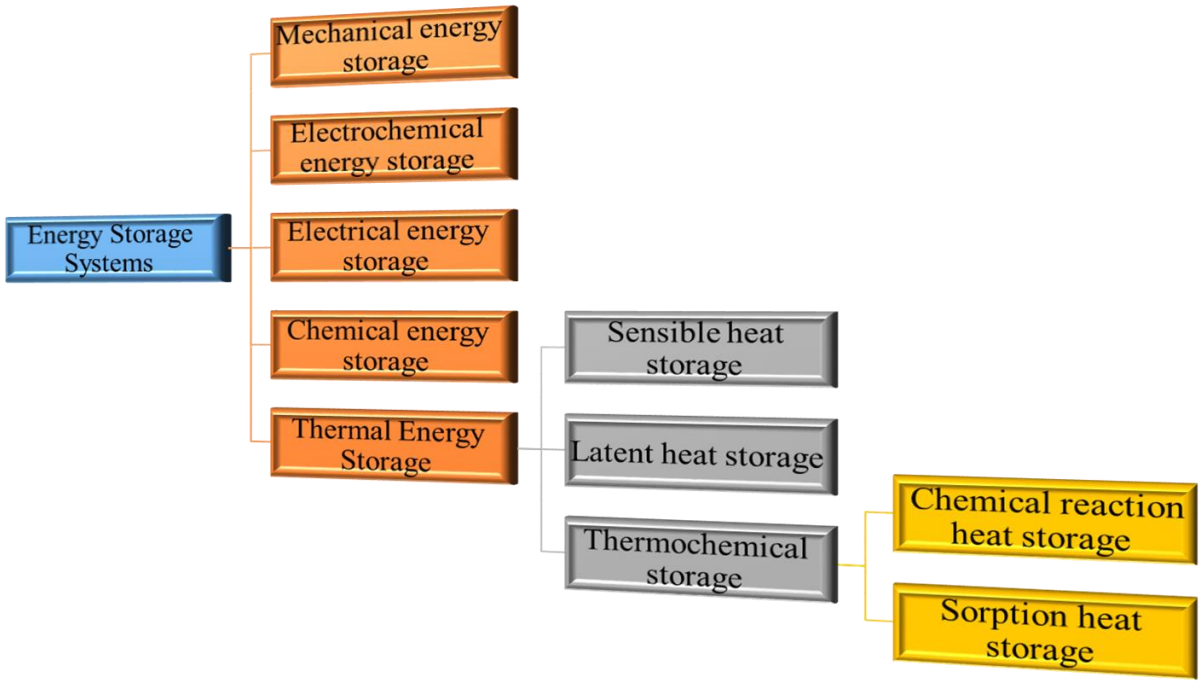

***Figure GI. 4** : Classification of energy storage systems with respect to various energy forms*

The objective of the Ph.D. thesis

In a general manner, the present Ph. D. thesis aims at proposing an alternative approach, and the related testing tools, to the development of the sorption-based storage system, sufficiently efficient, viable ecologically and economically for space heating in the building uses. The general objective is to search for appropriate porous materials and to study the sorption phenomena involved, also to quantify the related heat effects and the kinetics of heat evolvement (or absorption), so as to control the physical factors governing the performance and durability of the storage systems, as well as to rationalize the materials design and elaboration.

To attain this objective, our research strategy has passed through the following stages:
(i) Conception of an optimised storage system for uses in long-term sorption energy storage, including the selection of adequate storage materials and the determination of suitable operating conditions.
(ii) Development of appropriate thermodynamic tools for analysis and optimization of the sorption performance.

Based on the main conclusions drawn from the comprehensive review of the literature, our interest went towards two types of ion-exchange solid materials, including cerium-exchanged zeolite X (faujasite) and sulfonate-exchanged ionosilicas. It was mainly important to understand the sorption behaviour of water vapour in the selected solid adsorbents by following the mechanistic and energetic aspects of surface hydration phenomena. In order to understand the sorption mechanisms occurring at the macroscopic and microscopic scale, adsorption experiments were programmed aiming at determining the corresponding adsorption isotherms from the gas phase. They were supplemented by adequate spectroscopy, microscopy, and X-ray diffraction studies undertaken to establish the relationship between the structural and textural properties of the adsorbents and their sorption performance towards water vapour. Such characterisation techniques were selected with regards to the structural and chemical specificity

of the storing materials. Further calorimetry experiments carried out in both static and dynamic modes allowed quantifying and understanding the thermal effects accompanying the adsorption (hydration) and desorption (dehydration) phenomena involved in view of optimising the charging and discharging stages of the future storage units. Finally, a laboratory bench-scale testing facility was built up to continuously monitor the temperature changes accompanying the discharging step in a flow of carrier gas leaving the sorption reactor.

Structure of the manuscript

Beyond the present General Introduction, the manuscript contains 5 Chapters and the final General Conclusions and Future Outlook section.

Chapter 1 includes the general considerations about the thermal energy storage and a critical literature review presenting the current state-of-the-art on the low-temperature thermochemical storage involving the adsorption of water vapour from moist-air onto porous adsorbents in open sorption systems. This review has provided a base for the selection of materials and testing their sorption performance under particular experimental conditions.

Chapter 2 describes our strategy for the synthesis and/or surface modification of the selected adsorbents. Here the main idea was to improve their performance as adsorbents for water vapour at low humidity levels by exchanging their initial compensating cations (zeolites) or anions (ionosilicas) with other co-ions characterised by higher hydration energies. Various characterization methods used to evaluate structural and surface properties of the selected materials are detailed further, together with the research strategy and tools employed for studying the mechanisms of water vapour adsorption and the related heat effects.

Chapter 3 and Chapter 4 report the results of experimental and modelling studies undertaken on the two categories of the storing materials, i.e., cation-exchanged zeolites of type X and anion-exchanged ionosilicas, respectively. Here, the emphasis has been put on the

understanding of the detailed mechanisms by which water vapour is adsorbed on the surface, thereby providing appropriate quantities of thermal energy in the form of heat released into the surroundings. The effect of compensating ions on the performance of ion-exchanged samples under gas-flow conditions is particularly put forward in the interpretation of the results obtained.

In the last Chapter 5, the key parameters for assessing performance at work of the future storage units are identified and tested on the basis of the results achieved by means of the laboratory bench-scale testing facility.

Finally, the main conclusions obtained within the framework of the Ph.D. thesis and suggestions for the future work are presented in the final section.

References

[1] European Commission, Europe 2020: Europe's growth strategy, 2012. doi:10.2775/39976.

[2] Eurostat, Smarter, greener, more inclusive? Indicators to support the Europe 2020 strategy - 2018 edition, Publications Office of the European Union, Luxembourg, 2018. doi:10.2785/80156.

[3] EDF, Répartition de la consommation d'électricité au sein d'un foyer français, (2017). https://travaux.edf.fr/electricite/raccordement/repartition-de-la-consommation-d-electricite-au-sein-d-un-foyer-francais (accessed March 11, 2019).

[4] M. Roeb, M. Neises, N. Monnerie, C. Sattler, R. Pitz-Paal, Technologies and trends in solar power and fuels, Energy Environ. Sci. 4 (2011) 2503–2511. doi:10.1039/C1EE01128F.

[5] M. Cheng, S.S. Sami, J. Wu, Benefits of using virtual energy storage system for power system frequency response, Appl. Energy. 194 (2017) 376–385. doi:10.1016/j.apenergy.2016.06.113.

[6] X. Luo, J. Wang, M. Dooner, J. Clarke, Overview of current development in electrical energy storage technologies and the application potential in power system operation, Appl. Energy. 137 (2015) 511–536. doi:10.1016/j.apenergy.2014.09.081.

[7] C.J. Ferchaud, H.A. Zondag, A. Rubino, Seasonal Sorption Heat Storage – Research On Thermochemical Materials And Storage Performance, Proc. Heat Power Cycle 2012. (2012) 1–7. https://pure.tue.nl/ws/files/3821108/572851890456641.pdf.

[8] K. Nielsen, Thermal energy storage: A state-of-the-art. A report within the research program Smart Energy-Efficient Buildings at the Norwegian University of Science and Technology and SINTEF, 2003.

Chapter I

Bibliographic study:
A critical review of the state-of-the-art

I.1. Thermal energy storage technologies (TES)

For the purpose of balancing the energy supply and demand in the building applications, thermal energy storage is currently gaining credibility as a promising option for solar energy storage. Thermal energy storage (TES) is a technology for harvesting solar energy and storing it by increasing the internal energy of appropriate materials. This energy may be recovered at a later time for heating and cooling applications.

A good long-term TES system [1–3] provides high storage density while reducing greatly thermal energy losses and the size of the working system. Another criterion is related to the ease of regeneration, thus leading to the high efficiency of the stored thermal energy. They have not been exploited sufficiently due to some critical drawbacks, such as the complexity of design and high investment costs, as well as the heat and mass transfer limitations encountered in the actual systems [4].

Three main types of thermal energy storage technologies are common in practice [5]:

II.1.1. Sensible heat storage (SHS)

A sensible heat storage (SHS) system is the simplest TES unit, comprising a storage medium, a container and input/output devices. It is one of the most developed technologies for thermal storage in both the domestic and the industrial sector. Heat is stored by the temperature difference of the storage medium; its storage density is proportional to its specific heat and the temperature difference:

$$Q = \int_{T_i}^{T_f} m * Cp * dT \qquad (I.1)$$

Where:

Cp is the specific heat of the storing material;

m is the mass of the storage material;

dT is the temperature rise between initial and final temperature of the material, T_i and T_f, respectively.

Large aquifers, rock beds, solar ponds and large tanks are commonly used for long-term storage.

I.1.2. Latent heat storage (LHS)

A phase change of the storage material (PCM) is used during latent heat storage. Heat is absorbed or released when the PCM undergoes a fusion or condensation, phase changes occurring from solid to liquid or liquid to solid. Heat is then stored through the phase change process of a material at a constant temperature:

$$Q = m * L \qquad (I.2)$$

Where:

m is the mass of the storage material;

L is the latent heat of fusion.

The storage substances generally include ice, paraffin wax, fatty acids and salt hydrates.

The SHS and LHS systems are employed both on a small scale for domestic heating and on a larger scale in solar thermal power plants.

I.1.3. Thermochemical heat storage (THS)

Amongst various storage techniques, the thermochemical heat storage (THS) is a relatively new technology that has drawn a lot of attention in recent years. Here the operating principle corresponds to the use of the available solar energy via solar collectors to desorb a

fluid, called *sorbate*, confined in a solid or liquid storage material, called *sorbent*. The THS systems are based on sorption phenomena or chemical reactions allowing storing of the heat of adsorption or reversible thermochemical reactions. In particular, sorption thermal energy storage (STES) systems have recently shown a great potential in solar heat storage. Their advantages include relatively high storage capacities and the unique capacity to preserve energy for longer periods with limited heat losses. More interestingly, the storing principle relies on well-controlled changes in the chemical potential of a solid material which is far less sensitive to temperature variations between the charging and discharging steps.

In order to reveal the potential of this technology for the building applications, the state-of-the-art of the STES systems has been published in the form of a critical review untitled "A critical review of solid materials for low-temperature thermochemical storage of solar energy based on solid-vapour adsorption in view of space heating uses", *Molecules* 2019, 24, 945 DOI:10.3390/molecules24050945.

I.2. Manuscript published in the *Molecules* journal

molecules

MDPI

Review

A Critical Review of Solid Materials for Low-Temperature Thermochemical Storage of Solar Energy Based on Solid-Vapour Adsorption in View of Space Heating Uses

Hao Wu, Fabrice Salles and Jerzy Zajac *

Institut Charles Gerhardt Montpellier – UMR CNRS 5253, UM, ENSCM, Place E. Bataillon, CEDEX 05, 34095 Montpellier, France; hao.wu@umontpellier.fr (H.W.); fabrice.salles@umontpellier.fr (F.S.)

* Correspondence: jerzy.zajac@umontpellier.fr

Received: 11 February 2019; Accepted: 2 March 2019; Published: 7 March 2019

Abstract: The present report deals with low-temperature thermochemical storage for space heating, which is based on the principles of vapour adsorption onto solid adsorbents. With the aim of obtaining comprehensive information on the rationalized selection of adsorbents for heat storage in open sorption systems operating in the moist-air flow mode, various materials reported up to now in the literature are reviewed by referring strictly to the possible mechanisms of water vapour adsorption, as well as practical aspects of their preparation or their application under particular operating conditions. It seems reasonable to suggest that, on the basis of the current state-of-the-art, the adsorption phenomenon may be rather exploited in the auxiliary heating systems, which provide additional heat during winter's coldest days.

Keywords: energy storage; low-temperature thermochemical storage; space heating uses; solid-vapour adsorption; open sorption systems; adsorption of water vapour; moist-air flow operating mode; porous adsorbents

1. Introduction

The rapidly growing global population together with the general expectation for further improvement of life standards in different parts of the world are generating an unending spiral of increasing consumption of food and use of energy and thus have an enormous impact on the ecosystem. Over the past few decades, the overwhelming conviction has emerged that planning and operation of energy supply and energy usage are essential to keep the balance between the necessity of assuring permanent access to energy for the greatest possible proportion of the world population at affordable costs and the objectives of resource conservation, climate protection, and cost savings. As a notable example, the European Community has launched the "Europe 2020 strategy" including ambitious targets for reductions of greenhouse gas emissions, the use of renewable energy, and energy efficiency [1]. The research and development of a renewable energy plan has become imperative to tackle these environment and development issues, especially in relation with the use of energy in the building sector which is at a critical state in many developed countries [2–5] (e.g., building applications account for over 40% of total energy usage and 36% of CO_2 emission in the European Union). Furthermore, the greatest part of this energy usage in buildings is connected with space heating (e.g., over 60% in 2015 according to the French Environment and Energy Management Agency, ADEME [6]), and a long way ahead of electrical devices and domestic hot water supply. Several important initiatives have been taken by regional authorities to promote low-energy buildings using active solar and passive solar systems both to harness the energy and to reduce the overall energy

usage. Converting sunlight into heat and electricity remains certainly one of the most efficient solutions to reduce greenhouse gas emissions to safer levels in numerous countries located in regions of high annual solar radiation, e.g., in China, Japan, United States, India, or some parts of the European Union [7–10]. Nevertheless, in many regions around the world, important fluctuations of energy supply due to the intermittent nature of such a renewable energy source, progressing decentralization of energy conversion and supply, as well as the time and rate mismatch between supply and demand of energy may have serious repercussions on the short- and long-term effectiveness of the implemented solar technologies. In consequence, there is a growing need for adequate energy storage systems so as to solve many of the specific problems related to the energy management.

The existing technologies for short-term thermal energy storage in building applications are mature and robust enough to manage the daily mismatch between the energy supply and demand [11–17]. For any method of thermal storage, high-temperature solar energy is used in the initial step (i.e., *charging step*) to drive the underlying reactions or phenomena in the endothermic direction. The energy stored in the products is released on demand (i.e., *discharging step*) by lowering the temperature of the storage system and thus driving the reactions or phenomena in the exothermic direction. The selection of appropriate materials is a determinative point, which is done according to some common criteria, the most important being: (i) high energy density (i.e., the energy released in one charging-discharging cycle by a unit volume or mass of the working material), (ii) minimum deterioration in performance or degradation of the working material with repeated cycling, mostly related with the thermodynamic reversibility of the underlying reactions or phenomena, as well as the thermal stability of the material. Depending on the particularity of the storage method and construction of the storage unit, the choice is usually made for low-cost and non-toxic materials with low volume and weight. The sensible heat storage based on the heat capacity of the working material and the latent heat storage making use of a material which stores heat while changing phase or dissolving in an aqueous solution have been implemented industrially on large scale [18]. Nevertheless, they may be accompanied by a great loss of energy and costly investment in thermal insulation (c.f., Table 1).

Seasonal solar energy storage for space heating is an important challenge because the storage unit should store energy for many months (e.g., summer-winter cycle changeover) and release it without much loss. Since the investment costs of high-performance thermal insulation are prohibitive, thermochemical storage using chemical potential changes may be considered as the best compromise solution [14]. Theoretically, energy stored as chemical potential is not subject to thermal loss through the insulation and unlimited charging-discharging cycles can be envisaged. Moreover, most suitable reversible chemical reactions or sorption phenomena produce heat effects which are often one order of magnitude higher than latent heats of fusion and condensation. This category of storage systems is very heterogeneous and includes, among others, sorption phenomena, e.g., adsorption at the solid-gas interface, absorption of vapours in liquids [14], as well as reversible thermochemical reactions, e.g., carbonation or hydration of calcium, strontium, and barium oxides, sulphur-based redox cycles, metal oxide reduction–oxidation or perovskite-type hydrogen production [19–21]. The thermochemical reactions where the energy storage principle involves the breaking and forming of chemical bonds usually have high energy densities ranging between 1440 and 3960 MJ m^{-3} (i.e., between 400 and 1100 kWh m^{-3}). However, high temperatures (over 773 K) are generally required during the charging step, which makes such storage systems more appropriate for application in solar power plants where the solar heat is used directly to drive the reaction. Furthermore, the process flow diagrams for the energy storage cycle may be quite complex, thus contributing to higher cost and complexity of design for the material containers and auxiliary systems required for storage and delivery of energy.

Table 1. Physical properties of representative materials for thermal and thermochemical energy storage illustrating their storage performances [22–24].

Physical Property or Characteristics	Heat Storage Principle and Working Materials					
	Sensible Heat Storage		Latent Heat Storage		Adsorption Heat Storage	
	Water	Rock	Paraffin Wax	$CaCl_2.6H_2O$	Silica Gel/Water	Zeolite/Water
Latent heat of fusion (kJ kg^{-1})	-	-	174.4	160	-	-
Specific heat capacity (kJ kg^{-1} K^{-1})	4.18	0.9	-	-	1.13	1.07
Heat of adsorption (kJ kg^{-1} solid)	-	-	-	-	1380	1107
Density (kg m^{-3})	1000	2240	1802	1830	600	650
Volume of material for storing 1GJ (m^3)	4.8	9.9	3.2	3.4	1.2	1.4
Heat storage density (MJ m^{-3} solid)	209	100	310	292	767	713
Advantages	(1) simplicity of design and use (2) low implementation costs		(1) lower heat loss		(1) higher storage density (2) smaller volume of working materials (3) very low heat loss (4) lower charging and discharging temperatures	
Weaknesses	(1) low energy density (2) high heat loss (self-discharging effects possible) (3) space limitations (large volume of working materials)		(1) low thermal stability (risk of chemical decomposition at high temperatures) (2) costly investment in thermal insulation		(1) complexity of design and use (2) higher investment costs (3) heat and mass transfer limitations	

This review presents the state-of-the-art of research, which associates proposals for the use of solid materials as adsorbents in *low-temperature thermochemical energy storage by adsorption at the solid-gas interface* together with collection of fundamental data on which to base the rationalized approach to materials selection. Although the subject has been already treated in numerous review articles [14,15,22,25–28], the presentation of potential adsorbents is usually placed in a broader context of thermal and thermochemical storage of energy and, consequently, the particularity of the present case escapes readers' attention. Other and rarer articles on sorption heat storage focus on more or less advanced system prototypes making use of specific materials in a restricted number [28]. As a result, there is still a need to critically assess the potential candidates by referring strictly to the possible adsorption mechanisms, as well as practical aspects of their preparation or their application under particular operating conditions. The aim is to consider the impact the materials selection would have on the performance and durability of the storage cycle and thus on a successful technology implementation. The necessity of filling this gap has been the main motivation behind the present review. Finally, it has been also decided to put the emphasis on the adsorption of water vapour onto appropriate porous adsorbents, given the fact that this system was by far the most frequently reported case in the scientific literature on the subject, apparently posing less serious security and environmental threats or technical challenges.

From the fundamental point of view, the effectiveness of any heat storage unit mainly relies on reversible thermal phenomena or reactions which support the storage principles. In the context of heat storage by adsorption at the solid-gas interface, it should never be forgotten that adsorption arises due to presence of unbalanced forces at the surface of a solid phase and it can follow various reaction pathways controlled not only by the composition of an adsorption system but also by the experimental conditions applied. Since the phenomenon may switch from one pathway to another under different temperature and pressure regimes, the variability of operating conditions, unavoidable in industrial practice, will affect the adsorption reversibility and thus the quantity of energy exchanged with the surroundings during each discharging step.

Reversible adsorption of vapours onto high surface area solids actually appears to be the most promising alternative for thermochemical energy storage, especially in view of space heating uses. It is certainly worth noting here the first practical use of 7000 kg of zeolite 13X beads in energy storage on district heating net in Munich to store about 4680 MJ (i.e., 1300 kWh) during off-peak hours for the subsequent heating of a school building [13,14]. Two examples of solid materials (i.e., silica gel and zeolite) considered for the purpose of thermochemical heat storage by adsorption are given in Table 1; their physical properties and storage performances are compared with those of representative materials used in thermal energy storage.

2. Adequacy of Adsorption Phenomena in Heat Storage

Depending on the chemical nature of oncoming gaseous molecules (i.e., *adsorbate*) and the surface chemical state of the solid substrate (i.e., *adsorbent*), relatively weak intermolecular forces (mostly of the Van der Waals type) or stronger chemical bonds (e.g., hydrogen bonding, charge-transfer interactions, covalent bonds) operating between the adsorbate molecules and atoms, molecules or ions located at the adsorbent surface are responsible for physical or chemical adsorption at the Solid-Gas interface [29–32]. Some fundamental differences between chemisorption and physisorption fall within the context of the present energy storage applications.

Physical adsorption is an essentially exothermic phenomenon but it produces lower heat effects (25 kJ released at most per mole of gas adsorbed on the surface) and becomes significant when the gas adsorbs near or below the temperature of gas-liquid phase transition. One notable exception is the case of physical adsorption within micropores (i.e., *micropore filling* mechanism): when such pores are sufficiently narrow (in comparison with the size of adsorbing molecules), the enhancement of adsorption energy may result in higher heat values [33,34]. Physisorption does not require any activation energy and equilibrium is rapidly established provided that the adsorption kinetics is

not delayed by the mass transfer in the gaseous phase or diffusion inside the pores of a porous adsorbent. Generally, physisorption is easy to reverse simply by application of heat and/or vacuum (i.e., *desorption*). It should, however, be borne in mind that the phenomenon may become irreversible when the pore space in some mesoporous solids is filled with condensed liquid from the gas phase at higher relative pressures (i.e., *capillary condensation* mechanism).

In contrast to physical adsorption, chemisorption does not diminish rapidly with temperature elevation and it is accompanied by much higher heat effects, often exceeding 100 kJ mol^{-1} due to chemical bonds formed between the adsorbing molecules and the adsorbent surface. In the present context, it should be realised that, in very rare cases, chemisorption may have an endothermic character if it is accompanied by the dissociation of the adsorbed molecules on the solid surface (i.e., dissociative chemisorption) [35–37]. Given the nature and strength of adsorbate-adsorbent interactions involved, chemical adsorption occurs only if the adsorbate enters into direct interaction contact with the active surface (i.e., *localized monolayer adsorption on active surface sites*). It usually requires activation energy and is very difficult to reverse by vacuum treatment. In this case, desorption can be induced by a special treatment under severe conditions, e.g., high-temperature heating, ionic bombardment, and reductive or oxidative processes. In consequence, both the chemical structure of the adsorbing gaseous molecules and the adsorption properties of the adsorbent greatly change during adsorption.

The above short discussion on the differences between physical and chemical adsorption highlights a number of important issues that deserve special attention of researchers, engineers and technicians when selecting adsorbate-adsorbent couples appropriate for thermochemical energy storage based on solid-vapour adsorption. Within the same category of adsorption phenomena occurring for given adsorbate and adsorbent, the detailed mechanism and thus the amount of heat released during the discharging step may strongly depend on the experimental conditions applied, mostly the temperature and composition of the gas phase. Furthermore, physical and chemical adsorption phenomena are not exclusive and can occur on the same adsorbent surface in various experimental regimes (e.g., chemical adsorption of basic molecules on surface acid sites of mineral oxides followed by the formation of physically adsorbed multilayer [38–41]). In addition, when the gas phase is not pure but represents a gas mixture (e.g., water vapour, carbon dioxide and other gases in ambient air), adsorption often becomes a selective process as a result of the competition amongst the gas components for being retained on the adsorbent surface [42,43].

Finally, solid-gas adsorption may be used to underpin the working principle of a heat storage unit provided that the charging step in the storage process will be based on endothermic desorption and the discharging one on exothermic adsorption, according to the following reaction scheme, at fixed temperature, T, and equilibrium gas pressure, p:

$$n_a \cdot G - S + Q_a \rightleftarrows n_a \cdot G + S \tag{1}$$

where G and S denote, respectively, the gas and solid components of the working couple, n_a is the amount of gas adsorbed on the adsorbent surface, $n_a \cdot G - S$ stands for the working couple in a given adsorption state, Q_a is the *integral heat of adsorption* measuring the total energy change in both directions of the reversible process; the symbol S on the right hand side of Equation (1) refers to the adsorbent possessing a fully clean surface after a complete desorption of the adsorbate. The integral heat released upon exothermic adsorption is related to the *differential heat of adsorption*, q_a, defined as a partial derivative of the energy change of the system with respect to the quantity of adsorption (it can be thus regarded as a consequence of adsorbing infinitesimal amounts of gas); hence [44,45]:

$$Q_a = \int_0^{n_a} q_a dn_a \tag{2}$$

For a selected adsorbate-adsorbent couple performing at a given temperature, the amount of gas adsorbed and the differential heat of adsorption may change when the composition of the gas phase varies during the storage process. An *adsorption isotherm* representing the quantity of gas adsorption at a constant temperature as a non-decreasing function of the equilibrium gas pressure, p, i.e., $n_a = n_a(p)$, is the most common representation of adsorption. The differential heat of adsorption is usually plotted against the amount adsorbed, i.e., $q_a = q_a(n_a)$, and is determined either experimentally by direct calorimetry measurements or numerically from the temperature dependence of the adsorption isotherms (i.e., the so-called van't Hoff procedure) [31,46,47]. The latter procedure is usually applied to compute the so-called *isosteric heat of gas-phase adsorption* from experimental measurements, on the basis of the following expression [48,49]:

$$q_a^{st} = RT^2 \left(\frac{\partial lnp}{\partial T} \right)_{n_a} \quad (3)$$

Since the pressure p and temperature T are independent variables in such systems, the pressure may be tuned to hold the amount adsorbed n_a constant. It is worth noting here that, under equilibrium conditions, physisorption is sensitive to the energetic heterogeneity of solid surface which manifests itself as a monotonous decrease in the differential heat released when the amount of gas adsorbed increases [50]. On the contrary, chemisorption on the same surface sites is usually characterized by a constant differential heat, and hence by an integral heat increasing linearly with increasing n_a value.

In conclusion, the integral heat of adsorption and thus the energy storage density will be controlled by various physical factors which affect the amount adsorbed and differential heat of adsorption in strict relationship with the operative adsorption mechanism: chiefly, temperature, composition of the gas phase, specific surface area and mass of the adsorbent or accessibility of the porous structure of the adsorbent as a function of the adsorbate size and nature. Therefore, *to justify the selection of a new working couple*, adsorption isotherms and the related heat curves should be measured as systematically as possible under real conditions of use.

3. Practical Aspects of Heat Storage by Adsorption in Reference to Adsorption Mechanisms

The plant operating conditions under which the heat storage process is implemented may differ, sometimes significantly, from those used when the theoretical storage performance of a given working couple (i.e., adsorbate and adsorbent) has been tested in laboratories. Given the sensitivity of certain adsorption mechanisms to experimental conditions, this difference will inevitably result in altered performance of the real storage system and, therefore, should be taken into account at each stage of the design process.

The main point to be stressed here relates to the way in which adsorption and desorption procedures are carried out. In research laboratories, gas adsorption onto solids is routinely measured under conditions necessary to achieve adsorption equilibrium for each point of the adsorption isotherm in a static volumetric apparatus [32,51,52]. In such measurements, calibrated doses of a single reactive gas are brought into contact with the surface of the previously weighed adsorbent by means of an injection system equipped with a valve, the operating principle of which is based on pressure differences. Prior to adsorption experiment, the process of desorption is accomplished by degassing with the use of a high-performance vacuum pump. Economically speaking, *vacuum degassing is an energy-consuming process and, as such, it is not recommended for the charging step in heat storage units*. Perhaps the most convincing argument against this solution is that, once the degassing operation is completed, the adsorbent itself cannot be efficiently transported to a vacuum chamber or stay in a perfect vacuum inside the reactor during several hours or several months up to the next discharging step; the construction of gas-tight containers would be cost-prohibitive.

Adsorption and desorption procedures under dynamic gas flow conditions in which a non-adsorbing gas is constantly flowing through the adsorbent bed at a given flow rate do not require the use of vacuum and are thus more feasible to implement [32]. In adsorption, the flow of the

neutral gas plays the role of a carrier medium for the reactive gas and the adsorption isotherms agree quite well with those obtained by vacuum volumetric measurements on a large variety of samples. In desorption, the desorbed molecules are swept from the adsorption chamber via the continuous flow of inert gas. The partial pressure of the adsorbate released from the adsorbent surface to an inert stream is claimed to decrease in a manner similar to that monitored when applying the vacuum technique [53]. Moreover, a faster degassing is expected since the adsorbate species gain additional energy during collisions with the inert gas molecules striking the solid surface.

Whatever the technique used, simultaneous heating of the solid sample is a very efficient way to increase the degassing rate. Nevertheless, the quantity of exothermic adsorption will decrease at higher temperatures. Therefore, there is no point in applying the same temperature during the charging and discharging steps in order to comply with the reaction scheme given by Equation (1). The thermal energy collected from the sun is exploited during the charging step to purify completely the adsorbent surface. Basically, the temperature of desorption should generally be a compromise between the long-term thermal stability of the adsorbent and the efficiency in adsorbent regeneration. Then, the stability of this temperature will depend on the type of solar thermal collectors, heat exchangers, and heat transfer fluids employed in practice [54,55]. Contrary to the solution applied in solar power plants, mild charging conditions will be searched in heat storage by adsorption because even crystalline inorganic porous solids may undergo different structural and textural changes upon heating, especially when subject to a great number of repeated charge-discharge cycles [56–58].

In light of the above considerations, the energy storage density will be thoroughly controlled by the heat of adsorption released during the discharging step under the real experimental conditions applied. In order to avoid heat losses and investment costs in thermal insulation, the discharging step should be carried out at temperatures close to ambient [59,60]. This operating temperature limits the number of gases to be used as adsorbates. For illustrative purposes, physical and chemical properties of several potential candidates have been collected in Table 2. Helium and air, as well as the two major components of air, i.e., nitrogen and oxygen, cannot be physically adsorbed under ambient conditions because of their low critical temperatures. On the contrary, they may be used as neutral carrier gases or even heat transfer media, especially helium which is characterized by a higher thermal conductivity (*conductive heat transfer*) and a comparable heat capacity (*convective heat transfer*). Helium molecules have a small kinetic diameter which enables them to penetrate into smaller pores of porous adsorbents. Nevertheless, the possibility of taking air from the atmosphere for free or at negligible cost is certainly the main advantage of using it as the heat transfer fluid; any leakage from the storage unit will not cause environmental problems. Consequently, the endothermic desorption in the charging step may be performed by making use of ambient air with low levels of critical impurities (e.g., water vapour and carbon dioxide) pre-heated to a given temperature by simple solar air collectors [61–63].

From a thermodynamic viewpoint, other gases included in Table 2 are considered as potential candidates for adsorbates in the heat storage units. Polar water, ammonia, and alcohol molecules can be physisorbed on any polar or polarizable surface sites, whereas non-polar CO_2 with a total static polarizability of 2.86×10^{-30} m^3 in the gas phase [64] can interact via Debye induction or London dispersion forces. In comparison with ammonia and carbon dioxide, higher enthalpies of vaporization for water, methanol, and ethanol suggest a potential for higher energy densities in a storage system based on physical adsorption. On the other hand, ammonia and carbon dioxide are characterized by much higher vapour pressures [65], thereby providing an advantage in terms of increased quantities of adsorption and reduced mass transport limitations.

According to other data reported in Table 2, some of these gases can be chemisorbed onto solids that possess adequate active sites on the surface. More or less strong chemisorption from the gas phase will occur chiefly through acid-base interactions leading to the formation of surface donor-acceptor adducts, which include hydrogen bonds accompanied or not by a proton transfer (the stronger the H-bond the easier is the proton transfer) or covalent bonds for a typical Lewis acid-base pair. In line with higher proton affinities, molecules of water, ammonia and ethanol represent strong Brønsted

bases in the gas phase, capable of being chemisorbed on a solid surface having Brønsted acid sites (e.g., hydroxyl groups on mineral oxides). Simultaneously, they may act as hard Lewis bases, thereby bonding to such hard Lewis acid sites as extra-framework cations Al^{3+}, Li^{+}, Mg^{2+}, Na^{+}, or Ca^{2+} (their acid hardness parameters are 45.8, 35.1, 32.5, 21.1, 19.7 eV, respectively [66]), which occur in solids containing compensating cations (e.g., zeolites or clays). As a hard Lewis acid, carbon dioxide will form donor-acceptor adducts with hard Lewis base sites (e.g., extra-framework F^{-}, OH^{-}, Cl^{-} anions with base hardness parameters equal to 7.0, 5.6, 4.7 eV, respectively [66]). On the other hand, water and alcohols may also exhibit acidic character; the order of decreasing gas-phase acidity is as follows: $C_2H_5OH > CH_3OH > H_2O$ [67].

It should be also mentioned here that the flammability of adsorbate vapours creates potential safety issues and may restrict their use in heat storage. If a given adsorbate has negative health and environmental impacts, or when its contact with air is to be avoided for safety reasons, the heat storage unit should operate in a *closed sorption system* [68]. This technical solution precludes the release of the working gas to the environment and the exchange of thermal energy between the system and its surroundings is realized through appropriate heat exchangers. The gas desorbed from the adsorbent under the action of heat (e.g., via the internal heat exchanger) during the charging step flows into a liquefier, releases energy to the heating system, condenses and is stored on site in liquefied form, as depicted schematically in Figure 1. When the exothermic adsorption is to be carried out in the discharge mode (e.g., during winter), an external power source is necessary to transform the liquefied adsorbate back into vapour. Therefore, the closed storage systems require the presence of two storage tanks, one for the adsorbent and the other for the liquefied adsorbate. Such systems are suitable rather for small-scale applications [14].

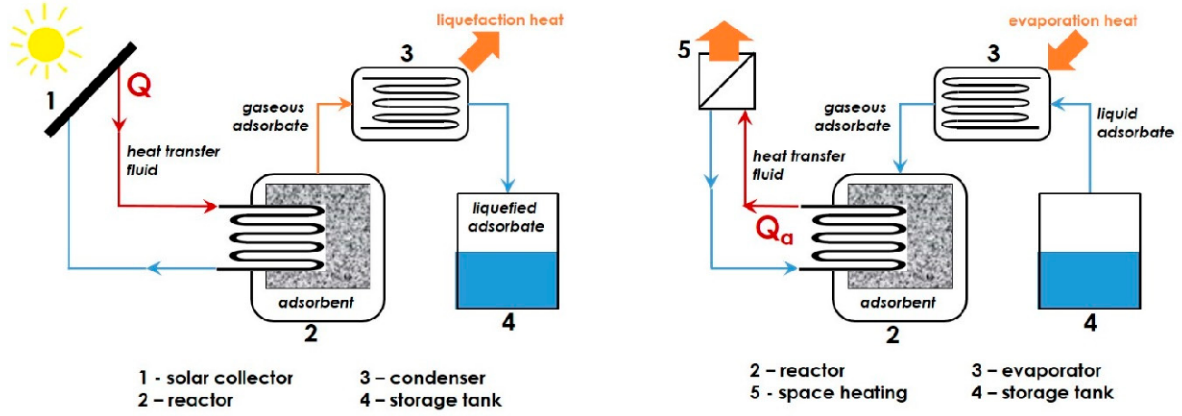

Figure 1. Simplified flow-sheets of the charging (left panel) and discharching (right panel) stages in the low-temperature thermochemical storage of solar energy based on Solid-Vapour adsorption in a closed sorption system.

Its sheer availability, low cost, non-flammability, and non-toxicity have made water vapour by far the most frequently studied adsorbate for the thermochemical energy storage by Solid-Gas adsorption [27,69–71]. In particular, this is the best candidate to be used in *open sorption systems*, together with porous adsorbents possessing a hydrophilic surface [15,63,72]. The temperature of the discharging step should range between 273 and 373 K (i.e., between 0 and 100 °C), unless antifreeze additives are added to or the adsorbate vapour is pressurized. Simplified flow-sheets of the charging and discharging stages are given in Figure 2 for illustrative purposes. During the charging step, the adsorbent is chiefly dried (i.e., endothermic desorption of water vapour) and the heat required for drying is provided to the reactor by an air flow of low relative humidity pre-heated due to harnessing solar energy or another heat source. Then, the dried adsorbent remains in the reactor filled with dry air at ambient temperature for a desired period of time until the next discharge phase. Classically, the adsorption onto previously dried adsorbent is carried out in the "*moist-air flow*" mode by using

outdoor air brought inside and additionally saturated with water in order to produce a gaseous flow with a stable humidity rate at a given temperature. The released heat of adsorption renders the air flowing out of the reactor warmer, thereby allowing its direct use for heating. The necessity of pre-heating intake air to the temperature of adsorption certainly reduces the overall efficiency of the storage process. However, this problem may be avoided quite easily by employing an additional heat exchanger where the heat from exhaust gas is transferred to the inlet air, as has been proposed within the framework of the German MONOSORP project [68]. In the particular case of space heating, the adsorbate can be removed directly from the inside of the heated building. The investment costs being lower than those associated with the closed systems, coupled with better heat and mass transfer conditions, as well as lower temperatures required for adsorbent regeneration, are sufficiently compelling arguments in favour of the open adsorption units [73,74]. Nevertheless, working with ambient air may present increased risk of competitive adsorption of water vapour and such major air impurities as CO_2, likely resulting in the disturbance of the thermal balance underlying the heat storage process.

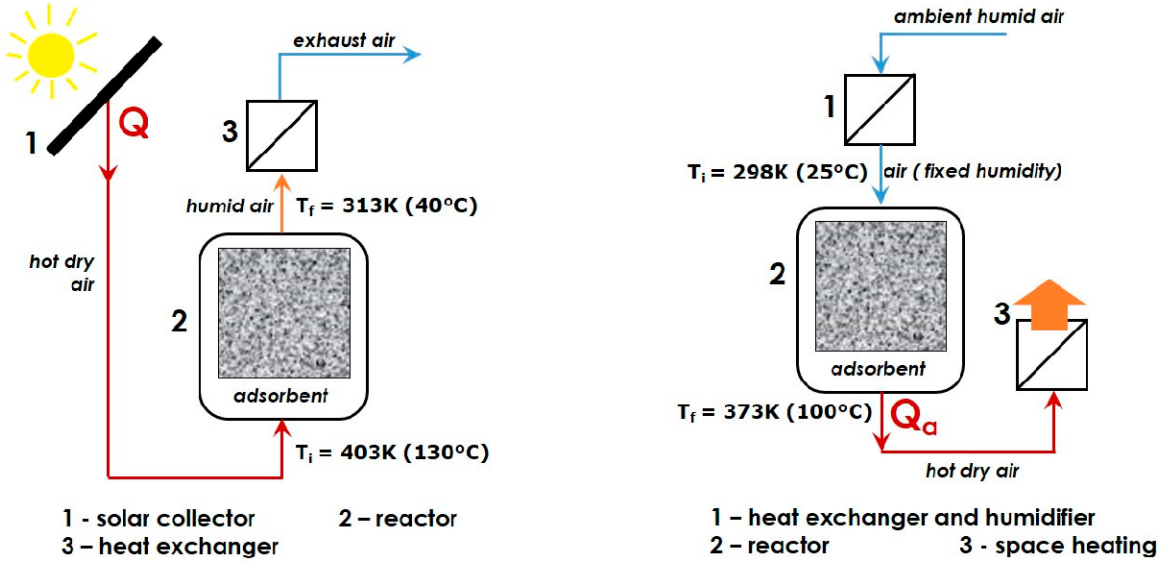

Figure 2. Simplified flow-sheets of the charging (left panel) and discharching (right panel) stages in the low-temperature thermochemical storage of solar energy based on adsorption of water vapour onto solid adsorbents in an open sorption system. Just to give the Reader an indication of the inlet, T_i, and outlet, T_f, temperatures at the reactor level, the experimental values have been taken from Ref [75].

Finally, the kinetics of adsorption may also affect the efficiency of the storage process. Indeed the rate at which the adsorbate is retained on the adsorbent surface will impact the heat and mass transport during adsorption, in relation with the thermal conductivity and specific heat capacity of the adsorbent used, composition and temperature of the inlet gas, type of the adsorbent bed, as well as the reactor dimensions [13,57,76,77]. With a fixed bed adsorption process in an open sorption system using air as the carrier gas, the temperature distribution at different positions within the reactor and, what is most important in view of space heating applications, the rate of adsorbate depletion in the outflowing air and the temperature variations of the latter are kinetics-sensitive technical characteristics. Appropriate adsorption kinetics resulting in a high thermal power output is considered as having a beneficial effect on the performance of the storage system [77]. On the other hand, such parameters as the volumetric feed-gas flow rate and feed composition, or mass of the adsorbent should be carefully optimised so as to control the length of time during which the total saturation of the adsorbent with the adsorbate is to be achieved, the stability in time of the output temperature, and thus the duration of the heating cycle.

Table 2. Physical and chemical properties of some selected substances encountered in thermochemical heat storage by adsorption at the Solid-Gas interface [66,78–81].

Substance	H_2O	NH_3	CO_2	C_2H_5OH	CH_3OH	N_2	O_2	He	Air (Dry)
Critical temperature (K)	647	405.3	304	513.9	512.4	126	154.4	2	132.5
Boiling point at 10^5 Pa (K)	373	239.7	194.5	351.3	337.6	77	90	5	-
Enthalpy of vaporization (kJ mol^{-1})	40.65	23.4	15.3	38.56	35.21	5.57	6.82	0.08	-
Saturated vapour pressure at 293 K (kPa)	2.34	857.1	$5.7 \cdot 10^3$	5.8	12.8	-	-	-	-
Isobaric heat capacity in the gas phase at 300 K and 10^5 Pa (J mol^{-1} K^{-1})	33.6	37.0	36.94	74	44.1	29.2	29.4	20.8	9.15
Thermal conductivity in the gas phase at 300 K and 10^5 Pa (mW m^{-1} K^{-1})	18.7	24.4	16.8	14.4	$26.2^{400\ K}$	25.8	26.3	156.7	26.2
Kinetic diameter of molecules (nm)	0.265	0.260	0.330	0.450	0.360	0.364	0.346	0.260	-
Dipole moment for molecules in the gas phase (in debyes)	1.85	1.47	0	1.69	1.7	0	0	-	-
Proton affinity (kJ mol^{-1})	697	853.5	548	788	761	495	422	178	-
Absolute hardness parameter (eV)	9.5	8.2	8.8	8.0	5.8	8.9	5.9	-	-

Flammability: Water and carbon dioxide are not flammable and cannot be ignited; the flammable range of NH_3, C_2H_5OH, and CH_3OH in air is (in percent by volume): 15–28, 3–19, and 6–37, respectively [82]. Toxicity: Ammonia vapours are highly toxic through inhalation and lead to irritation of the skin, eyes and respiratory tract [83]; they are corrosive upon contact and their use with copper or its alloys is to be avoided. Carbon dioxide (at concentrations in air greater than 10%) presents both acute and long-term toxicity with respect to the lungs, the cardiovascular system, and the bladder, showing inflammatory and possible carcinogenic effects, as well as it may induce multiple foetal malformations [84].

4. Comments on the Criteria for Selection of Working Materials as Adsorbents

Given the variety of technical problems associated with the available storage technologies, it is quite difficult to propose clear criteria for the selection of best adsorbents to be used in thermal energy storage by solid-gas adsorption. This difficulty lies in the fact that many of the criteria reported in the literature are contradictory or inconsistent [4,14,21,22]. Rather than wishing to find the perfect adsorbent, it should be admitted that suitable materials and systems depend on the task they have to fulfil under specific conditions.

In a more general sense, the working adsorbent-adsorbate couple has to insure high energy density and high energy efficiency while reducing investment and operating costs and minimizing the environmental issues and risks involved. Based on the considerations made in the two previous sections, good candidates for adsorbents may be evaluated with regard to:

(1) Specific surface area and pore volume for high adsorption capacity towards the selected adsorbate,
(2) Affinity between the active surface of the adsorbent and the adsorbate for high heat of adsorption,
(3) Selectivity towards a given adsorbate when adsorbed from a gas mixture,
(4) Ability to provide appropriate mass transport and kinetics of adsorption,
(5) Thermal conductivity and specific heat capacity for good heat transfer from/to the adsorbent bed,
(6) Ease of regeneration, thermal and chemical stability, and usable lifetime under operating conditions for long-term resistance to repeated cycles of charging and discharging,
(7) Toxicity, environmental impact, corrosiveness, flammability, and compatibility with materials of construction,
(8) Cost, availability, ease of handling, ease of shaping and up-scaling.

The above list is certainly not exhaustive, but it gives an idea of the needs and possibilities for optimising materials design. Some critical remarks about the general strategy for materials preparation and optimisation are given below.

The intra-particle porosity is one of the principal characteristics of the adsorbents that are pertinent to their use in thermochemical energy storage. The adsorption phenomena should be carried out making use of mesoporous (pore size in the range of 2–50 nm) or/and microporous (pore size less than 2 nm) solids in order to enhance the adsorbate uptake and intensify the heat exchange during each charge-discharge cycle [16,57,69,70,77,85–94]. This is the best way to increase the specific surface area, in line with the first criterion. Indeed, the specific surface areas of meso- and microporous adsorbents are in the range of hundreds or even thousands of square meter per gram (e.g., the highest experimental BET surface areas on the order of 7000 $m^2\ g^{-1}$ have been reported for metal–organic framework materials [95]), contrary to macroporous (pore size greater than 50 nm) or non-porous substrates with specific surface areas rarely exceeding 100 $m^2\ g^{-1}$.

High binding affinity and selectivity recommended according to the next two criteria are achieved essentially in three different ways: (i) careful matching of the chemical character between the adsorbate and the adsorbent surface (e.g., hydrophilic surfaces to adsorb water vapour), (ii) the use of solid substrates possessing uniform pores capable of confining selectively the main component of the gas mixture on the basis of differences in molecular size, (iii) surface modification of the existing supports by physical or chemical deposition of appropriate functionalities that will provide active sites for electrostatic or chemical binding of polar adsorbates [91,96–99]. For materials possessing charged surfaces, the substitution of the original charge-compensating ions by higher valence counter-ions has been also tested for energy storage by adsorption of polar vapours [100]. With small-pore supports, special attention should be paid to the functionalization procedures in order to prevent the modification of pore accessibility or even blocking the entrance of some pores [91].

Nevertheless, the main drawback of porous solids, and the microporous ones in particular, is their great sensitivity to deactivation by insufficient regeneration, which may compromise the reversibility of the charge-discharge cycle upon energy storage. It is worthwhile noting here that the insufficient regeneration usually leaves the adsorbate species held most strongly on the adsorbent

surface, i.e., the molecules which have been retained on adsorption sites characterized by the maximum energy of adsorption. Enhanced adsorption affinity and selectivity of the adsorbent towards the adsorbate molecules may pose similar regeneration issues, even though the adsorbent is non-porous or macroporous. In all such cases, harsh desorption conditions are usually necessary upon the charging phase to restore the maximum energy during the discharging step. High regeneration temperatures, in turn, can affect the structural integrity of the adsorbent and contribute to the complexity of the heat exchange processes and devices.

In addition, it is a technical challenge to keep the degassed adsorbent away from the adsorbate from the end of the charging phase until the subsequent adsorption step (i.e., maintain the perfect vacuum in closed sorption systems or keep the trapped air perfectly dry in open sorption systems). The use of adsorbents able to adsorb great amounts of adsorbate at low vapour pressures seems rather prohibitive.

It should also be remembered that the bulk and surface diffusion of the adsorbate in porous media often has a negative impact on the adsorption and desorption kinetics [101,102]. Size exclusion effect may even prevent the active surface sites located within very small pores from being accessed by large adsorbate molecules. In consequence, mesoporous materials seem to be the best compromise between high surface area and fast mass transport requirements. A good strategy to manage such kinetics problems lies in developing materials with tailored hierarchical porosity [103].

The use of powdered materials may have the undesirable consequence of increasing the flow resistance, especially in the particular case of open sorption systems. Solid adsorbents in a pre-shaped, monolithic or granular form are recommended to ensure good heat transfer between air flow and adsorbent surface or to reduce the pressure drop across the packed bed of adsorbent [77]. Special attention should be paid to materials up-scaling and shaping procedures when elaborating a strategy for large-scale production of materials with controlled properties [104–106]. In practice, the adsorption performance of pre-shaped materials up-scaled from research to industrial production need not always be as high as that evaluated for small powdered samples under idealized laboratory conditions. As an example, the synthesis up-scaling in continuous mode allows avoiding reproducibility and homogeneity issues that may arise due to batch synthesis [104]. Whenever possible, industrial manufacturing processes of powders compaction not requiring a massive addition of fillers and binders to create macroscopic objects of the desired shape and size are preferred because the filler and binder phases often significantly impact the dimensional change, mechanical, and thermal properties of adsorbents, or even can alter their surface properties (e.g., through pore-blocking effects) [107,108]. Direct synthesis routes to produce monolithic materials with hierarchical porosity have been also developed in parallel [109,110].

5. Presentation of Adsorbent Candidates for Adsorption-Based Thermochemical Storage of Energy

In this section, the most pertinent and relevant information is given about the structure and surface properties of potential candidates for adsorbents reported in the literature. In accordance with the arguments put forward in the previous sections, there appears to be much potential for thermochemical storage of energy related with the use of water vapour as the adsorbate. Therefore, the main emphasis here is placed on the type of surface interactions of the selected groups of materials with water molecules in the gas phase, as well as on their structural and textural integrity under hydrothermal conditions. There is also an overview of the principal synthetic routes to obtain target adsorbents or the surface modification procedures to enhance the adsorption properties of the natural solid supports. The more technical details related to their practical use, as considered by research teams in the framework of R&D projects, or inferred from laboratory-scale pilot testing or industrial practice, are presented whenever they have been published in the corresponding articles.

To enable feature comparison, various adsorbent groups are reported in Table 3 together with specific surface area, type of porosity, as well as characteristic adsorption capacity and heat data.

Table 3. Selected groups of materials considered for adsorption-based low-temperature thermochemical storage of energy.

Adsorbent Group	Working Couple	Textural Properties of Adsorbent		Adsorption Performance			Storage Performance Tests		Ref.
		Porosity Type	Specific Surface Area ($m^2\ g^{-1}$)	Capacity ($g\ g^{-1}$)	Heat ($kJ\ mol^{-1}$)	Target Storage Density ($kJ\ kg^{-1}$)	Operating Conditions	Information on Stability	
Amorphous SiO_2	silica aerogel & H_2O	micro-/meso-	783	1.35	-	-	*charging:* vacuum, 343 K, 24 h *discharging:* 293 K	Adsorption greatly decreasing after the first cycle (raw sample: 42%; calcined one: 26%), then remained stable over next 25 cycles	[111]
	silica gel LE32 & H_2O	macro-	-	0.6	25	86	*charging:* 363 K *discharging:* 313 K	-	[23]
Amorphous Al_2O_3	alumina aerogel & H_2O	micro-/meso-	453	1.25	-	-	*charging:* 343 K *discharging:* 293 K	adsorption slowly decreasing within 10 cycles, then remained stable	[111]
	30% alumina + 70% silica aerogel & H_2O	micro-/meso-	577	1.15	-	-		stable over 25 cycles	
Ordered SiO_2	MCM41 & H_2O	meso-	1137	0.04 at $p/p_0 = 0.3$	47–54	-	*charging:* 523 K, 3 h *discharging:* 293 K	-	[92]
	SBA15 & H_2O	meso-	554	0.02 at $p/p_0 = 0.3$	-	-		-	
Salt-oxide hybrids	$CaCl_2$-silica gel KSK (SWS-1L) & H_2O	meso-	230	0.7	43.9–63.1	475	*charging:* 353–423 K	-	[112–114]
	$Ca(NO_3)_2$-silica gel KSK (SWS-8L) & H_2O	meso-	60	0.23	47–52	-	*charging:* 348–353 K	-	[115]
	Al-MCM41 & H_2O	meso-	941–1021	0.17 at $p/p_0 = 0.3$	65	450–612	*charging:* 253 K *discharging:* 293 K	-	[92]
	Al-SBA15 & H_2O	meso-	541–550	0.09 at $p/p_0 = 0.3$	67	227–335		-	
Zeolites	4A & H_2O	micro-	-	0.22	72	670	*charging:* 463 K *discharging:* 298 K	-	[116]
	13X & H_2O	micro-	-	0.34	51.3	536	*charging:* 723 K *discharging:* 300 K	-	[69]
	MgNa-X & H_2O	micro-	-	0.212	53	630		-	
	$MgSO_4$-13X & H_2O	micro-	-	0.15	81.6	648	*charging:* 423 K	adsorption unchanged over 3 cycles	[117]
Zeotype materials	AlPO-18 & H_2O	meso-	-	0.34	55	875	*charging:* 268 K *discharging:* 313 K	-	[87]
	SAPO-34 & H_2O	meso-	-	0.3	56	730		-	
MOF materials	MIL-101 (Cr) & H_2O	meso-	4150	1.6	44.5	-	*charging:* 423 K *discharging:* 303 K	stable over 10 cycles	[118]
	MIL-100 (Fe) & H_2O	meso-	2300	0.87	49.5	-		stable over 10 cycles	

As has been argued before, the storage performance of a given working couple under specific conditions will depend on the mechanism by which water vapour is retained on the solid surface. This mechanism is usually reflected in the particular shape of the adsorption isotherm. Figure 3 shows some representative shapes of adsorption curves for selected adsorbents.

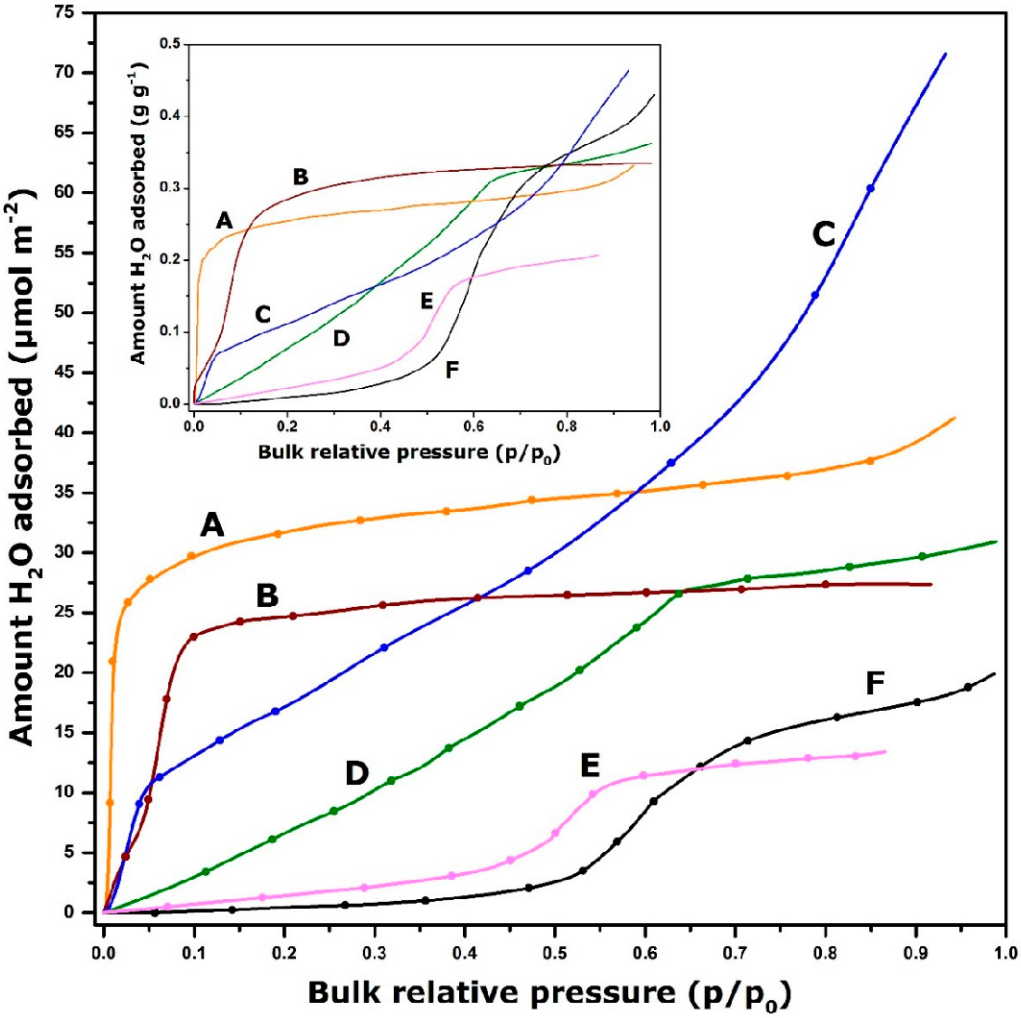

Figure 3. Representative shapes of equilibrium adsorption isotherms for water vapour onto different adsorbents at 298 K (with the exception of silica gel and ionosilica: data at 301 K and 313 K, respectively): zeolite 13X (Curve A); silicoaluminophosphate molecular sieve SAPO-34 (Curve B); activated alumina F-200 (Curve C); silica gel, Mobile Sorbead R (Curve D); ionosilica A-Cl (Curve E); activated carbon BPL (Curve F). The amount of H_2O adsorbed expressed in µmols of adsorbate per unit surface area of the adsorbent. The inset shows the same curves on a different ordinate scale: the quantity of adsorption expressed as mass of the adsorbate per unit mass of the adsorbent. Data adapted from [119–124].

By analogy with the IUPAC classification of experimental adsorption isotherms for gaseous nitrogen at the temperature of liquid nitrogen (77 K) [52,125], zeolite 13X exhibits an isotherm similar to the Type I curve possessing a very steep initial portion and a limiting water uptake at higher relative pressures of water vapour (curve A). These features reflect a high affinity of water vapour towards the solid surface even in the low pressure region. As a consequence, a much deeper regeneration of the adsorbent is needed upon drying (i.e., desorption) to remove all water molecules from the surface by going down to near zero relative pressure or/and by heating up to high temperatures so as to restore the maximum energy during the discharging step (i.e., adsorption). The Type II isotherm has been obtained with activated alumina (curve C). Here there is still a marked affinity

between the adsorbate and the adsorbent and the adsorption phenomenon likely follows unlimited monolayer-multilayer mechanism. In the case of activated carbon (curve F), the adsorption isotherm is convex to the axis of relative pressures up to a p/p_0 about 0.5. This points out the weak interaction of water molecules with a carbonaceous surface, despite the enhancement of the heat of adsorption within the micropores [126]. Further increase in the water uptake in the intermediate pressure region gives rise to the so-called *S-shaped adsorption curve* with the limiting water uptake over a range of high p/p_0 values. An adsorption isotherm of the same shape has been obtained when adsorbing water vapour onto ionosilica (curve E); the point of inflexion is shifted towards lower p/p_0 values. One advantage of such adsorption systems is that it may not be necessary to apply an effective deep vacuum evacuation or a high temperature treatment during the charging step, thereby making the adsorbent regeneration to proceed under milder conditions. For adsorbents giving stepped adsorption isotherms with a hysteresis between the adsorption and desorption branches (e.g., Type V isotherms), the lower is the relative pressure corresponding to the desorption step, the higher the regeneration temperature will be. Curves D and B are an intermediate between Types I and S-shaped isotherms in line with the more or less diminished adsorbent-adsorbate affinity, which manifests itself by a convex shape in the beginning of the adsorption range.

Nonetheless, it should be still remembered that the amount of water vapour retained on the surface, *on a per unit surface area basis*, between the charging and discharging steps is not the only condition to yield high energy gains. Certainly, it is strictly related to the surface density of reactive sites responsible for water adsorption. However, a higher specific surface area often compensates for lower density of surface sites, as is illustrated in the inset graph in Figure 3. Furthermore, the knowledge about the differential heat of water adsorption and its variations with the surface coverage ratio is crucial for the selection of suitable adsorbents.

5.1. Amorphous Silicas and Aluminoslicates

This large class of materials includes silica gels, aerogels, precipitated silica powders, pyrogenic silica, ordered mesoporous silicas and aluminosilicates, silicas and aluminosilicates with hierarchical porosity, silica nanoparticles with different pores, morphologies and sizes, periodic mesoporous organosilicas [127–133].

Pure silica gels are generally obtained by sol-gel processing in aqueous solutions where repeated hydrolysis of silane and condensation of the siloxane bonds result in aqueous polysilicate species evolving under appropriate conditions into essentially anhydrous SiO_2 in monolithic or powdered form. Silica aerogels having a sponge-like porous structure are produced by drying the aged silica gels under conditions necessary to prevent the collapse of the gel structure. Precipitated silica is manufactured by precipitation of sodium silicate by sulfuric acid under aqueous alkaline conditions, while stirring at elevated temperatures to avoid the formation of a gel. Pyrogenic or fumed silica is usually prepared by the hydrolysis of chlorosilane in a flame of hydrogen and oxygen at high temperatures (1273 K or higher). Although the density of pure amorphous silica is about 2200 kg m^{-3}, silica gels, aerogels or pyrogenic silica have much lower bulk densities because of their porosity. Monodispersed silica particles may be also synthesized by the so-called Stöber method in which the hydrolysis of silicon alkoxides occurs in a mixture of alcohol and water when making use of a catalyst. Such silica structures represent 3D networks of silicon-oxygen tetrahedra inter-connected via bridging oxygen atoms. If all tetrahedra possess silicon centres, the whole framework is electrically neutral.

Since the publication of the surfactant-assisted synthesis of periodic mesoporous silica of the MCM-41 type by the researchers of Mobil Research and Development Corporation [134,135], a great deal of effort has been devoted to the preparation of nanostructured oxide materials with tuneable pore sizes and shapes. With the use of supramolecular surfactant or polymer aggregates to template and direct the formation of porous structure based on either the Cooperative Self-Assembly or True Liquid Crystal Templating mechanism, it was possible to ensure, to the maximum extent possible, the control of not only the pore size, shape, and structural hierarchy, but also the size, shape and morphology of

particles. Typical members of this category of silicate materials prepared by ionic and neutral surfactant templating possess framework-confined uniform pores with a tuneable size located near the lower end of the mesopore range and amorphous pore walls of a given thickness; they have large specific surface areas in the order of 1000 m^2 g^{-1} and their porosity may be as high as 80% of the total volume [136–138]. The silica precursor (e.g., fumed or colloidal silica, tetramethyl- or tetraethylorthosilicate-TMOS or TEOS), surfactant template, auxiliary compounds (e.g., 1,3,5-trimethylbenzene, TMB), and reaction conditions (e.g., type of solvent, temperature, aging time, reactant mole ratio, and pH of the reaction medium) can be adjusted to control the pore architecture. Periodic Mesoporous Organosilicas (PMOs) were also developed on a similar basis by the combination of an appropriate surfactant template and a silsesquioxane as the organosilica precursor.

Depending on the chemical character and spatial distribution of functional groups localized on the surface after the synthesis pathway and post-synthesis treatments applied, the above solids exhibit surfaces with more or less pronounced hydrophobic-hydrophilic behaviour when interacting with water in a gaseous state and other polar vapours. The surface chemistry of silica materials may also be modified by a post-synthesis grafting of metal centres or organic functional groups due to the presence of hydroxyl groups that are chemically bonded to silicon atoms on the surface (i.e., external or surface silanol groups) which may act as anchoring sites for metal species or silane/silazane coupling agents for organic moieties [96,130,131,139]). It is also worth noting here that hydrothermal and mechanical stability of the porous structure in silica-based materials are usually regarded as closely related to surface hydrophobicity [131].

There exists an interesting way to create surface acidity on silica. Certain bases (e.g., ammonia, pyridine, or 2,6-dimethylpyridine) initially H-bonded to silanol groups on the silica surface may be protonated upon the addition of gaseous SO_3 or NO_2 [140]. It appears that sufficiently strong Lewis acids can interact directly with the oxygen atom of a silanol group (i.e., nucleophilic attack on the acid by the lone pairs on oxygen). Chemisorption of SO_3 or NO_2 molecules followed by a proton transfer from the silanol to the oxygen atom of the covalently bonded acid group leads to the formation of $S-OH$ or $N-OH$ functionalities with induced Brønsted acidity. Alternatively, a great variety of materials with enhanced surface acidity or basicity (e.g., amino, carboxylate or dihydroimidazole surface groups) for capture of basic or acidic gases may potentially be prepared through chemical modification with functionalized alkoxysilanes directly during the synthesis (i.e., co-hydrolysis with the appropriate silica precursor). In the case of aluminosilicates, the substitution of silicon atoms in their tetrahedral positions by aluminium ones, via one-pot direct synthesis using an adequate mixture of precursors, creates a negative charge which is neutralised mostly by protons or alkaline cations. It should be, however, noted that the degree of such an isomorphous substitution strongly depends on the preparation method and the aluminium precursor, frequently resulting in the appearance of extra-framework species (e.g., octahedrally co-ordinated aluminium) [130].

As a final remark, it is important to highlight here that the use of hybrid organic-siliceous materials for heat storage should be generally excluded not only when the surface reactivity towards water vapour is reduced to a considerable extent (e.g., hydrophobized surfaces), but also when the thermal degradability of organic moieties exposed on the silica surface could compromise the stability of repeated charging-discharging cycles.

5.1.1. Surface Reactivity and Hydrothermal Stability of Amorphous Silica Materials

The *surface reactivity* of silica is mainly due to the presence of *silanol groups* ($\equiv Si-OH$), which make such a surface hydrophilic, and *siloxane groups* ($\equiv Si-O-Si \equiv$), which impart more hydrophobic character to the surface because of the back bonding of oxygen lone pair electrons into d-orbitals of silicon. The permanent dipole moment of a silanol group is responsible for physical adsorption via dipole-dipole or dispersion interactions of the silica surface with polar molecules or aromatic hydrocarbons at the Solid-Gas interface. A rather weak acidity of silica surface, characterized by irreversible adsorption (i.e., *chemisorption*) of such basic molecules as pyridine or ammonia, is mostly

due to the hydrogen-bonding propensity of silanols; indeed, their proton transfer power was evaluated, by analogy with the acidity in aqueous solution, as corresponding to the apparent pK_a value being close to 7 [141]. Amongst various types of silanol groups that may be found on a silica surface, three types are believed to play a key role in determining the surface behaviour of silica materials: *isolated*, *geminal*, i.e., silanediols, $=Si(OH)_2$, and *vicinal*, i.e., adjacent OH groups hydrogen bonded to each other.

When interacting with water molecules adsorbed from the gas phase, the isolated and vicinal silanols can potentially act as hydrogen-bond acceptors and donors, thereby being involved in two H-bonds with two water molecules; the geminal OH groups likely form the hydrogen bonded ring structures. Based on ab initio molecular dynamics simulations at room temperature, Cimas et al. have also demonstrated that the interfacial water layer on amorphous silica was on average much more disordered and less mobile than that formed on a crystalline quartz surface [142]. As a corollary to these hypotheses, the zero-coverage heat of adsorption, corresponding to the exothermic adsorption of the first water molecules on a hydroxylated surface, was found to be about 60 and 80 kJ mol^{-1} for amorphous and crystalline silica, respectively [31]. When only one H-bond is formed per one adsorbate molecule on isolated silanols (e.g., on dehydroxylated silica), the corresponding heat of adsorption falls below 44 kJ mol^{-1} and hardly depends on the surface coverage ratio. For gaseous NH_3 molecules adsorbed onto amorphous silica, the zero-coverage heat of adsorption is about 80 kJ mol^{-1} on hydroxylated silica and it passes to about 60 kJ mol^{-1} after preliminary dehydroxylation [31].

The total density of the above mentioned surface functionalities, their mutual proportions, as well as their reactivity depend on the surface hydration state and the local surface topology, thereby being sensitive to the preparation method, thermal treatment applied, and porosity of the material [142–147]. The surface density of silanols on a completely hydroxylated amorphous silica has been a subject of controversy in the scientific literature; it should, however, be remembered that various data reported in numerous publications were obtained based on different experimental techniques and data processing methods. For example, considered as a physicochemical constant according to the Zhuravlev model (about 5 OH nm^{-2} [143,148]), the overall density of silanols attached to the surface of silica gels was found to range between 3.8 OH nm^{-2} and 6.7 OH nm^{-2} depending on the mechanism of silanol condensation during surface activation by heating (data inferred from thermogravimetric analysis) [149]. The vicinal silanols likely predominate on silica materials with fine pores and their concentration decreases with increasing pore size to the extent that they are practically absent from large-pore silica samples [144].

Dehydroxylation of a silica surface by vacuum or flow-degas treatment, or/and by heating at higher temperatures induces a progressive loss of silanols, which are converted to siloxane groups on the surface. The vicinal groups begin to condense at temperatures about 473–573 K, whereas the condensation of isolated silanols requires much higher temperatures (e.g., 973–1073 K) as a consequence of their limited mobility [147,150]. Despite some controversy about the reversibility of silica dehydroxylation, the siloxane-to-silanol interconversion during hydration-dehydration of amorphous silica is admitted to remain completely reversible at least until 673 K. The plausible explanation is that dehydration produces strained siloxane bonds belonging to multi-membered siloxane rings which are very reactive and may be thus easily re-opened upon exposure to water vapour to form more stable silanol-containing structures; high temperature-induced reorientation of silicon-oxygen tetrahedra to relieve the strain generated at the surface decreases the siloxane susceptibility to rehydration. Nevertheless, boiling of the dehydroxylated silica surface in water can restore completely or partially the maximum surface coverage with silanol groups, even though the thermal pre-treatment has been carried out at temperatures close to 1273 K [143,146].

In consequence, silica surfaces calcined or prepared at high temperatures possess substantially greater relative populations of siloxanes. For example, the surface of a pyrogenic silica is rich in siloxane groups and it has a predominantly hydrophobic character. The breaking of siloxane bonds via dissociative chemisorption of water vapour leading to the formation of surface silanols is still

possible [151]. On the contrary, non-calcined samples or those exposed to humid environment, like silica gels, aerogels, and precipitated silica, exhibit hydrophilic surface properties which may diminish when the activation temperature is raised [149].

5.1.2. Surface Reactivity and Hydrothermal Stability of Ordered Mesoporous Silicas and Alumino-silicates

In the case of amorphous aluminosilicates achieved by the isomorphous substitution of silicon by aluminium, clear evidence has been provided for the existence of strong Brønsted acid sites which take the form of hydroxyl groups located between aluminium and silicon atoms occupying the adjacent tetrahedra, i.e., the so-called *"bridging" hydroxyls*, $\equiv Si-O(H)-Al \equiv$ [141,152–154]. The most favourable sites for substitution are those that result in bridging structures involving a silicon atom bonded to three adjacent SiO_4 tetrahedra (i.e., Q_3 silicon atom according to the NMR formalism) [154]. Increasing aluminium content in the silica framework causes an increase in the surface density of bridging hydroxyls, thereby enhancing the surface acidity character. For example, the heat of NH_3 adsorption onto proton-exchanged aluminosilicate of the MCM-41 type at very low surface coverage ratios was measured to be about 150 kJ mol^{-1} [155]. In line with the well-known empirical observation referred to as Loewenstein's rule [156], the maximum substitution of the silicon in 3D frameworks and plane networks of tetrahedra by aluminium should not exceed 50% (i.e., the existence of $\equiv Al-O-Al \equiv$ bridges is to be avoided). The relationship between the surface density of bridging hydroxyls and the silicon-to-aluminium ratio is rarely linear because of the formation of extra-framework Lewis species, as a function of the synthesis pathway, aluminium precursor, or post-synthesis thermal treatment. The surface hydroxyl density of ordered mesoporous silicas and aluminosilicates is usually in the range of 2–4 OH nm^{-2} [155,157]. It is worthwhile noting that the surface energy characteristics of ordered mesoporous silicas and aluminosilicates are significantly smaller than those of typical hydrophilic silicas [155]. Finally, the preparation of silica-based composites via deposition of inorganic hygroscopic salts on the silica or aluminosilicate surface by incipient wetness impregnation should also be mentioned in the context of the present review [68].

The thermal and hydrothermal stability of ordered mesoporous silicas and aluminosilicates is usually lower than that of typical amorphous silica materials. For example, the pore structure of the MCM-41 silica was found to collapse at calcination temperatures above 1073 K [158]; the incorporation of Al in the framework of MCM-41 showed little effect on its hydrothermal stability in an air stream containing 3–20 vol% water vapour at 873 K [159]. The degradation mechanism for pure mesoporous silica is mainly related to the hydrolysis of $Si-O-Si$ bonds exposed to water vapour; it begins on the outer regions of the pore walls and propagates inwards [159,160]. Therefore, it is important to protect the exposed silica surface to improve the hydrothermal stability of the porous material. Among the different protection techniques available, the deposition of aluminium onto the silica framework is considered as being quite efficient, especially in the case of materials characterized by thicker pore walls [160,161]. Nevertheless, it should not be forgotten that, when significant amount of aluminium is introduced into the silica framework, the dealumination process upon activation or calcination at high temperatures not only compromises the hydrothermal stability, but it also results in a decrease in the Brønsted-type acidity of the sample, thus enhancing the Lewis-type acidity [153].

5.1.3. Adsorbents for Heat Storage by Gas-Solid Adsorption

Silica gels, like commercial type A and RD samples produced by Fuji Davison, exhibited a significant adsorption capacity towards water vapour with a maximum uptake being in the range of 0.4–0.45 g of water per gram of the solid sample. The related isosteric heat of adsorption was reported to be around 2.7 kJ g^{-1} under the typical operating conditions of adsorption chillers, namely the temperature and pressure ranging, respectively, between 298 and 338 K and between 500 and 7000 Pa [162]. The temperatures necessary for adsorbent regeneration were relatively low. For example, Ng et al. compared the regeneration and adsorption characteristics of Fuji Davison type A, 3A and

RD silica gels, and concluded that desorption at 363 K was sufficient to recover 95% of the initial adsorption performance in all cases [163]. Despite the good theoretical adsorption performance and easy regeneration, the main drawback of silica gels was considered to be related to the weak hydrophilic character of their surface within the particular working window including the desorption step carried out at 423 K and 5.6 kPa and the adsorption one performed at 308 K and 1.2 kPa, especially for closed storage systems [87].

Ito et al. synthesized a silica gel by adding aluminium ions as a silica growth inhibitor which resulted in a sample having a pore diameter reduced by about 10%; the water vapour adsorption by the sample at low relative pressures and its stability after 100 repeated adsorption-desorption cycles were shown to be improved [164]. Knez and Novak prepared a silica aerogel by supercritical CO_2 drying, thus achieving a significantly higher adsorption capacity towards water vapour in the range between 1 and 1.2 g g^{-1} mainly due to its much higher porosity up to 99%. Nevertheless, the adsorption capacity was found to decrease markedly after the first cycle owing to the collapse of the porous structure during the dehydration step. When physically mixing silica with alumina aerogels, it was possible to increase the number of stable cycles up to 25 [111].

In order to cover both the need for hot water and space heating in a single-family house, the Modular High Energy Density Sorption Heat Storage (MODESTORE) research project tested the use of the silica gel-water vapour working pair in a closed system [165,166]. The prototype was developed on the basis of 200 kg of silica gel contained in a cylindrically shaped reactor equipped with a heat-exchanger pipe arranged inside in a serpentine. Several shortcomings in the system, namely the temperature loss on account of the low heat conductivity of silica gel, some important losses in the sensible heat of liquid water after the charging step, or the need for additional heat of evaporation before the discharging step, reduced the efficiency of the prototype [165]. In 2005, a pilot using a MODESTORE reactor and a storage tank containing 1000 kg of silica gel was installed in Austria. Contrary to the expectation of a good performance, the energy density reached only 140 MJ m^{-3} (i.e., 39 kWh m^{-3}) much below the theoretical value of 684 MJ m^{-3} (i.e., 190 kWh m^{-3}) [166].

A new family of composite materials called *selective water sorbents* (SWS) was proposed in view of water sorption uses. Their synthesis was based on the concept of tailoring of the host porous matrix at nanometer level by adding an inorganic salt inside the pores (e.g., "a salt in a nanoporous matrix" composites) [167]. Such hygroscopic salts as $Ca(NO_3)_2$, $CaCl_2$, $LiNO_3$, LiBr, $MgCl_2$, $NaSO_4$ or $CuSO_4$ were introduced into micro- or meso-porous silica gels or aluminosilicates in order to enhance the surface hydrophilic character, thus improving both the water sorption capacity and the heat evolved during the discharging phase [91,114,115,167,168]. Nevertheless, the formation of saline solutions within the pores under certain hydration states was observed with a potential consequence of salt leakage leading to the reduced cyclability and thus requiring a proper organization of the process [169].

Ordered mesoporous silicates and aluminosilicates of the MCM-41 and SBA-15 type were also considered as efficient adsorbents for water vapour and the adsorption mechanisms, as well as the modification of their surface or textural properties, were studied by several research teams [92,170–173]. Llewellyn et al. argued that water molecules were initially adsorbed on hydroxyl groups present at a relatively hydrophobic surface of MCM-41 samples; this initial step was followed, when progressively increasing the equilibrium pressure of water vapour, by the formation of clusters and capillary condensation, therefore leading to a total filling of the pore volume and resulting in a type V isotherm according to the IUPAC classification [170]. Heating up to 500 K under vacuum conditions caused the loss of physisorbed water; above this temperature, the loss of chemisorbed water and surface dehydroxylation were observed. Kocherbitov and Alfredsson revealed two driving forces balancing the mass of condensed water and the surface area covered in the process of capillary condensation: saturation of hydrogen bonds of pre-adsorbed water molecules and condensation of water at low relative humidity values [171]. Kittaka et al. [172] demonstrated that adsorption-desorption hysteresis loops observed in the case of MCM-41 and SBA-15 samples shifted to higher pressures with an increase in the pore size, as for typical mesoporous materials. Rozwadowski et al. showed that the increasing Al

content in the framework of MCM-41 aluminosilicates caused a decrease in the BET surface area and an unexpected reduction in the sorption capacity towards water vapour [173]. These undesirable effects were explained by the formation of clusters of liquid water around the hydrophilic Al centres which resulted in clogging the pores. According to Jabbari et al. [92], the presence of an aluminium salt finely dispersed inside the pores of the substrate made the water molecules to be attracted within the pores which facilitated the hydration of both the salt and the supporting material. It is worth noting that various Al-MCM-41 and Al-SBA-15 composites exhibited much higher sorption capacities (i.e., up to 0.17 and 0.09 g of water vapour per gram of the sample, respectively) at a relative pressure of about 0.3 than those observed for pure host materials (0.04 and 0.02 g g^{-1} for MCM-41 and SBA-15, respectively). More recently, Thach et al. reported highly hydrophilic ionosilicas, known as mesoporous silica-based hybrid materials containing covalently bound ionic groups [124,174]. The hydrophilic character of such solids was shown to originate from both the silica network and the high number of immobilized ionic ammonium species. The preparation of the ammonium substructure of the precursor combined with an exchangeable counter-ion allowed not only to adjust this hydrophilic character but also to enhance cycling stability upon water adsorption.

5.2. Zeolitic Materials

Zeolites represent a broad family of microporous, aluminosilicate minerals that occur naturally and are also synthesized in the laboratory or produced industrially on a large scale. The crystalline aluminosilicate framework is built of [TO_4] tetrahedra inter-connected via bridging oxygen atoms, where T is either a tetravalent silicon atom or a trivalent aluminium one [157,175]. Like in the case of amorphous aluminosilicates, the formation of the three-dimensional structure of tetrahedra is consistent with the Loewenstein's rule [156]. Nevertheless, it is worthwhile to mention here that the first case of violations of the Loewenstein's rule in high and low silica (LS) zeolites in the protonated form has been recently predicted when screening the aluminium distribution on the basis of density functional theory [176]. The primary building units are assembled into some more complex structures called Secondary Building Units (SBU), like octahedra, cubes, truncated octahedra (also named *sodalite cages*) or prisms with a square or hexagonal base, which form a regular porous framework with cavities (or cages) and channels possessing calibrated dimensions [170]. Since the presence of $[AlO_4]^-$ tetrahedra makes the zeolite framework negatively charged, this negative charge is compensated by the adsorption of protons or other cations at the extra-framework positions. In the case of industrially produced zeolites, such *compensating cations* often include sodium Na^+ ions due to its importance in industrial processes [177]. Other cations of alkali or alkaline earth metals may also assure electroneutrality of the zeolite structure [178]. The general chemical formula of zeolites can be presented in the following form: $M_{\frac{x}{n}}[(AlO_2)_x(SiO_2)_y]\cdot mH_2$, where M and n stand for the compensating cation and its valence, respectively; x and y denote the numbers of $[AlO_4]^-$ and [SiO_4] tetrahedra, whereas m corresponds to the number of residual water molecules in the natural state.

Hydrothermal synthesis is the most commonly used procedure to prepare synthetic zeolites [157]. Typical synthesis carried out in batch reactors includes several steps. In the first step, solutions of sodium silicate, sodium aluminate, and sodium hydroxide (synthesis under basic conditions) are mixed together which leads to the formation of a gel in line with the condensation–polymerization pathway during which Si-O-Si and Si-O-Al chains are created. The zeolite structure is crystallized through a nucleation step, followed by a crystal growth involving assimilation of aluminosilicate from the solution phase in a closed hydrothermal system (an autoclave under autogenous pressures) at temperatures usually between 298 and 448 K [179]. The time for zeolite crystallization ranges from a few hours to several days [180]. By varying reaction conditions (e.g., temperature, time, and degree of agitation) or nature of the structuring agent, it is possible to create a large number of crystalline aluminosilicates with different pore sizes and silicon-to-aluminium ratios (i.e., Si:Al ratio) in the final material. It has been also demonstrated that the continuous flow synthesis of ZSM-5 may greatly

accelerate the crystallization from amorphous state to full crystallinity; namely, it can completed in the tens of seconds range or even within several seconds [181].

Cation exchange with alkali, alkaline-earth, and transition metals or lanthanides is an important method often used to modify the nature and number of compensating cations, thereby tuning the surface properties of zeolites [157,175,178,182–184]. The propensity of these materials to adsorb various adsorbates, and in particular water vapour, may be easily altered in such a way [100,178].

5.2.1. Surface Reactivity and Hydrothermal Stability of Zeolites

Microporous structure of zeolites imparts these crystalline materials with high specific surface areas (e.g., about 800 $m^2\ g^{-1}$ for zeolite 13X [185]), which enhances their capacity to adsorb great quantities of such gaseous molecules as H_2O and CO_2. The adsorption isotherms for water vapour are of type I according to the IUPAC classification, and they usually do not exhibit any hysteresis loop between the adsorption and desorption branches [186].

Sorption performance and hydrothermal stability of zeolites depend on whether they are present in the protonated form or in a metal cation-containing one [187–190]. The compensating metal cations can be located within different Secondary Building Units or at regular polygon windows ensuring communication between such units [178]. They are not chemically bonded to the zeolite framework but they occupy various crystallographic positions characterized by different potential energies. Three physical factors appear crucial for cation location: (i) coordination with oxygens of the zeolite framework, (ii) cation-cation repulsions, and (iii) coordination with negatively charged moieties of the adsorbate species. Two types of zeolite structures are of interest for industrial uses in adsorption, namely types A zeolites (Linde Type A or LTA) and faujasites (FAU) of type X or Y.

The LTA framework consists of sodalite units which are connected by their square faces through square prisms. The unit cell is cubic with $Fm\bar{3}c$ symmetry. Eight sodalite cages arranged in a cubic structure surround the so-called *supercage* with a minimum free diameter of 1.14 nm, which constitutes the primary type of pore in the zeolite (c.f., Figure 4). These pores are disposed perpendicular to each other in the x, y, and z planes and form a 3-dimensional pore structure. The access to supercages is ensured through eight-member oxygen-rings (windows) with a minimum diameter of 0.44 nm. The size of the windows depends also on the number and nature of charge-compensating cations [157,177]. Figure 4 shows the most probable locations for the compensating cations in the LTA zeolite: (i) site I, at the centre of a six-member oxygen ring constituting one of the eight corners of the supercage; (ii) site II, close to the eight-member oxygen window thus directly obstructing the entrance to the supercage; (iii) site III, close to the four-member oxygen ring inside the cavity [157].

In the FAU framework, the sodalite units are linked through hexagonal prisms and 10 truncated octahedra surround a supercage (the minimum free diameter is equal to 1.25 nm), to which the access is through 12-member oxygen rings (windows) with a free diameter of about 0.74 nm [157]. The unit cell is also cubic with $Fd\bar{3}m$ symmetry. The FAU framework is characterized by the greatest supercage volume amongst all known zeolites and its total void fraction is about 50%. Types X and Y zeolites have the same skeletal structure; the only difference is that the formers contain between 96 to 77 aluminium tetrahedra of the total 192 tetrahedra in the unit cell (i.e., Si:Al ratio varies from 1 to 1.5) and the latters contain between 76 and 48 $[AlO_4]^-$ tetrahedra (i.e., Si:Al ratio changes from 1.5 to 3).

The principal crystallographic sites for the location of charge-compensating cations are shown in Figure 4. They include: (i) site I, in the hexagonal prism, either in its centre or shifted from it; (ii) site I′, in the sodalite cage toward the hexagonal prism (i.e., close to the 6-ring window); (iii) site II, in the supercage, at the centre of the 6-ring window between the sodalite cage and the supercage; (iv) site II′, in the sodalite cage close to the 6-ring window; (v) sites III and III′, in the supercage, close to its 12-ring window [178]. In the case of Y type faujasites containing monovalent compensating cations, the increase in the cation size favours the occupation of the most confined sites I, whereas for divalent cations sites I′ are the preferred positions [178,183] It is important to realize here that hydration of zeolites will affect the location of compensating cations, thus leading to cation redistribution upon water

adsorption as a function of the hydration extent [100,178,192,193]. For example, Di Lella et al. [192] reported cation redistribution upon water adsorption for sodium faujasite Y (i.e., NaY) with varying cation contents (Si:Al ratio = 1.53–3). For a dehydrated sample containing initially less than 16 Na^+ in site I, cation migration towards site I′ was postulated as a consequence of too small space being offered for hydrated cations within the hexagonal prism. For NaX zeolites with low Si:Al ratio [193], numerous extra-framework Na^+ cations were supposed to be mainly located in sites I′ and II, and also occupy sites III′ at the dry state; the sodium distribution appeared hardly affected upon water adsorption. A complete ion exchange of sodium by calcium in faujasites was shown to be possible and sites I and II were regarded as the preferred centres for calcium location [178]. However, in samples containing a mixture of Na^+ and Mg^{2+}, the two types of compensating cations shared mostly sites I′ and II. The trend for moving towards more confined sites to occupy to a larger extent the sites II close to the sodalite cages was revealed at higher temperatures (≥723 K [100]), irrespective of the cation nature. In the case of hydrated MgNaX and CaX zeolites, Na^+ cations tended to occupy more sites I and IV (i.e., at the centre of the supercage), and less sites of the type II, whereas divalent analogues were rather located on sites I′, II, and III [100].

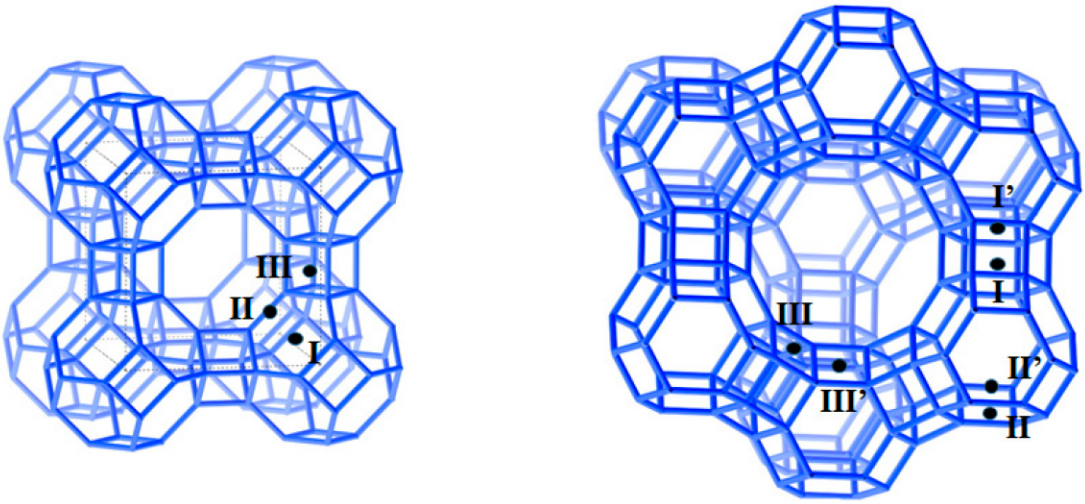

Figure 4. LTA (left) and FAU (right) zeolite structures showing the principal crystallographic sites for the location of charge-compensating cations. Made on the basis of the two zeolite structures extracted from database [191].

Brønsted and Lewis acid sites may be present in different zeolites [45]. The Brønsted acid sites represent a hydrogen atom bonded to an oxygen one to form a surface hydroxyl group, in which the oxygen either belong to a framework aluminium tetrahedron (i.e., terminal –OH) or constitutes a bridge between adjacent silicon and aluminium tetrahedra (i.e., bridging –OH). Such surface acidic sites may be formed in four different ways: (i) by exchanging the pristine compensating cations with ammonium ones followed by a calcination step to eliminate ammonia, (ii) by cation exchange in acidic medium (high silica zeolites), (iii) by breaking an Al–O–Si bond in the zeolite framework, thus resulting in the formation of surface Si–OH and Al–OH groups, and (iv) via hydrolysis of multivalent compensating cations [183]. Lewis acid sites in zeolites represent electron deficient groups which tend to accept electrons when interacting with extra-framework molecules. The following three chemical moieties may exhibit this behaviour: (i) tri-coordinated aluminium atoms exposed at the surface as a consequence of the dehydration of some Brønsted acid sites during calcination or ion exchange (ii) extra-framework aluminium oxide clusters, AlO^+ or $Al_xO_y^{n+}$, produced by delamination process, and (iii) exchangeable compensating cations [194]. In general, decreasing the Si:Al ratio in the zeolite framework causes an increase in the number of compensating cations or protons, thereby enhancing the surface acidic character. Nevertheless, when the pore space becomes crowded with protons, the

strength of the related Brønsted acid sites may decrease. For example, in high silica zeolites (Si:Al > 10), the acidic sites are isolated and strong, though they are present in small quantities; on the contrary, in low silica zeolites, these sites are more numerous but weaker.

Synthetic or cation-exchanged X and Y zeolites with a low Si:Al ratio possess only a few protons as charge-compensating species and, therefore, their surface reactivity will be dominated by Lewis-type acidic sites including mostly the extra-framework cations and other electron deficient centres; the presence of bridging hydroxyls groups representing strong acid centres of the Brønsted type is to be rather neglected [100]. Following the molecular dynamics simulation done by Shirono et al. [195], water molecules were shown to adsorb onto NaX (Si:Al = 1) via a three-step mechanism including: (1) adsorption around sodium cations, (2) formation of one molecule-thick adlayer on the pore walls, and (3) pore filling in the supercage during which water molecules were localized around the 12-member oxygen windows. Similar mechanism was postulated for water adsorption onto NaY (Si:Al = 2) with the exception of intermediate hydration states, where the formation of water clusters around Na^+ cations appeared more plausible than the monolayer adsorption [195].

The adsorption of water vapour onto such protonated zeolites as HY or H-ZSM-5 was argued to occur mainly on Brønsted acid sites, thus resulting in two types of local structures: (i) a neutral complex of two water molecules hydrogen-bonded to a Brønsted acid site and a framework oxygen atom, (ii) an "ion pair" complex formed during simultaneous adsorption of two water molecules by transferring the surface acidic proton to the water dimer [189,190,196,197]. Since the capacity of water vapour adsorption was proven to depend also on the surface topology and the spatial confinement, the exclusive presence of "ion pair" complexes was predicted for HY zeolites by Jungsuttiwong et al. [190].

When accompanied by the migration of charge-compensating cations among various crystallographic sites, hydration and dehydration of zeolites may affect the site accessibility or even block the entrance of some pores. Moreover, marked evolution of the pore architecture of a pre-shaped sample of Na-contained 13X zeolite subject to numerous repeated hydration-dehydration cycles was revealed by Storch et al. [57]. In a general manner, zeolites with a Si:Al ratio $\geq$ 3.80 appear very stable, whereas those having a Si:Al ratio $\leq$ 1.28 are quite unstable [58]. Protonated zeolites are usually considered as showing lower thermal stability compared to their sodium-containing analogues, the latter being less stable with increasing framework aluminium [198].

Framework dealumination is the method the most frequently used to enhance the hydrothermal stability of faujasites with higher Si:Al ratios (generally above 2.2). At the industrial scale, zeolite NaY is commonly dealuminated in water steam without collapse of its framework [199]. This can be accompanied by introduction of ammonium ions into the framework and steaming process of NH_4Y, thus creating extra-framework aluminium at the crystal surface; in consequence H-DAY sample is achieved [200,201]. N. Salman et al. demonstrated that more framework damage by a sour hydrolysis occurred in steam at lower temperatures (473 K), rather than at higher ones (573–973 K) [202]. Nevertheless, the comparison of 3A, 13X and DAY samples in terms of water adsorption capacity and heat of adsorption effect led Kim et al. to conclude that the sorption performance of DAY was weaker than those of the two other samples [185]. Ristic et al. showed that a post-synthesis modification of zeolite Y by a mild HCl treatment and a chemical treatment with H_4EDTA could diminish (below 413 K) the temperature at which the zeolite should be regenerated to remove all physically adsorbed water [203]. A two-step acid treatment of Mg-exchanged sample could, on the one hand, improve the water sorption capacity, but on the other hand, rise the desorption temperature up to 473 K [203]. Buhl et al. studied the hydrothermal stability of a series of cation-exchanged 13X (Si:Al = 1.18) and LSX (Si:Al = 1.02) zeolites [204]. No framework decomposition was observed up to 473 K for Li^+, Na^+, and Ca^{2+} compensating cations, whereas more or less marked framework collapse was detected for K^+, Rb^+, Sr^{2+}, and Ba^{2+} because of stronger vibrations and repulsive forces exhibited by large cations with increasing temperature, thus destabilizing the framework [204]. Fischer et al. also reported the research work done on the effect of temperature (473–623 K), water vapour pressure, and treatment time on the hydrothermal stability of powdered 13X zeolite and 13X beads [205]. Their results showed

that the crystallinity could degrade above 473 K due to the hydrothermal stress, especially under high water vapour pressures. At temperatures in the range of 473–523 K, 13X beads exhibited better hydrothermal stability under lower water vapour pressures.

5.2.2. Zeolitic Adsorbents for Heat Storage by Gas-Solid Adsorption

Though solar energy storage using zeolite-water vapour working couples has drawn much attention since the late twentieth century [16,206], zeolites were intensively studied mainly in view of uses in heterogeneous catalysis. More recently, Gaeini et al. analysed the effect of kinetics and gas flow rate on the thermal performance of a laboratory-scale thermochemical heat storage system, which possessed a fixed-bed reactor filled with zeolite 13X [207]. It was found that slower adsorption process reduced both the efficiency (from around 83% to around 80%) and the power of the reactor (from around 1.4 kW to around 0.6 kW), when the kinetics coefficient was below a threshold value. For each reactor size, an optimum flow rate was established.

Studies of water vapour adsorption onto different cation-exchanged zeolites (Li^+, Ca^{2+}, Mg^{2+}) of types X, Y, and A led Jänchen et al. to conclude that the adsorption capacity and integral heat of sorption could be increased as a result of ion exchange with cations of different sizes and charges [69]. Their laboratory-scale storage system based on the use of granulated zeolites yielded storage energy densities up to 810 kJ kg^{-1} (an increase in the storage density of 145%) after the charging step carried out at 453 K. It was also shown later on [208] that a 10–15% higher adsorption capacity and faster kinetics accompanied the storage process performed on binderless zeolite beads of types A and X. The 13X sample appeared as the most promising storage material for charging temperatures up to 470 K. Above this temperature, some degradation of 13X zeolite was observed, especially at high pressures of water vapour, and more stable binderless 4Å zeolite was a better choice in view of potential implementation issues in open and closed storage systems. Herzog et al. attempted to adjust the hydrophilic character of Y-type zeolites by a steaming process and the dealumination was found to lower the desorption temperatures [209]. Gómez-Álvarez et al. concluded, on the basis of molecular simulations, that the nature of the compensating cation affected the adsorption of water vapour to a greater extent than the density of such cations did [210]. It was argued that higher affinity of calcium cations towards water vapour resulted in a more hydrophilic character of the zeolite framework in comparison with that shown by the sodium-exchanged sample, thereby changing the mechanism of surface clustering of water molecules. Li et al. demonstrated that Y-type zeolites finely tailored by ion exchange with Mg^{2+} ions exhibited significantly enhanced vapour uptake capacity, adsorption energy, and intra-crystalline diffusivity compared to the parent samples [211]. Similar conclusions were drawn by Alby et al. for water vapour adsorption of Mg- and Ca-exchanged X-type zeolites under dynamic conditions of gas flow [100]. For example, a Mg-exchanged 13X sample with a cation-exchange ratio of 70% was demonstrated to have much better performance in terms of integral heat release compared to the original Na-X, even though the regeneration conditions were insufficient to remove completely water vapour adsorbed onto zeolite. Stach et al. also showed that Mg^{2+} ions enhanced the water adsorption capacity and integral adsorption heat [212]. They argued that the thermochemical storage performance for various adsorbents depended on the temperatures describing adsorption, desorption, condensation, and evaporation stages.

Some other researchers have tested alternative ways for modification of zeolite performance by salt hydrate encapsulation in a porous structure or by impregnation of the zeolite surface with hygroscopic salts [93,94,117,188]. Cindrella and Dyer compared various zeolites of 4A, X and Y types achieved either by cation exchange with Mg^{2+} and Zn^{2+} ions or by encapsulation of $MgCl_2$ and $Zn(NO_3)_2$ salts. Strong interactions were found to occur between the zeolite framework and the salt hydrates, whereas the fibrous structure of the salt-encapsulated zeolite X exhibited an increased surface area for water uptake and promising structural features amenable to thermal energy storage [188]. Whiting et al. tested the use of composite materials obtained on the basis of NaX, mordenite, NaY and HY zeolites impregnated with $MgSO_4$ or $MgCl_2$ [93,94]. They showed that Na–Y and H–Y samples containing

15 wt% $MgSO_4$ produced higher heats upon hydration and dehydration stages (1090 and 876 J g^{-1} of solid, respectively) compared to those of Na–X and MOR composites (731 and 507 J g^{-1} of solid, respectively). Na–Y and H–Y composites containing 15 wt% $MgCl_2$ yielded the highest heats of water adsorption (1173 and 970 J g^{-1}, respectively), due to the lower deliquescence relative humidity (DRH) of $MgCl_2$. Nevertheless, the use of great quantities of $MgSO_4$ resulted in significant pore blocking, thus limiting the access of water molecules to the dehydrated salt species. Hongois et al. constructed a storage reactor with 200 g of $MgSO_4$-impregnated zeolite 13X [117]. An energy density of 648 J g^{-1} (i.e., 0.18 Wh g^{-1}) was achieved during hydration tests and this performance remained unchanged over three charging-discharging cycles, according to adequate micro-calorimetry measurements.

Besides some fundamental research made on open and closed storage systems [77,213,214], several large-scale prototypes have been constructed to test the storage performance under more realistic conditions. Tatsidjodoung et al. built an open prototype operating in the moist-air mode making use of zeolite 13X beads as an adsorbent. With 40 kg of zeolite, an average temperature lift of 38 K was recorded at the outlet of each zeolite vessel for 8 h during the discharging step carried out with an airflow inlet at 293 K, a specific air humidity of 10 g kg^{-1} of dry air, and a flow rate of 180 m^3 h^{-1} [215]. Johannes et al. designed a STAID prototype composed of two reactors, each containing 40 kg of 13X zeolite [216]. The thermal power output provided about 2.25 kW (namely 27.5 W per kg of the adsorbent) during 6 h [216]. For the purpose of E-Hub project, De Boer et al. realized a storage prototype with 150 kg of 13X zeolite divided in two separate reactors [217]. Unfortunately, the thermal losses due to convection, conduction, and air leakages, as well as the low efficiency of the air-to-air heat recovery unit resulted in a low thermal power output from the system, corresponding only to the 15% efficiency. Gaeini et al. based their 250 L setup on a gas-solid reaction between water vapour and zeolite 13X [206]. The reactor contained four segments of 62.5 L each operating in different modes. A maximum power of around 4 kW was obtained by running the segments in a parallel mode. The Institute for Thermodynamics and Thermal Engineering (ITW) attached to the University of Stuttgart (Germany) was involved in the development of an open storage system called "MONOSORP" [218]. The MONOSORP prototype was developed based on the use of 8 m^3 of 4A zeolite monolith in the honeycomb structure to improve the adsorption kinetics. With an inlet temperature of about 293 K and a humidity of 6 g kg^{-1} (gram of water per kg of dry air), a maximum temperature lift of around 22 K was achieved. Another open sorption system making use of 13X zeolite as an adsorbent was studied and developed by ZAE Bayern [56]. It was connected to a district heating network in Munich, thus relying on the thermal energy excess produced during night and being independent of the grid during peak demand. The storage density was equal to 446 MJ m^{-3} (i.e., 124 kWh m^{-3}) for heating stages, which corresponded to a performance coefficient (COP) value of 0.9.

5.3. Other Zeotype Materials

Zeotype aluminophosphates (AlPO) and silico-aluminophosphates (SAPO) possessing frameworks and pore arrangement similar to those of zeolites have attracted much attention in view of adsorbent development for thermal energy storage using water adsorption–desorption cycles. The tetrahedral-framework aluminophosphate (AlPO) was first discovered in the early 1980s by Union Carbide [219]. The zeotype framework was constructed by strictly alternating $[AlO_4]^-$ and $[PO_4]^+$ tetrahedra to obtain an electrically neutral structure. As a consequence of this strict ordering, the framework possessed no odd-membered rings. The surface of such a neutral AlPO framework with no extra-framework cations exhibited more hydrophilic character than that of pure silicate, due to the difference in the electronegativity between aluminium (1.5) and phosphorus (2.1), as well as due to the structural defects in the form of surface P–OH groups [220]. Nevertheless, it still showed less affinity towards water vapour compared to zeolites of type A or type X with anionic aluminosilicate framework and the compensating cations [219].

Because of the moderate hydrophilic behaviour of AlPO framework, the water adsorption isotherms are often of type V, according to the IUPAC classification [221]. This particular behaviour may

be advantageous for the heat storage uses: a steep increase in the water uptake within a narrow range of relative vapour pressure argues in favour of low-temperature working conditions, thus decreasing significantly the regeneration temperature of materials down to 363–413 K. [86,222]. However, the total water uptake is somewhat lower when compared with that of faujasites [70]. In order to tune the surface properties, incorporating a fraction of Si atoms into an AlPO framework can produce negatively charged Brønsted acid sites and form a silico-aluminophosphate (SAPO) framework with enhanced hydrophilic character of the material surface [223]. Furthermore, it is also possible to substitute Al and P atoms with some metallic elements to obtain metal-aluminophosphates (i.e., MAlPO), like in the case of FAM-Z01 containing iron cations within the framework.

Typical synthesis of AlPO or SAPO is carried out at relatively high temperatures (373–523 K) in line with the hydrothermal pathway by making use of structure-directing agents or templates, starting from traditional chemicals containing individual Si, Al, and P atoms or lamellar aluminophosphates afforded from appropriate chemicals. Many parameters may affect the framework formation, such as the source materials, batch composition, pH of the reaction mixture, chemical structure of the template, type of solvent, as well as the crystallization temperature and time [219,224–228].

Two main drawbacks of these materials have limited their massive use as adsorbents in heat storage systems. The first one is related to the framework degradation after a few charging-discharging cycles under hydrothermal conditions [229]. The other one is due to significant preparation costs, especially when expensive templates are to be used (e.g., diethylamine or tetraethylammonium hydroxide) [87,230,231]. Nevertheless, some of these materials have already been commercialized, for example by Mitshubishi Plastics under the name of AQSOA-Z or AQSOA- Functional Adsorbent Material-Zeolite (FAM-Z) [232,233].

Amongst all known AlPO and SAPO materials, AlPO-5, AlPO-18 and SAPO-34 are the most commonly studied samples for thermochemical heat storage uses [60,87,123,167,222,229,232,234–238]. AlPO-5 (or AQSOA-Z05) possesses a particular two-dimensional zeolite-type framework structure having pores with a diameter of 0.74 nm; AlPO-18 has pores with a smaller diameter of 0.38 nm; SAPO-34 (or AQSOA-Z02) framework bears cages with the 0.37 nm windows [239,240].

The mechanism of water vapour adsorption onto AlPO has been investigated by several researchers. Goldfarb et al. used solid state NMR to reveal two types of water molecules retained by AlPO-5: the first type concerned molecules coordinated to the framework Al and the other one represented water molecules physisorbed within the channels of AlPO-5 [241]. Newalkar et al. reported the variations of the isosteric heat of water adsorption onto AlPO-5 as a function of the surface coverage ratio: it was about -88 kJ mol^{-1} at very low coverage ratios and increased sharply to -50 kJ mol^{-1}, which was close to the heat of liquefaction of water vapour (-41 kJ mol^{-1}). Then it remained almost constant with a further increase in the surface coverage. The authors also suggested that the increase in the water uptake at relative vapour pressures in the 0.2–0.3 range was due to capillary condensation; the initial water uptake occurred within the secondary 6-membered ring channels, and then water molecules filled the primary 12-membered ring channels [220]. Floquet et al. investigated the capillary condensation mechanism by carrying out neutron scattering experiments in the temperature range 280–300 K [236]. For relative vapour pressures below 0.1, the AlPO-5 channels remained empty due to the relative hydrophobic character of the framework. Further increase in the relative pressure up to 0.35 led to the retention of water molecules via interactions only with framework aluminium in octahedral coordination or with defects. Water molecules started to fill the AlPO-5 channels at a relative pressure of 0.35, which was followed by the crystallization of water to form a confined ice-like phase [236]. For AlPO-18 and SAPO-34 samples dried at low temperatures (368 K), Henninger et al. reported water uptake values of 254 g kg^{-1} and 200 g kg^{-1}, respectively [86]. They also revealed a steep water retention within a narrow relative pressure range, although the adsorption-desorption isotherm for AlPO-18 contained an undesirable desorption hysteresis. The SAPO-34 samples synthesized by using morpholine as a template were not stable under hydrothermal stress. Changing the template could improve the stability, however

this was accompanied by a significant increase in the synthesis cost [86,242]. Goldsworthy studied the adsorption of water vapour onto commercial samples AQSOA-Z02 and AQSOA-Z05 and obtained type IV adsorption isotherms [238]. The maximum water uptake was 0.33kg kg^{-1} for AQSOA-Z02 and 0.235 kg kg^{-1} for AQSOA-Z05. According to Shimooka et al. [232], between two samples FAM-Z05 and FAM-Z02, the former had lower regeneration temperature, though simultaneously lower adsorption capacity. Ristic et al. investigated the influence of the elemental composition and framework structure on the sorption characteristics of AlPO-18, SAPO-34, and a new APO-Tric sample characterized by a triclinically distorted chabazite framework [222]. The heat of adsorption was found to be about 55 kJ mol^{-1} for the three samples, which resulted in an energy density of 864 MJ m^{-3} (i.e., 240 kWh m^{-3}) for a regeneration temperature of 413 K. The APO-Tric showed better low-temperature performance and hydrothermal stability, contrary to the gradual water uptake and amorphization of the crystalline structure of more classical SAPO materials after adsorption-desorption cycles.

Van Heyden et al. [243] evaluated the performance of AlPO-18 coated on aluminium supports with polyvinyl alcohol (PVOH) as a binder for heat exchanger applications by measuring the kinetics of water adsorption onto AlPO-18. The AlPO-18 layers showed the decreased heat and mass transfer characteristics with increasing the thickness and crystals size (from nano- to micron-sized). However, with diffusion limitation of microporous AlPO taken into consideration, they concluded that a critical layer thickness was about 200 µm. Below this limit value, fast heat exchange cycles were observed thereby allowing for appropriate heat transformation. Furthermore, in view of potential uses as adsorbents in the thermochemical energy storage operating as open and closed storage systems, the effective thermal conductivity of AQSOA FAM-Z02 packed bed adsorbers was modelled as a function of such physical factors as water uptake, number of adsorbent layers, particle size, bed porosity, temperature, contact pressure, and interstitial gas pressure. The model was confronted with the experimental results achieved by means of heat flow meter method by Rouhani et al. [244]. The effective thermal conductivity of the 2 mm-size FAM- Z02 was found to lie between 0.188 (at 283 K) and 0.204 W m^{-1} K^{-1} (at 353 K). With the 0.32 g g^{-1} of water uptake at 303K, the 2 mm FAM-Z02 open system displayed the effective thermal conductivity 2.2 times higher than that measured for the closed system, i.e., 0.1031 against 0.0474 m^{-1} K^{-1}. Based on this model, an optimum particle size could be estimated for any given bed thickness in order to achieve the highest thermal conductivity.

5.4. Metal-Organic Framework Structures (MOFs)

Owing to their well-characterized crystalline structure and high specific surface areas, metal-organic frameworks (MOFs), also called porous coordination polymers, constitute another class of synthetic porous materials of interest for uses in adsorption, separation, heat storage, and catalysis [245].

MOFs are crystalline inorganic-organic hybrid materials, comprising single metal ions or polynuclear metal clusters connected by organic linkers with a one, two or three- dimensional framework through coordination bonds. With different organic linkers and metal centre combinations, there exists practically an endless possibility of various structures and a high chemical versatility. The nanosized cavities and/or open channels formed by the two or three-dimensional framework of MOFs provide enormous potential for adsorption applications.

During the last two decades, tremendous efforts have been made to the design and synthesis of MOF materials. These materials have been developed through four different generations [246,247]. The first three generations were described in the work of Kitagawa and Kondo [248]: the first generation materials unfortunately collapsed after the removal of guest (adsorbates) and they lost the crystallinity and porosity; the stability was reinforced in the MOFs of second generation possessing rigid frameworks even upon guest (adsorbates) removal; the third-generation MOFs were characterized by a great flexibility of their frameworks due to temperature and pressure or upon adsorption of gas molecules (e.g., thermal and guest-induced structural transformations between the Large (LP) and Narrow Pore (NP) forms of the MIL-53 materials referred to as "breathing" phenomenon [249,250]).

The fourth-generation MOFs have been achieved by means of the post-synthesis modifications, recently developed to adjust pore size and surface chemistry so as to accommodate different guest species without losing the inherent topology and structural integrity [246,247,251,252]. More recently, MOFs with complex systems containing defects or being non-stoichiometric (Solid Solution) [246], were included into the latest fourth generation, together with other types of MOFs combining a rigid framework with self-switching pores that could adapt themselves to a particular guest through the rearrangement of extra-framework counter-ions or reorientation of flexible linkers.

The conventional synthesis of MOFs is usually carried out by following the "one-pot" procedure involving either slow diffusion or direct mixing of metal ions and organic precursors under solvothermal conditions [253,254]. The main advantage of the synthesis of MOFs in comparison with other template-assisted preparation procedures (e.g., SAPO-34) is strictly related to the use of appropriate solvent which itself acts as the main template and for which high-temperature calcination is not necessary to remove it so as to generate the porosity [88]. While conventional synthesis methods of MOFs have relatively matured, Stock and Biswas reviewed such other approaches as mechano-, sono- and electrochemical, or microwave-assisted procedures, as well as high-throughput synthesis [253]. These methods have shown to be applicable to certain compounds, often under milder reaction conditions, thus yielding materials possessing different particle sizes and other properties. Further tuning of the material's properties by introducing functional groups into MOFs, covering covalent and dative modifications, as well as post-synthesis deprotection of functions, were reviewed by Cohen et al. to emphasize the progress in the post-synthesis modification of MOFs [251,252,254].

Given the numerous studies previously and actually made on MOFs, the present review is focused on some selected cases related to the sorption of water vapour being of potential interest for thermochemical storage.

Surface Reactivity and Hydrothermal Stability of MOFs in View of Their Uses as Water Vapour Adsorbents

A lot of experimental and theoretical studies including adsorption measurements or simulations have been carried out to illustrate the capacity of MOFs to adsorb water vapour [255–263]. The subject has been already described in several review articles, where specific criteria are given for the selection of MOFs as adsorbents [70,88,264–266].

Henninger et al. [88] considered the use of some MOFs in Adsorption Heat Pumps by determining their water uptake capacity, heat of adsorption and cycle stability. Canivet et al. [263,264] proposed two important indicators to evaluate the adsorptive properties on the basis of adsorption isotherms, namely the capacity of water adsorption (in cm^3 of water per g of sample) and the relative pressure $\alpha = p/p_0$ at which half of the total water adsorption is reached. The α parameter was regarded as a measure of the hydrophobic-hydrophilic surface character, independent of the water adsorption capacity. Indeed it increased upon increasing the hydrophobic character and showed an inflexion point in the case of type V adsorption isotherms. De Lange et al. [70] also used α factor to differentiate among various samples, including the uptake in- and outside of the operating window, in parallel with the enthalpy of adsorption and the pore volume as other comparators. They additionally took into account the hydrothermal and cycling stability in view of uses in adsorption heat pumps. A more systematic study of the water stability in MOFs, including both the thermodynamic and the kinetic stability, was made by Burtch et al. [266]. Like in the work of Furukawa et al. [265], the emphasis was put on the condensation pressure of water vapour within the pores, in addition to water uptake, cycling performance and water stability. Although a steep water uptake at low relative pressures may be of interest in dehumidification or water capture systems, its use for the purpose of thermochemical storage was criticized since the extra energy input for conservation and more rigorous regeneration conditions were required.

Canivet et al. [264] identified the following three main mechanisms of water adsorption onto MOFs: (i) the uptake of water molecules on metallic clusters altering the first coordination sphere

of the metal ion (chemisorption), (ii) reversible adsorption in the form of layers or clusters, and (iii) irreversible capillary condensation. De Lange et al. [70] proposed three different types of sites for the formation of water clusters: (i) coordinatively unsaturated sites (or unsaturated metal centres) on the metal ions after solvent removal, (ii) terminal hydroxyl groups on the metal-ions of the cluster, when occurring in the system (iii) additional nucleation sites providing hydrophilic functional groups attached to the organic linkers.

One of the first discovered 3-dimensional microporous MOFs, HKUST-1 or Cu-BTC [267,268] (commercialized as Basolite C300 by BASF) has been tested for water adsorption since last decade [86,229,268–276]. In the early studies, the unstable framework in the presence of water over several gas sorption-regeneration cycles made this MOF material unsuitable for the storage purposes. Its building unit contained two central Cu^{2+} ions coordinated by four trimesate molecules through their carboxylate groups to form the paddlewheel-like structure of copper acetate $Cu_2(CH_3COO)_4(H_2O)_2$, with a Fm3m symmetry, and the main pore diameter of 0.9 nm [86,267,275]. Li and Yang first reported a water vapour uptake of 0.26 g g^{-1} onto HUKST-1 at 298K and a suitable hydrothermal stability until p/p_0 of 0.7 [270]. The framework integrity was confirmed by XRD studies. Unfortunately, this hydrothermal stability could not be reproduced and the framework degradation upon water adsorption was revealed by other researchers [268,271–273]. Al-Janabi et al. studied the mechanism of this degradation and showed that water vapour broke the Cu-BTC bonds (BTC for benzenetricarboxylate), thus leading to the formation of BTC-acid [274]. Strong water-Cu coordination was found to displace the carboxylate bonds of BTC ligands from Cu centres which resulted in irreversible change of the framework. Although the cycle stability was accompanied by a partial degradation, the material showed promising water adsorption capacity for the use in sorption processes. Henninger et al. tested HKUST-1 for heat transformation [86] and estimated its water loading capacity at about 0.324 g g^{-1}, which was 2.9 times higher than the adsorption capacity of silica gel [86]. A much higher water uptake of 0.55 g g^{-1} was reported by Küsgens et al. [269]. However, the HKUST-1 sample exhibited a continuous degradation of the framework with increasing the number of cycles [229]. Recently, HKUST-1 was demonstrated to keep its structural integrity under dynamic, non-equilibrium conditions when exposed to low humidity and room temperature (600 Pa and 298 K) for up to 48 h of cyclic operations [270].

Another microporous MOF, namely CPO-27 (also named MOF-74), exhibited interesting adsorptive properties with enhanced hydrothermal stability. CPO-27 may use a variety of metallic centres, such as Ni^{2+}, Mg^{2+}, Co^{2+}, and Zn^{2+}. The one-dimensional helical chains of cis-edge-connected metal–oxygen coordination octahedra resulted in honeycomb topology with a channel diameter of 1.1 nm. Water uptake was found to occur primarily at very low p/p_0 values due to the irreversible adsorption of water molecules on the coordinatively unsaturated sites of the metal incorporated in the structure, the adsorption isotherms being generally of type I [255,268,277–281]. The first water adsorption isotherm for CPO-27(Ni) was measured by Liu et al. [282] and presented a saturation capacity of 32 mmol g^{-1} at 298K. More recently, Elsayed et al. reported a maximum water uptake of 0.47 g g^{-1} by CPO-27(Ni) [277]. Schoenecker et al. obtained an adsorption capacity of 37 mmol g^{-1} onto CPO-27(Mg) based on the measurements of adsorption isotherms [268]. Li et al. made a simulation study on CPO-27(Zn) [255]. They demonstrated that multiple adsorption of H_2O molecules was possible on Zn sites, thus yielding stable H_2O clusters at low temperatures. The first adsorbed water molecules could be dissociated only at high temperatures, therefore reducing the sorption cyclability [283–285]. Tan et al. [284] related the framework destabilization to the water dissociation within the framework at high temperatures. However, like in the case of zeolites, the strong coordinatively unsaturated sites of CPO-27 required higher temperatures to desorb the bound water molecules. Zr-based UiO-66 was also tested for the adsorption of water vapour. The $Zr_6O_4(OH)_4$ octahedron was shown to form lattices with 12-fold connection through benzenedicarboxylate(BDC) linker, resulting in a highly packed fcc structure possessing cages with tetrahedral (0.74 nm) and octahedral (0.84 nm) shapes (i.e., tetrahedral and octahedral pores) [286,287]. As in the case of

microporous zeolites, the adsorption of water vapour was demonstrated to generally follow a pore-filling mechanism. However, UiO-66 appeared more hydrophobic and produced a two-step adsorption isotherm. The first loading step was shown to lie in a p/p_0 interval of 0.2–0.4, in line with the filling phenomenon within tetrahedral and/or octahedral pores. The second step at $p/p_0 > 0.8$ was due to interparticle condensation [288]. One important advantage of UiO-66 was that its adsorptive property and stability could be tuned by post-synthesis modification via direct ligand substitution [287]. A maximum water loading of 0.4 g g^{-1} was found by Jeremias et al. [288], with the average heat of water adsorption being equal to 41.3 kJ mol^{-1}. Amino-functionalized UiO-66(Zr)-NH_2 yielded a more interesting average heat of water adsorption of 89.5 kJ mol^{-1}. Unfortunately, it lost 38% of the water adsorption capacity after 40 successive adsorption-desorption cycles. On the contrary, Decoste et al. [289] observed no degradation of UiO-66(Zr) and UiO-66(Zr)-NH_2 when exposed to water vapour at room temperature.

Among the most studied MOFs for the water adsorption applications, mesoporous and hydrothermally stable mesoporous MIL-100(Cr) and MIL-101(Cr) outstand from the others because of their high water sorption capacities and low regeneration temperatures. They were first synthesized, studied, and named by Ferey et al. [290]. Their structure consisted of super-tetrahedra (ST) building units, which were formed by rigid terephthalic or trimesic acid linkers and trimeric chromium (III) oxide octahedral clusters, with cavity diameters of 0.29 nm and 0.34 nm. Isostructural compounds with Fe^{3+} or Al^{3+} instead of Cr^{3+} could also be obtained [291]. A high water uptake of 1.01 g g^{-1} onto MIL-101(Cr) was reported by Ehrenmann et al. who obtained an S-shaped adsorption isotherm [89]. Higher water uptake of 1.2 g g^{-1} and 1.47 g g^{-1} were measured, respectively, by Akiyama et al. and Elsayed et al. [277,292]. MIL-101(Cr) exhibited a steep retention of water vapour in a relative pressure range between 0.30 and 0.6 [89]. This hydrophilic-hydrophobic switching behaviour was considered as making the regeneration easier under 363 K. MIL-100(Cr) possessing smaller pores of 2.5 nm and 2.9 nm, was shown to adsorb less water vapour (ca. 0.5–0.8 g g^{-1}) due to smaller pore volumes [26]. Recently Cui et al. constructed a MIL-100(Fe) coated heat exchanger with a silica sol binder and tested it in the high temperature cooling system [293]. The theoretical power density was evaluated at 82 W L^{-1} of air. The mechanism of water adsorption onto MIL-100(Cr) and MIL-101(Cr) was studied by De Lange et al. who applied both the experimental and the simulation approach [261]. Water-MOF and water-water interactions were demonstrated to control the adsorption process: at low water loadings, prior to the saturation of all coordinatively unsaturated sites of Cr, the adsorbent-adsorbate interactions determined the shape of the adsorption isotherm; at higher loadings, adsorbate-adsorbate interactions became dominant. Some loss of water adsorption capacity upon cycling was recorded by Ehrenmann et al. (1.9% over 20 cycles and 3.2% over 40 cycles compared to the initial amount of water vapour retained by the MOF framework) [89]. Because of the presence of mesopores having diameters of 2.9–3.4 nm, capillary condensation occurred at undesirably high relative pressures, thus resulting in an adsorption-desorption hysteresis loops. An effort was made to tune the hysteresis loops by functionalizing the MOF structure to obtain MIL-101(–NO_2), MIL-101(–NH_2), or MIL-101(–SO_3H) analogues [292,294]. By varying the hydrophobic character of the functional groups introduced into the linker moiety, more suitable water sorption behaviour could be obtained in view of heat storage uses.

MIL-53 was another material of this family tested for water adsorption. Unexpectedly, this microporous MOF was also shown to display a hysteresis loop in the adsorption-desorption isotherm [260,295,296]. This particular sorption behaviour was ascribed to the irreversible change in the framework flexibility induced by the sorption of some guest molecules, coinciding with the hysteresis loop. Salles et al. [260] concluded that the "breathing" effect was paralleled by a modification of the hydrophobic-hydrophilic character of the MIL-53(Cr) surface. Although the water adsorption capacity of MIL-53 was only about 0.2 g g^{-1} in comparison with that of MIL-100 or MIL-101, it offered an alternative to tuning the sorption properties towards water vapour by functionalization of the framework with either hydrophobic or hydrophilic groups.

An interesting property of Prussian Blue Analogues was reported quite recently by Boudjema et al. [297]. While the completely dehydrated material showed a hydrophobic surface behaviour, a switch to a hydrophilic character was induced by overcoming the water relative pressure threshold at $p/p_0 \sim 0.03$. It is worth noting that much interest has been devoted lately to new MOF materials, which currently constitute one of the most intensively studied adsorbents in the literature. For example, a newly discovered robust large-pore zirconium carboxylate MOF, called MIP-200, was described by Wang et al. [298]. It was found to produce S-shaped adsorption isotherms with a water uptake of 0.39 g g^{-1} below $p/p_0 = 0.25$. It was characterized by easy regeneration and good cycling, as well as a notably high coefficient of performance of 0.78 for refrigeration at a low driving temperature below 343 K.

5.5. Other Adsorbents and Adsorbates

Besides the four classes of adsorbents detailed in the previous sections, other materials have been considered for the purpose of adsorption of water vapour and they are discussed below.

Activated alumina (Al_2O_3) has been widely used in the moisture capture and catalysis processes [122,299–303]. Commercial activated alumina is generally synthesized by thermal dehydration or activation of aluminium trihydrate, $Al(OH)_3$, and the specific surface area depends on the pre-treatment temperature [157,304]. As early as 1971, Carruthers et al. studied the adsorption of water vapour onto various forms of alumina [305]. They revealed five different mechanism schemes which may be followed: 1) H-bonding between water molecules and surface hydroxyl groups (i.e., aluminols), 2) surface hydration of the exposed surface cations by water molecules, 3) dissociative chemisorption in the case of α-alumina, 4) hydration in depth of poorly ordered Al^{3+}, originally solvated and not fully coordinated in the oxide structure, 5) hydroxide or oxide-hydroxide formation in depth, e.g., rehydration of transition alumina. Marcussen investigated the kinetics of water adsorption onto alumina based on his model which included a nonlinear adsorption isotherm and simultaneous resistance to mass transfer in the pore system of the solid and in a film surrounding the solid particles [303]. Given a good agreement between the theoretical and experimental data, an effective diffusion coefficient in the pores of 3.6×10^{-6} m^2 s^{-1} and a gas film resistance of 0.85 $Re^{-0.5}$ were determined. Close and Pryor made theoretical study on packed beds containing activated alumina for uses in energy storage units [299,306]. Although activated alumina showed a significant advantage over gravel beds in terms of thermal losses, it was demonstrated to have poorer performance when compared with silica gel beds. Shi et al. summarized 14 models for isotherms of water adsorption onto activated alumina [301]. Desai et al. pointed out that the choice of the regeneration temperature for the water-loaded alumina depended critically on the desired humidity level [307]. A lower regeneration temperature was sufficient at relatively high humidity, as it was neither necessary nor desirable to remove the chemisorbed water. Serbzov et al. measured isotherms for the adsorption of water vapour onto activated alumina F-200 at 278, 288, 298, and 308 K in the range from 0 to about 95% of relative humidity and obtained a maximum water adsorption of about 25 mmol g^{-1} [122,308]. Higher temperatures under vacuum conditions were needed to completely regenerate the adsorbent. Ferreira et al. compared the adsorption capacity of 13X zeolite, activated alumina and pure silica towards water vapour and carbon dioxide from air on the basis of the equilibrium adsorption isotherms at 308 K [309]. They found that 13X exhibited the highest adsorption capacity towards both adsorbates at low relative pressures. The S-shape of adsorption isotherms in the case of activated alumina (maximum amount adsorbed of 4.55 mol kg^{-1}) and silica (2.66 mol kg^{-1}), with an inflection point at an intermediate relative pressure, gave these materials an important advantage over zeolite within the interval of higher relative pressures. Furthermore, the cycling stability of activated alumina was worse compared to silica. This instability was confirmed by Knez and Novak [111] since alumina aerogel was shown to lose almost half of its water adsorption capacity (from 1.2 to 0.6 g g^{-1}) after 10 adsorption-desorption cycles.

Clay materials have been investigated in heat storage owing to their large specific surface areas, low cost and high availability. Their surface area ranges between 300 and 700 $m^2\ g^{-1}$ and they are known for their ability to adsorb much water in quantity corresponding to about 7–10 times their volume [310], thus resulting in strong expansion (swelling) of the interlayer space. Clays are built of negatively charged aluminosilicate layers kept together by some compensating cations [311–315]. Heat of adsorption can be released upon contact with water vapour through the penetration of water molecules between the layers due to hydrogen bonding with the hydroxyl groups present in the clay structure and also through the hydration of the exchangeable cations [311,314]. Such "interlayer swelling" depends on the nature of clay and that of compensating cations.

Hydration-dehydration behaviour of bentonite, consisting mostly of montmorillonite, has been widely studied in view of heat storage uses [310,313,316–320]. Konta compared bentonites with different compensating cations, such as Ca^{2+} and Na^{+} [311], and concluded that Na-bentonite tended to be highly dispersed in water, whereas Ca-bentonite showed a tendency to coagulate. Sadek and Mekhemer [310,316] argued the suitability of using Ca- and Na-montmorillonite clays as thermal energy storage materials. With pre-heating at 398 K, the adsorption capacity towards water and energy storage reached the following values: 0.25 g g^{-1} and 1360 J g^{-1} (i.e., 435 cal g^{-1}) for Ca-montmorillonite; 0.29 g g^{-1} and 2843 J g^{-1} (i.e., 679 cal g^{-1}) for Na-montmorillonite, respectively. They indicated that the compensating cation, its size and its ionic charge played a significant role in determining the capacity of storing thermal energy. Salles et al. [312] confirmed that the driving force for hydration of the montmorillonite type clays was generally a function of the nature of the interlayer cation. Furthermore, the presence of two types of cation (e.g., Na^{+} and Ca^{2+}) may produce the heat release stages at various values of relative humidity, which could be of interest for storage uses [321]. Finally, Castrillo et al. [322] demonstrated that the regeneration of bentonite at low temperatures (below 373 K) was not 100% effective, leading to a slow decrease in the adsorption capacity after successive regeneration steps (i.e., loss of 15–17% after 5 cycles).

Activated carbons have also been widely used as adsorbents owing to their large micropore and mesopore volumes, as well as their high surface areas ranging between 300 and 4000 $m^2\ g^{-1}$. The manufacturing process usually involves: (i) raw material preparation, (ii) low-temperature carbonization, and (iii) activation procedures [157]. The main specificity of activated carbon is related to its weak polar character mainly in relation with the presence of surface oxide groups, various heteroatoms inserted in polyaromatic rings or inorganic impurities. When water molecules are adsorbed on the carbonaceous surface at low vapour pressures, the direct adsorbent-adsorbate interactions are of the van der Waals type. As a consequence, isotherms of water adsorption represent type V curves. At higher vapour pressures, clusters of water molecules are formed and eventually pore filling occurs through hydrogen bonding [323].

Experimental study of water adsorption on activated carbons at low surface coverage ratios led Salame and Bandosz to conclude on the dependence of water sorption on the surface chemistry and porosity of the adsorbent [324]. A significant contribution to the isosteric heats of adsorption due to water-water interactions was recorded even at very low relative pressures. Huber et al. proposed a monolithic nitrogen-doped carbon as a water sorbent for adsorption refrigeration technology [325]. This carbonaceous sample was prepared from a resorcinol-melamine-formaldehyde resin moulded into monolithic shapes before pyrolysis and chemical activation with KOH. At the 2300 Pa pressure of water vapour, the specific cooling power arrived at 192 W kg^{-1} of water vapour for a temperature decrease from 363 K to 323 K and 389 W kg^{-1} when the temperature passed from 333 K to 303 K. This cooling performance was higher than that of commercial silica gel. Given the weak polarity of carbon surface, other adsorbates, less polar than water, were adsorbed onto activated carbon. For example, Critoph demonstrated the potential of methanol and ammonia as adsorbates for small solar-powered refrigerators [326]. Nevertheless, the use of such adsorbates should be limited to closed systems for security and health reasons.

The adsorption of methanol or ethanol onto MOF materials may be also of interest for the storage applications. De Lange et al. studied the adsorption of methanol or ethanol as the working fluid onto 18 different MOF structures for uses in adsorption-driven heat pumps and chillers [327]. They arrived at the following conclusions, in comparison with water vapour employed as the adsorbate: (i) adsorption occurred at lower relative pressures in the case of methanol and even much lower for ethanol, (ii) larger pores could be utilized more efficiently, since the hysteresis loops were absent until the pore size attained at least 3.4 nm (only 2 nm for water), (iii) larger pore sizes were needed to ensure the desired stepwise adsorption, (iv) the impact of functional groups in the MOF framework was far less pronounced, (v) the energy released or stored up per one cycle was lower, but the heat and mass transfers were enhanced, (vi) the framework stability would be less of an issue, with notable exceptions of UiO-67 and CAU-8.

MIL-100 and MIL-101 were not appropriate for the present uses because of the high temperatures required for desorption in relation with the type I adsorption isotherms. From the thermodynamic viewpoint, UiO-67, CAU-3, and ZIF-8 samples appeared more adequate for adsorption of methanol and ethanol. Because of moderate desorption temperatures, these materials could outperform activated carbons. Even though UiO-67 was not completely stable during adsorption of ethanol and methanol, both CAU-3 and ZIF-8 showed great potential for applications, especially in sub-zero temperature adsorption chillers. The choice of methanol (higher energy capacity) or ethanol (higher temperature lift) was found to depend on the evaporation temperature required for a given application.

6. Concluding Remarks

Amongst various concepts considered in the scientific and technical literature to harvest solar energy during summer season and store it until wintertime in view of space heating uses, low-temperature thermochemical storage based on solid-vapour adsorption seems to constitute a promising alternative because the storing principle relies on quite well-controlled changes in the chemical potential of a solid material and is far less sensitive to temperature variations between the charging and discharging steps. Contrary to thermal storage methods using sensible or latent heat, the charging (i.e., endothermic vapour desorption from the adsorbent surface) and discharging (i.e., exothermic vapour adsorption onto adsorbent) temperatures do not need to be the same and the energy storage density depends to a much smaller extent on the discharging (adsorption) temperature. Open sorption systems operating in the *moist-air flow mode* offer the advantage of operating under atmospheric pressure and ambient temperature, thereby avoiding potentially detrimental conditions of high partial pressures of adsorbate in combination with elevated temperatures. Nevertheless, the thermochemical storage technology is still at too low maturity level, the only industrial implementation known nowadays corresponds to a short-term (day-night cycle changeover) heat storage unit using zeolite 13X beds to adsorb water vapour and thus heat a school building. The selection of materials should be carefully adapted to real operating conditions and this is probably the main reason that has continuously motivated the researchers to propose new adsorbents performing under particular conditions of use.

In order to avoid creating or aggravating problems related to the adsorbent regeneration (application of vacuum and high-temperature degassing processes) or long-term storage of the adsorbent between the charging and discharging steps without loss of its activity (use of vacuum-tight tanks), materials exhibiting a very hydrophilic surface character and strongly adsorbing much water vapour already at low vapour pressures are not necessarily the best candidates for low-temperature heat storage by adsorption of water vapour. The adequate adsorption isotherm should rather exhibit a particular, stepwise shape, as those exemplified in Figure 5. In such systems, even if all adsorbed water is not released from the solid surface during the charging step, the increase in the water uptake in the intermediate pressure region may be sufficiently high for the adsorbent to be of interest for use in heat storage. Hence the relative vapour pressure employed during the discharging step (e.g., the humidity level in the carrier air flow) has to be high enough to reach the adsorption plateau value. It is thus

clear that the location of the quasi-vertical portions of the adsorption and desorption isotherms should be chosen in line with the operating conditions. The inset graph in Figure 5 additionally illustrates the fact that this location is not constant for a given type of solid material and may, for example, depend on the pore size, which makes the adsorbent selection less evident.

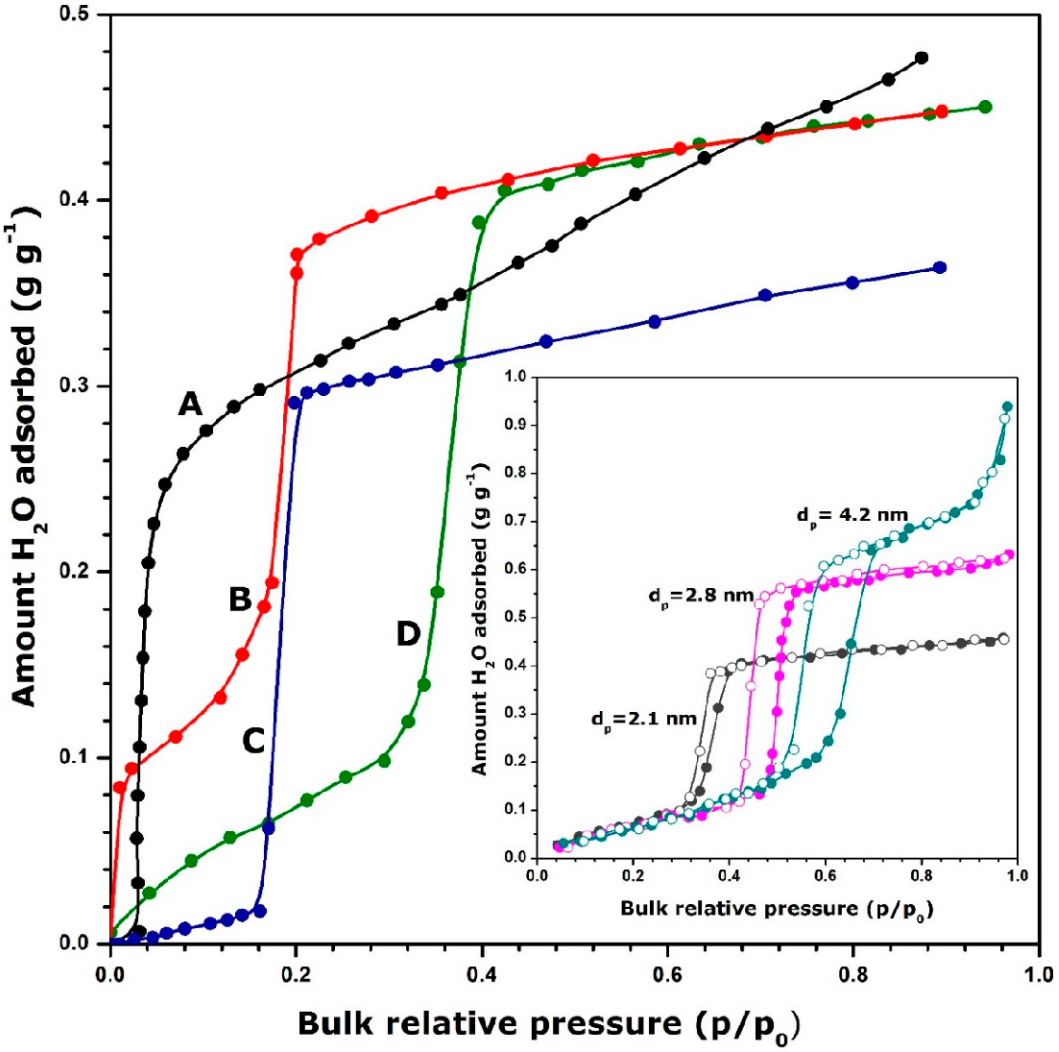

Figure 5. Examples of S-shaped adsorption isotherms for water vapour onto different adsorbents at 298 K (with the exception of Prussian Blue Analogue and MIP-200: data at 303 K): Prussian Blue Analogue (Curve A); zeotype silico-aluminophosphate, MIP-200 (Curve B); Metal Organic Framework, CAU-10 (Curve C); ordered mesoporous silica of the MCM-41 type (Curve D). The amount of H_2O adsorbed expressed as mass of the adsorbate per unit mass of the adsorbent. The inset shows the effect of the pore size on the location of the adsorption (solid circles) and desorption (open circles) isotherms obtained with ordered mesoporous silicas of the MCM-41 type. Data adapted from [172,297,298,328].

Synthetic materials possessing uniformly structured porosity with high specific surface areas and tuneable or switchable hydrophobic-hydrophilic surface character seem to meet the above requirements and they will certainly constitute the adsorbents of the future. This may be the case of certain ordered mesoporous silicas, microporous MOF materials, or Prussian Blue Analogues, provided that they meet the requirements of hydrothermal stability, shaping and up-scaling. Moreover, much more effort will be necessary to further assess the performance of selected adsorbents on pilot scale with simulated operating conditions before considering their use in full-scale applications in thermochemical storage of energy by sorption.

In light of the discussion on the properties of materials considered in the present review, it seems appropriate to reflect on the potential effectiveness of the thermochemical storage by sizing the process for space heating in the building sector. Figure 6 presents the results of simulation of the mass of various adsorbents required to cover, during 22 winter's coldest days, the energy needs for space heating in 100 m^2 houses located in the Parisian (North of France) and Marseille (South of France) regions which comply with the current RT2018 standards. It is important to realise that the energy input during this reference period accounts for almost one third of the total annual needs for space heating.

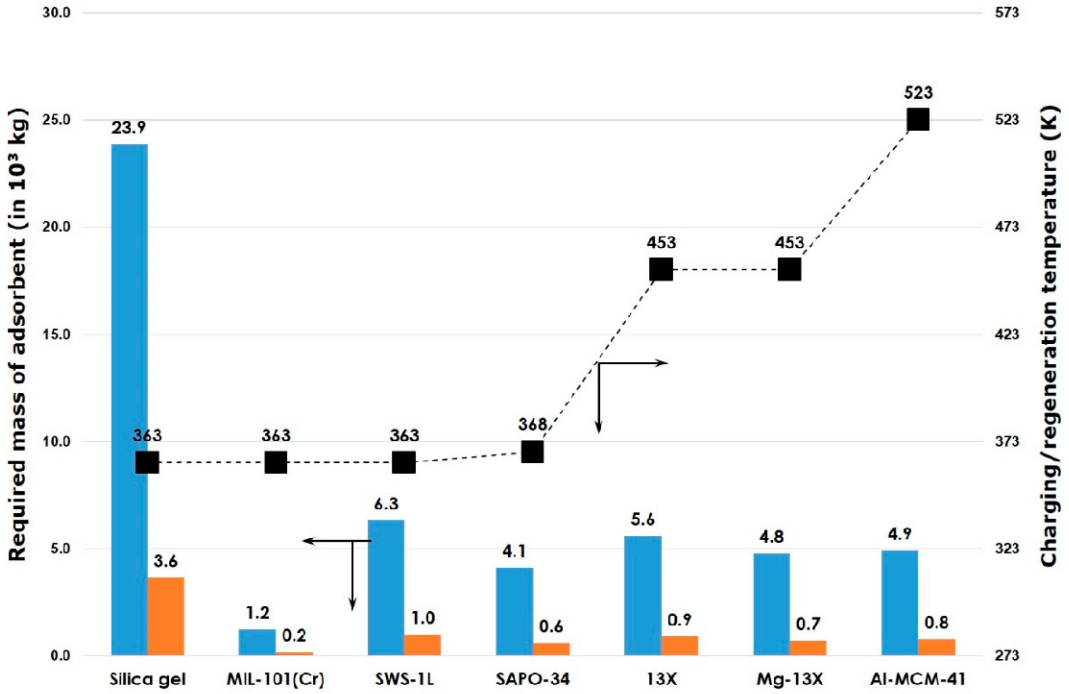

Figure 6. Assessing the efficiency of thermochemical storage by adsorption of water vapour onto selected adsorbents: simulation of the mass of adsorbent required to cover, during 22 winter's coldest days, the energy needs for space heating in a 100 m^2 house located in the Parisian (North of France, in blue) and Marseille (South of France, in orange) regions which comply with the new RT2018 standards, namely 3000 MJ (i.e., 836 kWh) and 460 MJ (i.e., 128 kWh), respectively, to maintain the indoor temperature at 292 K [329]. The energy density and charging/regeneration temperature data have been taken from [23,69,87,92,112].

It is clear from the figure that the principle of thermochemical storage by water adsorption onto porous adsorbents is not capable of covering alone the energy needs for space heating in homes, small businesses and public buildings if the quantity of the working materials employed should remain within reasonable limits. The phenomenon may be rather exploited in the auxiliary heating systems, which provide additional heat on just the coldest days, for example during 22 "EJP" peak tariff days set by the French electricity provider EDF [329,330].

Author Contributions: Data curation, H.W.; conceptualization and supervision, J.Z.; writing-original draft preparation, H.W., F.S., and J.Z.; writing- review and editing, F.S., J.Z.

Funding: This research received no external funding.

Acknowledgments: H. Wu gratefully acknowledges his Ph.D. scholarship from the French Ministry of Higher Education, Research and Innovation (Ministère de l'Enseignement supérieur, de la Recherche et de l'Innovation, MESRI).

Conflicts of Interest: The authors declare no conflict of interest.

References

1. European Commission. *Europe 2020: Europe's Growth Strategy*; European Commission: Brussels, Belgium, 2012; ISBN 9789279239724. [CrossRef]
2. Pérez-Lombard, L.; Ortiz, J.; Pout, C. A review on buildings energy consumption information. *Energy Build.* **2008**, *40*, 394–398. [CrossRef]
3. Lin, H.-W.; Hong, T. On variations of space-heating energy use in office buildings. *Appl. Energy* **2013**, *111*, 515–528. [CrossRef]
4. Lizana, J.; Chacartegui, R.; Barrios-Padura, A.; Valverde, J.M. Advances in thermal energy storage materials and their applications towards zero energy buildings: A critical review. *Appl. Energy* **2017**, *203*, 219–239. [CrossRef]
5. Sajn, N. *European Parliamentary Research Service: Energy Efficiency of Buildings: A Nearly Zero-Energy Future?* European Parliament: Brussels, Belgium, 2016.
6. Agence de l'Environnement et de la Maîtrise de l'Energie (ADEME). *Climat, air et énergie: Chiffres-clés*; ADEME éditions: Angers, France, 2017.
7. Roeb, M.; Neises, M.; Monnerie, N.; Sattler, C.; Pitz-Paal, R. Technologies and trends in solar power and fuels. *Energy Environ. Sci.* **2011**, *4*, 2503–2511. [CrossRef]
8. Aydin, D.; Casey, S.P.; Riffat, S. Theoretical analysis of the potential for thermochemical heat storage under Mediterranean climate conditions: Northern Cyprus Case. *Future Cities Environ.* **2015**, *5*, 231–295. [CrossRef]
9. Renewable Energy Policy Network for the 21st Century (REN21). *Renewables 2017: Global Status Report*; REN21: Paris, France, 2017; Volume 72, ISBN 978-3-9818107-0-7. [CrossRef]
10. International Energy Agency (IEA); Bahar, H. *Renewables 2017*; International Energy Agency: Paris, France, 2017; ISBN 978-92-64-28187-5. [CrossRef]
11. Anisur, M.R.; Mahfuz, M.H.; Kibria, M.A.; Saidur, R.; Metselaar, I.H.S.C.; Mahlia, T.M.I. Curbing global warming with phase change materials for energy storage. *Renew. Sustain. Energy Rev.* **2013**, *18*, 23–30. [CrossRef]
12. Moth-Poulsen, K.; Ćoso, D.; Börjesson, K.; Vinokurov, N.; Meier, S.K.; Majumdar, A.; Vollhardt, K.P.C.; Segalman, R.A. Molecular solar thermal (MOST) energy storage and release system. *Energy Environ. Sci.* **2012**, *5*, 8534–8537. [CrossRef]
13. Haji Abedin, A.; Rosen, M.A. Energy and exergy analyses of an open thermochemical energy storage system: Methodology and illustrative application. *Open Renew. Energy J.* **2012**, *5*, 41–48. [CrossRef]
14. Yu, N.; Wang, R.Z.; Wang, L.W. Sorption thermal storage for solar energy. *Prog. Energy Combust. Sci.* **2013**, *39*, 489–514. [CrossRef]
15. N'Tsoukpoe, K.E.; Liu, H.; Le Pierrès, N.; Luo, L. A review on long-term sorption solar energy storage. *Renew. Sustain. Energy Rev.* **2009**, *13*, 2385–2396. [CrossRef]
16. Shigeishi, R.A.; Langford, C.H.; Hollebone, B.R. Solar energy storage using chemical potential changes associated with drying of zeolites. *Sol. Energy* **1979**, *23*, 489–495. [CrossRef]
17. Schmidt, T.; Mangold, D.; Müller-Steinhagen, H. Central solar heating plants with seasonal storage in Germany. *Sol. Energy* **2004**, *76*, 165–174. [CrossRef]
18. Nielsen, K. *Thermal Energy Storage: A State-Of-The-Art. A Report within the Research Program Smart Energy-Efficient Buildings at the Norwegian University of Science and Technology and SINTEF*; Department of Geology and Mineral Resources Engineering NTNU: Trondheim, Norway, 2003.
19. André, L.; Abanades, S.; Flamant, G. Screening of thermochemical systems based on solid-gas reversible reactions for high temperature solar thermal energy storage. *Renew. Sustain. Energy Rev.* **2016**, *64*, 703–715. [CrossRef]
20. André, L.; Abanades, S. Evaluation and performances comparison of calcium, strontium and barium carbonates during calcination/carbonation reactions for solar thermochemical energy storage. *J. Energy Storage* **2017**, *13*, 193–205. [CrossRef]
21. Prieto, C.; Cooper, P.; Fernández, A.I.; Cabeza, L.F. Review of technology: Thermochemical energy storage for concentrated solar power plants. *Renew. Sustain. Energy Rev.* **2016**, *60*, 909–929. [CrossRef]
22. Aydin, D.; Casey, S.P.; Riffat, S. The latest advancements on thermochemical heat storage systems. *Renew. Sustain. Energy Rev.* **2015**, *41*, 356–367. [CrossRef]

23. Bales, C.; Gantenbein, P.; Hauer, A.; Henning, H.-M.; Jaenig, D.; Kerskes, H.; Nuñez, T.; Visscher, K. *Thermal Properties of Materials for Thermo-Chemical Storage of Solar Heat: Report B2 of Subtask B*; The Solar Heating and Cooling Programme: Cedar, MI, USA, 2005.
24. Singh, H.K.; Buddhi, D. Experimental investigation on $CaCl_2.6H_2O$ for subcooling behavior and its correction for low temperature thermal energy storage. *Int. J. Appl. Eng. Res.* **2018**, *13*, 9858–9867.
25. Henninger, S.K.; Ernst, S.J.; Gordeeva, L.; Bendix, P.; Fröhlich, D.; Grekova, A.D.; Bonaccorsi, L.; Aristov, Y.; Jaenchen, J. New materials for adsorption heat transformation and storage. *Renew. Energy* **2017**, *110*, 59–68. [CrossRef]
26. Cabeza, L.F.; Solé, A.; Barreneche, C. Review on sorption materials and technologies for heat pumps and thermal energy storage. *Renew. Energy* **2017**, *110*, 3–39. [CrossRef]
27. Frazzica, A.; Freni, A. Adsorbent working pairs for solar thermal energy storage in buildings. *Renew. Energy* **2017**, *110*, 87–94. [CrossRef]
28. Scapino, L.; Zondag, H.A.; Van Bael, J.; Diriken, J.; Rindt, C.C.M. Sorption heat storage for long-term low-temperature applications: A review on the advancements at material and prototype scale. *Appl. Energy* **2017**, *190*, 920–948. [CrossRef]
29. Steele, W.A. *The Interaction of Gases with Solid Surfaces*; Pergamon Press: Oxford, UK, 1974.
30. Gregg, S.J.; Sing, K.S.W. *Adsorption, Surface Area, and Porosity*, 2nd ed.; Academic Press: London, UK, 1982.
31. Bolis, V. Fundamentals in adsorption at the solid-gas interface. Concepts and thermodynamics. In *Calorimetry and Thermal Methods in Catalysis*; Auroux, A., Ed.; Springer: Berlin/Heidelberg, Germany, 2013; pp. 3–50. ISBN 978-3-642-11954-5. [CrossRef]
32. Lowell, S.; Shields, J.E.; Thomas, M.A.; Thommes, M. *Characterization of Porous Solids and Powders: Surface Area, Pore Size and Density*; Springer: Berlin/Heidelberg, Germany, 2004; Volume 16, ISBN 978-90-481-6633-6. [CrossRef]
33. Sing, K.S.W. The use of gas adsorption for the characterization of porous solids. *Colloids Surf.* **1989**, *38*, 113–124. [CrossRef]
34. Everett, D.H.; Powl, J.C. Adsorption in slit-like and cylindrical micropores in the Henry's law region: A model for the microporosity of carbons. *J. Chem. Soc. Faraday Trans. Phys. Chem. Condens. Phases* **1976**, *72*, 619–636. [CrossRef]
35. Healey, F.; Carter, R.N.; Worthy, G.; Hodgson, A. Endothermic dissociative chemisorption of molecular D2 on Ag(111). *Chem. Phys. Lett.* **1995**, *243*, 133–139. [CrossRef]
36. De Boer, J.H. 50 endothermic chemisorption and catalysis. In *Advances in Catalysis*; Farkas, A., Ed.; Academic Press: Cambridge, MA, USA, 1957; Volume 9, pp. 472–480. ISBN 0360-0564. [CrossRef]
37. Álvarez-Falcón, L.; Viñes, F.; Notario-Estévez, A.; Illas, F. On the hydrogen adsorption and dissociation on Cu surfaces and nanorows. *Surf. Sci.* **2016**, *646*, 221–229. [CrossRef]
38. Zajac, J.; Dutartre, R.; Jones, D.J.; Roziere, J. Determination of surface acidity of powdered porous materials based on ammonia chemisorption: Comparison of flow-microcalorimetry with batch volumetric method and temperature-programmed desorption. *Thermochim. Acta* **2001**, *379*, 123–130. [CrossRef]
39. Auroux, A. Acidity characterzation by microcalorimetry and relationship with reactivity. *Top. Catal.* **1997**, *4*, 71–89. [CrossRef]
40. Stošić, D.; Bennici, S.; Sirotin, S.; Calais, C.; Couturier, J.L.; Dubois, J.L.; Travert, A.; Auroux, A. Glycerol dehydration over calcium phosphate catalysts: Effect of acidic-basic features on catalytic performance. *Appl. Catal. A Gen.* **2012**, *447–448*, 124–134. [CrossRef]
41. Damjanović, L.; Auroux, A. Determination of acid/base properties by temperature programmed desorption (TPD) and adsorption calorimetry. In *Zeolite Characterization and Catalysis: A Tutorial*; Chester, A.W., Derouane, E.G., Eds.; Springer: Dordrecht, The Netherlands, 2009; pp. 107–167. ISBN 978-1-4020-9678-5. [CrossRef]
42. Ottiger, S.; Pini, R.; Storti, G.; Mazzotti, M. Measuring and modeling the competitive adsorption of CO_2, CH_4, and N_2 on a dry coal. *Langmuir* **2008**, *24*, 9531–9540. [CrossRef] [PubMed]
43. Bellat, J.-P. Study of selective adsorption of gases by calorimetry. In *Calorimetry and Thermal Methods in Catalysis*; Auroux, A., Ed.; Springer: Berlin/Heidelberg, Germany, 2013; pp. 273–318. ISBN 978-3-642-11954-5. [CrossRef]
44. Rouquerol, F.; Rouquerol, J.; Everett, D.H. Gas—Solid interactions. General derivation of reaction enthalpies from the data of isothermal microcalorimetry. *Thermochim. Acta* **1980**, *41*, 311–322. [CrossRef]

45. Auroux, A. *Calorimetry and Thermal Methods in Catalysis*; Springer: New York, NY, USA, 2013; Volume 154, ISBN 978-3-642-11954-5. [CrossRef]
46. Tian, Y.; Wu, J. Differential heat of adsorption and isosteres. *Langmuir* **2017**, *33*, 996–1003. [CrossRef] [PubMed]
47. Mohr, R.; Rao, M.B. Isosteric Heat of Adsorption: Theory and Experiment. *J. Phys. Chem. B* **1999**, *103*, 6539–6546. [CrossRef]
48. Builes, S.; Sandler, S.I.; Xiong, R. Isosteric heats of gas and liquid adsorption. *Langmuir* **2013**, *29*, 10416–10422. [CrossRef] [PubMed]
49. Sircar, S. Excess properties and column dynamics of multicomponent gas adsorption. *J. Chem. Soc. Faraday Trans. Phys. Chem. Condens. Phases* **1985**, *81*, 1541–1545. [CrossRef]
50. Rudzinski, W.; Everett, D.H. *Adsorption of Gases on Heterogeneous Surfaces*, 1st ed.; Press, A., Ed.; Academic Press: London, UK, 1992; ISBN 978-0-12-601690-1. [CrossRef]
51. Knor, Z. Static volumetric methods for determination of absorbed amount of gases on clean solid surfaces. *Catal. Rev.* **1968**, *1*, 257–313. [CrossRef]
52. Thommes, M.; Kaneko, K.; Neimark, A.V.; Olivier, J.P.; Rodriguez-Reinoso, F.; Rouquerol, J.; Sing, K.S.W. Physisorption of gases, with special reference to the evaluation of surface area and pore size distribution (IUPAC Technical Report). *Pure Appl. Chem.* **2015**, *87*, 1051–1069. [CrossRef]
53. Degas Options for Micropore Samples, Application Note N° 160, Micromeritics' Application Notes and Technical Tips, Norcross, USA. September 2012. Available online: https://www.micromeritics.com/Library/ (accessed on 1 February 2019).
54. Bejan, A.S.; Labihi, A.; Croitoru, C.; Catalina, T. Air solar collectors in building use—A review. In Proceedings of the E3s Web Conf., Bucharest, Romania, 24 November 2017. [CrossRef]
55. D'Antoni, M.; Saro, O. Massive solar-thermal collectors: A critical literature review. *Renew. Sustain. Energy Rev.* **2012**, *16*, 3666–3679. [CrossRef]
56. Fabian, F.; Eberhard, L. Multiple sample setup for testing the hydrothermal stability of adsorbents in thermal energy storage applications. *Meas. Sci. Technol.* **2015**, *26*, 65603. [CrossRef]
57. Storch, G.; Reichenauer, G.; Scheffler, F.; Hauer, A. Hydrothermal stability of pelletized zeolite 13X for energy storage applications. *Adsorption* **2008**, *14*, 275–281. [CrossRef]
58. Cruciani, G. Zeolites upon heating: Factors governing their thermal stability and structural changes. *J. Phys. Chem. Solids* **2006**, *67*, 1973–1994. [CrossRef]
59. Fischer, U.R. What is the best possible heat storage density for a seasonal adsorptive thermal energy storage. In Proceedings of the Effstock 2009, Thermal Energy Storage for Efficiency and Sustainability: 11th International conference on Thermal Energy Storage, Stockholm, Sweden, 14–17 June 2009.
60. Jänchen, J.; Ackermann, D.; Weiler, E.; Stach, H.; Brösicke, W. Calorimetric investigation on zeolites, AlPO4's and CaCl2 impregnated attapulgite for thermochemical storage of heat. *Thermochim. Acta* **2005**, *434*, 37–41. [CrossRef]
61. Zettl, B.; Englmair, G.; Steinmaurer, G. Development of a revolving drum reactor for open-sorption heat storage processes. *Appl. Therm. Eng.* **2014**, *70*, 42–49. [CrossRef]
62. Energy-Hub for Residential and Commercial Districts and Transport (E-HUB), Report on a Combination of Thermal Storage Techniques and Components. Available online: https://www.e-hub.org/pdf/D3.2_Thermal_storage_techniques_components.pdf (accessed on 18 March 2014).
63. Paksoy, H.Ö. (Ed.) *Thermal Energy Storage for Sustainable Energy Consumption: Fundamentals, Case Studies and Design*; Springer: Berlin/Heidelberg, Germany, 2007; ISBN 978-1-4020-5290-3. [CrossRef]
64. Nir, S.; Adams, S.; Rein, R. Polarizability calculations on water, hydrogen, oxygen, and carbon dioxide. *J. Chem. Phys.* **1973**, *59*, 3341–3355. [CrossRef]
65. Perry, R.H.; Green, D.W. *Perry's Chemical Engineers' Handbook*, 7th ed.; Perry, R.H., Green, D.W., Maloney, J.O., Eds.; McGraw-Hill: New York, NY, USA, 1997; ISBN 0070498415. [CrossRef]
66. Parr, R.G.; Pearson, R.G. Absolute hardness: Companion parameter to absolute electronegativity. *J. Am. Chem. Soc.* **1983**, *105*, 7512–7516. [CrossRef]
67. Brauman, J.I.; Biairlb, L.K. Gas-phase acidities of alcohols. *J. Am. Chem. Soc.* **1970**, *2821*, 5986–5992. [CrossRef]
68. Mette, B.; Kerskes, H.; Drück, H. Concepts of long-term thermochemical energy storage for solar thermal applications—Selected examples. *Energy Procedia* **2012**, *30*, 321–330. [CrossRef]

69. Jänchen, J.; Ackermann, D.; Stach, H.; Brösicke, W. Studies of the water adsorption on Zeolites and modified mesoporous materials for seasonal storage of solar heat. *Sol. Energy* **2004**, *76*, 339–344. [CrossRef]
70. De Lange, M.F.; Verouden, K.J.F.M.; Vlugt, T.J.H.; Gascon, J.; Kapteijn, F. Adsorption-driven heat pumps: The potential of metal-organic frameworks. *Chem. Rev.* **2015**, *115*, 12205–12250. [CrossRef] [PubMed]
71. Demir, H.; Mobedib, M.; Ülkü, S. A review on adsorption heat pump: Problems and solutions. *Renew. Sustain. Energy Rev.* **2008**, *12*, 2381–2403. [CrossRef]
72. Fischer, F.; Lävemann, E.; Krönauer, A.; Hauer, A. *BIOWKK Workshop Dortmund 2012 Open Adsorption Systems for Thermal Energy Storage Applications*; Bavarian Centre for Applied Energy Research: Wuerzburg, Germany, 2012.
73. Kerskes, H.; Mette, B.; Bertsch, F.; Asenbeck, S.; Drück, H. Chemical energy storage using reversible solid/gas-reactions (CWS)—Results of the research project. *Energy Procedia* **2012**, *30*, 294–304. [CrossRef]
74. Hauer, A. Evaluation of adsorbent materials for heat pump and thermal energy storage applications in open systems. *Adsorption* **2007**, *13*, 399–405. [CrossRef]
75. Hauer, A. Thermal energy storage with zeolite for heating and cooling applications. In Proceedings of the International Sorption Heat Pump Conference 2002, Shanghai, China, 24–27 September 2002; pp. 385–390.
76. Stritih, U.; Koželj, R. Analysis of adsorption thermal storage device for solar energy storage. *Int. J. Green Technol.* **2017**, *3*, 23–34. [CrossRef]
77. Mette, B.; Kerskes, H.; Drück, H.; Müller-Steinhagen, H. Experimental and numerical investigations on the water vapor adsorption isotherms and kinetics of binderless zeolite 13X. *Int. J. Heat Mass Transf.* **2014**, *71*, 555–561. [CrossRef]
78. Poling, B.E.; Prausnitz, J.M.; O'Connell, J.P. *Properties of Gases and Liquids*, 5th ed.; McGraw-Hill Education: New York, NY, USA, 2001; ISBN 0071499997. [CrossRef]
79. Lide, D.R. (Ed.) *CRC Handbook of Chemistry and Physics*, 85th ed.; Taylor & Francis: Abingdon, UK, 2004; ISBN 0849304849. [CrossRef]
80. Lias, S.G.; Liebman, J.F.; Levin, R.D. Evaluated gas phase basicities and proton affinities of molecules; Heats of formation of protonated molecules. *J. Phys. Chem. Ref. Data* **1984**, *13*, 695–808. [CrossRef]
81. Nelson, J.R.D.; Lide, J.D.R.; Maryott, A.A. *Selected Values of Electric Dipole Moments for Molecules in the Gas Phase*; U.S. Department of Commerce: Washington, DC, USA, 1967.
82. Michaels, R.; Satterfield, W.J.; Colonna, G. *NFPA 325, 1994 Edition: Fire Hazard Properties of Flammable Liquids, Gases, and Volatile Solids. Fire Hazard Properties of Flammable Liquids, Gases, and Volatile Solids*; NFPA: Quincy, MA, YSA, 1994.
83. O'Kane, G.J. Inhalation of ammonia vapour. A report on the management of eight patients during the acute stages. *Anaesthesia* **1983**, *38*, 1208–1213. [CrossRef] [PubMed]
84. Guais, A.; Brand, G.; Jacquot, L.; Karrer, M.; Dukan, S.; Grévillot, G.; Molina, T.J.; Bonte, J.; Regnier, M.; Schwartz, L. Toxicity of carbon dioxide: A review. *Chem. Res. Toxicol.* **2011**, *24*, 2061–2070. [CrossRef] [PubMed]
85. Henninger, S.K.; Schmidt, F.P.; Henning, H.M. Water adsorption characteristics of novel materials for heat transformation applications. *Appl. Therm. Eng.* **2010**, *30*, 1692–1702. [CrossRef]
86. Henninger, S.K.; Jeremias, F.; Kummer, H.; Schossig, P.; Henning, H.M. Novel sorption materials for solar heating and cooling. *Energy Procedia* **2012**, *30*, 279–288. [CrossRef]
87. Henninger, S.K.; Jeremias, F.; Kummer, H.; Janiak, C. MOFs for use in adsorption heat pump processes. *Eur. J. Inorg. Chem.* **2012**, 2625–2634. [CrossRef]
88. Ehrenmann, J.; Henninger, S.K.; Janiak, C. Water adsorption characteristics of MIL-101 for heat-transformation applications of MOFs. *Eur. J. Inorg. Chem.* **2011**, 471–474. [CrossRef]
89. Jabbari-Hichri, A.; Bennici, S.; Auroux, A. Water sorption heats on silica-alumina-based composites for interseasonal heat storage. *J. Therm. Anal. Calorim.* **2014**, *118*, 1111–1118. [CrossRef]
90. Jabbari-Hichri, A.; Bennici, S.; Auroux, A. Enhancing the heat storage density of silica–alumina by addition of hygroscopic salts ($CaCl_2$, $Ba(OH)_2$, and $LiNO_3$). *Sol. Energy Mater. Sol. Cells* **2015**, *140*, 351–360. [CrossRef]
91. Jabbari-Hichri, A.; Bennici, S.; Auroux, A. Effect of aluminum sulfate addition on the thermal storage performance of mesoporous SBA-15 and MCM-41 materials. *Sol. Energy Mater. Sol. Cells* **2016**, *149*, 232–241. [CrossRef]

92. Whiting, G.; Grondin, D.; Bennici, S.; Auroux, A. Heats of water sorption studies on zeolite–$MgSO_4$ composites as potential thermochemical heat storage materials. *Sol. Energy Mater. Sol. Cells* **2013**, *112*, 112–119. [CrossRef]
93. Whiting, G.T.; Grondin, D.; Stosic, D.; Bennici, S.; Auroux, A. Zeolite–$MgCl_2$ composites as potential long-term heat storage materials: Influence of zeolite properties on heats of water sorption. *Sol. Energy Mater. Sol. Cells* **2014**, *128*, 289–295. [CrossRef]
94. Henninger, S.K.; Habib, H.A.; Janiak, C. MOFs as adsorbents for low temperature heating and cooling applications. *J. Am. Chem. Soc.* **2009**, *131*, 2776–2777. [CrossRef] [PubMed]
95. Farha, O.K.; Eryazici, I.; Jeong, N.C.; Hauser, B.G.; Wilmer, C.E.; Sarjeant, A.A.; Snurr, R.Q.; Nguyen, S.T.; Yazaydın, A.Ö.; Hupp, J.T. Metal–Organic Framework materials with ultrahigh surface areas: Is the sky the limit? *J. Am. Chem. Soc.* **2012**, *134*, 15016–15021. [CrossRef] [PubMed]
96. Titinchi, S.J.J.; Piet, M.; Abbo, H.S.; Bolland, O.; Schwieger, W. Chemically modified solid adsorbents for CO_2 capture. *Energy Procedia* **2014**, *63*, 8153–8160. [CrossRef]
97. Tarasevich, Y.I. The surface energy of hydrophilic and hydrophobic adsorbents. *Colloid J.* **2007**, *69*, 212–220. [CrossRef]
98. Derouane, E.G.; Védrine, J.C.; Pinto, R.R.; Borges, P.M.; Costa, L.; Lemos, M.A.N.D.A.; Lemos, F.; Ribeiro, F.R. The acidity of zeolites: Concepts, measurements and relation to catalysis: A review on experimental and theoretical methods for the study of zeolite acidity. *Catal. Rev.* **2013**, *55*, 454–515. [CrossRef]
99. Kawabuchi, Y.; Sotowa, C.; Kishino, M.; Kawano, S.; Whitehurst, D.D.; Mochida, I. Chemical vapor deposition of heterocyclic compounds over active carbon fiber to control its porosity and surface function. *Langmuir* **1997**, *13*, 2314–2317. [CrossRef]
100. Alby, D.; Salles, F.; Fullenwarth, J.; Zajac, J. On the use of metal cation-exchanged zeolites in sorption thermochemical storage: Some practical aspects in reference to the mechanism of water vapor adsorption. *Sol. Energy Mater. Sol. Cells* **2018**, *179*, 223–230. [CrossRef]
101. Medved', I.; Černý, R. Surface diffusion in porous media: A critical review. *Microporous Mesoporous Mater.* **2011**, *142*, 405–422. [CrossRef]
102. Fletcher, A.J.; Yüzak, Y.; Thomas, K.M. Adsorption and desorption kinetics for hydrophilic and hydrophobic vapors on activated carbon. *Carbon* **2006**, *44*, 989–1004. [CrossRef]
103. Schwieger, W.; Machoke, A.G.; Weissenberger, T.; Inayat, A.; Selvam, T.; Klumpp, M.; Inayat, A. Hierarchy concepts: Classification and preparation strategies for zeolite containing materials with hierarchical porosity. *Chem. Soc. Rev.* **2016**, *45*, 3353–3376. [CrossRef] [PubMed]
104. Colmenares, M.G.; Simon, U.; Cruz, O.; Thomas, A.; Goerke, O.; Gurlo, A. Batch and continuous synthesis upscaling of powder and monolithic ordered mesoporous silica COK-12. *Microporous Mesoporous Mater.* **2018**, *256*, 102–110. [CrossRef]
105. Martens, J.A.; Jammaer, J.; Bajpe, S.; Aerts, A.; Lorgouilloux, Y.; Kirschhock, C.E.A. Simple synthesis recipes of porous materials. *Microporous Mesoporous Mater.* **2011**, *140*, 2–8. [CrossRef]
106. John, V.B. The shaping of materials. In *Introduction to Engineering Materials*; Palgrave Macmillan UK: London, UK, 1983; pp. 137–177. ISBN 978-1-349-17190-3. [CrossRef]
107. Hausner, H.H. New methods for the consolidation of metal powders. In *Perspectives in Powder Metallurgy*; Hausner, H.H., Roll, K.H., Johnson, P.K., Eds.; Springer: Boston, MA, USA; New York, NY, USA, 1967; p. 255. ISBN 978-1-4899-6209-6. [CrossRef]
108. Akhtar, F.; Andersson, L.; Ogunwumi, S.; Hedin, N.; Bergström, L. Structuring adsorbents and catalysts by processing of porous powders. *J. Eur. Ceram. Soc.* **2014**, *34*, 1643–1666. [CrossRef]
109. Nickel, W.; Oschatz, M.; Von Der Lehr, M.; Leistner, M.; Hao, G.P.; Adelhelm, P.; Müller, P.; Smarsly, B.M.; Kaskel, S. Direct synthesis of carbide-derived carbon monoliths with hierarchical pore design by hard-templating. *J. Mater. Chem. A* **2014**, *2*, 12703–12707. [CrossRef]
110. Wang, W.; Long, H.; Li, T.; Wang, Y.; Liu, S.; Ru, H. Hierarchical trimodal macro-mesoporous silica monoliths with co-continuous macrostructures and isotropic skeletons constructed by randomly oriented SBA-15-type primary particles. *Microporous Mesoporous Mater.* **2018**, *258*, 262–268. [CrossRef]
111. Knez, Z.; Novak, Z. Adsorption of water vapor on silica, alumina, and their mixed oxide aerogels. *J. Chem. Eng. Data* **2001**, 858–860. [CrossRef]

112. Aristov, Y.I. Selective water sorbents, a new family of materials for adsorption cooling/heating: State of the art. In Proceedings of the Vminsk International Seminar "Heat Pipe, Heat Pumps, Refrigerators", Minsk, Belarus, 8–11 September 2003; pp. 379–390.
113. Dawoud, B.; Aristov, Y. Experimental study on the kinetics of water vapor sorption on selective water sorbents, silica gel and alumina under typical operating conditions of sorption heat pumps. *Int. J. Heat Mass Transf.* **2003**, *46*, 273–281. [CrossRef]
114. Freni, A.; Russo, F.; Vasta, S.; Tokarev, M.; Aristov, Y.I.; Restuccia, G. An advanced solid sorption chiller using SWS-1L. *Appl. Therm. Eng.* **2007**, *27*, 2200–2204. [CrossRef]
115. Simonova, I.A.; Freni, A.; Restuccia, G.; Aristov, Y.I. Water sorption on composite "silica modified by calcium nitrate". *Microporous Mesoporous Mater.* **2009**, *122*, 223–228. [CrossRef]
116. Gorbach, A.; Stegmaier, M.; Eigenberger, G. Measurement and modeling of water vapor adsorption on zeolite 4A–Equilibria and kinetics. *Adsorption* **2004**, *10*, 29–46. [CrossRef]
117. Hongois, S.; Kuznik, F.; Stevens, P.; Roux, J.J. Development and characterisation of a new $MgSO_4$-zeolite composite for long-term thermal energy storage. *Sol. Energy Mater. Sol. Cells* **2011**, *95*, 1831–1837. [CrossRef]
118. Seo, Y.K.; Yoon, J.W.; Lee, J.S.; Hwang, Y.K.; Jun, C.H.; Chang, J.S.; Wuttke, S.; Bazin, P.; Vimont, A.; Daturi, M.; et al. Energy-efficient dehumidification over hierachically porous metal-organic frameworks as advanced water adsorbents. *Adv. Mater.* **2012**, *24*, 806–810. [CrossRef] [PubMed]
119. Barton, S.S.; Evans, M.J.B.; Holland, J.; Koresh, J.E. Water and cyclohexane vapour adsorption on oxidized porous carbon. *Carbon* **1984**, *22*, 265–272. [CrossRef]
120. Pedram, E.O.; Hines, A.L. Pure vapor adsorption of water on Mobil Sorbead R silica gel. *J. Chem. Eng. Data* **1983**, *28*, 11–14. [CrossRef]
121. Li, G.; Xiao, P.; Webley, P.A.; Zhang, J.; Singh, R. Competition of CO_2/H_2O in adsorption based CO_2 capture. *Energy Procedia* **2009**, *1*, 1123–1130. [CrossRef]
122. Serbezov, A. Adsorption equilibrium of water vapor on F-200 activated alumina. *J. Chem. Eng. Data* **2003**, *48*, 421–425. [CrossRef]
123. Teo, H.W.B.; Chakraborty, A.; Fan, W. Improved adsorption characteristics data for AQSOA types zeolites and water systems under static and dynamic conditions. *Microporous Mesoporous Mater.* **2017**, *242*, 109–117. [CrossRef]
124. Thach, U.D.; Trens, P.; Prelot, B.; Zajac, J.; Hesemann, P. Tuning the interfacial properties of mesoporous ionosilicas: Effect of cationic precursor and counter anion. *J. Phys. Chem. C* **2016**, *120*, 27412–27421. [CrossRef]
125. Sing, K.S.W. Reporting physisorption data for gas/solid systems with special reference to the determination of surface area and porosity (Recommendations 1984). *Pure Appl. Chem.* **1985**, *57*, 603–619. [CrossRef]
126. Gregg, S.J.; Nashed, S.; Malik, M.T. The adsorption of water vapour on a microporous carbon black. *Powder Technol.* **1973**, *7*, 15–19. [CrossRef]
127. Brinker, C.J.; Scherer, G.W. (Eds.) *Sol-Gel Science: The Physics and Chemistry of Sol-Gel Processing*; Elsevier Science: Boston, MA, USA, 2013; ISBN 978-0-08-057103-4. [CrossRef]
128. Iler, R.K. *The Chemistry of Silica: Solubility, Polymerization, Colloid and Surface Properties and Biochemistry of Silica*; Wiley Intersciences Publications: New York, NY, USA, 1979.
129. Soleimani Dorcheh, A.; Abbasi, M.H. Silica aerogel; synthesis, properties and characterization. *J. Mater. Process. Technol.* **2008**, *199*, 10–26. [CrossRef]
130. Kleitz, F. *Ordered Microporous and Mesoporous Materials*, 2nd ed.; Klabunde, K.J., Richards, R.M., Eds.; Wiley: Hoboken, NJ, USA, 2009; ISBN 9780470222706. [CrossRef]
131. Van Der Voort, P.; Esquivel, D.; De Canck, E.; Goethals, F.; Van Driessche, I.; Romero-Salguero, F.J. Periodic mesoporous organosilicas: From simple to complex bridges; A comprehensive overview of functions, morphologies and applications. *Chem. Soc. Rev.* **2013**, *42*, 3913–3955. [CrossRef] [PubMed]
132. Wu, S.-H.; Mou, C.-Y.; Lin, H.-P. Synthesis of mesoporous silica nanoparticles. *Chem. Soc. Rev.* **2013**, *42*, 3862. [CrossRef] [PubMed]
133. Yuan, Z.-Y.; Su, B.-L. Insights into hierarchically meso–macroporous structured materials. *J. Mater. Chem.* **2006**, *16*, 663–677. [CrossRef]
134. Kresge, C.T.; Leonowicz, M.E.; Roth, W.J.; Vartuli, J.C.; Beck, J.S. Ordered mesoporous molecular sieves synthesized by a liquid-crystal template mechanism. *Nature* **1992**, *359*, 710–712. [CrossRef]
135. Alothman, Z.A. A review: Fundamental aspects of silicate mesoporous materials. *Materials* **2012**, *5*, 2874–2902. [CrossRef]

136. Ying, J.Y.; Mehnert, C.P.; Wong, M.S. Synthesis and applications of supramolecular-templated mesoporous materials. *Angew. Chem. Int. Ed.* **1999**, *38*, 56–77. [CrossRef]
137. Neimark, A.V.; Ravikovitch, P.I.; Grün, M.; Schüth, F.; Unger, K.K. Pore size analysis of MCM-41 type adsorbents by means of nitrogen and argon adsorption. *J. Colloid Interface Sci.* **1998**, *207*, 159–169. [CrossRef] [PubMed]
138. Tanev, P.T.; Pinnavaia, T.J. Mesoporous silica molecular sieves prepared by ionic and neutral surfactant templating: A comparison of physical properties. *Chem. Mater.* **1996**, *8*, 2068–2079. [CrossRef]
139. Markowitz, M.A.; Schoen, P.E.; Kust, P.; Gaber, B.P. Surface acidity and basicity of functionalized silica particles. *Colloids Surf. A Physicochem. Eng. Asp.* **1999**, *150*, 85–94. [CrossRef]
140. Tsyganenko, A.A.; Storozheva, E.N.; Manoilova, O.V.; Lesage, T.; Daturi, M.; Lavalley, J.C. Brønsted acidity of silica silanol groups induced by adsorption of acids. *Catal. Lett.* **2000**, *70*, 159–163. [CrossRef]
141. Rouxhet, P.G.; Sempels, R.E. Hydrogen bond strengths and acidities of hydroxyl groups on silica-alumina surfaces and in molecules in solution. *J. Chem. Soc. Faraday Trans. Phys. Chem. Condens. Phases* **1974**, *70*, 2021–2032. [CrossRef]
142. Cimas, Á.; Tielens, F.; Sulpizi, M.; Gaigeot, M.P.; Costa, D. The amorphous silica-liquid water interface studied by ab initio molecular dynamics (AIMD): Local organization in global disorder. *J. Phys. Condens. Matter* **2014**, 26. [CrossRef]
143. Zhuravlev, L.T. The surface chemistry of amorphous silica. Zhuravlev model. *Colloids Surf. A Physicochem. Eng. Asp.* **2000**, *173*, 1–38. [CrossRef]
144. Snyder, L.R.; Ward, J.W. The surface structure of porous silicas. *J. Phys. Chem.* **1966**, *70*, 3941–3952. [CrossRef]
145. Warring, S.L.; Beattie, D.A.; McQuillan, A.J. Surficial siloxane-to-silanol interconversion during room-temperature hydration/dehydration of amorphous silica films observed by ATR-IR and TIR-Raman spectroscopy. *Langmuir* **2016**, *32*, 1568–1576. [CrossRef] [PubMed]
146. Wan, Q.; Ramsey, C.; Baran, G. Thermal pretreatment of silica composite filler materials. *J. Therm. Anal. Calorim.* **2010**, *99*, 237–243. [CrossRef] [PubMed]
147. Souza, A.S.D.; Pantano, C.G. Hydroxylation and dehydroxylation behavior of silica glass fracture surfaces. *J. Am. Ceram. Soc.* **2002**, *85*, 1499–1504. [CrossRef]
148. Zhuravlev, L.T. Concentration of hydroxyl groups on the surface of amorphous silicas. *Langmuir* **1987**, *3*, 316–318. [CrossRef]
149. De Farias, R.F.; Airoldi, C. Thermogravimetry as a reliable tool to estimate the density of silanols on a silica gel surface. *J. Therm. Anal. Calorim.* **1998**, *53*, 751–756. [CrossRef]
150. Morrow, B.A.; McFarlan, A.J. Surface vibrational modes of silanol groups on silica. *J. Phys. Chem.* **1992**, *96*, 1395–1400. [CrossRef]
151. Mahadevan, T.S.; Garofalini, S.H. Dissociative chemisorption of water onto silica surfaces and formation of hydronium ions. *J. Phys. Chem. C* **2008**, *112*, 1507–1515. [CrossRef]
152. Hensen, E.J.M.; Poduval, D.G.; Ligthart, D.A.J.M.; van Veen, J.A.R.; Rigutto, M.S. Quantification of strong Bronsted acid sites in aluminosilicates. *J. Phys. Chem. C* **2010**, *114*, 8363–8374. [CrossRef]
153. Corma, A.; Fornes, V.; Navarro, M.T.; Perezpariente, J. Acidity and stability of MCM-41 crystalline aluminosilicates. *J. Catal.* **1994**, *148*, 569–574. [CrossRef]
154. Perez-Beltran, S.; Balbuena, P.B.; Ramírez-Caballero, G.E. Surface structure and acidity properties of mesoporous silica SBA-15 modified with aluminum and titanium: First-principles calculations. *J. Phys. Chem. C* **2016**, *120*, 18105–18114. [CrossRef]
155. Meziani, M.J.; Zajac, J.; Douillard, J.-M.; Jones, D.J.; Partyka, S.; Rozière, J. Evaluation of surface enthalpy of porous aluminosilicates of the MCM-41 type using immersional calorimetry: Effect of the pore size and framework Si:Al ratio. *J. Colloid Interface Sci.* **2001**, *233*, 219–226. [CrossRef] [PubMed]
156. Loewenstein, W. The distribution of aluminum in the tetrahedra of silicates and aluminates. *Am. Mineral.* **1954**, *39*, 92–96. [CrossRef]
157. Yang, R.T. *Adsorbents: Fundamentals and Applications*; John Wiley & Sons, Inc.: Hoboken, NJ, USA, 2003; ISBN 0471297410. [CrossRef]
158. Chen, L.Y.; Jaenicke, S.; Chuah, G.K. Thermal and hydrothermal stability of framework-substituted MCM-41 mesoporous materials. *Microporous Mater.* **1997**, *12*, 323–330. [CrossRef]
159. Shen, S.; Kawi, S. Understanding of the effect of al substitution on the hydrothermal stability of MCM-41. *J. Phys. Chem. B* **1999**, *103*, 8870–8876. [CrossRef]

160. Mokaya, R. Alumination pathways to mesoporous aluminosilicates with high-temperature hydrothermal stability. *ChemPhysChem* **2002**, *3*, 360–363. [CrossRef]
161. Mokaya, R. Influence of pore wall thickness on the steam stability of Al-grafted MCM-41. *Chem. Commun.* **2001**, 633–634. [CrossRef]
162. Chua, H.T.; Ng, K.C.; Chakraborty, A.; Oo, N.M.; Othman, M.A. Adsorption Characteristics of Silica Gel + Water Systems. *J. Chem. Eng. Data* **2002**, 1177–1181. [CrossRef]
163. Ng, K.C.; Chua, H.T.; Chung, C.Y.; Loke, C.H.; Kashiwagi, T.; Akisawa, A.; Saha, B.B. Experimental investigation of the silica gel-water adsorption isotherm characteristics. *Appl. Therm. Eng.* **2001**, *21*, 1631–1642. [CrossRef]
164. Ito, M.; Watanabe, F.; Hasatani, M. Improvement of both adsorption performance of silica gel and heat transfer characteristics by means of heat exchange modulation for a heat pump. *Heat Transf. Jpn. Res.* **1996**, *25*, 420–433. [CrossRef]
165. Jaehnig, D.; Hausner, R.; Wagner, W.; Isaksson, C. Thermo-chemical storage for solar space heating in a single-family house. In Proceedings of the ECOSTOCK Conference, Pomona, NJ, USA, 31 May–2 June 2006.
166. Hadorn, J. *IEA Solar Heating and Cooling Programme Task 32: Advanced Storage Concepts for Solar and Low Energy Buildings*; International Energy Agency: Paris, France, 2014.
167. Aristov, Y.I. Novel materials for adsorptive heat pumping and storage: Screening and nanotailoring of sorption properties. *J. Chem. Eng. Jpn.* **2007**, *40*, 1242–1251. [CrossRef]
168. Aristov, Y.I.; Glaznev, I.S.; Freni, A.; Restuccia, G. Kinetics of water sorption on SWS-1L (calcium chloride confined to mesoporous silica gel): Influence of grain size and temperature. *Chem. Eng. Sci.* **2006**, *61*, 1453–1458. [CrossRef]
169. Gordeeva, L.G.; Aristov, Y.I. Composites' salt inside porous matrix' for adsorption heat transformation: A current state-of-the-art and new trends. *Int. J. Low-Carbon Technol.* **2012**, 288–302. [CrossRef]
170. Llewellyn, P.L.; Schueth, F.; Grillet, Y.; Rouquerol, F.; Rouquerol, J.; Unger, K.K. Water sorption on mesoporous aluminosilicate MCM-41. *Langmuir* **1995**, *11*, 574–577. [CrossRef]
171. Kocherbitov, V.; Alfredsson, V. Hydration of MCM-41 studied by sorption calorimetry. *J. Phys. Chem. C* **2007**, *111*, 12906–12913. [CrossRef]
172. Kittaka, S.; Ishimaru, S.; Kuranishi, M. Enthalpy and interfacial free energy changes of water capillary condensed in mesoporous silica, MCM-41 and SBA-15. *Phys. Chem. Chem. Phys.* **2006**, 3223–3231. [CrossRef] [PubMed]
173. Rozwadowski, M.; Lezanska, M.; Wloch, J.; Erdmann, K.; Golembiewski, R.; Kornatowski, J. Mechanism of adsorption of water, benzene, and nitrogen on Al-MCM-41 and effect of coking on the adsorption. *Langmuir* **2001**, *17*, 2112–2119. [CrossRef]
174. Thach, U.D.; Hesemann, P.; Yang, G.; Geneste, A.; Le Caër, S.; Prelot, B. Ionosilicas as efficient sorbents for anionic contaminants: Radiolytic stability and ion capacity. *J. Colloid Interface Sci.* **2016**, *482*, 233–239. [CrossRef] [PubMed]
175. Auerbac, S.M.; Carrado, K.A.; Dutt, P.K. (Eds.) *Handbook of Zeolite Science and Technology*; Marcel Dekker: New York, NY, USA, 2003; ISBN 0824740203.
176. Fletcher, R.E.; Ling, S.; Slater, B. Violations of Löwenstein's rule in zeolites. *Chem. Sci.* **2017**, *8*, 7483–7491. [CrossRef] [PubMed]
177. Xu, R.; Pang, W.; Yu, J.; Huo, Q.; Chen, J. *Chemistry of Zeolites and Related Porous Materials Synthesis and Structure*; John Wiley & Sons (Asia) Pte Ltd.: Singapore, 2007; ISBN 9780470822333.
178. Frising, T.; Leflaive, P. Extraframework cation distributions in X and Y faujasite zeolites: A review. *Microporous Mesoporous Mater.* **2008**, *114*, 27–63. [CrossRef]
179. Culfaz, A.; Sand, L.B. Mechanism of nucleation and crystallization of zeolites from gels. *Mol. Sieves* **1973**, 140–151. [CrossRef]
180. Thompson, R.W. Recent advances in the understanding of zeolite synthesis. *Mol. Sieves* **1998**, *1*, 1–33. [CrossRef]
181. Liu, Z.; Okabe, K.; Anand, C.; Yonezawa, Y.; Zhu, J.; Yamada, H.; Endo, A.; Yanaba, Y.; Yoshikawa, T.; Ohara, K.; et al. Continuous flow synthesis of ZSM-5 zeolite on the order of seconds. *Proc. Natl. Acad. Sci. USA* **2016**, *113*, 14267–14271. [CrossRef] [PubMed]
182. Abrioux, C. Modélisation moléculaire de l'adsorption et de la diffusion de molécules polaires dans un solide nanoporeux de type zéolithique. Ph.D. Thesis, Université Montpellier II, Montpellier, France, 2010.

183. Santos, V. Caractérisation et modification de l'acidité résiduelle de zéolithes cationiques. Ph.D. Thesis, Université de Poitiers, Poitiers, France, 2008.
184. Kramer, G.J.; Van Santen, R.A.; Emeis, C.A.; Nowak, A.K. Understanding the acid behaviour of zeolites from theory and experiment. *Nature* **1993**, *363*, 529–531. [CrossRef]
185. Kim, K.M.; Oh, H.T.; Lim, S.J.; Ho, K.; Park, Y.; Lee, C.H. Adsorption equilibria of water vapor on zeolite 3A, zeolite 13X, and dealuminated Y zeolite. *J. Chem. Eng. Data* **2016**, *61*, 1547–1554. [CrossRef]
186. Simonot-Grange, M.H.; Elm'Chaouri, A.; Weber, G.; Dufresne, P.; Raatz, F.; Joly, J.F. Characterization of the dealumination effect into H faujasites by adsorption: Part 1. The water molecule as a structural aluminum ion selective probe. *Zeolites* **1992**, *12*, 155–159. [CrossRef]
187. Moıse, J.C.; Bellat, J.P.; Méthivier, A. Adsorption of water vapor on X and Y zeolites exchanged with barium. *Microporous Mesoporous Mater.* **2001**, *43*, 91–101. [CrossRef]
188. Cindrella, L.; Dyer, A. Ion-exchanged and salt hydrates-encapsulated zeolites for solar refrigeration. *Sol. Energy Mater. Sol. Cells* **2009**, *93*, 161–166. [CrossRef]
189. Zygmunt, S.A.; Curtiss, L.A.; Iton, L.E.; Erhardt, M.K. Computational studies of water adsorption in the zeolite H-ZSM-5. *J. Phys. Chem. 1996* **1996**, 6663–6671. [CrossRef]
190. Jungsuttiwong, S.; Limtrakul, J.; Truong, T.N. Theoretical study of modes of adsorption of water dimer on H-ZSM-5 and H-faujasite zeolites. *J. Phys. Chem. B* **2005**, *109*, 13342–13351. [CrossRef] [PubMed]
191. Baerlocher, C.; McCusker, L.B. Database of Zeolite Structures. Available online: http://www.iza-structure.org/databases/ (accessed on 11 September 2018).
192. Di Lella, A.; Desbiens, N.; Boutin, A.; Demachy, I.; Ungerer, P.; Bellat, J.-P.; Fuchs, A.H. Molecular simulation studies of water physisorption in zeolites. *Phys. Chem. Chem. Phys.* **2006**, *8*, 5396–5406. [CrossRef] [PubMed]
193. Abrioux, C.; Coasne, B.; Maurin, G.; Henn, F.; Jeffroy, M.; Boutin, A. Cation behavior in faujasite zeolites upon water adsorption: A combination of monte carlo and molecular dynamics simulations. *J. Phys. Chem. C* **2009**, *113*, 10696–10705. [CrossRef]
194. Auroux, A. Microcalorimetry methods to study the acidity and reactivity of zeolites, pillared clays and mesoporous materials. *Top. Catal.* **2002**, *19*, 205–213. [CrossRef]
195. Shirono, K.; Endo, A.; Daiguji, H. Molecular dynamics study of hydrated Faujasite-type zeolites. *J. Phys. Chem. B* **2005**, 3446–3453. [CrossRef] [PubMed]
196. Semmer, V.; Batamack, P.; Dorémieux-Morin, C.; Fraissard, J. NMR studies of the Brønsted acidity of solids. Application to superacidic solids. *Top. Catal.* **1998**, *6*, 119–125. [CrossRef]
197. Batamack, P.; Vincent, R.; Fraissard, J. Acidity of partially and non-dealuminated HY zeolites measured by 4-K broad-line and 300-K high-resolution magic-angle spinning 1H nuclear magnetic resonance spectroscopy: Synergy between Briinsted and Lewis acid sites. *Microporous Mater.* **1994**, *2*, 515–524. [CrossRef]
198. Rao, G.N.; Kotasthane, A.N. Thermal and hydrothermal stabilities of zeolite EU-1. *Appl. Catal. Ageneral* **1994**, *119*, 33–43. [CrossRef]
199. Lutz, W. Zeolite Y: Synthesis, modification, and properties—A Case Revisited. *Adv. Mater. Sci. Eng.* **2014**, *2014*. [CrossRef]
200. Pu, X.; Liu, N.; Shi, L. Microporous and mesoporous materials acid properties and catalysis of USY zeolite with different extra-framework aluminum concentration. *Microporous Mesoporous Mater.* **2015**, *201*, 17–23. [CrossRef]
201. Dimitrijevic, R.; Lutz, W.; Ritzmann, A. Hydrothermal stability of zeolites: Determination of extra-framework species of H-Y faujasite-type steamed zeolite. *J. Phys. Chem. Solids* **2006**, *67*, 1741–1748. [CrossRef]
202. Salman, N.; Rüscher, C.H.; Buhl, J.-C.; Lutz, W.; Toufar, H.; Stöcker, M. Effect of temperature and time in the hydrothermal treatment of HY zeolite. *Microporous Mesoporous Mater.* **2006**, *90*, 339–346. [CrossRef]
203. Ristic, A.; Fischer, F.; Hauer, A.; Logar, N.Z. Improved performance of binder-free zeolite Y for low-temperature sorption heat storage. *J. Mater. Chem. A* **2018**, *6*, 11521–11530. [CrossRef]
204. Buhl, J.; Gerstmann, M.; Lutz, W.; Ritzmann, A. Hydrothermal stability of the novel zeolite type LSX in comparison to the traditional 13X modification. *Z. Anorg. Allg. Chem.* **2004**, 604–608. [CrossRef]
205. Fischer, F.; Lutz, W.; Buhl, J.C.; Laevemann, E. Insights into the hydrothermal stability of zeolite 13X. *Microporous Mesoporous Mater.* **2018**, *262*, 258–268. [CrossRef]
206. Gopal, R.; Hollebone, B.R.; Langford, C.H.; Shigeishi, R.A. The rates of solar energy storage and retrieval in a zeolite-water system. *Sol. Energy* **1982**, *28*, 421–424. [CrossRef]

207. Gaeini, M.; Zondag, H.A.; Rindt, C.C.M. Effect of kinetics on the thermal performance of a sorption heat storage reactor. *Appl. Therm. Eng.* **2016**, *102*, 520–531. [CrossRef]
208. Jänchen, J.; Schumann, K.; Thrun, E.; Brandt, A.; Unger, B.; Hellwig, U. Preparation, hydrothermal stability and thermal adsorption storage properties of binderless zeolite beads. *Int. J. Low-Carbon Technol. Adv. Access* **2012**, 1–5. [CrossRef]
209. Herzog, T.H.; Jänchen, J.; Kontogeorgopoulos, E.M.; Lutz, W. Steamed zeolites for heat pump applications and solar driven thermal adsorption storage. *Energy Procedia* **2014**, *48*, 380–383. [CrossRef]
210. Gómez-Álvarez, P.; Perez-Carbajo, J.; Balestra, S.R.G.; Calero, S. Impact of the nature of exchangeable cations on LTA-type zeolite hydration. *J. Phys. Chem. C* **2016**, *120*, 23254–23261. [CrossRef]
211. Li, X.; Narayanan, S.; Michaelis, V.K.; Ong, T.C.; Keeler, E.G.; Kim, H.; McKay, I.S.; Griffin, R.G.; Wang, E.N. Zeolite y adsorbents with high vapor uptake capacity and robust cycling stability for potential applications in advanced adsorption heat pumps. *Microporous Mesoporous Mater.* **2015**, *201*, 151–159. [CrossRef] [PubMed]
212. Stach, H.; Mugele, J.; Jänchen, J.; Weiler, E. Influence of cycle temperatures on the thermochemical heat storage densities in the systems water/microporous and water/mesoporous adsorbents. *Adsorption* **2005**, *11*, 393–404. [CrossRef]
213. Lass-Seyoum, A.; Borozdenko, D.; Friedrich, T.; Langhof, T.; Mack, S. Practical test on a closed sorption thermochemical storage system with solar thermal energy. *Energy Procedia* **2016**, *91*, 182–189. [CrossRef]
214. Jänchen, J.; Herzog, T.H.; Gleichmann, K.; Unger, B.; Brandt, A.; Fischer, G.; Richter, H. Performance of an open thermal adsorption storage system with Linde type A zeolites: Beads versus honeycombs. *Microporous Mesoporous Mater.* **2015**, *207*, 179–184. [CrossRef]
215. Tatsidjodoung, P.; Le Pierrès, N.; Heintz, J.; Lagre, D.; Luo, L.; Durier, F. Experimental and numerical investigations of a zeolite 13X/water reactor for solar heat storage in buildings. *Energy Convers. Manag.* **2016**, *108*, 488–500. [CrossRef]
216. Johannes, K.; Kuznik, F.; Hubert, J.L.; Durier, F.; Obrecht, C. Design and characterisation of a high powered energy dense zeolite thermal energy storage system for buildings. *Appl. Energy* **2015**, *159*, 80–86. [CrossRef]
217. De Boer, R.; Smeding, S.F.; Zondag, H.A.; Krol, G. Development of a prototype system for seasonal solar heat storage using an open sorption process. *Eurotherm Semin.* **2014**, *99*, 28–30.
218. Bales, C.; Gantenbein, P.; Jaenig, D.; Kerskes, H.; Summer, K.; Van Essen, M.; Weber, R. *Laboratory Tests of Chemical Reactions and Prototype Sorption Storage Units*; International Energy Agency: Paris, France, 2008.
219. Wilson, S.T.; Lok, B.M.; Messina, C.A.; Cannan, T.R.; Flanigen, E.M. Aluminophosphate molecular sieves: A new class of microporous crystalline inorganic solids. *J. Am. Chem. Soc.* **1982**, *104*, 1146–1147. [CrossRef]
220. Newalkar, B.L.; Jasra, R.V.; Kamath, V.; Bhat, S.G.T. Sorption of water in aluminophosphate molecular sieve AlPO4-5. *Microporous Mesoporous Mater.* **1998**, *20*, 129–137. [CrossRef]
221. Kohler, T.; Hinze, M.; Müller, K.; Schwieger, W. Temperature independent description of water adsorption on zeotypes showing a type V adsorption isotherm. *Energy* **2017**, *135*, 227–236. [CrossRef]
222. Ristić, A.; Logar, N.Z.; Henninger, S.K.; Kaučič, V. The performance of small-pore microporous aluminophosphates in low-temperature solar energy storage: The structure-property relationship. *Adv. Funct. Mater.* **2012**, *22*, 1952–1957. [CrossRef]
223. Lok, B.M.; Messina, C.A.; Patton, R.L.; Gajek, R.T.; Cannan, T.R.; Flanigen, E.M. Silicoaluminophosphate molecular sieves: Another new class of microporous crystalline inorganic solids. *J. Am. Chem. Soc.* **1984**, *106*, 6092–6093. [CrossRef]
224. Oliver, S.; Kuperman, A.; Coombs, N.; Lough, A.; Ozin, G.A. Lamellar aluminophosphates with surface patterns that mimic diatom and radiolarian microskeletons. *Nature* **1995**, *378*, 47–50. [CrossRef]
225. Sayari, A.; Moudrakovski, I.; Reddy, J.S.; Gk, C.; Ratcliffe, C.I.; Ripmeester, J.A.; Preston, K.F. Synthesis of mesostructured lamellar aluminophosphates using supramolecular templates. *Chem. Mater.* **1996**, *4756*, 2080–2088. [CrossRef]
226. Li, D.; Yao, J.; Wang, H. Hydrothermal synthesis of AlPO4-5: Effect of precursor gel preparation on the morphology of crystals. *Prog. Nat. Sci. Mater. Int.* **2012**, *22*, 684–692. [CrossRef]
227. Afeworki, M.; Kennedy, G.J.; Dorset, D.L.; Strohmaier, K.G. Synthesis and characterization of a new microporous material. 2. AlPO and SAPO forms of EMM-3. *Chem. Mater.* **2006**, *18*, 1705–1710. [CrossRef]
228. Lü, J.M.; Ranjit, K.T.; Rungrojchaipan, P.; Kevan, L. Synthesis of mesoporous aluminophosphate (AlPO) and investigation of zirconium incorporation into mesoporous AlPOs. *J. Phys. Chem. B* **2005**, *109*, 9284–9293. [CrossRef] [PubMed]

229. Henninger, S.K.; Munz, G.; Ratzsch, K.-F.; Schossig, P. Cycle stability of sorption materials and composites for the use in heat pumps and cooling machines. *Renew. Energy* **2011**, *36*, 3043–3049. [CrossRef]
230. Krese, G.; Koželj, R.; Butala, V.; Stritih, U. Thermochemical seasonal solar energy storage for heating and cooling of buildings. *Energy Build.* **2018**, *164*, 239–253. [CrossRef]
231. Tatsidjodoung, P.; Le Pierrès, N.; Luo, L. A review of potential materials for thermal energy storage in building applications. *Renew. Sustain. Energy Rev.* **2013**, *18*, 327–349. [CrossRef]
232. Shimooka, S.; Oshima, K.; Hidaka, H.; Takewaki, T.; Kakiuchi, H.; Kodama, A.; Kubota, M.; Matsuda, H. The evaluation of direct cooling and heating desiccant device coated with FAM. *J. Chem. Eng. Jpn.* **2007**, *40*, 1330–1334. [CrossRef]
233. Mitsubishi Plastics Zeolitic Water Vapor Adsorbent AQSOA™. Available online: http://www.mpi.co.jp/infopdf/AQSOA.pdf (accessed on 22 September 2018).
234. Bauer, J.; Herrmann, R.; Mittelbach, W.; Schwieger, W. Zeolite/aluminum composite adsorbents for application in adsorption refrigeration. *Int. J. Energy Res.* **2009**, *33*, 1233–1249. [CrossRef]
235. Jänchen, J.; Stach, H. Shaping adsorption properties of nano-porous molecular sieves for solar thermal energy storage and heat pump applications. *Sol. Energy* **2013**, *104*, 16–18. [CrossRef]
236. Floquet, N.; Coulomb, J.P.; Dufau, N.; Andre, G. Structure and dynamics of confined water in AlPO4-5 zeolite. *J. Phys. Chem. B* **2004**, *108*, 13107–13115. [CrossRef]
237. Freni, A.; Bonaccorsi, L.; Calabrese, L.; Caprì, A.; Frazzica, A.; Sapienza, A. SAPO-34 coated adsorbent heat exchanger for adsorption chillers. *Appl. Therm. Eng.* **2015**, *82*, 1–7. [CrossRef]
238. Goldsworthy, M.J. Measurements of water vapour sorption isotherms for RD silica gel, AQSOA-Z01, AQSOA-Z02, AQSOA-Z05 and CECA zeolite 3A. *Microporous Mesoporous Mater.* **2014**, *196*, 59–67. [CrossRef]
239. Baerloher, C.; Meier, W.M.; Olson, D.H. *Atlas of Zeolite Frameworks Type*, 5th ed.; Elsevier: Amsterdam, The Netherlands, 2001; ISBN 978-0-444-53064-6. [CrossRef]
240. Li, J.; Yu, J.; Xu, R. Progress in heteroatom-containing aluminophosphate molecular sieves. *Proc. R. Soc. A Math. Phys. Eng. Sci.* **2012**, *468*, 1955–1967. [CrossRef]
241. Goldfarb, D.; Li, H.; Davis, M.E. Dynamics of water molecules in VPI-5 and AlPO4-5 studied by NMR spectroscopy. *J. Am. Chem. Soc.* **1992**, 3690–3697. [CrossRef]
242. Askari, S.; Halladj, R.; Sohrabi, M. An overview of the effects of crystallization time, template and silicon sources on hydrothermal synthesis of SAPO-34 molecular sieve with small crystals. *Rev. Adv. Mater. Sci.* **2012**, *32*, 83–93.
243. Van Heyden, H.; Munz, G.; Schnabel, L.; Schmidt, F.; Mintova, S.; Bein, T. Kinetics of water adsorption in microporous aluminophosphate layers for regenerative heat exchangers. *Appl. Therm. Eng.* **2009**, *29*, 1514–1522. [CrossRef]
244. Rouhani, M.; Huttema, W.; Bahrami, M. Thermal conductivity of AQSOA FAM-Z02 packed bed adsorbers in open and closed adsorption thermal energy storage systems. *Int. J. Refrig.* **2018**, 1–11. [CrossRef]
245. Yaghi, O.M.; O'Keeffe, M.; Ockwig, N.W.; Chae, H.K.; Eddaoudi, M.; Kim, J. Reticular synthesis and the design of new materials. *Nature* **2003**, *423*, 705–714. [CrossRef] [PubMed]
246. Zhang, S.-Y.; Jensen, S.; Tan, K.; Wojtas, L.; Roveto, M.; Cure, J.; Thonhauser, T.; Chabal, Y.J.; Zaworotko, M.J. Modulation of water vapor sorption by a 4th generation metal-organic material with a rigid framework and self-switching pores. *J. Am. Chem. Soc.* **2018**, *140*, jacs.8b07290. [CrossRef]
247. Liu, J.; Chen, L.; Cui, H.; Zhang, J.; Zhang, L.; Su, C.Y. Applications of metal-organic frameworks in heterogeneous supramolecular catalysis. *Chem. Soc. Rev.* **2014**, *43*, 6011–6061. [CrossRef] [PubMed]
248. Kitagawa, S.; Kondo, M. Functional micropore chemistry of crystalline metal complex-assembled compounds. *Chem. Soc. Jpn.* **1998**, *71*, 1739–1753. [CrossRef]
249. Bousquet, D.; Coudert, F.X.; Fossati, A.G.J.; Neimark, A.V.; Fuchs, A.H.; Boutin, A. Adsorption induced transitions in soft porous crystals: An osmotic potential approach to multistability and intermediate structures. *J. Chem. Phys.* **2013**, 138. [CrossRef] [PubMed]
250. Boulé, R.; Roland, C.; Le Pollés, L.; Audebrand, N.; Ghoufi, A. Thermal and guest-assisted structural transition in the NH2-MIL-53(Al) Metal Organic Framework: A molecular dynamics simulation investigation. *Nanomaterials* **2018**, *8*, 531. [CrossRef] [PubMed]
251. Cohen, S.M. The postsynthetic renaissance in porous solids. *J. Am. Chem. Soc.* **2017**, *139*, 2855–2863. [CrossRef] [PubMed]

252. Cohen, S.M. Postsynthetic methods for the functionalization of metal-organic frameworks. *Chem. Rev.* **2012**, *112*, 970–1000. [CrossRef] [PubMed]
253. Stock, N.; Biswas, S. Synthesis of metal-organic frameworks (MOFs): Routes to various MOF topologies, morphologies, and composites. *Chem. Rev.* **2012**, *112*, 933–969. [CrossRef] [PubMed]
254. Wang, Z.; Cohen, S.M. Postsynthetic modification of metal-organic frameworks. *Chem. Soc. Rev.* **2009**, *38*, 1315–1329. [CrossRef] [PubMed]
255. Li, Y.; Wang, X.; Xu, D.; Chung, J.D.; Kaviany, M.; Huang, B. H_2O adsorption/desorption in MOF-74: Ab Initio Molecular Dynamics and experiments. *J. Phys. Chem. C* **2015**, *119*, 13021–13031. [CrossRef]
256. Eddaoudi, M.; Li, H.; Yaghi, O.M. Highly porous and stable metal-organic frameworks: Structure design and sorption properties. *J. Am. Chem. Soc.* **2000**, *122*, 1391–1397. [CrossRef]
257. Planchais, A.; Devautour-Vinot, S.; Salles, F.; Ragon, F.; Devic, T.; Serre, C.; Maurin, G. A joint experimental/computational exploration of the dynamics of confined water/Zr-based MOFs systems. *J. Phys. Chem. C* **2014**, *118*, 14441–14448. [CrossRef]
258. Cadiau, A.; Lee, J.S.; Damasceno Borges, D.; Fabry, P.; Devic, T.; Wharmby, M.T.; Martineau, C.; Foucher, D.; Taulelle, F.; Jun, C.H.; et al. Design of hydrophilic Metal Organic Framework water adsorbents for heat reallocation. *Adv. Mater.* **2015**, *27*, 4775–4780. [CrossRef] [PubMed]
259. Weber, G.; Bezverkhyy, I.; Bellat, J.P.; Ballandras, A.; Ortiz, G.; Chaplais, G.; Patarin, J.; Coudert, F.X.; Fuchs, A.H.; Boutin, A. Mechanism of water adsorption in the large pore form of the gallium-based MIL-53 metal-organic framework. *Microporous Mesoporous Mater.* **2016**, *222*, 145–152. [CrossRef]
260. Salles, F.; Bourrelly, S.; Jobic, H.; Devic, T.; Guillerm, V.; Llewellyn, P.; Serre, C.; Ferey, G.; Maurin, G. Molecular insight into the adsorption and diffusion of water in the versatile hydrophilic/hydrophobic flexible MIL-53(Cr) MOF. *J. Phys. Chem. C* **2011**, *115*, 10764–10776. [CrossRef]
261. De Lange, M.F.; Gutierrez-Sevillano, J.-J.; Hamad, S.; Vlugt, T.J.H.; Calero, S.; Gascon, J.; Kapteijn, F. Understanding adsorption of highly polar vapors on mesoporous MIL-100(Cr) and MIL-101(Cr): Experiments and molecular simulations. *J. Phys. Chem. C* **2013**, *117*, 7613–7622. [CrossRef]
262. Li, S.; Chen, Y.; Pei, X.; Zhang, S.; Feng, X.; Zhou, J.; Wang, B. Water purification: Adsorption over Metal-Organic Frameworks. *Chin. J. Chem.* **2016**, *34*, 175–185. [CrossRef]
263. Canivet, J.; Bonnefoy, J.; Daniel, C.; Legrand, A.; Coasne, B.; Farrusseng, D. Structure-property relationships of water adsorption in metal-organic frameworks. *New J. Chem.* **2014**, *38*, 3102–3111. [CrossRef]
264. Canivet, J.; Fateeva, A.; Guo, Y.; Coasne, B.; Farrusseng, D. Water adsorption in MOFs: Fundamentals and applications. *Chem. Soc. Rev.* **2014**, 5594–5617. [CrossRef] [PubMed]
265. Furukawa, H.; Gándara, F.; Zhang, Y.-B.; Jiang, J.; Queen, W.L.; Hudson, M.R.; Yaghi, O.M. Water adsorption in porous metal-organic frameworks and related materials. *J. Am. Chem. Soc.* **2014**, *136*, 4369–4381. [CrossRef] [PubMed]
266. Burtch, N.C.; Jasuja, H.; Walton, K.S. Water stability and adsorption in metal-organic frameworks. *Chem. Rev.* **2014**, *114*, 10575–10612. [CrossRef] [PubMed]
267. Chui, S.S.-Y.; Lo, S.M.-F.; Charmant, J.P.H.; Orpen, A.G.; Williams, I.D. A chemically functionalizable nanoporous material $[Cu_3(TMA)_2(H_2O)_3]_n$. *Science* **1999**, *3*, 1148–1150. [CrossRef]
268. Schoenecker, P.M.; Carson, C.G.; Jasuja, H.; Flemming, C.J.J.; Walton, K.S. Effect of water adsorption on retention of structure and surface area of Metal−Organic Frameworks. *Ind. Eng. Chem. Res.* **2012**, 6513–6519. [CrossRef]
269. Küsgens, P.; Rose, M.; Senkovska, I.; Fröde, H.; Henschel, A.; Siegle, S.; Kaskel, S. Characterization of metal-organic frameworks by water adsorption. *Microporous Mesoporous Mater.* **2009**, *120*, 325–330. [CrossRef]
270. Al-Janabi, N.; Martis, V.; Servi, N.; Siperstein, F.R.; Fan, X. Cyclic adsorption of water vapour on CuBTC MOF: Sustaining the hydrothermal stability under non-equilibrium conditions. *Chem. Eng. J.* **2018**, *333*, 594–602. [CrossRef]
271. Soubeyrand-lenoir, E.; Vagner, C.; Yoon, J.W.; Bazin, P.; Ragon, F.; Hwang, Y.K.; Serre, C.; Chang, J.; Llewellyn, P.L. How water fosters a remarkable 5-Fold increase in low-pressure. *J. Am. Chem. Soc.* **2012**, 10174–10181. [CrossRef] [PubMed]
272. Liang, Z.; Marshall, M.; Chaffee, A.L. CO_2 adsorption-based separation by metal organic framework (Cu-BTC) versus zeolite (13X). *Energy Fuels* **2009**, 2785–2789. [CrossRef]

273. Gul-E-Noor, F.; Jee, B.; Pöppl, A.; Hartmann, M.; Himsl, D.; Bertmer, M. Effects of varying water adsorption on a $Cu_3(BTC)_2$ metal–organic framework (MOF) as studied by 1H and 13C solid-state NMR spectroscopy. *Phys. Chem. Chem. Phys* **2011**, 7783–7788. [CrossRef] [PubMed]
274. Al-Janabi, N.; Alfutimie, A.; Siperstein, F.R.; Fan, X. Underlying mechanism of the hydrothermal instability of $Cu_3(BTC)_2$ metal-organic framework. *Front. Chem. Sci. Eng.* **2016**, *10*, 103–107. [CrossRef]
275. Vishnyakov, A.; Ravikovitch, P.I.; Neimark, A.V.; Bu, M.; Wang, Q.M. Nanopore structure and sorption properties of Cu−BTC Metal−Organic Framework. *Nano Lett.* **2003**, *3*, 713–718. [CrossRef]
276. DeCoste, J.B.; Peterson, G.W.; Schindler, B.J.; Killops, K.L.; Broweb, M.A.; Mahleb, J.J. The effect of water adsorption on the structure of the carboxylate containing metal–organic frameworks Cu-BTC, Mg-MOF-74, and UiO-66. *J. Mater. Chem. A* **2013**, *1*, 11922–11932. [CrossRef]
277. Elsayed, E.; AL-Dadah, R.; Mahmoud, S.; Anderson, P.A.; Elsayed, A.; Youssef, P.G. CPO-27(Ni), aluminium fumarate and MIL-101(Cr) MOF materials for adsorption water desalination. *Desalination* **2017**, *406*, 25–36. [CrossRef]
278. Shi, B.; Al-Dadah, R.; Mahmoud, S.; Elsayed, A.; Elsayed, E. CPO-27(Ni) metal-organic framework based adsorption system for automotive air conditioning. *Appl. Therm. Eng.* **2016**, *106*, 325–333. [CrossRef]
279. Dietzel, P.D.C.; Blom, R.; Fjellvåg, H. Base-induced formation of two magnesium metal-organic framework compounds with a bifunctional tetratopic ligand. *Eur. J. Inorg. Chem.* **2008**, 3624–3632. [CrossRef]
280. Dietzel, P.D.C.; Panella, B.; Hirscher, M.; Blom, R.; Fjellvåg, H. Hydrogen adsorption in a nickel based coordination polymer with open metal sites in the cylindrical cavities of the desolvated framework. *Chem. Commun.* **2006**, *1*, 959–961. [CrossRef] [PubMed]
281. Dietzel, P.D.C.; Morita, Y.; Blom, R.; Fjellvåg, H. An in situ high-temperature single-crystal investigation of a dehydrated metal-organic framework compound and field-induced magnetization of one-dimensional metal-oxygen chains. *Angew. Chem. Int. Ed.* **2005**, *44*, 6354–6358. [CrossRef] [PubMed]
282. Liu, J.; Wang, Y.; Benin, A.I.; Jakubczak, P.; Willis, R.R.; LeVan, M.D. CO_2/H_2O adsorption equilibrium and rates on metal-organic frameworks: HKUST-1 and Ni/DOBDC. *Langmuir* **2010**, *26*, 14301–14307. [CrossRef] [PubMed]
283. Zuluaga, S.; Fuentes-Fernandez, E.M.A.; Tan, K.; Arter, C.A.; Li, J.; Chabal, Y.J.; Thonhauser, T. Chemistry in confined spaces: Reactivity of the Zn-MOF-74 channels. *J. Mater. Chem. A* **2016**, *4*, 13176–13182. [CrossRef]
284. Tan, K.; Zuluaga, S.; Gong, Q.; Canepa, P.; Wang, H.; Li, J.; Chabal, Y.J.; Thonhauser, T. Water reaction mechanism in metal organic frameworks with coordinatively unsaturated metal ions: MOF-74. *Chem. Mater.* **2014**, *26*, 6886–6895. [CrossRef]
285. Zuluaga, S.; Fuentes-Fernandez, E.M.A.; Tan, K.; Xu, F.; Li, J.; Chabal, Y.J.; Thonhauser, T. Understanding and controlling water stability of MOF-74. *J. Mater. Chem. A* **2016**, *4*, 5176–5183. [CrossRef]
286. Cavka, J.H.; Jakobsen, S.; Olsbye, U.; Guillou, N.; Lamberti, C.; Bordiga, S.; Lillerud, K.P. A new zirconium inorganic building brick forming metal organic frameworks with exceptional stability. *J. Am. Chem. Soc.* **2008**, *130*, 13850–13851. [CrossRef] [PubMed]
287. Cmarik, G.E.; Kim, M.; Cohen, S.M.; Walton, K.S. Tuning the adsorption properties of UiO-66 via ligand functionalization. *Langmuir* **2012**, *28*, 15606–15613. [CrossRef] [PubMed]
288. Jeremias, F.; Lozan, V.; Henninger, S.K.; Janiak, C. Programming MOFs for water sorption: Amino-functionalized MIL-125 and UiO-66 for heat transformation and heat storage applications. *Dalton Trans.* **2013**, *42*, 15967–15973. [CrossRef] [PubMed]
289. Decoste, J.B.; Peterson, G.W.; Jasuja, H.; Glover, T.G.; Huang, Y.G.; Walton, K.S. Stability and degradation mechanisms of metal-organic frameworks containing the $Zr_6O_4(OH)_4$ secondary building unit. *J. Mater. Chem. A* **2013**, *1*, 5642–5650. [CrossRef]
290. Férey, G.; Mellot-Draznieks, C.; Serre, C.; Millange, F.; Dutour, J.; Surblé, S.; Margiolaki, I. A Chromium Terephthalate–based solid with unusually large pore volumes and surface area. *Science* **2005**, *309*, 2040. [CrossRef] [PubMed]
291. Soubeyrand-Lenoir, E. Adsorption et Separation de gaz en Mode Dynamique sur des Materiaux Hybrides. Ph.D. Thesis, Université d'Aix-Marseille, Marseille, France, 2012.
292. Akiyama, G.; Matsuda, R.; Sato, H.; Hori, A.; Takata, M.; Kitagawa, S. Effect of functional groups in MIL-101 on water sorption behavior. *Microporous Mesoporous Mater.* **2012**, *157*, 89–93. [CrossRef]

293. Cui, S.; Qin, M.; Marandi, A.; Steggles, V.; Wang, S.; Feng, X.; Nouar, F.; Serre, C. Metal-Organic Frameworks as advanced moisture sorbents for energy-efficient high temperature cooling. *Sci. Rep.* **2018**, *8*, 15284. [CrossRef] [PubMed]
294. Khutia, A.; Rammelberg, H.U.; Schmidt, T.; Henninger, S.; Janiak, C. Water sorption cycle measurements on functionalized MIL-101Cr for heat transformation application. *Chem. Mater.* **2013**, *25*, 790–798. [CrossRef]
295. Férey, G. Structural flexibility in crystallized matter: From history to applications. *Dalton Trans.* **2016**, *45*, 4073–4089. [CrossRef] [PubMed]
296. Bourrelly, S.; Moulin, B.; Rivera, A.; Maurin, G.; Devautour-Vinot, S.; Serre, C.; Devic, T.; Horcajada, P.; Vimont, A.; Clet, G.; et al. Explanation of the adsorption of polar vapors in the highly flexible metal organic framework MIL-53(Cr). *J. Am. Chem. Soc.* **2010**, *132*, 9488–9498. [CrossRef] [PubMed]
297. Boudjema, L.; Long, J.; Salles, F.; Larionova, J.; Guari, Y.; Trens, P. Switch in the hydrophobic-hydrophilic character of the Prussian Blue Analogues: An affinity control for smart gas sorption. *Chem. A Eur. J.* **2018**. [CrossRef] [PubMed]
298. Wang, S.; Lee, J.S.; Wahiduzzaman, M.; Park, J.; Muschi, M.; Martineau-corcos, C.; Tissot, A.; Cho, K.H.; Marrot, J.; Shepard, W.; et al. A robust large-pore zirconium carboxylate metal-organic framework for energy-efficient water-sorption-driven refrigeration. *Nat. Energy* **2018**, 1–10. [CrossRef]
299. Pryor, T.L.; Close, D.J. The behaviour of adsorbent energy storage beds. *Sol. Energy* **1976**, *18*, 287–292. [CrossRef]
300. Solomon, I.; Ribeiro, A.M.; Santos, J.C.; Loureiro, J.M.; Rodrigues, A.E.; Sandu, I.; Mamaliga, I. Adsorption equilibrium of water vapor on activated carbon and alumina and carbon and alumina impregnated with hygroscopic salt. *Turk. J. Chem.* **2013**, *37*, 358–365. [CrossRef]
301. Shi, Y.F.; Liu, X.J.; Nie, H.J.; Liu, Y.S. The water adsorption isotherm models on activated alumina. *Appl. Mech. Mater.* **2012**, *229–231*, 100–104. [CrossRef]
302. Li, G.; Xiao, P.; Webley, P. Binary adsorption equilibrium of carbon dioxide and water vapor on activated alumina. *Langmuir* **2009**, *25*, 10666–10675. [CrossRef] [PubMed]
303. Marcussen, L. The kinetics of water adsorption on porous alumina. *Chem. Eng. Sci.* **1970**, *25*, 1487–1499. [CrossRef]
304. Rouquerol, J.; Sing, K.S.W.; Llewellyn, P. Adsorption by metal oxides. In *Adsorption by Powders and Porous Solids: Principles, Methodology and Applications*; Academic Press: London, UK, 1999; pp. 287–354, ISBN 9780080970356. [CrossRef]
305. Carruthers, J.D.; Payne, D.A.; Sing, K.S.W.; Stryker, L.J. Specific and nonspecific interactions in the adsorption of argon, nitrogen, and water vapor on oxides. *J. Colloid Interface Sci.* **1971**, *36*, 205–216. [CrossRef]
306. Pryor, T.L.; Close, D.J. Measurements of the behaviour of adsorbent energy storage beds. *Sol. Energy* **1978**, *20*, 151–155. [CrossRef]
307. Desai, R.; Hussain, M.; Ruthven, D.M. Adsorption of water vapour on activated alumina. I-equilibrium behaviour. *Can. J. Chem. Eng.* **1992**, *70*, 699–706. [CrossRef]
308. Moore, J.D.; Serbezov, A. Correlation of adsorption equilibrium data for water vapor on F-200 activated alumina. *Adsorption* **2005**, *11*, 65–75. [CrossRef]
309. Ferreira, D.; Magalhães, R.; Taveira, P.; Mendes, A. Effective adsorption equilibrium isotherms and breakthroughs of water vapor and carbon dioxide on different adsorbents. *Ind. Eng. Chem. Res.* **2011**, *50*, 10201–10210. [CrossRef]
310. Sadek, O.M.; Mekhemer, W.K. Ca-montmorillonite clay as thermal energy storage material. *Thermochim. Acta* **2000**, *363*, 47–54. [CrossRef]
311. Konta, J. Clay and man: Clay raw materials in the service of man. *Appl. Clay Sci.* **1995**, *10*, 275–335. [CrossRef]
312. Salles, F.; Douillard, J.M.; Bildstein, O.; Gaudin, C.; Prelot, B.; Zajac, J.; Van Damme, H. Driving force for the hydration of the swelling clays: Case of montmorillonites saturated with alkaline-earth cations. *J. Colloid Interface Sci.* **2013**, *395*, 269–276. [CrossRef] [PubMed]
313. Musyoka, N.M.; Langmi, H.W. Clay and clay-supported materials for energy storage applications. In *Bentonite*; Mishra, A.K., Ed.; Nova Science Publishers, Inc.: Hauppaug, NY, USA, 2015; ISBN 9781634821421.
314. Hensen, E.J.M.; Smit, B. Why clays swell. *J. Phys. Chem. B* **2002**, *106*, 12664–12667. [CrossRef]
315. Hendricks, S.B.; Nelson, R.A.; Alexander, L.T. Hydration mechanism of the clay mineral Montmorillonite saturated with various cations. *J. Am. Chem. Soc.* **1940**, *62*, 1457–1464. [CrossRef]

316. Sadek, O.M.; Mekhemer, W.K. Na-montmorillonite clay as thermal energy storage material. *Thermochim. Acta* **2001**, *370*, 57–63. [CrossRef]
317. Caballero, E.; Jiménez de Cisneros, C. Hydration properties of bentonites from Cabo de Gata (SE, Spain). Isotopic study (18O/16O;2H/H) of the hydration water. *Chem. Erde* **2011**, *71*, 389–395. [CrossRef]
318. Desai, R.R.; Erwin Desa, J.A.; Aswal, V.K. Hydration studies of Bentonite clay. *AIP Conf. Proc.* **2012**, *1447*, 197–198. [CrossRef]
319. Chiou, C.T.; Rutherford, D.W. Effects of exchanged cation and layer charge on the sorption of water and EGME vapors on montmorillonite clays. *Clays Clay Miner.* **1997**, *45*, 867–880. [CrossRef]
320. Tajeddine, L.; Gailhanou, H.; Blanc, P.; Lassin, A.; Gaboreau, S.; Vieillard, P. Hydration-dehydration behavior and thermodynamics of MX-80 montmorillonite studied using thermal analysis. *Thermochim. Acta* **2015**, *604*, 83–93. [CrossRef]
321. Salles, F.; Douillard, J.-M.; Denoyel, R.; Bildstein, O.; Jullien, M.; Beurroies, I.; Van Damme, H. Hydration sequence of swelling clays: Evolutions of specific surface area and hydration energy. *J. Colloid Interface Sci.* **2009**, *333*, 510–522. [CrossRef] [PubMed]
322. Castrillo, N.; Mercado, A.; Bolzone, C. Reversibility studies of clay hydration degree in its natural and composite condition. *Procedia Mater. Sci.* **2015**, *9*, 135–141. [CrossRef]
323. Rouquerol, J.; Sing, K.S.W.; Llewellyn, P. Adsorption by active carbons. In *Adsorption by Powders and Porous Solids: Principles, Methodology and Applications*; Academic Press: London, UK, 1999; pp. 237–280.
324. Salame, I.I.; Bandosz, T.J. Experimental study of water adsorption on activated carbons. *Langmuir* **1999**, *15*, 587–593. [CrossRef]
325. Huber, L.; Ruch, P.; Hauert, R.; Saucke, G.; Matam, S.K.; Michel, B.; Koebel, M.M. Monolithic nitrogen-doped carbon as a water sorbent for high-performance adsorption cooling. *RSC Adv.* **2016**, *6*, 25267–25278. [CrossRef]
326. Critoph, R.E. Activated carbon adsorption cycles for refrigeration and heat pumping. *Carbon* **1989**, *27*, 63–70. [CrossRef]
327. De Lange, M.F.; Van Velzen, B.L.; Ottevanger, C.P.; Verouden, K.J.F.M.; Lin, L.C.; Vlugt, T.J.H.; Gascon, J.; Kapteijn, F. Metal-organic frameworks in adsorption-driven heat pumps: The potential of alcohols as working fluids. *Langmuir* **2015**, *31*, 12783–12796. [CrossRef] [PubMed]
328. Reinsch, H.; Van Der Veen, M.A.; Gil, B.; Marszalek, B.; Verbiest, T.; De Vos, D.; Stock, N. Structures, sorption characteristics, and nonlinear optical properties of a new series of highly stable aluminum MOFs. *Chem. Mater.* **2013**, *25*, 17–26. [CrossRef]
329. Hongois, S. Stockage de Chaleur Inter-Saisonnier par voie Thermochimique pour le Chauffage Solaire de la Maison Individuelle. Ph.D. Thesis, Institut National des Sciences Appliquées de Lyon, Villeurbanne, France, 2011.
330. Agence de l'Environnement et de la Maîtrise de l'Energie (ADEME). *L'effacement de consommation électrique en France: Rapport Final*; E-CUBE Strategy Consultants, CEREN: Anger, France, 2017.

I.3. Conclusion

The main intention of this review has been to provide arguments that the low-temperature (i.e., temperature of the charging step , $T_{charging}$ < 423 K) thermochemical storage based on the adsorption of water vapour from moist-air onto porous adsorbents in open sorption systems constitutes a promising alternative to various thermal storage technologies which are frequently considered in the scientific and technical literature. Indeed, it meets the requirements of increasing use of renewable energy, improving energy efficiency, and reducing greenhouse effects. Besides the advantage of using water vapour as a low cost "green" and cheap adsorbate, the energy storage density has much smaller dependency on the discharging (adsorption) temperature which makes the charging step easier to be tuned into the requirements of a complete adsorbent regeneration without compromising its structural or textural integrity and stability. More particularly, the open sorption systems operating in the moist-air flow mode by adsorbing water vapour from outdoor air offers the advantage of operating under atmospheric pressure and ambient temperature, thereby avoiding potentially detrimental conditions of high partial pressures of adsorbate in combination with elevated temperatures.

Nevertheless, this thermochemical storage technology is still at low maturity level. The main challenge is that the working adsorbent-water vapour couple should insure high energy density and efficiency, while reducing investment and operating costs, as well as minimizing the environmental issues and risks involved. Furthermore, the selection of materials should be carefully adapted to the real operating conditions. It is necessary to note that, in the above review article, the energy storage density of silica gel assessed at 767 MJ m^{-3} solid (c.f., Table 1 on page 3/50) appears much greater than the average of 180 MJ m^{-3} solid reported by other researchers [7]. The reason is that the value of 767 MJ m^{-3} solid was calculated on the basis of the maximum heat value obtained for this adsorbent upon adsorption of water vapour.

As pointed out in the review, synthetic materials possessing uniformly structured porosity with high specific surface areas and tuneable or switchable hydrophobic-hydrophilic surface character seem to meet these requirements and they will certainly constitute the adsorbents of the future. By comparing different types of materials, two families of porous adsorbents have been selected for the purpose of the present work. These are the faujasite type zeolite and hybrid ionosilica.

The faujasite type zeolite has already been proved as a promising adsorbent thanks to its high porosity, its affinity and selectivity towards water vapour and long-term resistance to repeated cycles of charging and discharging. Contrary to the zeolite framework, ionosilica is a new amorphous hybrid silica material which, to the best of our knowledge, has never been studied in view of the heat storage uses. The only work related to its adsorption capacity towards water vapour has pointed out the great potentiality of this substrate yielding a stepwise adsorption isotherm, i.e., adsorbing small amounts of water vapour at low vapour pressures and great amounts at higher pressures [6]. According to our opinion, this behaviour is adequate for the low temperature thermochemical storage by limiting the loss of activity of the adsorbent during the regeneration, and particularly between the charging and discharging steps of the long-term storage. Further modification of the selected materials, such as ion exchange and group functionalization, aimed at improving the heat storage performance by exploiting high hydration energy of their extra-framework compensating ions, is another idea put forward in the present study.

Considering these solids, different experimental techniques described in Chapter II will be combined with molecular simulations in order to characterize the structural, textural and thermodynamical properties at different scales.

References

[1] Thermal energy storage for sustainable energy consumption: Fundamentals, case studies and design; Paksoy, H.Ö., Ed.; Springer, 2007; DOI:10.1007/978-1-4020-5290-3; ISBN:978-1-4020-5290-3; ISBN:978-1-4020-5290-3.

[2] Sarbu, I. A comprehensive review of thermal energy storage. Sustainability 2018, 10, 191 DOI:10.3390/su10010191.

[3] Dincer, I. Thermal energy storage systems as a key technology in energy conservation. Int. J. Energy Res. 2002, 26, 567–588 DOI:10.1002/er.805.

[4] Schreiber, H.; Lanzerath, F.; Reinert, C.; Grüntgens, C.; Bardow, A. Heat lost or stored: Experimental analysis of adsorption thermal energy storage. Appl. Therm. Eng. 2016, 106, 981–991 DOI:10.1016/j.applthermaleng.2016.06.058.

[5] Yu, N.; Wang, R.Z.; Wang, L.W. Sorption thermal storage for solar energy. Prog. Energy Combust. Sci. 2013, 39, 489–514 DOI:10.1016/j.pecs.2013.05.004 Review.

[6] Thach, U.D.; Trens, P.; Prelot, B.; Zajac, J.; Hesemann, P. Tuning the interfacial properties of mesoporous ionosilicas: Effect of cationic precursor and counter anion. J. Phys. Chem. C 2016, 120, 27412–27421 DOI:10.1021/acs.jpcc.6b09457.

[7] C. Bales, P. Gantenbein, D. Jaenig, H. Kerskes, K. Summer, M. Van Essen, et al., Laboratory tests of chemical reactions and prototype sorption storage units, 2008. http://task32.iea-shc.org/publications.

Chapter II

Materials and Methods:
Materials synthesis, characterization methods and methodological development

After the introductory bibliographic study on the state of the art of thermochemical storage [1], we selected two types of materials: an ion-exchanged zeolite X and a new hybrid functionalized silica. Both kinds of materials were considered to have good potential as water vapour adsorbents in this application and could be modified either using ion exchange or directly during the synthesis. They allowed releasing heat once exposed to moist air in an open sorption thermochemical storage system, while regeneration of the materials remained in a relatively low temperature range compatible with the implementation of the solar collectors. In the next step of this thesis work, appropriate samples have been prepared and characterized.

Firstly, since the adsorption properties are the keys for the thermochemical storage materials, the adsorption performances of 13X zeolites and ionosilicas were analysed in terms of their water vapour uptake and thermal energy exchange. This information could be obtained by determining the quantity of water vapour adsorption and its associated adsorption heat. These were the main experimental methods considered in this work to evaluate the adsorptive properties of the materials. They were employed in two different modes [2–6]: 1) the static one, by using a home-made adsorption apparatus based on manometric measurements under equilibrium conditions and 2) the dynamic mode, with a gas flow microcalorimeter under dynamics conditions, which may also provide information about kinetics of the process.

In order to understand fundamentally the adsorption-desorption of water vapour (or hydration-dehydration processes), a fine microscopic scale structure study may be useful. However, the two types of materials considered here differ in structure (zeolite is crystalline and ionosilica is amorphous) and morphologies. Consequently, different methodological approaches should be applied so as to elucidate their mechanisms of hydration.

The sorption properties of faujasite-type zeolite depend largely on the extra-framework species, notably the compensating cations [7–12]. The localization and migration of the compensating cations at different hydration states provide important information on the

mechanism of water vapour sorption. Starting from the crystalline structure of zeolite and combining with a series of *in-situ* X-ray diffraction experiments in order to locate the position of these cations within the pores, a full zeolite structure was thus refined and the cations migration under different humidity conditions was elucidated by the resulting diffractograms via a computational structural resolution using *Le bail* [13] and *Rietveld* [14] methods. Furthermore, the results were compared with those obtained by Monte Carlo simulations, performed at the AIME laboratory by Dr. F. Salles, on the zeolite structures and it was then possible to determine both the values of adsorption energy and the isotherms for the adsorption of water molecules onto Ce-13X zeolite (with Ce^{3+} or Ce^{4+}).

It is worth mentioning that, in the case of the ionosilicas, the amorphous structure makes X-ray diffraction experiments unusable for mechanistic studies. Therefore, an alternative method is necessary to obtain the information at both the surface and the bulk level. In the present study, the hydration-dehydration phenomena of different functionalized ionosilicas upon several hydration-dehydration cycles were studied by solid state ^{29}Si NMR.

A more detailed description of main characterization methods and experimental techniques used throughout the present study is given in the rest of this chapter.

II.1. Selected standard protocols for the synthesis and functionalization of materials

II.1.1. Preparation of 13X-Ce zeolite by ion-exchange

The Ce2-13X sample was prepared from the commercial 13X zeolite purchased from Sigma Aldrich, following a standard ion–exchange procedure which had been used in several previous studies [15–17] (c.f., Figure II.1). In a typical functionalization step, a 0.05 M stock solution containing Ce^{3+} was prepared by dissolving $Ce(NO_3)_3.6H_2O$ (Sigma Aldrich) in ultrapure water having a resistivity of 18.2 megohm. After adding 1 g of 13X zeolite in 50 mL

of stock solution, the mixture was stirred at 343 K for 3 hours in order to maximize the exchange rate of Cerium cations according to work of Ames [18] (c.f., Figure II.2). Then the solid phase was separated from the liquid one by centrifugation at 11000 rpm during 10 minutes. The supernatant was eliminated and the process was repeated successively three times. It should be noted that the third centrifugation lasted for 24 hours to attain the maximum ion exchange ratio. The resulting solid was then washed with 50 mL ultrapure water, stirred for 2 hours and centrifuged in the same way as before. The stirring procedure was repeated 5 times, with the last stirring lasting for 24 hours. At the end of the exchange procedure, a freeze-drying (lyophilisation) was carried out to remove traces of water and dry the solid. This sample was named as Ce2-13X.

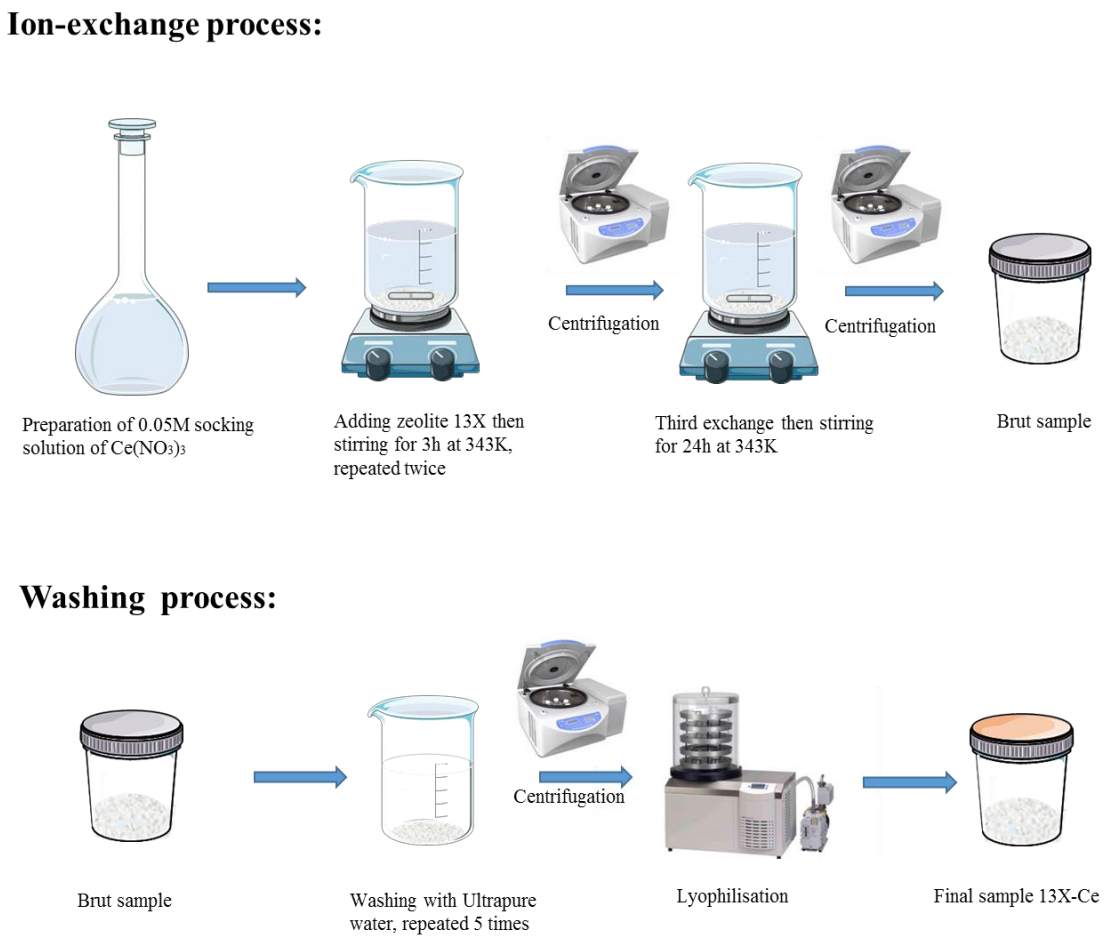

Figure II. 1: Flow-sheet of the preparation of Ce2-13X zeolite including 1) ion exchange and 2) washing steps.

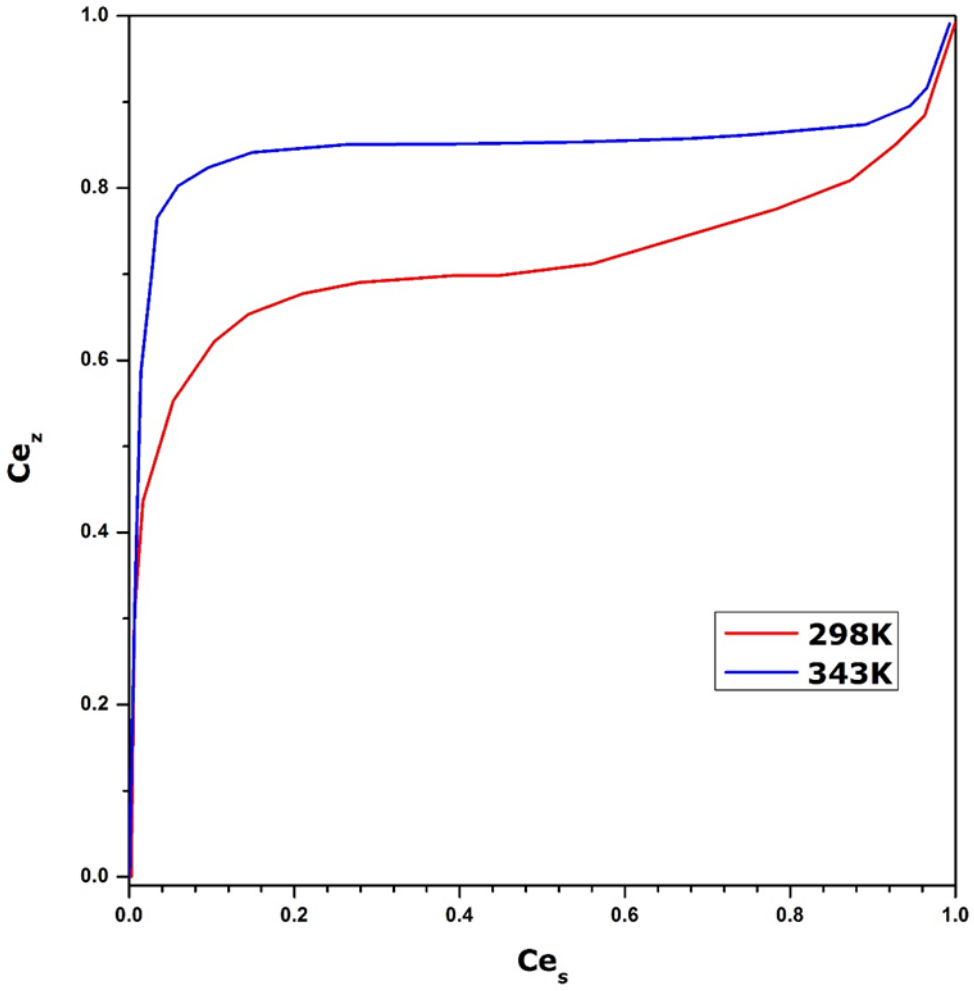

***Figure II. 2**: Cation exchange isotherm for Ce^{3+} in X-zeolite at 298K and 343K respectively; the exchange reaction is as follow: $3Na_z + Ce_s \leftrightarrow Ce_z + 3Na_s$ where Ce_z stands for equivalent fraction of cerium inside the zeolite, and Ce_s represents equivalent fraction of cerium in the equilibrium bulk solution. Adapted from [18].*

As reported in the literature, it is difficult to achieve a total exchange ratio because there is always a fraction of residual Na^+ remaining in the pores of 13X zeolite [19]. To overcome this difficulty, an extra ammonium exchange can be performed to remove the remaining Na^+ by adding a $(NH_4)_2SO_4$ solution [19]. In accordance with this idea, we applied a stepwise approach in order to substitute as much Na^+ as possible. For this purpose, after washing the previously obtained solid with ultrapure water, an exchange step with 50 mL of 0.05 M $(NH_4)_2SO_4$ solution was first performed during 2 hours. Then we repeated again the same exchange with 50 mL of Ce^{3+} stock solution before washing and centrifuging steps. At the end

of the exchange, a freeze-drying was carried out to remove traces of water and dry the solid. This sample was referred to as Ce3-13X.

Hunter also mentioned that a great fraction of Ce^{3+} cations would go through an oxidation to Ce^{4+} cations during the calcination at high temperature in air [19]. Partial conversion could cause some unknown defects to the zeolite framework or reduce the total amount of compensating cations. Nevertheless, it should be noted that the presence of Ce^{4+} cations in the extra-framework of zeolite still may be advantageous in the context of the present application because of their high hydration enthalpy (i.e., -6325 kJ mol^{-1}) which is almost twice that of Ce^{3+} (i.e., -3365 kJ mol^{-1}) [20]. To obtain a 13X zeolite sample which also contains Ce^{4+} as compensating cations, the previously obtained solid was heated in an oven to 723 K for 12 hours under air. A change of colour from white to pale yellow was systematically observed. This sample was named as Ce4-13X.

II.1.2 Synthesis of functionalized ionosilica ISA100

Ionosilica materials containing different types of cations or zwitterions have been successfully synthesized during the last decade [21–27]. In the present study, we focused on the use of trisilylated ammonium precursors containing different functional groups for the formation of hybrid ionosilica materials. The incorporation of some functional groups within hybrid ionosilicas may enhance the hydration enthalpy [20] and also allows modulating the hydrophilic-hydrophilic character of the solid surface [28].

The first type of ionosilica sample containing sulfate anions, named as ISA100, was synthesized by following the procedure detailed below.

The precursor of the hybrid material, tris (3-(trimethoxysilyl)propyl)amine, further denoted as TrisN as shown in Figure II.3, was first synthesized according to previously published procedures [23,25].

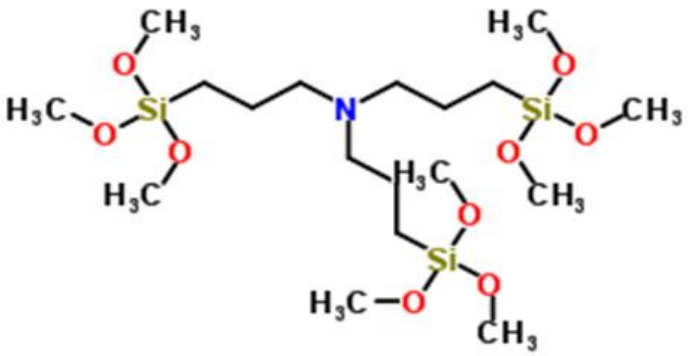

Figure II. 3*: Skeletal structural formula of the precursor of ISA100 ionosilica sample, The precursor* ***TrisN****: tris (3-(trimethoxysilyl)propyl)amine*

11.1g of TrisN precursor were mixed with 60 mL of ethanol and 0.2 mL of 1 vol% Tetra-n-butylammonium fluoride (TBAF) in Tetrahydrofuran (THF) solution under vigorous agitation [29]. The resulting suspension was stirred for 5 minutes, then maintained without stirring at room temperature. After a period of 40 minutes, the gel started to form, and the subsequent ripening process was performed during 5 days at room temperature, during which the system was protected from light with an aluminium paper cover. The so-formed gel was then filtered and washed three times, firstly with ethanol then with acetone before being dried in the oven at 343 K for 24 hours. The resulting solid was poured into an ethanolic solution of sulfuric acid (100 mL ethanol/1.4 g of 95 %-98 % sulfuric acid) for 12 minutes, then washed with ethanol, filtered and dried at 343 K for 24 hours. The ionosilica ISA100 containing sulfate groups was finally obtained after a simple grinding.

Ionosilica ISA100 synthesis:

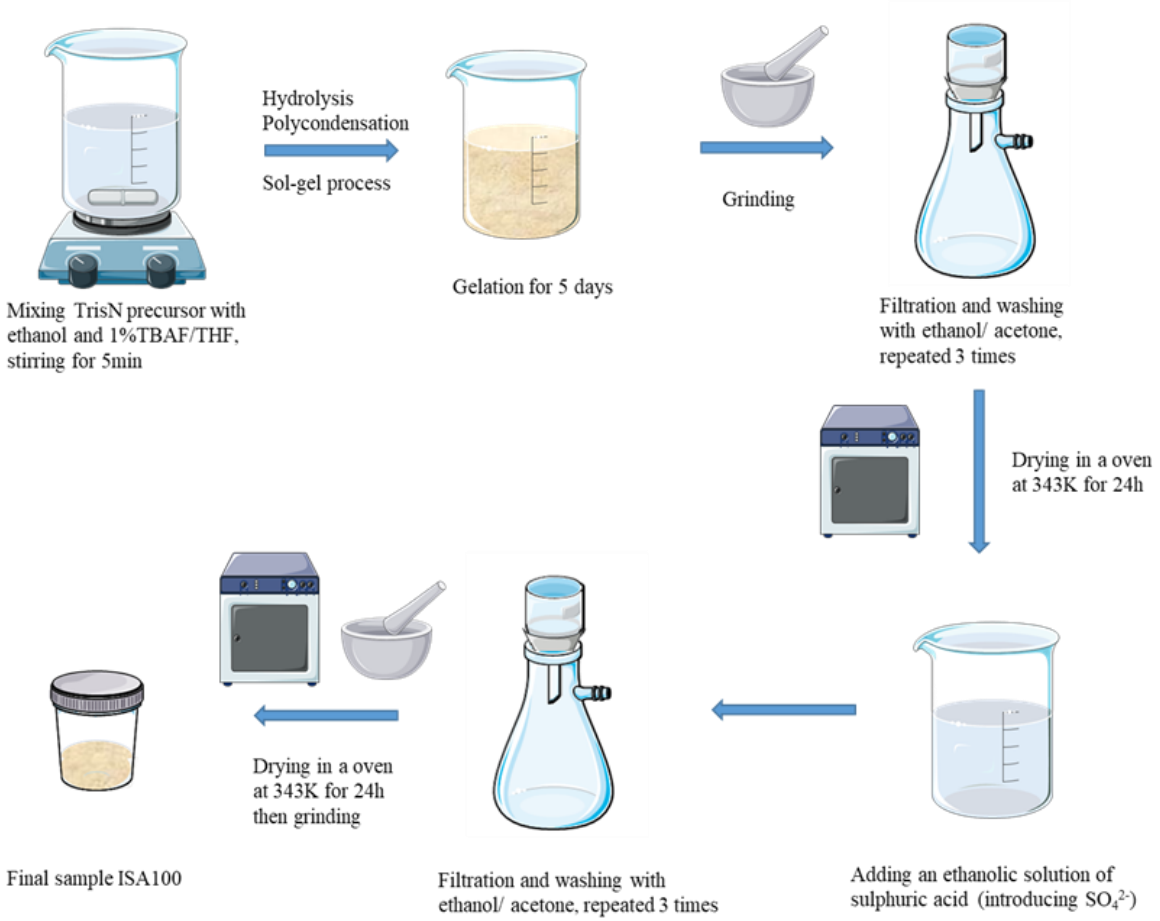

***Figure II. 4**: Flow-sheet of the preparation of ionosilica ISA100 sample.*

II.1.3 The exchange of sulfate anions onto ionosilica DSM19

The ionosilica sample referred to as DSM19 was synthesized previously in the laboratory of Molecular Chemistry and Solid Organization (CMOS) belonging to the Charles Gerhardt institute (ICGM). The synthesis procedure included the addition of TrisN into an EtOH solution (96% MERCK) in the presence of 1 vol%TBAF/THF as catalyst and without any structuring surfactant. At the end of the gelation process, the resulting material was filtered and washed three times with an ethanolic solution of hydrochloric acid in order to introduce Cl^- as compensating anion. The solid was finally dried in an oven at 343 K for 1 day.

The surface modification procedure developed within the framework of this thesis aimed at replacing the compensating chloride anions by sulfate ones. Prior to the exchange procedure, a sulfate stock solution was prepared by dissolving 7 g Na_2SO_4 in 1 L of mixed solution containing 50 vol% of ethanol and 50 vol% of water. The raw DSM19 sample (about 0.5 g) was then added to 200 mL of stock solution and the system was stirred for 2 hours. The solid was removed by filtration and washed 5 times with ultrapure water. The resulting material, named as ISA8, was dried overnight in the oven at 343 K.

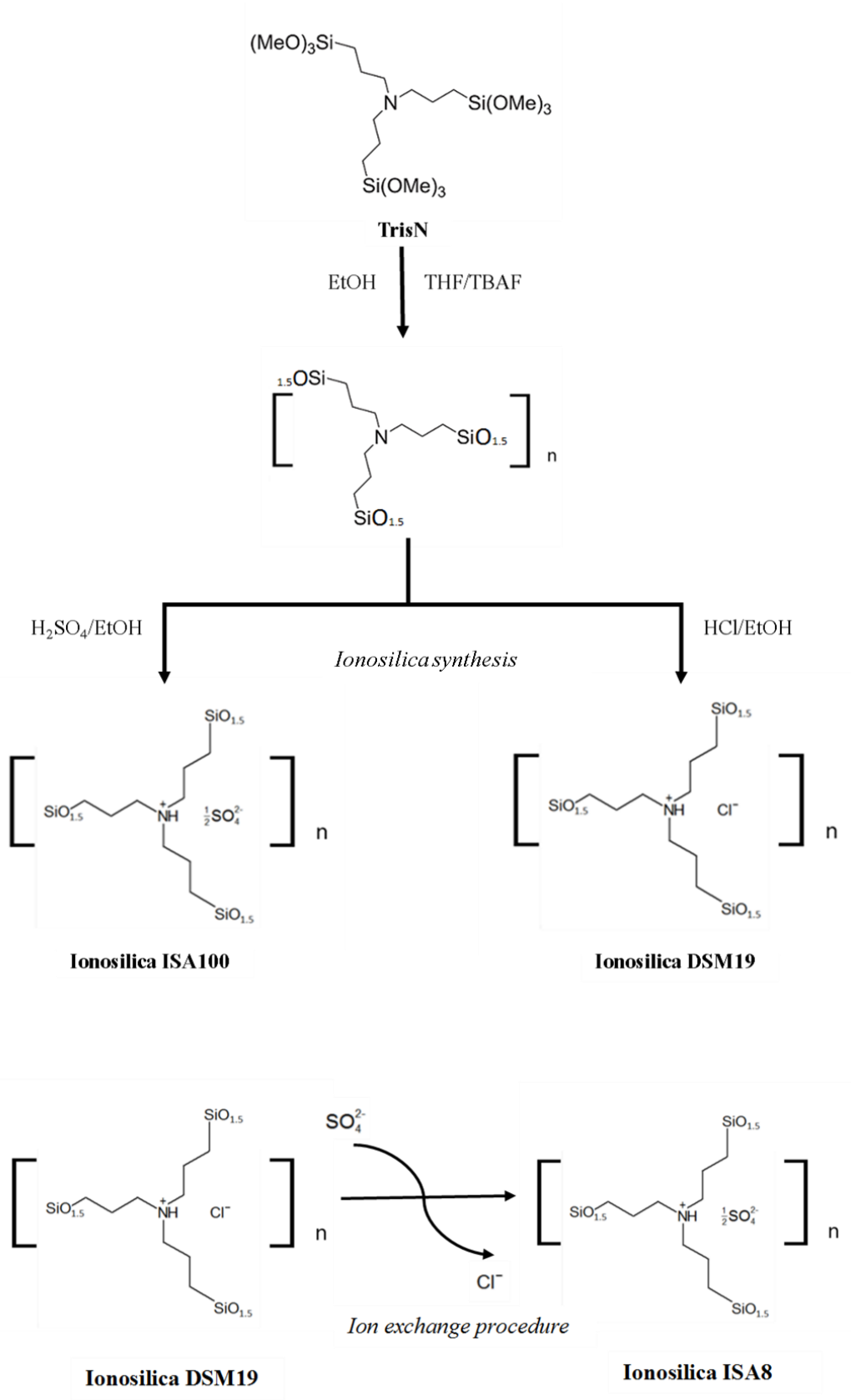

Figure II. 5*: Skeletal structural formula of reactants and products together with the flow-sheet of the preparation of DSM19 (Cl^-), ISA100 (SO_4^{2-}) and ISA8 (Cl^-/ SO_4^{2-})*

II.2. Structural and textural characterization techniques

The adsorption of water (i.e., hydration) onto a solid material depends strongly on the surface properties of the solid, as well as the nature of interactions operating between water molecules and the surface. On the other side, these interactions may also affect the structural integrity and hydrothermal stability of the adsorbent, thus determining its resistance to repeated hydration-drying cycles.

To gain a more precise idea of overall behaviour of our materials upon sorption phenomena, a variety of characterization techniques were used. Firstly, to validate our synthesis, the chemical formulas were determined based on the results of measurements by X-ray fluorescence spectrometry (EDXRF) coupled with the energy dispersive analysis (EDS). The thermogravimetric analysis (TGA) was used to check the thermal stability but also to calculate the water content in the initial samples.

To verify the structural integrity of zeolites after ion exchange, the X-ray diffraction (XRD) measurement was performed. The Fourier transform infrared spectroscopy (FTIR) was used to confirm the presence of specific functional groups in the ionosilica structure. The measurement of adsorption isotherms for gaseous nitrogen at 77 K allowed the BET specific surface area to be determined.

Furthermore, such imaging techniques as scanning electron microscopy (SEM) and transmission electron microscopy (TEM) were used to provide the first information about the porosity. In complement, the environmental scanning electron microscope (ESEM) gave an insight into the behaviour of the samples under moist environment.

II.2.1. Scanning electron microscopy (SEM)/ Energy Dispersive X-ray Spectroscopy (EDS)

Scanning electron microscopy making use of a FEI Quanta 200 FEG instrument allows the observation of the morphology of the samples by scanning an electron beam at the surface. It is possible to perform simultaneously the EDS (Energy Dispersive X-ray Spectroscopy) microanalyses. An incident electrons beam, typically in the range of 10-20 keV, can excite an atom of the sample, which subsequently emits X photons when returning to its fundamental state. Since X photons energies are characteristic of the emitting atom, it is thus possible to identify the atomic species present in the sample. The number of photons emitted by a chemical species in the volume of analysed sample is proportional to the mass concentration of these species. The emitting signals allow the photons to be sorted by energy, to assign each photon detected to a chemical element (qualitative analysis) but also to count the photons according to their energy (in eV). By moving the electron beam across the material, each element in the sample can be identified with the exception of elements having low atomic number (under 4). It should be noted that the X photons are reemitted from a region of the solid up to 2 microns in depth from its surface. It is therefore possible to carry out a localized semi-quantitative chemical analysis of the surface of a sample and thus determine, in our case, the quantity of ions exchanged within our samples of zeolites and ionosilica, as well as get an idea about their chemical formulas.

Some representative SEM images of ionosilicas and zeolite 13X are shown in Figure II.6. The commercial 13X sample is in the form of beads with the size being more or less homogenous (~80 μm). Differently, the ionosilica samples have the typical shape of amorphous materials. Due to the resolution limit of SEM, it was not possible to observe the porosity. Therefore, the TEM experiments were then performed in order to get more information in this respect.

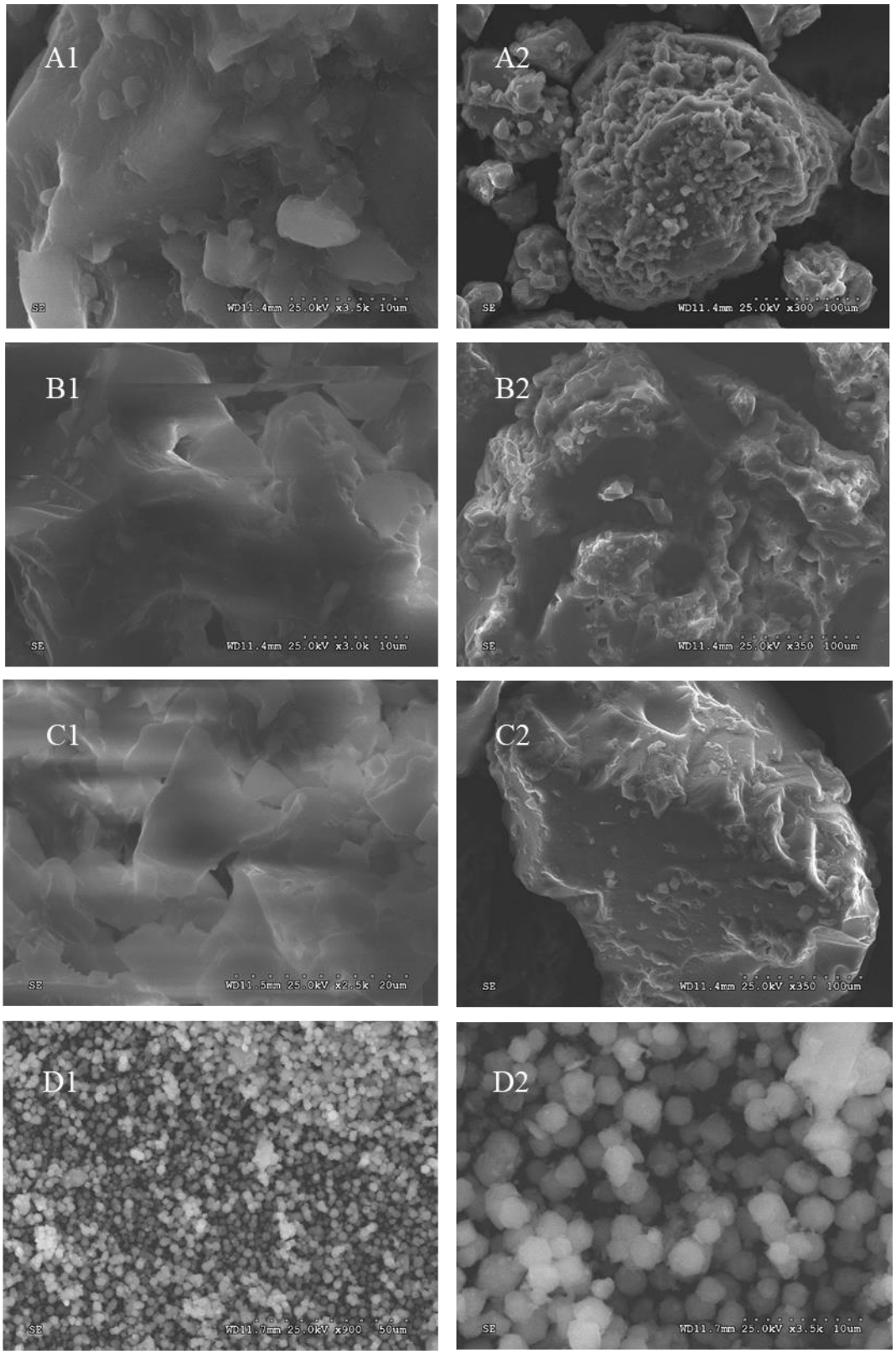

Figure II. 6*: SEM images of ionosilicas and zeolite at various magnifications: A1 and A2: DSM19; B1 and B2:ISA8; C1 and C2: ISA100; D1 and D2: 13X.*

II.2.2 Transmission electron microscopy (TEM)

Transmission electron microscopy FEG JEOL 2200FS was used to observe the morphology and porosity on the ionosilica samples, with a greater resolution until nanometer scale compare to that of the SEM. The images are taken by operating with an acceleration voltage of 200 kV and an Oxford Instruments EDS (Energy Dispersive Scattering) SDD (Silicon Drift Detector) for the detection of elements with atomic numbers greater than 4.

Since the particles size distribution is not homogenous and the mean size is generally larger than 1 µm due to the simple manual grinding, the ionosilica samples must be cut into ultrafine sections before observation in order to be traversed by the electron beam. For our purpose, they were cut to a thickness of 80 µm by a diamond blade before being deposited on a microscopic copper grid covered with a thin layer of resin for the fixation. Then these samples were placed under the electron beam and the image was projected on a fluorescent screen that transformed the electronic image into an optical image.

The so-obtained images are shown in Figure II.7. At first glance, DSM19 and ISA8 exhibit similar amorphous morphologies, and no pores can be observed. This may indicate that the morphology of the raw DSM19 sample is not modified during the ion exchange procedure. As far as ISA100 is concerned, a surprisingly different fiber-form structure can be seen comparing to the two other samples. Also a non-negligible population of pores is observed; they are sized between 2 and 8 nm and randomly dispersed at the surface. This information has been confirmed by the determination of specific surface area and pore size based on the gaseous N_2 adsorption-desorption experiments (c.f., Figure II.8).

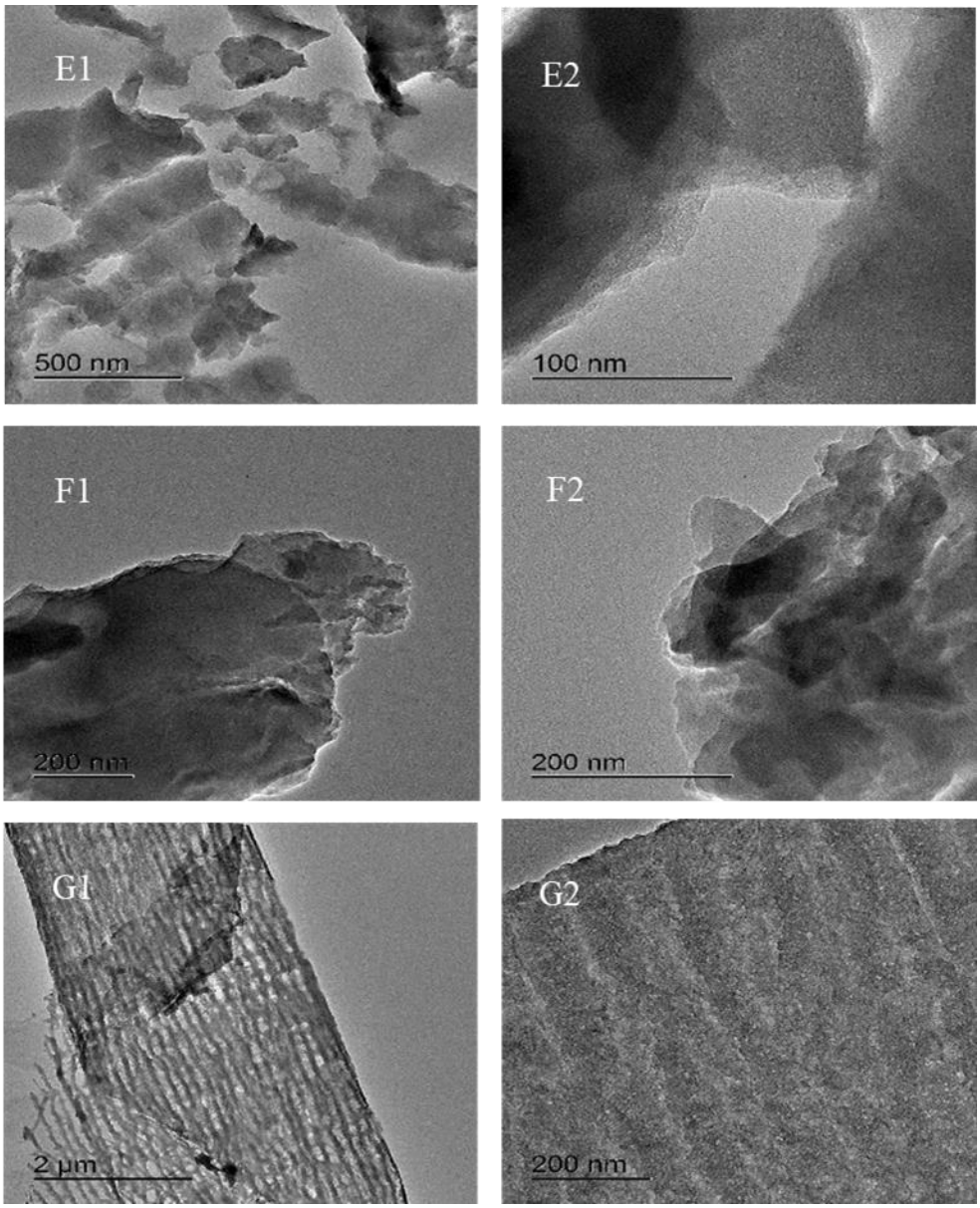

Figure II. 7*: TEM images of the ionosilica materials: E1 and E2: DSM19; F1 and F2:ISA8; G1 and G2: ISA100.*

II.2.3. Environmental scanning electron microscopy (ESEM)

Environmental scanning electron microscopy (ESEM) is a scanning electron microscopy mode that allows non-conductive samples to be studied in the presence of a gas (usually water vapour) in the sample chamber. The same scanning electron microscopy is used, namely FEI Quanta 200 FEG switching to the ESEM mode. Since the temperature and the pressure of the chamber may be varied respectively from 248 K to 328 K and from 10 to 4000

Pa, one can study the solid samples under different hydration states. For the purpose of our study, the experiment was carried out at a fixed temperature of 275 K. It was possible to monitor the behaviour of the ionosilica samples under low relative humidity values owing to the use of a Peltier cooling plate. In light of a good resolution of imaging, this technique was used to compare the behaviour of various ionosilica particles with different compensating anions surrounded by a small amount of water vapour when subjected to the same water vapour pressures from 200 Pa to 710 Pa.

II.2.4. Wavelength Dispersive X-ray Fluorescence (WDXRF)

Wavelength dispersive X-ray fluorescence (WDXRF) is a non-destructive technique for determining the elemental composition of solid or liquid samples. The X-rays produced by the source in the spectrometer are used to excite the atoms contained in the sample, thus stimulating the emission of X-rays at wavelengths characteristic of the elements present. The measurement of the intensity of the X-rays emitted at different wavelengths makes it possible to evaluate the concentration of different elements. By using an appropriate database, XRF analysis can accurately quantify the elemental composition of the sample. The principle of XRF is similar to that of EDS, except that, in XRF, secondary target fluorescence is used to excite the sample, instead of a direct electron beam. Different crystals can be used depending on the element that is required to be detected, which gives XRF a higher resolution (1-2 eV) compare to EDS (>100 eV). Since only one element is detected at a time, the acquisition time is generally longer.

The spectrometer used for XRF analyses was a PANalytical AXIOS Max. It was equipped with an SST-mAX50 X-ray source specifically adapted for the detection of light elements, as well as a sample and cell changer for the analysis of solid and liquid samples. The majority of elements could be analysed with a satisfied precision. However, for the elements with lower atomic numbers such as C, N, O, the detection limits are slightly higher.

Sample	Chemical formula	Si/Al	Exchange ratio
13X	$Na_{87,8}(SiO_2)_{108,9}(AlO_2)_{83,1}$,$XH_2O$	1,27	-
Ce2-13X	$Na_{10,6}Ce_{24,2}(SiO_2)_{109,6}(AlO2)_{82,4}$, XH_2O	1,33	88%
Ce3-13X	$Na_{2,6}Ce_{27,4}(SiO_2)_{109}(AlO_2)_{83}$, X H_2O	1,31	97%
Ce4-13X	-	-	-
DSM19	$C_9H_{19}(SiO_{1,5})_3NCl$ (theoretical)	-	-
ISA8	$C_9H_{19}(SiO_{1,5})_3N(SO_4)_{0,25}Cl_{0,5}$ (theoretical)	-	53%
ISA100	$C_9H_{19}(SiO_{1,5})_3N(SO_4)_{0,5}$ (theoretical)	-	-

Table II. 1*: Chemical formulas, atomic Si:Al ratios, and degrees of cation exchange for samples, as calculated by combining XRF and EDS.*

When studying the zeolite samples, it was discovered that, even making use of two highly pure, commercial samples of Cerium salts to establish the calibration curves, the Cerium concentration in the ion-exchanged samples appeared significantly lower than expected. This would suggest incorrectly the presence of an excess of negative charge on the zeolite structure. In consequence, the following two hypotheses were checked thoroughly: (1) the extra framework positions are occupied by protons, or (2) the actually used sensor of the XRF detecting system is not suitable for detecting Cerium atoms. After having compared with the results of EDS measurement, the second hypothesis based on the equipment issue was validated. Finally, the chemical formulas of the three zeolite samples selected for further tests were calculated by combining the results obtained from the two above-mentioned techniques. The results are given in Table II.1. As for 13X-Ce4 sample, it was not possible to determine the chemical formula with the same method in spite of the mass percentage of cerium ions being unchanged during the thermal treatment. The proportion of the different oxidation states of

cerium ions has stayed unknown. An X-ray photoelectron spectroscopy (XPS) might be considered as a way to determine the different oxidation states of cerium ions, unfortunately this step of work was not able to be fulfilled within our work.

In the case of ionosilica samples, getting a precise percentage of each element was more difficult since it contained bigger amounts of C, N and O. The other reason was that the amorphous silica framework made the composition more heterogeneous. Consequently, the efficiency of the synthesis procedure and the exchange ratio for sulfate anions were verified based on the concentrations of S and Cl in the samples.

II.2.5 Fourier-transform infrared spectroscopy (FTIR)

The FTIR analyses were performed with a transmission Fourier transform infrared spectrometer (Belkin Elmer-spectrum BX). Infrared (IR) spectra were recorded between 4000-500 cm^{-1} on samples dispersed in potassium bromide (KBr) pellets (4 wt%). In a typical run, the sample was dried overnight in an oven at 353 K in air. Then the samples were crushed in a mortar and mixed with KBr before being compressed into thin self-supporting discs using a pressure of 7 tons m^{-3} for 5 minutes. All spectra were recorded with a resolution of 4 cm^{-1} and an accumulation of 32 scans. The baseline of KBr was subtracted from all spectra.

II.2.6 X-ray diffraction (XRD)

X-ray diffraction provides important structural information on zeolite. It is also possible to determine the position of the extra-network compensating cations. A monochromatic and parallel X-ray beam strikes a crystal and is then diffracted in a given direction by each of the families of reticular planes, according to Bragg's law. A detector measures the intensity of the diffracted X-ray radiation in certain directions. It rotates around the same axis, but at twice the speed of the sample. This recording provides the curve of the intensity of the diffracted X-rays

as a function of the diffraction angle 2θ. The diffractometer used was a Philips X'Pert PRO MPD equipped with an X'Celerator Scientific detector. The radiation source was an Empyrean Cu LFF HR copper anticathode X-ray tube ($\lambda(K\alpha1) = 1.54059$ Å, $\lambda(K\alpha2) = 1.54442$ Å, $I_2/I_1 = 0.5$) with a power of 45 kV x 30 mA. The divergence was reduced for the acquisitions by front divergence slots set at 0.125 ° and by Soller slots at 0.04 rad. Acquisitions were made in 0.02 ° steps.

II.2.7. Thermogravimetric analysis (TGA)

Thermogravimetric analysis (TGA) is a technique in which the change in the sample mass is monitored as a function of time or temperature while the sample temperature is programmed in a controlled atmosphere. TGA can be used to study the thermal stability of materials and to evaluate their sorption/desorption capacity towards water vapour. This information allows calculating the quantity of water molecules physisorbed onto solid, as well as determining more precisely the temperature of sample regeneration, and consequently the potential temperature to be applied during the charging step in a thermochemical storage system. For the purpose of the present study, the TGA studies were carried out on NETZSCH Jupiter STA 449 apparatus, under a flow of Argon with a flow rate of 50 mL min^{-1}. The samples were heated in an aluminium oxide crucible with a heating rate of 5 K min^{-1}, by starting from 298 K to 823 K for zeolite samples, and to 573 K for ionosilica samples.

II.2.8. Adsorption of gaseous nitrogen at 77 K

The determination of textural properties was done based on physical adsorption of gaseous nitrogen at 77 K with the aid of an ASAP2010 automated sorption device (Micromeritics). The samples were preheated to 473 K for zeolites, or to 383 K for ionosilica for 6 hours under secondary vacuum to remove the species adsorbed on the sample, i.e., mainly

water contained within the pores. To construct a complete adsorption isotherm, about 48 measuring points were considered. In the case of zeolites, 30 of 48 points were taken below a $p/p_0 < 0.1$, so as to get more precise information about micropore filling. The specific surface area was calculated using the BET equation obtained from the theoretical model of Brunauer, Emmett and Teller from the 77 K nitrogen physisorption isotherm [30].

$$\frac{x}{V(1-x)} = \frac{1}{V_m \cdot C_{BET}} + \frac{x \cdot (C_{BET}-1)}{V_m \cdot C_{BET}} \qquad (II.1)$$

Where:

V is the volume of adsorbed molecules at standard temperature and pressure (STP) [273.15 K and atmospheric pressure (1.013×10^5 Pa)];

V_m is the monolayer volume under STP conditions;

x is the relative pressure (p/p_0);

C_{BET} is the BET constant: $C_{BET} = \exp(\frac{E_1 - E_l}{RT})$ where E_1 and E_l are the adsorption energy of the first layer and the condensation energy of the adsorbate, respectively.

The above model of ad-layer formation does not hold for microporous solids, like for example in the case of zeolites. Since the adsorption of most nitrogen vapour onto microporous zeolite 13X occurs at very low relative pressures, the monolayer capacity inferred from the BET model in reality would fall within the micropore filling range. With this monolayer capacity, the micropore area cannot be accurately determined through BET equation [48, 49]. However, the use of the BET equation is still admitted provided that the adsorption data at relatively low pressures are taken into account to ensure the best linearity of the BET plot, as well as to obtain a positive value of C, as suggested by Rouquerol *et al.* [30]. The resulting *apparent surface*

area permits the comparison among various microporous solids having the same surface chemistry. In the present case, the adsorption data have been transformed within the p/p_0 interval from 0.001 to 0.05, instead of the standard BET range between 0.05 and 0.35.

In order to evaluate more precisely the micropore volume of the zeolite samples, the Dubinin–Radushkevich (DR) model could be considered, as it is more suitable for describing the pore filling mechanism in microporous materials [48]. The DR model is based on the assumption of a change in the potential energy between the gas and adsorbed phases and a characteristic energy of a given solid. In this DR model, it is assumed that the adsorbed molecules in micropores behave like a liquid phase, due to the strong interactions with the micropore walls [48]. The basic form of the DR equation is written as follows:

$$\frac{W}{Wo} = exp[-(RT\ ln(p/p_0)/E)^2] \qquad (II.2)$$

$$E = \beta E_0 \qquad (II.3)$$

Where:

W and W_0 are volume adsorbed micropore volume respectively;

E is the characteristic energy for a given fluid–solid system, E_0 is the characteristic energy of adsorbate with respect to the given solid.

β is the DR constant.

Figure II.8 shows the experimental N_2 adsorption-desorption isotherm of ionosilica sample ISA100. The isotherms and the resulting apparent surface area of 13X and Ce2-13X are shown in Figure AIII.1 and table AIII.1 of Appendix III.

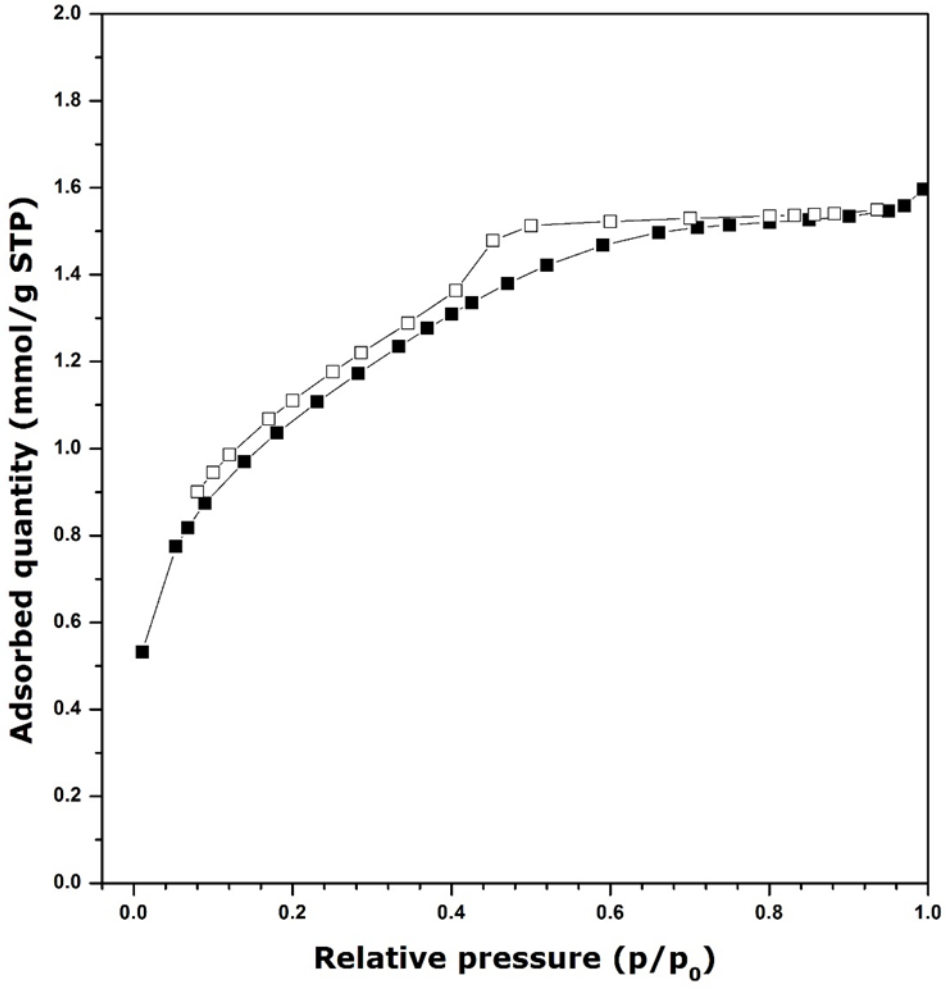

***Figure II. 8**: Experimental N_2 adsorption-desorption isotherm of ionosilica sample ISA100 outgassed at 383 K overnight under secondary vacuum. The filled and empty symbols correspond to the adsorption and desorption isotherms, respectively.*

The pore volume and pore radius distribution of ionosilicas were determined by referring to the Barret, Joyner and Hallenda (BJH) method which exploited the gaseous nitrogen desorption isotherm making use of the Kelvin model of mesopore filling [30]:

$$ln\frac{p}{p_0} = \frac{2\gamma V_l}{r_k RT} \qquad (II.4)$$

Where:

p/p_0 is the relative vapour pressure;

γ is the surface tension;

V_l is the molar volume of the liquid;

R is the universal gas constant;

r_k is the Kelvin radius of the pore;

T is the absolute temperature.

The BJH method is based on the following assumptions:

1) equation of Kelvin is applicable throughout the whole mesoporous domain with only mesopores being present in the solid;

2) the solid contains non-deformable mesopores with a well-defined geometry;

3) the filling of a pore does not depend on its location in the porous network, and adsorption occurs according to the same principles as it would occur on an open surface;

4) contact angle θ is zero and the curvature radius of meniscus is only controlled by the size and the shape of the pore.

This method is based on the analysis of the desorption branch, starting from the equilibrium relative pressure of saturation plateau on the adsorption-desorption isotherm which corresponds to the total filling of the mesopores. At each point of the desorption curve, corresponding to a given relative pressure, the desorbed vapour originates simultaneously from the desorption of the condensed gas, and the decrease in the thickness of the multimolecular layer which remains adsorbed on the pore walls, when the pore is previously emptied of its condensed gas. The pore wall area and the volume of each category of pores can then be recursively calculated. The sum of these values leads to a cumulated specific surface area and a cumulative pore volume, which makes it possible to obtain the volume distribution of the size of the mesopores as a function of the average pore width, as follow:

$$V_{pn} = \left(\frac{r_{pn}}{r_{Kn}+\Delta\, t_n/2}\right)^2 \left(\Delta V_n - \Delta t_n \sum_{j=1}^{n-1} Ac_j\right) \qquad (II.5)$$

Where:

r_p is the pore radius;

V_p is the pore volume;

r_K is the Kelvin radius of the pore;

Δt is the thickness of the adsorbed layer of nitrogen;

A_c is the area exposed by the pore from which the physically adsorbed gas has just been desorbed.

II.3. Structural resolution of zeolite faujasite 13X

As already discussed in Chapter I, the position of extra-network or compensating cations is very important because these cations are directly involved in the molecular mechanisms occurring in zeolites during the water adsorption. A more precise knowledge of these positions is therefore useful to understand the water vapour adsorption mechanisms for the purpose of the present study. This may be done by applying structural resolution procedure divided into following three steps:

(i) Data acquisition from X-ray diffraction under *operando* mode

For this purpose, a high-resolution Malvern Panalytical Empyrean diffractometer, equipped with Cu K-alpha radiation, which is operational under controlled atmosphere and at variable temperatures between 10 and 1900 K, was used for the analysis of samples *in situ*.

Figure II. 9*: High resolution X-ray diffractometer Malvern Panalytical Empyrean used in the present study.*

In an oven which has been heated up under air, a few drops of water containing zeolite were placed on a platinum plate heated to 373 K to evacuate the water until it formed a thin and uniform layer. The study started from a sample completely hydrated at 298 K. Then, water molecules were desorbed from the surface by increasing the temperature. X-ray diagrams were recorded with the same Ce2-13X sample at different temperatures (303 K, 353 K, 423 K, 573 K, 723 K then cooled down to 303 K) corresponding to the different hydration states.

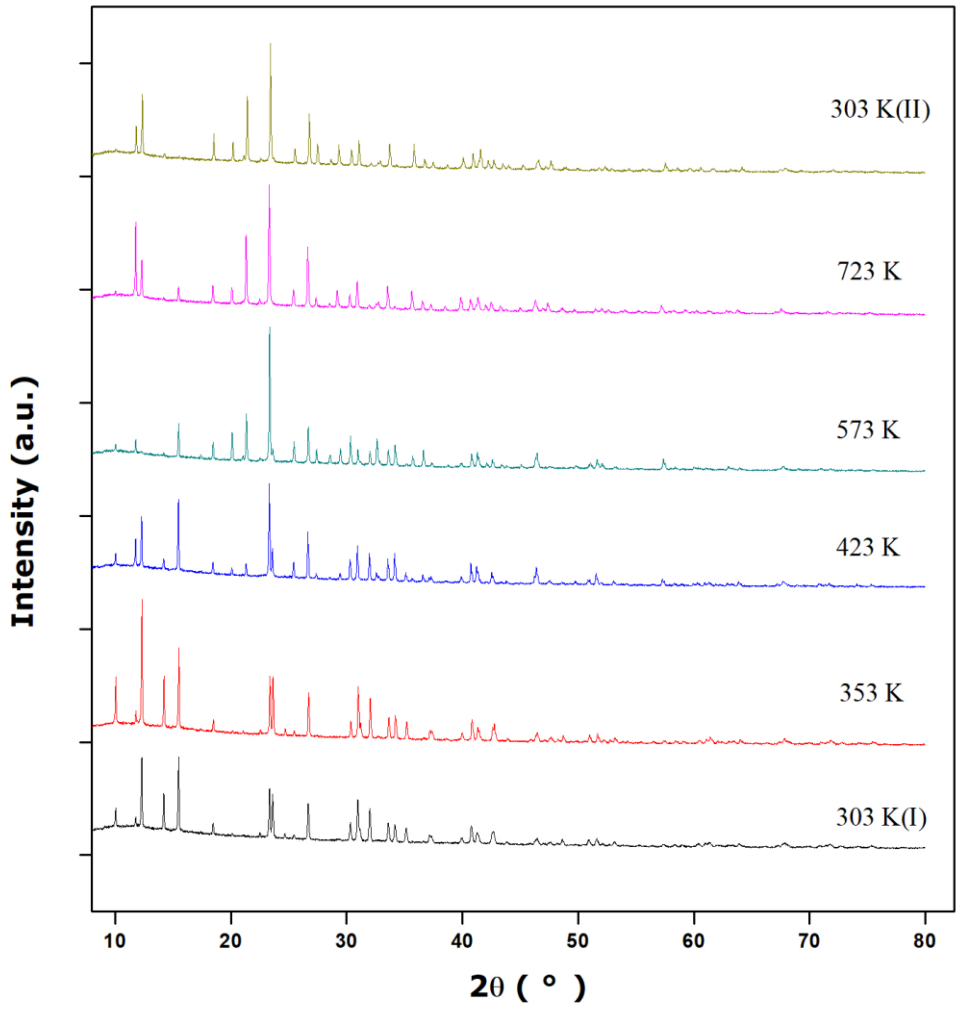

***Figure II. 10**: In situ X-ray diffraction patterns of Ce2-13X at different temperatures*

(ii) Positioning and intensity of reflections

This step was carried out to define the maximum number of reflections in order to index the diagram later on [31]. *WinPLOTR* software was used which included a semi-automatic reflection search function based on the search for the minimum of the second derivative of the signal [32]. In comparison with the previous XRD experience performed to confirm the framework integrity, several device settings had been changed such as the acquisition rate and Soller slots in order to get better resolution.

(iii) Profile decomposition and modelling

A first analysis of the profile can be carried out based on the mesh parameters (Lattice parameters a, b, c, α, β, γ and space group) previously searched in the literature [33]. The purpose of this procedure is to find the best agreement between the observed profile and a calculated profile. For this purpose, the diagram is decomposed according to the mesh considered and each peak of the diagram is simulated using standard functions.

The first method of profile decomposition, the so-called "pattern matching", was developed by Pawley then generalized and improved by Le Bail. Each position of the reflections is determined by the mesh parameters obtained previously.

In order to obtain the complete profile of a detected signal, it is necessary to take into account its different contributions, both intrinsic and instrumental. The intrinsic contribution includes the Darwin width of the diffracted signal, as well as the effect of microstructure such as distortions of the crystal lattice (strain), crystallite size or preferential orientation. The instrumental contribution manifests itself rather in the asymmetry of the signal. All these contributions can be simulated independently by associated functions which can simulate the Gaussian, Lorentzian and asymmetric components of the diagram profile.

Gaussian and Lorentzian functions

- The Gaussian function is defined as follows:

$$G(2\theta_i, \Gamma_k) = \frac{2I_0}{\Gamma_k}\sqrt{\frac{\ln 2}{\pi}}\exp(-\frac{4\ln 2}{{\Gamma_k}^2}(2\theta_i - 2\theta_k)^2) \qquad (II.6)$$

Where:

I_0 is the integrated signal intensity;

$2/\Gamma_k\sqrt{\ln 2/\pi}$ is the Gaussian normalization factor;

$2\theta_i$ and $2\theta_k$ are the angles at point i of the profile and at the reflection k of the crystal respectively;

Γ_k is the width of the reflection k.

- The Lorentzian function is defined by the expression:

$$L(2\theta_i, \Gamma_k) = \frac{I_0\sqrt{C}}{\pi\,\Gamma_k}\left[1 + C(\frac{2\theta_i - 2\theta_k}{\Gamma_k})^2\right]^{-m} \qquad (II.7)$$

Where:

$C = 4(2^{1/m} - 1)$, m being the Lorentzian order which can take any positive values or zero;

$I_0\sqrt{C}/\pi\,\Gamma_k$ is the normalization factor of the Lorentzian function.

Given the complexity of the convolution procedure for the profile modelling, the Pseudo-Voigt function was applied in JANA2006, representing the convolution of the Lorentzian and Gaussian functions which could therefore describe better the form of a reflection.

The pseudo-Voigt function $pV(2\theta)$, combines a Lorentzian contribution $L(\Gamma)$ and a Gaussian contribution $G(\Gamma)$ weighted by a factor η :

$$pV(2\theta, \Gamma) = \eta\, L(2\theta, \Gamma) + (1 - \eta)\, G(2\theta, \Gamma) \qquad (II.8)$$

Where the reflection Γ width and parameter η are derived from the formulas:

$$\Gamma = (\Gamma_G^5 + 2.69296\Gamma_G^4\Gamma_L + 2.428432.69296\Gamma_G^3\Gamma_L^2 + 4.47163\Gamma_G^2\Gamma_L^3 + 0.07842\Gamma_G\Gamma_L^4 + \Gamma_L^5)^{1/5} \quad \textit{(II.9)}$$

$$\eta = 1.36603\frac{\Gamma_L}{\Gamma} - 0.47719(\frac{\Gamma_L}{\Gamma})^2 + 0.11116(\frac{\Gamma_L}{\Gamma})^3 \quad \textit{(II.10)}$$

with Γ_G and Γ_L representing the widths of the Gaussian and Lorentzian components, respectively.

The latter contributions are given by the formulas:

$$\Gamma_G = \sqrt{U\ \tan^2\theta + V\tan\theta + W + \frac{P}{\cos^2\theta}} \quad \textit{(II.11)}$$

$$\Gamma_L = X\tan\theta + {}^{Y}/_{\cos\theta} \quad \textit{(II.12)}$$

Therefore, with the 5 adjustable parameters U, V, W, P, X, Y, one can refine the structure to obtain the best match. The difference between the observed profile and the calculated profile can be assessed by R-weighted profile factor R_{wp}, as introduced by Rietveld. An example of profile modelling is shown in Figure II.11.

$$R_{wp} = \sum_i w_i(Y_{io} - Y_{ic})^2 \quad \textit{(II.13)}$$

Where:

Y_{io} and Y_{ic} represent the intensity observed or calculated at each point i of the diagram;

w_i is a weighing factor.

The resolution of the structure is ended by *Superflip* using "charge flipping" algorithm, which is based on the assumption of the positivity of the electron density, in order to converge the structure with targeted atoms (namely Si, Al, O, Ce or Na in the present case). An example of structural resolution is shown in Figure II.12, for a 13X framework containing no compensating cations, as resulted from the *JANA2006* simulation.

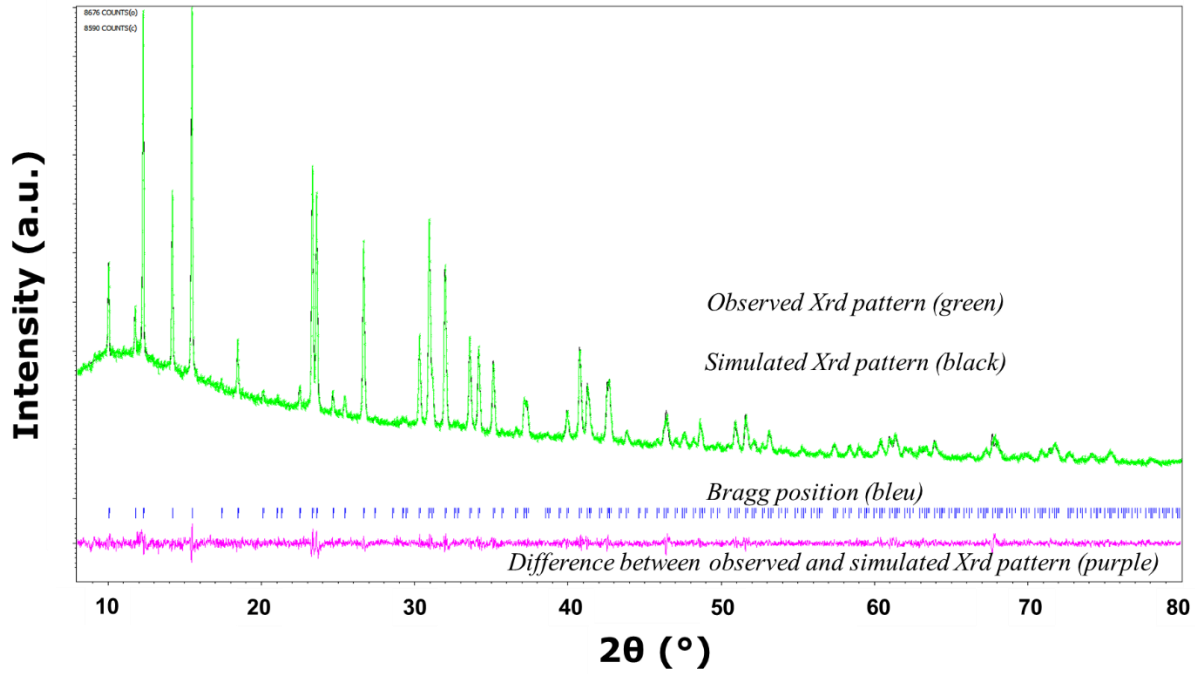

***Figure II. 11**: Comparison of XRD diagram for Ce2-13X observed at 303 K and the one simulated by JANA2006.*

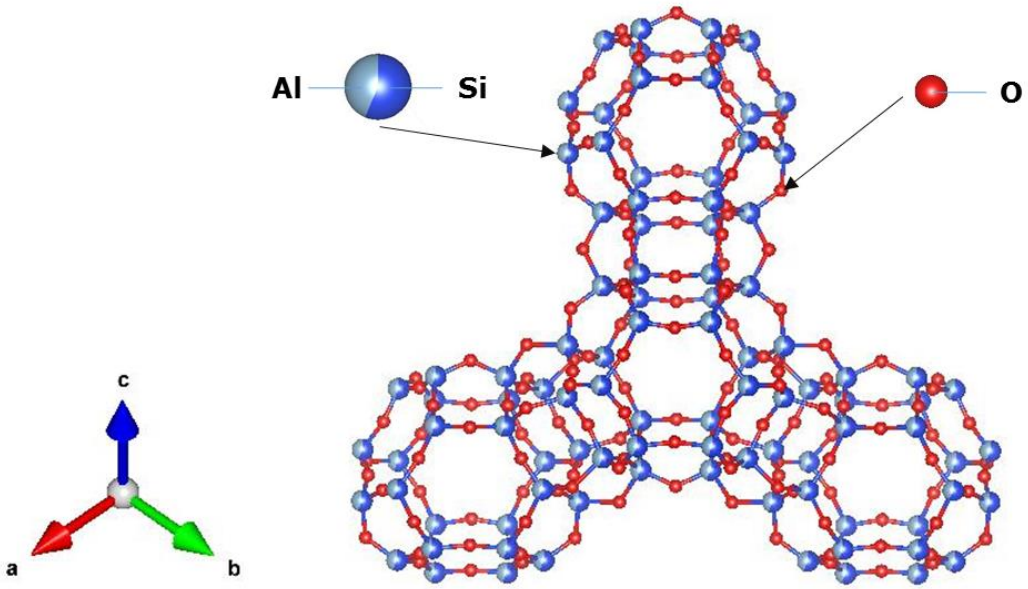

***Figure II. 12**: Structural resolution of the 13X framework without compensating cations by JANA2006 [Si(blue), Al(light blue) and O(red)]*

II.4. ^{29}Si solid-state NMR

Solid-state NMR can be used for the characterization of structures, textures and dynamics of solids, by probing specifically elements with non-zero nuclear spin. In this work, ^{29}Si nuclei is studied to provide general information on the chemical environment of all silicon atoms present in the ionosilica sample for describing its structure and related interaction water-adsorbent [34]. This technique is not utilized in the present work for the zeolite since it has already been well discussed [35–37].

For this purpose, all ionosilica samples were treated by three consecutive hydration-dehydration cycles. The hydration was carried out in a closed container under humid environment at ambient temperature for 2 days. 500 µL of sample were kept for the NMR analysis, and the rest was then used for the dehydration at 383 K under primary vacuum for 24 hours.

Some special techniques are usually needed, including Magic Angle Spinning (MAS), Cross Polarization (CP) to ensure the high resolution of distinct sites on solid-state NMR spectra. The Magic Angle Spinning (MAS) technique removes many sources of line broadening leading to high resolution solid state NMR spectra. MAS introduces artificial motion by placing the axis of the sample rotor at the magic angle $\theta_m = 54.74°$ relative to the magnetic field direction B_0 (c.f., Figure II.13) with a rate of MAS greater than or equal to the magnitude of the anisotropic interaction so as to average it into zero.

Cross Polarization (CP) can be combined with MAS (CP-MAS) to enhance the signal obtained from weakly coupled nuclei such as ^{29}Si. In CP-MAS, polarization from abundant nuclei like ^{1}H can be transferred to the low-abundance nuclei like ^{29}Si through the heteronuclear dipolar interaction. Thus, the CP-MAS experiment increases the magnitude of the signal-to-noise ratio of low-sensitivity nuclei. Since abundant spins are strongly dipolar coupled, they are subject to large fluctuating magnetic fields resulting from motion. This induces rapid spin-

lattice relaxation at the abundant nuclei. As a consequence, CP-MAS reduces greatly the analysis time. In our study, once performed CP-MAS, it was possible to rapidly fix the width and positions of every peak, and then carried out the ^{29}Si NMR experiment with One Pulse (OP) sequence, thus leading to a more quantitative analysis of spectrum in comparison with the CP-MAS experiment.

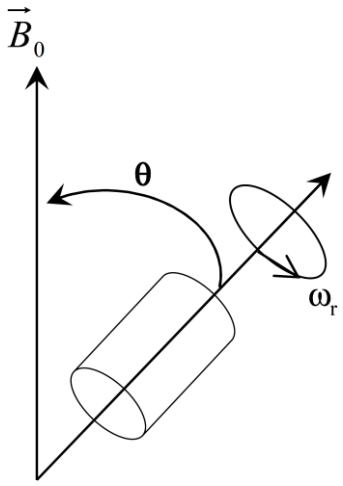

Figure II. 13*: Rotation of the rotor at a speed ω_r around an axis inclined by an angle θ with respect to the axis of the static magnetic field B_0.*

The solid state NMR experiments in the ^{29} Si CP MAS modes were performed on a 400 MHz Bruker spectrometer using a two-channel probe with 7.5 mm and 3.5 mm ZrO_2 rotors respectively. ^{29} Si solid NMR spectra were recorded using the CP MAS and OP sequences with samples running at 6 kHz. CP MAS was used to obtain a high signal-to-noise ratio with a contact time of 5 ms and a recycling delay of 5 s. For the OP experiments, the p/6 pulse and the 60s recycling delay were used to obtain quantitative information on the degree of silane-silanol condensation.

II.4.1.Si configuration by the ^{29}Si solid NMR

Silicon atoms present in the silica are designated by their connectivity to the adjacent oxygen atoms in the tetrahedral SiO_2 framework. One can generally observe two different types of entities:

(i) Q^n entities associated with siloxane groups $[Si(OSi)_n(OR)_{4-n}$; n=0,1,2,3,3,4],

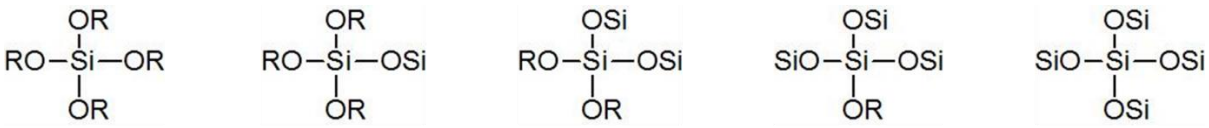

Q^0 **Q^1** **Q^2** **Q^3** **Q^4**

With R denoting H, Methyl group or Ethyl moiety [38]

Silicon atoms involved in bulk siloxanes which are connected to four other silicon atoms through adjacent oxygen bridges are designated as Q^4; silicon atoms which are connected to three other silicon atoms and one hydrogen or alkyl group through adjacent oxygen bridges are designated Q^3, a single hydroxyl group (or lone silanol groups) is usually find on such entities; those having two hydroxyl groups (geminal silanol groups) are referred to as Q^2 (c.f., Figure II.14).

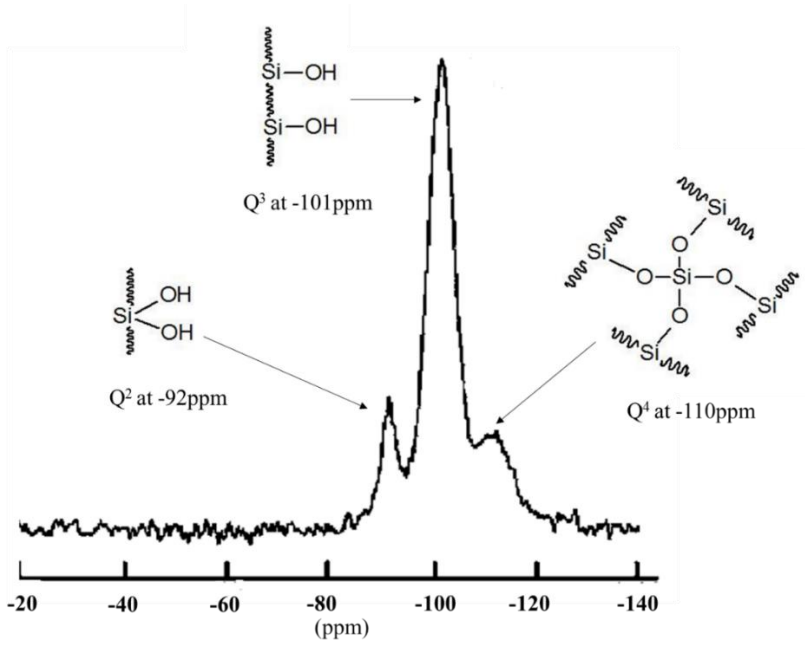

Figure II. 14: Entities Q^n of pur silica on the ^{29}Si CPMAS NMR spectra [39]

(ii) *T^m entities associated with organosiloxane groups [R'Si(OSi)$_m$(OR)$_{3-m}$, m=0,1,2,3]*

T^0 **T^1** **T^2** **T^3**

With R= H, Methyl group or Ethyl group;

R'=Alkyl group [39]

Type T entities are found in functionalized silicas, they are formed by a silicon atom bound to 3 oxygen atoms (bridging or non-bridging) and to a carbon atom. In addition, depending on the bridging or non-bridging nature of the oxygen atoms bound to the silicon atom under consideration, it is possible to distinguish different substructures (Q^n and T^m) with different isotropic chemical displacements (c.f., Figure II.15).

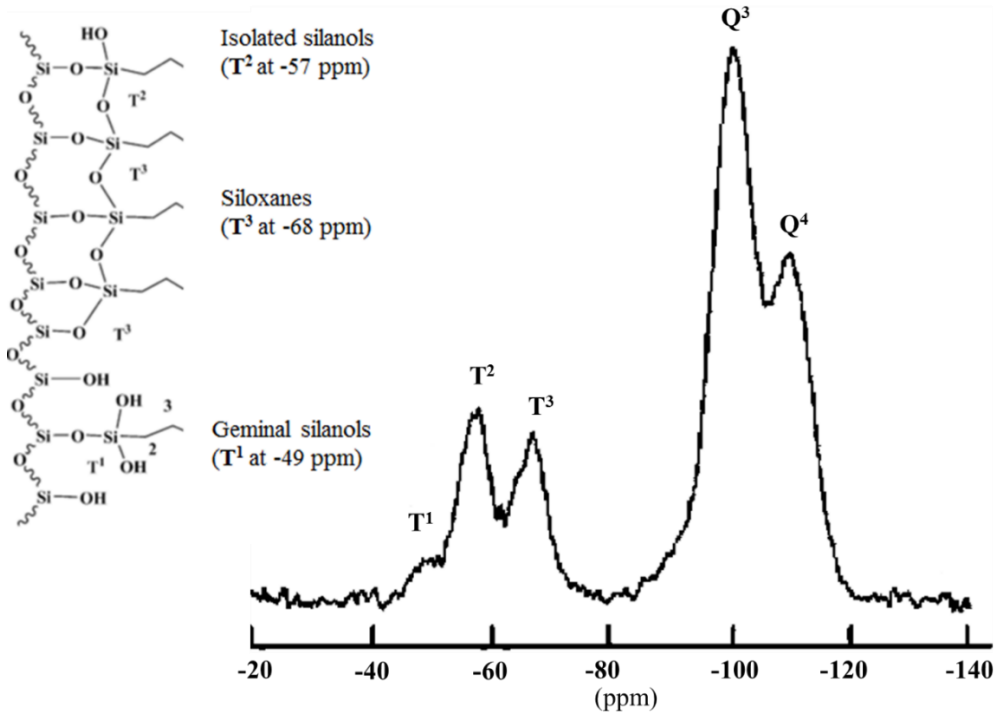

***Figure II. 15**: Entities T^m and Q^n of a functionalized silica on the ^{29}Si CPMAS NMR spectra [39]*

For the study of organic-inorganic hybrid materials, ^{29}Si NMR enables the incorporation of organic motifs to be checked based on the presence of the T^m type resonances. In addition, the degree of condensation of the silica network may be evaluated in reference to the Q^n type resonances.

II.5. Studying adsorption properties of the materials towards water vapour

The adsorption-desorption capacity of materials studied here and the associated heat effects are the most important properties for thermochemical storage systems. Therefore, experimental studies of water vapour adsorption under equilibrium conditions were made to elucidate the relationship between the structure and performance of these materials (i.e., adsorption isotherms, amount adsorbed, adsorption heat, nature of adsorption sites, impact of compensating ions, hydration), as well as the adsorption mechanisms. To better understand the behaviour of storage materials during adsorption-desorption cycles, thermal cycles under dynamic conditions were analysed using a gas flow calorimeter.

It is worth mentioning that as an exothermic phenomenon, adsorption is accompanied by a release of Gibbs free energy from the system caused by the decrease in the internal energy of the solid adsorbent when the molecules adsorb on its surface and by the decrease in the entropy of the adsorbed phase, which corresponds to the restriction of its degrees of freedom compared to the gas or liquid phase. Two different terms of characteristic heat of adsorption were determined by the static and dynamic mode experiments in the present study: the integral heat (Q_{ads}) and the differential one (q_{ads}). These two quantities differ from each other as the integral heat of adsorption expresses the total heat generation for the complete adsorption procedure, while the differential heat of adsorption is defined as the heat evolution when unit adsorption takes place in an isolated system with respect to the adsorbed amount at a given temperature, pressure [40].

II.5.1. Water vapour adsorption in a static mode

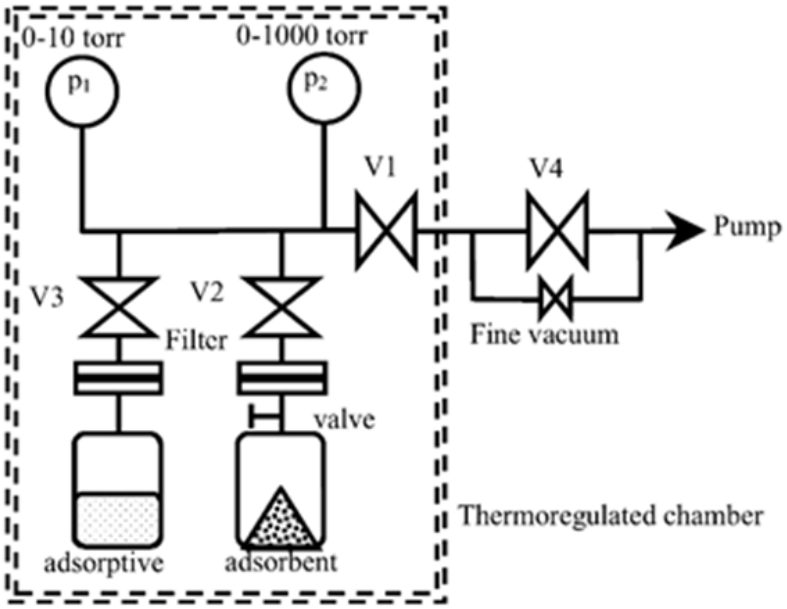

Figure II. 16*: Experimental rig for studying the adsorption of water vapour in a static mode [41].*

This homemade adsorption apparatus was designed and assembled by Prof. P.TRENS at the MACS laboratory of ICGM. The measuring principle is based on the determination of pressure changes during the adsorption process (c.f., Figure II.16). The adsorption is monitored by applying two capacitive pressure gauges sensing the pressure up to 10 and 1000 Torr, respectively, and with temperature being compensated at 318 K to eliminate the temperature dependent measurement error. To activate a sample, the cell was disconnected from the system for being degassed at 423 K (zeolite) or 353 K (ionosilica) during 24 hours, under a vacuum of 10^{-5} Torr. Three Pt100 thermal probes (supplied by Serv' Instrumentation) were placed in the cell, with the adsorption cell and main connecting tube being used as a calibrated tank. The water vapour was generated by heating the adsorptive tank constantly at 313 K and the device was placed in a climatic chamber allowing a thermal stability better than 0.1 K from 250 to 350 K. A program specially designed for this apparatus made the experiments fully automatic from

the degassing stage of the sample, the introduction of successive small doses of water vapour onto the sample, adsorption until the attainment of equilibrium, to the end of the desorption procedure.

The quantity of water vapour adsorbed at the Solid-Gas interface was calculated on the basis of volumetric measurement of the gas remaining non-adsorbed in the closed adsorbent cell after the attainment of adsorption equilibrium. For each measuring point of adsorption quantity, 7.4 KPa of water vapour (generated in the adsorptive tank at 313 K) were initially introduced until reaching the equilibrium. Then the procedure was repeated until the heat effect upon water vapour fully vanished, which indicated the total water saturation of the adsorbent surface.

The adsorption isotherm could be plotted point by point as a function of the relative equilibrium pressure at a given temperature. This means that the amount of water vapour injected into the calibrated reference volume was increased in a controlled manner and then it was expanded in the measuring ampoule containing the solid sample. An equilibrium was established after a certain laps of time between the adsorbed phase and the free gas, the latter constituting the equilibrium bulk phase. A change in the amount of vapour adsorbed during a given *n* step was calculated as follows:

$$\Delta n_{ads} = \frac{1}{RT}\left[(p_n \cdot V_r + p_{n-1} \cdot V_r) - p_n(V_a + V_r)\right] \qquad \textit{(II.14)}$$

Where:

p_n is the equilibrium pressure in the balance (and therefore in the adsorbent ampoule);

p_{n-1} is the initial pressure in the adsorbent ampoule;

V_r is the calibrated reference volume;

V_a is the volume of the adsorbent ampoule.

An important information about the adsorbate-adsorbent interactions involved could be deduced by analysing the slope of the adsorption isotherm at low pressures. This provided a reasonable estimate of the affinity of water vapour towards the solid surface.

In addition to the adsorption isotherms, the differential adsorption heat could be measured *in situ* with respect to each batch of water vapour adsorbed at 313 K by combining a Tian-Calvet differential and isothermal microcalorimeter linked to the static volumetric system. The obtained data were presented as differential heats versus the amount of water vapour adsorbed, the former being defined as follows:

$$q_{ads}(\theta) = \frac{dQ_{ads}}{dn^{\sigma}(\theta)} \qquad \textit{(II.15)}$$

Where:

q_{ads} is the differential adsorption heat;

Q_{ads} is the integral adsorption heat;

n^{σ} is the adsorbed quantity for each batch of water vapour introduced in the closed adsorbent chamber;

θ is the recovery rate of water vapour onto the adsorbent surface

II.5.2. Gas flow microcalorimetric measurements of heat effects in a dynamic mode

In view of potential application considered in the present work, it appeared crucial to perform the adsorption measurements in a dynamic mode in order to place the materials under the conditions which were the most similar to the real operating conditions. Indeed, the kinetics of adsorption can have a non-negligible influence on the behaviour of the adsorption system studied compared to that observed in a static mode [5]. Gas flow microcalorimetry is a technique allowing the simultaneous measurement of the amount adsorbed and integral heat of

adsorption [42–44]. The measuring principle is depicted schematically in Fig II.17. Generally speaking, the heat flow rate induced by the temperature difference between the sample-containing calorimetric cell and the calorimetric block is monitored as a function of time by appropriate temperature sensors (thermocouples or thermistors) placed between both parts of the calorimetric device.

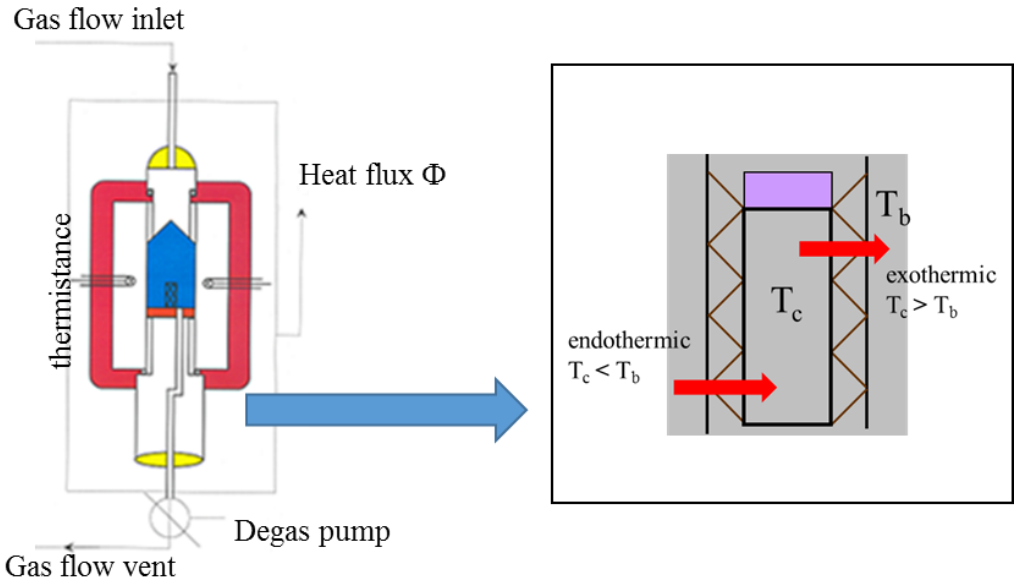

***Figure II. 17**: Scheme of the 4Vms Microscal gas flow microcalorimeter used in the present work together with the measuring principle.*

The general principle of calorimetry is based on the first law of thermodynamics: $\Delta U = W + Q$. When an isolated system exchanges heat with another one, the amount of heat received ($Q_1 > 0$) is equal to, and of opposite sign, to the amount of heat transferred by the other ($Q_2 < 0$). Since no volume work is done in a closed gas-solid chamber, thus $Q_1 + Q_2 = 0$.

In the present study, the calorimetric measurements are carried out in a thermoregulated room at 295 K by means of a Tian-Calvet type calorimeter commercialized by Microscal, Ltd in London (4Vms Microscal flow microcalorimeter). Here, the temperature of the calorimetric cell passively follows that of the thermostat (i.e., calorimetric block). The device contains two thermal sensors controlling heat exchange between the adsorbent and the calorimetric bloc.

With this microcalorimeter, it is possible to measure very small quantities of heat with a high sensitivity. The instantaneous heat flux Φ is then determined by the following equation:

$$\Phi = \frac{Q}{\Delta t} \qquad (II.16)$$

The thermal transfer released by Joule effect gives a signal which is recorded in the form of thermal peak. The corresponding quantity of heat evolved or absorbed during the adsorption or desorption step is determined by integrating the thermal peak according to the theoretical equation of Tian [45]:

$$Q_{ads} = \int_0^t \Phi(t)dt = \frac{\lambda}{g}\int_0^t \Delta dt + \frac{\Lambda}{g}\int_{\Delta_1}^{\Delta_2} d\Delta \qquad (II.17)$$

Where

λ is the thermal conductivity of conducting surface between the measuring cell and the calorimetric bloc, g is the proportional constant, and the term $\frac{\lambda}{g}$ can be evaluated during the calibration run;

Λ is the heat capacity constant of the calorimetric cell with its content;

Δ is the voltage signal produced by the sensor at time t, where $\Delta = g\,(T_{cell}-T_{bloc})$.

The first term on the right hand side of equation II.15 represents the heat exchange between the bloc and the cell monitored by the sensor during the experiment, whereas the second term corresponds to the temperature change in the calorimetric cell. This temperature change equals to zero when the sensor signal returns to the baseline ($\Delta_1=\Delta_2$), therefore the integral adsorption heat Q_{ads} is determined by integrating $\Delta=\Delta(t)$ during the experiment.

Three types of experimental protocol used in the present study are detailed below.

(i) Water vapour injection in batch mode.

In order to determine the activation conditions of the zeolite and ionosilica samples, 2 mL of helium containing 300 ppm of water vapour were injected into the calorimetric cell containing a given mass of solid sample activated under the different conditions: under a flow of He or in vacuum, at room temperature or heated to 353 K or 423 K. The measured heat effect represented the integral enthalpy of adsorption on the most energetic surface sites. It also provided valuable information about the efficiency of the degassing step.

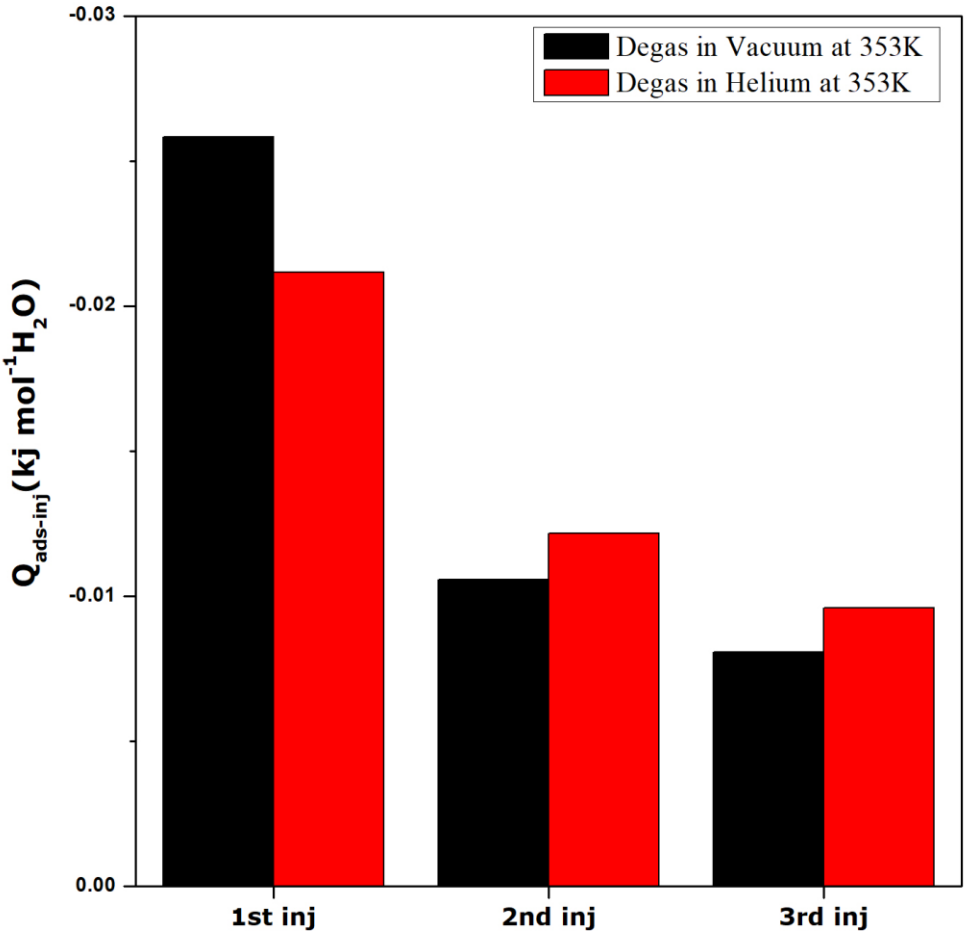

***Figure II. 18**: Adsorption heat for 3 consecutive water vapour injections onto Ce2-13X*

Figure II.18 gives an example of the heat evolution corresponding to 3 injections of the same amount of water vapour onto Ce2-13X, each injection being followed by an appropriate degassing step. It is worth noting that the first injection is made on the dry surface of Ce2-13X.

It seems that, beside the first injection, the degassing procedure under a constant He flow is more efficient for desorbing water molecules from the sample surface. This is an important argument about saving energy necessary for the regeneration of materials.

(ii) Sample pre-treatment prior to calorimetric measurement.

The first activation of zeolite samples was carried out outside the calorimetric device making use of a classical degassing rig provided with the commercial sorption apparatus (ASAP 2020, Micromeritics). This procedure consisted of flowing argon at a rate of 50 ml min^{-1} throughout the solid sample contained in a glass ampoule and heating it simultaneously with a ramp 5 K min^{-1} up to 423 K. Then, the sample was kept overnight at 423 K, before cooling it down to room temperature. These conditions were adopted based on the paper of Hongois *et al*. dealing with the adsorption of water vapour onto zeolite [46].

The activation of the ionosilica samples were made *in situ*, directly inside the calorimetric cell, under a helium flow of 120 ml h^{-1} at 353 K for 24 hours before cooling down to room temperature. The activation temperature was adopted based on the results of TGA experiments.

(iii) Adsorption-desorption cycles [45,47]:

The system is designed to allow adsorption and desorption of water vapour to take place *in situ*, without taking the sample out of the measuring cell for reactivation. The calorimetric device together with the protocol for adsorption and desorption cycling tests are presented in Figure II.19. They were used to evaluate the heat of water vapour adsorption onto samples and their cycling stability under low humidity conditions.

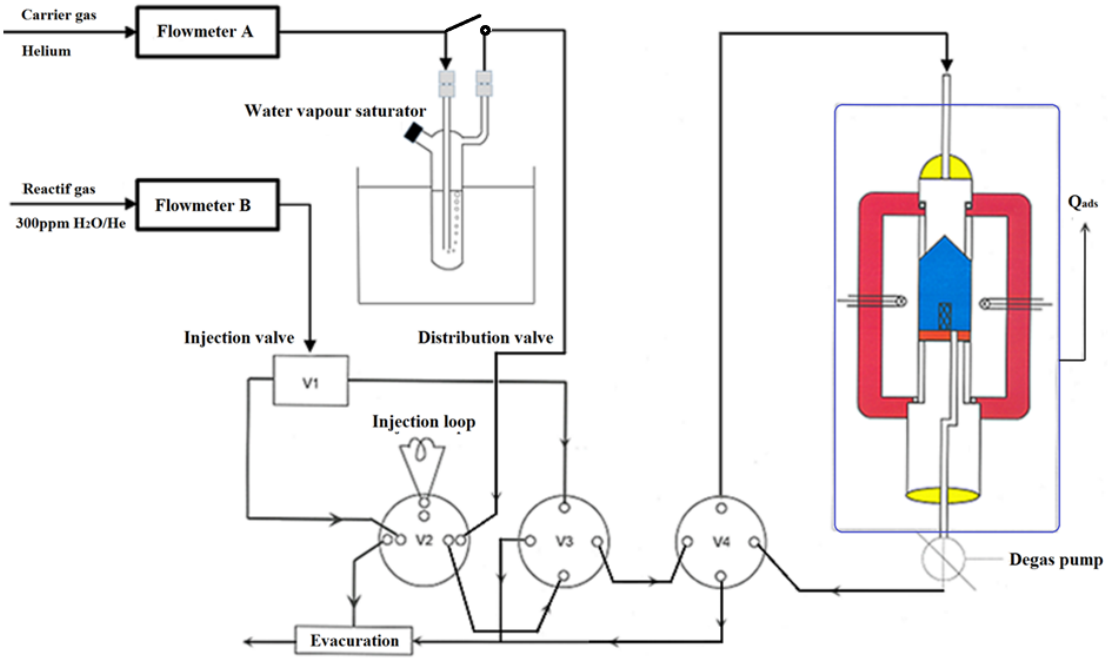

***Figure II. 19**: Scheme of the 4Vms Microscal gas flow microcalorimeter operating in the saturation mode used in the present work*

A given amount of water vapour was injected into the carrier gas flowing through a special saturating vessel specially constructed for our study (c.f., Fig. II.19). The partial vapour pressure could be calculated from the Clausius-Clapeyron equation:

$$\ln\left(\frac{p_{eq}}{p_{ref}}\right) = \frac{\Delta H_{vap}}{R}\left(\frac{1}{T_{ref}} - \frac{1}{T_{eq}}\right) \qquad (II.18)$$

Where:

p_{eq} and p_{ref} are the equilibrium vapour pressure at T_{eq} and T_{ref}, respectively;

ΔH_{vap} is the enthalpy of vaporization;

R is the gas constant (8.3145 J mol^{-1} K^{-1}).

The carrier gas containing a constant amount of water vapour was constantly sent to the calorimetric device until the complete saturation of the solid surface and the corresponding heat

effect measured by integrating the related thermal peak. The adsorption step was carried out by flowing the carrier gas at a rate of 120 ml h^{-1}. The temperature of the saturating vessel was kept at 296 K, thus providing a partial pressure of water vapour, p_{vapeur}, equal to 25 mbar. The thermal peak value was then monitored by computer until it decreased to zero which means until a complete saturation of the surface by water vapour. A calibration thermal signal of 3 mJ sent by the central unit was used for the determination of the integral heat of adsorption. The desorption step was performed by bypassing the water vapour saturator and sending directly the flowing pure helium through the calorimetric cell under the same temperature and flow rate conditions. Prior to it, the sample was re-activated by heating at 353 K. The calorimeter cell was cooling down to 296 K for 24 hours and prepared for the next cycle test.

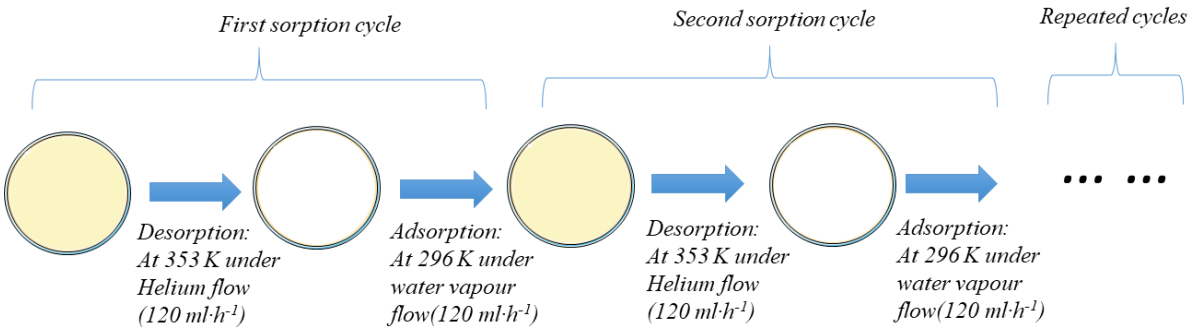

***Figure II. 20**: Protocol of cycling sorption experiment with the use of water vapour by means of a gas flow microcalorimeter operating in a dynamic mode*

References

[1] Wu, H.; Salles, F.; Zajac, J. A critical review of solid materials for low-temperature thermochemical storage of solar energy based on solid-vapour adsorption in view of space heating uses. Molecules 2019, 24, 945 DOI:10.3390/molecules24050945.

[2] Wei Benjamin Teo, H.; Chakraborty, A.; Fan, W. Improved adsorption characteristics data for AQSOA types zeolites and water systems under static and dynamic conditions. Microporous Mesoporous Mater. 2017, 242, 109–117 DOI:10.1016/j.micromeso.2017.01.015.

[3] CECA ARKEMA GROUP Static and dynamic adsorption capacity; 2010; http://www.cecachemicals.com/export/sites/ceca/.content/medias/downloads/news/en/molecular-sieves/2010/ceca-newsletter-september-2010.pdf (accessed September 6, 2018).

[4] Hassanali, A.A.; Singer, S.J. Static and dynamic properties of the water/amorphous silica interface: A model for the undissociated surface. J. Comput. Mater. Des. 2007, 14, 53–63 DOI:10.1007/s10820-006-9038-5.

[5] Lenz, K.; Beste, Y.A.; Arlt, W. Comparison of static and dynamic measurements of adsorption isotherms. Sep. Sci. Technol. 2002, 37, 1611–1629 DOI:10.1081/SS-120002739.

[6] Díaz, E.; Ordóñez, S.; Auroux, A. Comparative study on the gas-phase adsorption of hexane over zeolites by calorimetry and inverse gas chromatography. J. Chromatogr. A 2005, 1095, 131–137 DOI:10.1016/j.chroma.2005.07.117.

[7] Yang, R.T. Adsorbents: fundamentals and applications; John Wiley & Sons, Inc.: Hoboken, NJ, USA, 2003; DOI:10.1002/047144409X; ISBN:0471297410.

[8] Handbook of zeolite science and technology; Auerbac, S.M., Carrado, K.A., Dutt, P.K., Eds.; Marcel Dekker: New York , Basel, 2003; ISBN:0824740203.

[9] Abrioux, C. PhD Thesis: Modélisation moléculaire de l'adsorption et de la diffusion de molécules polaires dans un solide nanoporeux de type zéolithique, Université Montpellier II, 2010.

[10] Santos, V. PhD thesis: Caractérisation et modification de l'acidité résiduelle de

z éolithes cationiques, Universit é de Poitiers, 2008.

[11] Kramer, G.J.; Van Santen, R.A.; Emeis, C.A.; Nowak, A.K. Understanding the acid behaviour of zeolites from theory and experiment. Nature 1993, 363, 529–531 DOI:10.1038/363529a0.

[12] Frising, T.; Leflaive, P. Extraframework cation distributions in X and Y faujasite zeolites: A review. Microporous Mesoporous Mater. 2008, 114, 27–63 DOI:10.1016/j.micromeso.2007.12.024.

[13] Le Bail, A.; Duroy, H.; Fourquet, J.L. Ab-initio structure determination of LiSbWO6 by x-ray powder diffraction. Mater. Res. Bull. 1988, 23, 447–452 DOI:10.1016/0025-5408(88)90019-0.

[14] Rietveld, H.M. A profile refinement method for nuclear and magnetic structures. J. Appl. Crystallogr. 1969, 2, 65–71 DOI:10.1107/s0021889869006558.

[15] Cindrella, L.; Dyer, A. Ion-exchanged and salt hydrates-encapsulated zeolites for solar refrigeration. Sol. Energy Mater. Sol. Cells 2009, 93, 161–166 DOI:10.1016/j.solmat.2008.09.057.

[16] Alby, D.; Salles, F.; Fullenwarth, J.; Zajac, J. On the use of metal cation-exchanged zeolites in sorption thermochemical storage: Some practical aspects in reference to the mechanism of water vapor adsorption. Sol. Energy Mater. Sol. Cells 2018, 179, 223–230 DOI:https://doi.org/10.1016/j.solmat.2017.11.020.

[17] Moïse, J.C.; Bellat, J.P.; Méthivier, A. Adsorption of water vapor on X and Y zeolites exchanged with barium. Microporous Mesoporous Mater. 2001, 43, 91–101 DOI:10.1016/S1387-1811(00)00352-8.

[18] Ames, L.L. Zeolite type X equilibria with trivalent cerium and yttrium cations. J. Inorg. Nucl. Chem. 1965, 27, 885–894 DOI:10.1016/0022-1902(65)80451-1.

[19] Hunter, F.D. Cation Positions in Cerium X Zeolites. J. Catal. 1971, 246259, 246–259. DOI:10.1016/0021-9517(71)90086-8

[20] Marcus, Y. A simple empirical model describing the thermodynamics of hydration of ions of widely varying charges, sizes, and shapes. Biophys. Chem. 1994, 51, 111–127 DOI:10.1016/0301-4622(94)00051-4.

[21] Nguyen, T.P.; Hesemann, P.; Gaveau, P.; Moreau, J.J.E. Periodic mesoporous organosilica containing ionic bis-aryl-imidazolium entities: Heterogeneous precursors for silica-hybrid-supported NHC complexes. J. Mater. Chem. 2009, 19, 4164–4171 DOI:10.1039/b900431a.

[22] El Hankari, S.; Motos-Pérez, B.; Hesemann, P.; Bouhaouss, A.; Moreau, J.J.E. Periodic mesoporous organosilica from zwitterionic precursors. Chem. Commun. 2011, 47, 6704–6706 DOI:10.1039/c1cc11649e.

[23] Nguyen, T.P.; Hesemann, P.; Linh Tran, T.M.; Moreau, J.J.E. Nanostructured polysilsesquioxanes bearing amine and ammonium groups by micelle templating using anionic surfactants. J. Mater. Chem. 2010, 20, 3910 DOI:10.1039/b925352a.

[24] Thach, U.D.; Trens, P.; Prelot, B.; Zajac, J.; Hesemann, P. Tuning the interfacial properties of mesoporous ionosilicas: Effect of cationic precursor and counter anion. J. Phys. Chem. C 2016, 120, 27412–27421 DOI:10.1021/acs.jpcc.6b09457.

[25] El Hankari, S.; Motos-Pérez, B.; Hesemann, P.; Bouhaouss, A.; Moreau, J.J.E. Pore size control and organocatalytic properties of nanostructured silica hybrid materials containing amino and ammonium groups. J. Mater. Chem. 2011, 21, 6948–6955 DOI:10.1039/c1jm10422e.

[26] Bouchal, R.; Miletto, I.; Thach, U.D.; Prelot, B.; Berlier, G.; Hesemann, P. Ionosilicas as efficient adsorbents for the separation of diclofenac and sulindac from aqueous media. New J. Chem. 2016, 40, 7620–7626 DOI:10.1039/C6NJ01473A.

[27] El Hankari, S.; Bouhaouss, A.; Hesemann, P. Anionic surfactants as versatile soft-templates to access nanostructured ionosilicas from functional amine and ammonium precursors. Microporous Mesoporous Mater. 2013, 180, 196–208 DOI:10.1016/j.micromeso.2013.06.018.

[28] Thach, U.D.; Prelot, B.; Hesemann, P. Hybrid ionosilica containing aromatic groups. Eur. Phys. J. Spec. Top. 2015, 224, 1669–1674 DOI:10.1140/epjst/e2015-02489-4.

[29] Braun, M.; Thach, U.D.; Prelot, B.; Hesemann, P.; Esposito, D. Pd@ionosilica as heterogeneous hydrogenation catalyst for continuous flow reductive upgrade of cinnamaldehyde. J. Chem. Technol. Biotechnol. 2017, 92, 2229–2235 DOI:10.1002/jctb.5278.

[30] Françoise ROUQUEROL, Laurent LUCIANI, Philip LLEWELLYN, Renaud DENOYEL, J.R. Texture des matériaux pulvérulents ou poreux. Tech. l'Ingénieur 2003, P1050, 1–24.

[31] Dinnebier, R. Rietveld refinement from powder diffraction data; 2001; Vol. December 2; ISBN:4971168915.

[32] Roisnel, T.; Rodríguez-Carvajal, J. WinPLOTR: a Windows tool for powder diffraction patterns analysis. Mater. Sci. Forum 2001, 378–381, 118–123.

[33] Baerlocher, C.; McCusker, L.B. Database of Zeolite Structures Available online: http://www.iza-structure.org/databases/ (accessed on Sep 11, 2018).

[34] Solid-state NMR spectroscopy principles and applications; Duer, M.J., Ed.; Blackwell Science Ltd, 2002; ISBN:0632053518.

[35] Mafra, L.; Vidal-Moya, J.A.; Blasco, T. Structural characterization of zeolites by advanced solid state NMR spectroscopic methods; 2012; Vol. 77; DOI:10.1016/B978-0-12-397020-6.00004-0; ISBN:9780123970206.

[36] Pérez-Pariente, J.; Sanz, J.; Fornés, V.; Corma, A. 29Si and 27Al MAS NMR study of Zeolite β with Different Si/Al ratios. J. Catal. 1990, 124, 217–223.

[37] Stepanov, A.G. Basics of solid-state NMR for application in zeolite science; Elsevier B.V., 2016; DOI:10.1016/b978-0-444-63506-8.00004-5; ISBN:9780444635068.

[38] Lutz, W.; Täschner, D.; Kurzhals, R.; Heidemann, D.; Hübert, C. Characterization of silica gels by ^{29}Si MAS NMR and IR spectroscopic measurements. Zeitschrift für Anorg. und Allg. Chemie 2009, 635, 13–14 DOI:10.1002/zaac.200900237.

[39] Ciogli, A.; Simone, P.; Villani, C.; Gasparrini, F.; Laganà, A.; Capitani, D.; Marchetti, N.; Pasti, L.; Massi, A.; Cavazzini, A. Revealing the fine details of functionalized silica surfaces by solid-state NMR and adsorption isotherm measurements: The case of fluorinated stationary phases for liquid chromatography. Chem. - A Eur. J. 2014, 20, 8138–8148 DOI:10.1002/chem.201304330.

[40] Inglezakis, V.J.; Zorpas, A.A. Heat of adsorption, adsorption energy and activation energy in adsorption and ion exchange systems. Desalin. Water Treat. 2012, 39, 149–157 DOI:10.5004/dwt.2012.3000.

[41] Tanchoux, N.; Trens, P.; Maldonado, D.; Di Renzo, F.; Fajula, F. The adsorption of hexane over MCM-41 type materials. Colloids Surfaces A Physicochem. Eng. Asp. 2004, 246, 1–8 DOI:10.1016/j.colsurfa.2004.06.033.

[42] Zajac, J.; Dutartre, R.; Jones, D.J.; Roziere, J. Determination of surface acidity of powdered porous materials based on ammonia chemisorption: comparison of flow-microcalorimetry with batch volumetric method and temperature-programmed desorption. Thermochim. Acta 2001, 379, 123–130 DOI:10.1016/s0040-6031(01)00611-6.

[43] Kargol, M.; Zajac, J.; Jones, D.J.; Roziere, J. Selectivity of gas phase adsorption of propene and propane onto mesoporous silica materials derivatised with Ag(I) and Cu(II) at low surface coverages: comparison between equilibrium adsorption and flow microcalorimetry studies. Thermochim. Acta 2005, 434, 15–21 DOI:10.1016/j.tca.2005.01.003.

[44] Brown, D.R.; Groszek, A.J. Heats of adsorption of ammonia on a zeolite catalyst and an acid-activated clay catalyst determined by flow adsorption microcalorimetry. Langmuir 2000, 16, 4207–4212 DOI:10.1021/la990897h.

[45] Zajac, J.J. Calorimetry at the solid–liquid interface. In Calorimetry and Thermal Methods in Catalysis; Auroux, A., Ed.; Springer Berlin Heidelberg, 2013; pp. 197–270; DOI:doi.org/10.1007/978-3-642-11954-5_6; ISBN:978-3-642-11954-5.

[46] Hongois, S.; Kuznik, F.; Stevens, P.; Roux, J.J. Development and characterisation of a new MgSO4-zeolite composite for long-term thermal energy storage. Sol. Energy Mater. Sol. Cells 2011, 95, 1831–1837 DOI:10.1016/j.solmat.2011.01.050.

[47] Bolis, V. Fundamentals in adsorption at the solid-gas interface. Concepts and thermodynamics. In Calorimetry and Thermal Methods in Catalysis; Auroux, A., Ed.; Springer Berlin Heidelberg: Berlin, Heidelberg, 2013; pp. 3–50; DOI:10.1007/978-3-642-11954-5_1 LB - Bolis2013; ISBN:978-3-642-11954-5.

[48] D.D. Do, Pure component adsorption in microporous solids, in: Adsorption analysis: equilibria and kinetics, Imperial College Press, 1998, 149–190. DOI: 10.1142/9781

[49] J. Rouquerol, P. Llewellyn, F. Rouquerol, Is the BET equation applicable to microporous adsorbents? Stud. Surf. Sci. Catal. 2007, 160, 49–56. DOI:10.1016/s0167-2991(07)80008-5.

Chapter III

Experimental and modelling studies of the hydration mechanism in Ce-exchanged zeolites with the aim of optimizing its further uses as an adsorbent in low-temperature thermochemical storage of solar energy by adsorption of water vapour

Enhanced density of heat storage by various zeolite and zeolite-based structures compared with other storage materials have provided strong arguments supporting their potential use as adsorbents in thermochemical storage of solar energy by adsorption of water vapour or solar refrigeration [1–8]. By the way, zeolite 13X was the first adsorbent practically applied in short-term low-temperature thermochemical storage for daily building space heating [9,10]. Nevertheless, some disadvantages may seriously limit the action of zeolites as effective adsorbents for water vapour. In order to ensure the complete regeneration of the adsorbent after each discharging stage (adsorption of water vapour), harsh drying conditions are necessary. Otherwise, the heat release upon adsorption will be greatly reduced, thus compromising the reversibility of the sorption phenomena involved and the cyclability of the storage process. When subject to a great number of repeated drying-hydration cycles, 13X-type zeolites appear to be undergoing a progressive amorphisation and the concomitant evolution of the pore structure [11]. Furthermore, the migration of extra-framework cations among various crystallographic sites accompanying hydration and dehydration sequences may be difficult to control or even to handle. Therefore, the starting idea within the framework of this Ph.D. thesis was to consider the preparation of cation-exchanged zeolites that would allow the adsorbent regeneration to be performed under mild conditions. The unavoidable decrease in the amount of heat released upon subsequent adsorption step could be compensated by the enhanced integral heat of adsorption due to more exothermic hydration of the extra-framework compensating cations.

The present chapter is thus devoted to experimental and modelling studies of the hydration mechanism in Ce-exchanged zeolites. The evolution of the hydration patterns for cation-exchanged samples containing trivalent and quadrivalent cerium cations (i.e., Ce^{3+}, Ce^{4+}) is compared with that observed for the pristine 13X sample possessing Na^{+} compensating ions. The adsorptive properties of the materials are determined on the basis of the measurements of

the equilibrium adsorption isotherms for water vapour and the corresponding differential and integral heats of adsorption obtained under both static and dynamic conditions. The Rietveld refinement analysis of the X-ray diffractions patterns and the Grand Canonical Monte Carlo simulations of the basic adsorption observables are exploited with a view to improving the understanding of the hydration mechanism at the molecular level. At the end, the main advantages and disadvantages of using Ce-exchanged zeolites in storage applications are discussed. The aim of this approach is to verify the extent to which the drying-hydration cycles may be controlled with such adsorbents, and, therefore, to gain a more precise idea about the possibility of avoiding the drastic adsorbent regeneration without greatly reducing the heat storage density in the future thermochemical storage of solar energy by adsorption of water vapour.

The above-mentioned results and the related discussion are further presented in the form of written manuscript which will be submitted to the journal of *Microporous and Mesoporous Materials*. The supporting information of the article can be found in II.

III.1. Written manuscript to be submitted in Microporous and Mesoporous Materials

Comprehensive description of the hydration mechanism in Ce-exchanged zeolites in view of potential uses in low-temperature thermochemical storage of energy

Hao Wu, Philippe Trens, Bernard Fraisse, Fabrice Salles*, Jerzy Zajac*

Institut Charles Gerhardt (ICGM), Université de Montpellier, CNRS, ENSCM. Place Eugène Bataillon, 34095 Montpellier Cedex 5, France,

E-mail: fabrice.salles@umontpellier.fr, jerzy.zajac@umontpellier.fr

Key Words: 13X zeolite, water vapour adsorption, heat of adsorption, calorimetry, cation distribution, Monte Carlo, mild adsorbent regeneration

Abstract

Faujasite 13X-type zeolite has been tested as water vapour adsorbent in view of potential uses in low-temperature thermochemical storage of solar energy based on vapour sorption cycles. Facing the necessity of avoiding adsorbent regeneration under drastic temperature and vacuum conditions, a commercial 13X sample was modified by exchanging extra-framework Na^+ ions for Ce^{3+} and Ce^{4+} in order to increase the amount of heat released during the discharging stage. Three selected Ce-exchanged samples were characterized by Wavelength Dispersive X-Ray Fluorescence, Energy Dispersive X-ray Spectroscopy, X-ray diffraction, Thermogravimetric analysis, adsorption of gaseous nitrogen at 77K and water vapour at 40 °C, as well as by batch calorimetry measurements of water adsorption in aim to establish the relationship between the structural and surface properties of the adsorbents and their capacity of adsorbing water vapour. The results of experimental studies were rationalised by Rietveld refinement analysis and Grand Canonical Monte Carlo simulations, thus resulting in the hydration mechanism in such exchanged zeolites.

Sorption cycles were also studied by flow microcalorimetry, allowing for the determination of consecutive heat of sorption as well as the reversibility of the sorption processes. It was demonstrated that, in the mild desorption conditions used, some water molecules remained in the materials. Consequently, the heat of adsorption could not attain the expected maximum

value. Compared to the pristine zeolite 13X, the cerium-exchanged zeolite samples were proven better candidates for thermochemical storage applications under the experimental conditions investigated.

Introduction

The increasing energy demand and the decrease of fossil fuels resources, combined with growing greenhouse emissions, require the development of ambitious alternatives to move towards a sustainable, renewable and environment-friendly way to provide energy. Renewable energy has become one of the most promising alternative to the traditional energy resources, especially in the building applications, responsible for approximately 40% of energy consumption in the EU [1]. In attempts to circumvent issues due to the intermittent nature of renewable energy, many studies have focused on converting it into more useful forms such as thermal energy or electricity [2–6]. Amongst the numerous possibilities for energy conversion, solar energy harvested in abundance during summer may be exploited to increase the internal energy of an appropriate storage material and thus be stored until winter when the heating supply system is under pressure. Converted subsequently into heat during the discharging step, it may be used as a supplemental source of space heating.

In view of potential applications in low-temperature thermochemical storage of energy, solid or liquid materials involved in sorption phenomena have potential to deliver high storage densities [5,6]. Here the heat released from the adsorption process upon discharging serves to increase the temperature of the incoming fresh air, which is subsequently directed to the space heating loop of the heated building. With the use of water vapour as an adsorbate, solid materials capable of being reversibly dried and hydrated, and additionally characterised by good hydrothermal stability, under given operating conditions are considered as good candidates for the thermochemical storage (TCS) uses [6]. Even though many hydrophilic adsorbents are available for such purposes [7–16], zeolites stand out as combining high specific surface areas and strong hydrophilic character of their surface with good thermal/hydrothermal stability [17,18]. Nevertheless, a major drawback of their use as adsorbents in the TCS systems is related with the necessity of applying high temperatures (> 200 ℃) for the complete dehydration of their porous structure. One solution to this issue could be to modulate their hydrophilic surface character by ion exchange or to modify the substitution ratio [19]. Surface modification by ion exchange were reported for these solids showing promising results. Indeed, it was proven that

the nature of the extra-framework cations had a strong influence on the hydration energy in porous solids [20–24].

In the present work, the emphasis was placed on the need for enhancing the sorption properties of a commercially available 13X type zeolite, while avoiding the regeneration cycle to be performed under harsh conditions. Therefore, the challenge is to increase the heat released upon adsorption when starting with a zeolite structure which has not been completely dehydrated during the preceding desorption step. By referring to the research strategy developed previously [21], zeolite samples exchanged with trivalent and tetravalent cerium cations (*i.e.* Ce^{3+}, Ce^{4+}) were elaborated and their energy storage performance was compared with that of the pristine sample saturated with Na^{+} ions. The increase in the heat release upon adsorption was expected to be related to higher hydration energies of such multivalent cations [25,26]. Furthermore, the conditions of desorption were also optimized to ensure an optimum energy release during the discharging phase. By combining water adsorption isotherms, X-ray diffraction patterns, and Monte Carlo simulations, the hydration mechanism occurring in the Ce-exchanged zeolites was elucidated. The motion of the extra-framework cations in the structure was monitored by coupling X-Ray diffraction with structural resolution and Monte Carlo simulations. In addition, calorimetry measurements coupled with Monte Carlo simulations allowed determining the energy performances of the investigated solids, as well as their resistance to the hydration-dehydration cycles. In the light of these results, the use of cerium-exchanged zeolites for thermochemical storage was considered.

Experimental section

Sample preparation

The following ion exchange procedure was used to obtain zeolite samples saturated with Ce^{3+} as extra-framework compensating cations. A 0.05 M Ce^{3+} solution was prepared from the solid $Ce(NO_3)_3.6H_2O$ powder (Sigma Aldrich). After the addition of 1 g of 13X zeolite (Sigma Aldrich) to 50 mL of stock solution, the solution was stirred at 65 ℃ for 3 hours and then centrifuged for 10 minutes at 11000 rpm. The supernatant liquid was subsequently eliminated. This procedure was repeated twice. The final agitation cycle lasted 24 hours. The solid was then shaken with 50 mL of ultrapure water for two hours and centrifuged in the same way as before. This step was repeated 5 times, and the final agitation cycle lasted 24 hours. The obtained sample was denoted as Ce2-13X.

In order to obtain a higher exchange ratio, after washing the pristine sample with ultrapure water, an initial exchange step with 50 mL of $(NH_4)_2SO_4$ solution was performed for 2 hours. This step aimed at substituting Na^+ by NH_4^+ cations in order to facilitate further ion exchange with cerium cations. The same exchange procedure was then repeated with 50 mL of solution containing Ce^{3+} at a concentration of 0.005 M, before washing and centrifuging the so-obtained solid. The obtained sample was named as Ce3-13X.

In both cases, drying was performed by freezing-drying in order to remove traces of water from the samples.

A 13X zeolite saturated with Ce^{4+} as compensating cation was also prepared. For this purpose, a part of the Ce3-13X sample was heated at 450 °C in air during 12 hours. As a result, a change of colour was observed from white to pale yellow. This sample was referred to as Ce4-13X.

Classical characterization of the samples

The chemical formulas of the initial 13X and Ce-exchanged 13X samples were determined using Wavelength Dispersive X-Ray Fluorescence (WDXRF) spectrometer (Axios Max, PANalytical) and Energy Dispersive X-ray Spectroscopy (EDX) on the scanning electron microscope (SEM) (FEI Quanta 200 FEG).

Textural properties of the samples were inferred from N_2 adsorption/desorption isotherms at 77 K using a micromeritics ASAP2010 sorption machine. Samples were degassed at 473 K for 12 h under secondary vacuum prior to nitrogen adsorption measurements. The equivalent specific surface areas were calculated using the BET equation obtained from the theoretical model of Brunauer, Emmett and Teller employed to the nitrogen physisorption isotherms in the relative pressure range $0.05 < p/p° < 0.15$, taking 0.162 nm^2 as a cross sectional area for one adsorbed N_2 molecule [27] .

Thermogravimetric analyses (TGA) were performed on a NETZSCH Jupiter STA 449, under argon with a flow rate of 50 mL min^{-1} to quantify the mass loss during the dehydration process. It must be emphasized that air was not used in these TGA experiments in order to avoid any oxidation of the Ce^{3+} ions. Samples were heated from 25 °C to 550 °C in an alumina crucible using a heating ramp of 5 °C min^{-1}.

In order to determine the evolution of the zeolite crystalline structure upon ion exchange, X-Ray diffraction experiments were performed at room temperature with Cu-Kα radiation on a Philips X'Pert PRO MPD with X'Celerator Scientific detector using 0.04 rad Soller slits.

The high temperature *in situ* analysis was performed with Cu-Kα radiation too, on a Panalytical Empyrean diffractometer with Pixcel3D detector, using 0.02 rad Soller slits to improve the peaks shape. This diffractometer was equipped with an Anton Paar HTK16 chamber with platinum heating filament, and used under air. The zeolite sample was suspended in a few drops of water and deposited on the platinum plate to form a thin and uniform layer after water evaporation. Starting from a completely hydrated sample at 25 ℃, then by increasing the temperature, the water was desorbed from the surface and the desorption process was performed in this way. X-ray patterns of the same Ce2-13X sample were recorded at different temperatures (25 ℃, 80 ℃, 150 ℃, 300 ℃ and 450 ℃) in order to reproduce different hydration states.

Water vapour adsorption measurements under equilibrium conditions and calorimetry measurements under dynamic conditions

Water vapour adsorption under equilibrium conditions was measured with a home-made adsorption apparatus based on a manometric principle previously described in the literature [28]. The zeolites samples underwent an initial thermal treatment at 150 ℃ under vacuum of 10^{-5} Torr, before measuring water adsorption. During the adsorption experiments, the temperature of the chamber was set to 40 ℃ and an adsorption isotherm was measured for each sample by a volumetric technique.

To study the adsorption of water vapour onto the zeolite samples under dynamic conditions, calorimetry experiments were performed on a 4 V ms Microscal flow microcalorimeter in a saturation mode [29]. Helium (ALPHAGAZ 2, France) was used as a carrier gas at a flow rate of 2 mL min^{-1}. Sample (about 80 mg) was degassed at 80 ℃ for 24 h and then cooled down to ambient temperature prior to the introduction of water vapour. A saturator vessel operating at 23 ℃ was employed to obtain a flow of carrier gas containing water vapour at a pressure of 2.8 kPa. The total saturation of zeolite sample was reached until the thermal peak value decreased down to zero. The total heat measured during the adsorption corresponds to the integral heat change accompanying the adsorption of water vapour onto our materials.

Structural resolution

In addition to the structural characterization, a structure resolution was performed using a Rietveld refinement on each X-ray powder diffraction pattern collected during the *in situ* experiment. The XRD profile of the sample was refined by using Le Bail method and the SUPERFLIP software to solve the crystal structure of Ce2-13X at different hydration states

[30]. Furthermore, the JANA2006 software was used to refine the crystal structure [31] and precise the location of the extra-framework Ce cations.

Computational section

Grand Canonical Monte Carlo simulations were performed using a home-made code to localize the position of extra-framework cations and the water adsorption properties in the investigated zeolite structures. The 13X zeolite structure belongs to the space group *Fd*3*m* with a unit cell parameter of 24.85 ± 0.03 Å [32]. In the unit cell, 16 hexagonal prisms, 8 sodalite cages and 8 supercages composed the structure, thus resulting in a general chemical formula of $M_x/nAl_xSi_{192-x}O_{384} \cdot yH_2O$, with M^{n+} as a compensating cation, x varying from 0 to 96, y corresponding to the number of water molecules in the unit cell. In our study, the atomic Si/Al ratio ranged between 1.0 and 1.5 and a rigid framework was considered: 88 substitutions of Si^{4+} by Al^{3+} distributed randomly following the Loewenstein law.

Calculations were performed at 300 K using 10^7 Monte Carlo production steps following 10^7 equilibration steps. The partial atomic charges (c.f., Table S1. from Supporting Information) and the 12-6 Lennard-Jones (LJ) atomic parameters for the framework were taken from the literature [21] and UFF respectively, while formal charges and UFF were used for the extra-framework cations. Water molecules were considered as rigid by using the four-site charged LJ TIP4P/2005 model [21].

The parameters of the adsorbate/adsorbent LJ interatomic potential were then calculated using the Lorentz-Berthelot combining rule. A cut-off radius of 12 Å was applied to all LJ interactions, and the long-range electrostatic interactions were handled by applying the summation Ewald technique. In these calculations, extra-framework cations were allowed to move in the porous structure.

Results and Discussion

Before studying the performances of the solids for the thermal energy storage application, it was necessary to verify whether the zeolite structure was preserved upon ion exchange by cerium cations and after oxidation of Ce^{3+} into Ce^{4+} cations. Once all solids were prepared, the X-ray diffraction patterns were thus recorded to study the impact of the ion exchange on the crystal structure. The experimental XRD patterns are given in Figure 1 for all samples.

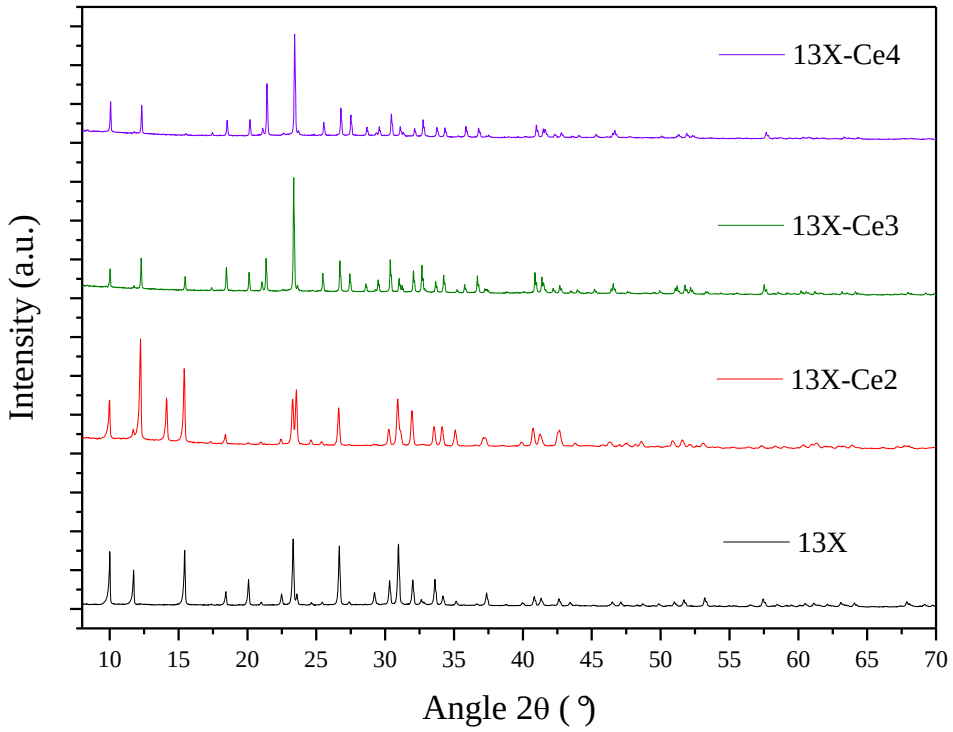

Figure 1. X-ray diffraction patterns measured at room temperature for initial 13X (containing only Na^+), Ce2-13X (containing Ce^{3+}), Ce3-13X (containing Ce^{3+} with a higher exchange ratio) and Ce4-13X (containing Ce^{4+}) as defined in the text.

As observed on the different diffractograms recorded in the presence of Ce^{3+} or Ce^{4+}, the relative intensity of the peaks changes but the number and the positions of the peaks are always the same for the four samples, with the exception of Ce2-13X for which a new peak at 13.2 °2θ has been obtained which corresponds to $Ce(NO_3)_3.4H_2O$ (used for the exchange) (c.f., Figure S1 from the Supporting Information). Some other peaks can also be attributed to the $Ce(NO_3)_3.4H_2O$ but have minor intensities. This suggests that the ion exchange in the 13X faujasite does not imply a strong modification of the structure, thereby confirming that the structure is close to be rigid upon ion adsorption, as already reported in the literature [33]. Some modifications of the peaks intensity can be observed due to the modification of the electronic density inside the pores. Furthermore, the number of compensating cations has no effect on the structure since the modification of Ce^{3+} into Ce^{4+} has no influence on the diffractograms (if we consider the positions of the peaks, in contrast with the intensity which is influenced by the electronic density inside the pores).

Moreover, the temperature effect was also investigated in order to probe the impact of the temperature on the crystallographic positions of the atoms within the framework, as well as on

the positions of the extra-framework cations. Additionally, it was possible to analyse the impact of the oxidation state of cerium (from Ce^{3+} to Ce^{4+}) on the host structure.

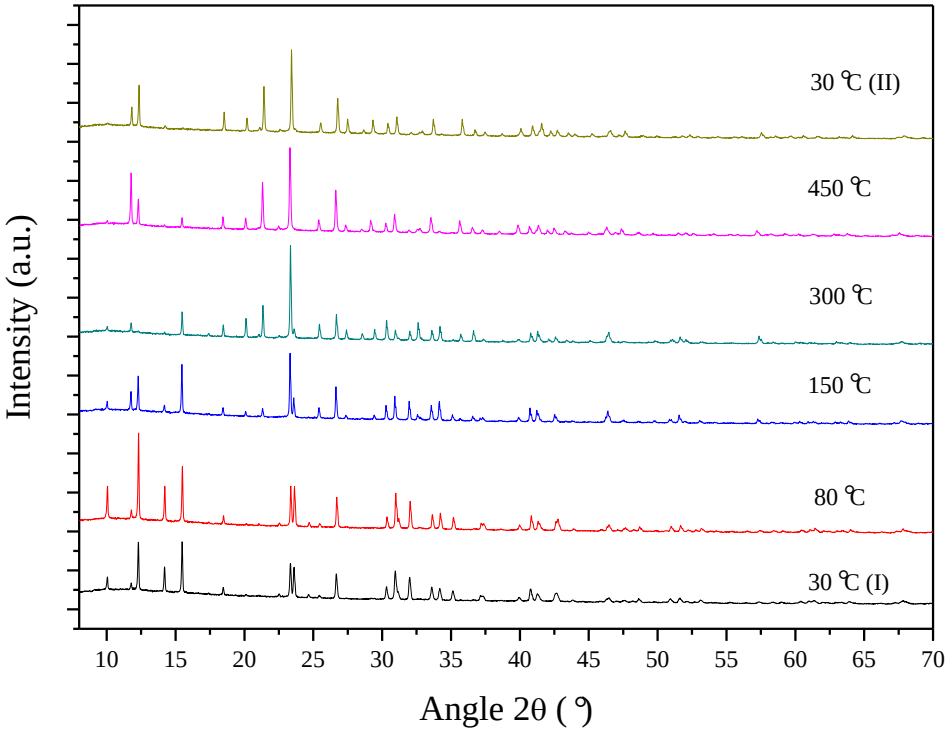

Figure 2. In situ X-ray diffraction patterns of Ce2-13X at different temperatures.

Considering Figure 2, which shows the diffractograms as a function of the temperature for Ce2-13X, it is possible to observe that the diffraction peaks intensities are modified upon temperature change. This suggests that the electronic density has been modified when the temperature increased. Such a modification can be explained by the modification of the positions of the extra-framework cations in the structure when the temperature increases. Indeed, when the temperature is modified, the hydration state of the zeolites is also modified, hence leading to a modification of the position of the extra-framework cations.

It can be noticed that the diffractograms at 30 ℃ recorded in the beginning and at the end of the experiment are not strictly equivalent to each other. This can be due to some irreversible modification of the positions of the extra-framework cations.

Using the structural resolution performed on the results of X-ray diffraction measurements, it was possible to analyse the positions of the extra-framework cations and to compare them with the simulated results. The different structures as a function of the temperature are given in Figure S2 from the Supporting Information. The resulting positions of

the extra-framework cations obtained both experimentally and by molecular simulations (see cif files for the distributions of the cations at the dry and hydrated states obtained by Monte Carlo) are listed in Table 1.

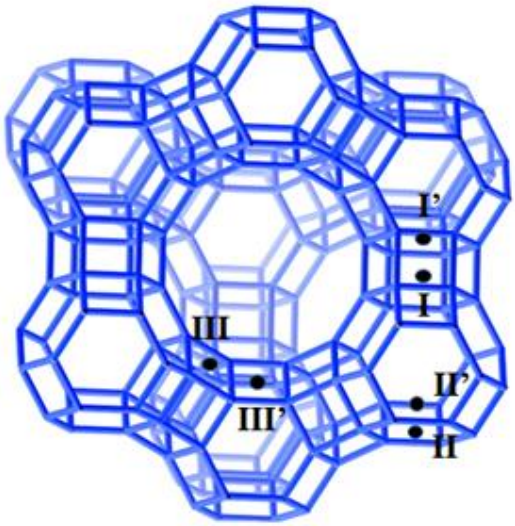

Figure 3. FAU zeolite structures showing the principal crystallographic sites for the location of charge-compensating cations, extracted from database [34].

Table 1. Positions of the extra-framework cations in the structure 13X as a function of the oxidation state of the cerium cations.

Ce3-13X		Simulation	Experimental
	Hydrated	6 I' + 9 II + 9 III + 5 SC	4 I' + 22 II
	Dry	7 (I + I') + 16 II + 6 III'	20 I' + 5 II
Ce4-13X			
	Hydrated	6 I' + 3 II + 9 III' + 4 SC	31 I'
	Dry	8 (I + I') + 9 II + 5 III'	31 I'

From the experimental structure refinement, the sites I’ and II are the preferential sites for both hydrated and dry states in the case of the zeolites saturated with Ce^{3+} and Ce^{4+}. These results are in relative good agreement with calculations performed on structures saturated with such cations. Indeed the main adsorption sites obtained from molecular simulations are I’, II and III. Such a repartition is also in good agreement with the repartition already reported in the literature for the dry state in the case of Na^{+}, Cs^{+} and Co^{2+} containing zeolites [32,35–38].

If one focuses on the hydrated samples (c.f., Table 1), the structural refinement performed from the experimental data shows no difference compared to the dry samples. This

means therefore that the hydration process has no effect on the position of the extra-framework cations. This can be explained by the high charges of the Ce^{3+} and Ce^{4+} cations and the strong electrostatic interactions existing between them and the framework. The comparison with the simulated results confirms these observations since the same adsorption sites are revealed, even if some cations have been found close to the supercages. The latter result is probably due to the high hydration energy of the supercages, thus justifying the mobility of the extra-framework cations located close to the supercages inside these supercages. It should be remembered that the repartition of the aluminium moieties can also strongly influence the distribution of the extra-framework cations. However, the molecular simulations provide only a valuable support to elucidate the water adsorption mechanism occurring in the Ce-samples and the following redistribution of the cations inside the pores [39].

In the literature, in the case of Na^+ as compensating cations, the modification of the positions of the cations upon water adsorption was demonstrated to be rather weak since similar adsorption sites were determined for both hydrated and dehydrated states [36].

After having elucidated the structural properties of Ce-zeolites, further focus is on the sorption properties of these solids, by coupling Monte Carlo simulations with experimental adsorption isotherms and enthalpy of adsorption profiles obtained with the exchanged samples. The experimental and simulated adsorption isotherms are plotted in Figure 4.

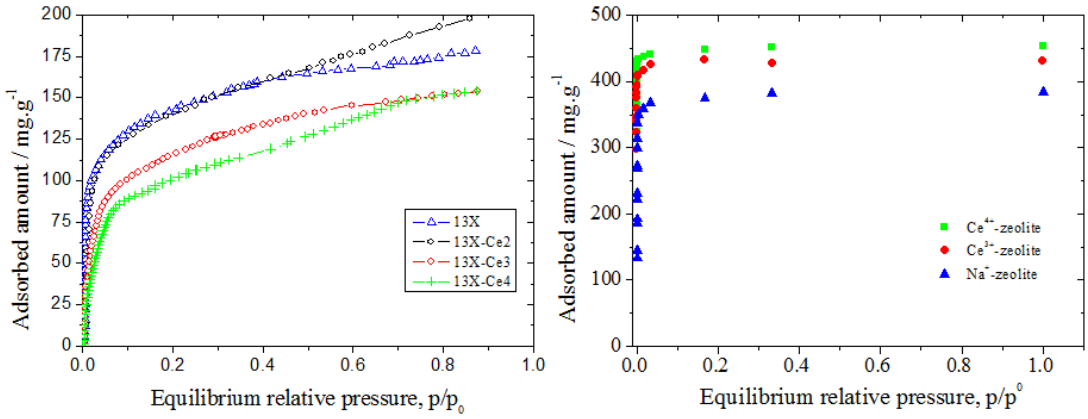

Figure 4. Experimental (left) and simulated (right) adsorption isotherms for water vapour at 313 K.

The comparison of the experimental adsorption isotherms between 13X (i.e., the Na^+-saturated sample), Ce2-13X (containing both Na^+ and Ce^{3+} extra-framework cations), Ce3-13X (containing mainly Ce^{3+} as a compensating cation) and Ce4-13X (containing mainly Ce^{4+} as a compensating cation) clearly evidence the impact of the extra-framework cations on the shape

of the adsorption isotherms, and therefore the adsorbent-adsorbate affinity and the saturation capacity of the adsorbent towards water vapour.

Regarding the affinity as a function of the cation (taken as the slope of the sorption isotherm at very low coverage), the following sequence can be inferred from the experimental results: 13X ~ Ce2-13X >Ce3-13X > Ce4-13X. This means that the affinity towards water is better for 13X (saturated with Na^{+}) than for Ce4-13X (saturated with Ce^{4+}), in contradiction with the order of increasing hydration energy of these cations in aqueous solutions. This is also at variance with the sequence of the simulated enthalpy obtained from Monte Carlo calculations for the first water molecule adsorbed onto zeolites, namely: -90 kJ mol^{-1} in the case of 13X saturated with Na^{+}; -320 kJ mol^{-1} in the case of 13X saturated with Ce^{3+} and -400 kJ mol^{-1} in the case of 13X saturated with Ce^{4+}. It is worth noting that these simulated values are in very good agreement with the experimental enthalpy of adsorption for 13X and they are also of the same order of magnitude as those obtained for samples containing extra-framework cations with higher charges (c.f., Figure 5).

The discrepancy between the affinity sequences as deduced from the experimental adsorption isotherms and the simulated values of the adsorption enthalpy can be explained by the difference between the procedures applied prior to the adsorption measurements in order to activate the samples. Indeed, according to the results of thermal analysis in Figure 6, the hydration shells around the compensating cations have not been totally removed at 150 ℃ and some water molecules are still present. The differences in the hydration energy between the compensating cations can explain the differences observed for the affinity sequence: even though the cerium cations release more energy than the Na^{+} ones upon hydration, the energy required to remove the last water molecules present around the cerium cations is higher than the energy necessary in the case of Na^{+}. This means that the last adsorbed water molecules, which can be desorbed only at higher temperatures, remain in the samples before the adsorption step. This explanation is also consistent with the experimental saturation capacities which increase in the following sequence: Ce2-13X > 13X > Ce3-13X ~ Ce4-13X, in contrast with the theoretically expected order in the saturation capacity being as follows: Ce4-13X > Ce3-13X > 13X.

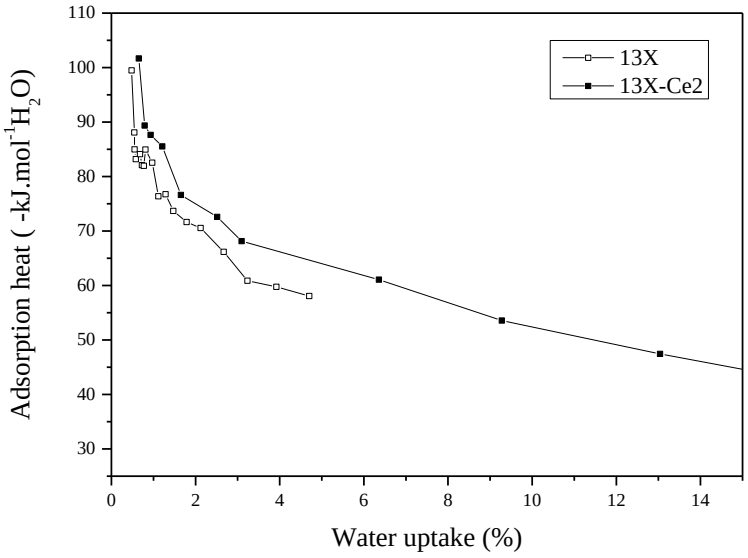

Figure 5. Experimental heat of adsorption for 13X and Ce2-13X as a function of the water loading.

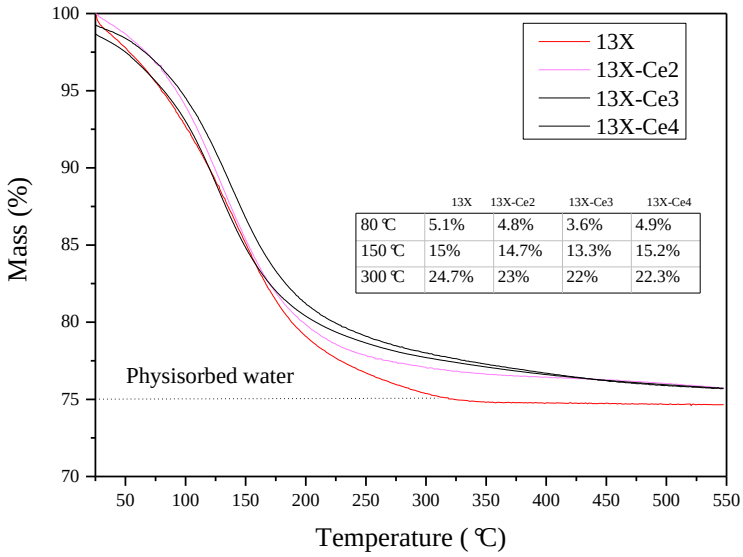

	13X	13X-Ce2	13X-Ce3	13X-Ce4
80 ℃	5.1%	4.8%	3.6%	4.9%
150 ℃	15%	14.7%	13.3%	15.2%
300 ℃	24.7%	23%	22%	22.3%

Figure 6. Thermogravimetric analysis performed on the different materials.

In the final part of this work, the potential of Ce-exchanged zeolites as candidates for the thermochemical energy storage was considered based on the adsorption of water vapour under dynamic conditions of a gas flow. For this purpose, the heat of water vapour adsorption was measured for three successive sorption cycles performed at 23 ℃ by means of a flow microcalorimeter. Figure 7 presents the integral heat of adsorption released during each cycle

for the different materials. In general terms, it can be noted that ion exchange using cerium cations enhances the enthalpy of hydration of the materials. This can be noted for the first sorption cycle, but also for the following sorption cycles. Concerning the first hydration cycle (*i.e.* after the drastic initial activation procedure), Ce4-13X is able to release the greatest heat (> 1100 kJ kg^{-1} of the solid), whereas 13X saturated with Ce^{3+} or Na^{+} provide less energetic hydration stages (~ 950 kJ kg^{-1} and ~ 800 kJ kg^{-1}, respectively). After mild desorption stages, less energy is recovered upon the second and the third cycles: about 700 kJ kg^{-1}, Ce2-13X, Ce3-13X, and Ce4-13X; 550-600 kJ kg^{-1}, 13X. These enthalpies of hydration are similar in the case of the third hydration stage, apart from 13X for which the enthalpy of hydration decreases. It can be deduced that the desorption stage is drastic enough to recover the same amount of surface sites in the case of the exchanged-13X materials, whereas the desorption stage is not sufficient for recovering the surface sites of 13X. This can be regarded as an additional advantage of the exchanged-13X materials compared to the pristine faujasite. Additionally, it can be noted that the heat values are far from the theoretical adsorption heats equal to 3300 kJ mol^{-1} of cation (corresponding to 6048 kJ kg^{-1} of solid) and 6300 kJ mol^{-1} of cation (corresponding to 9550 kJ kg^{-1} of solid) as calculated, respectively, for Ce^{3+} and Ce^{4+} on the basis of the hydration enthalpies [40].

Despite this discrepancy, the present results support the initial hypothesis that the presence of Ce^{3+}/Ce^{4} in the faujasite enhances the heat released during the adsorption step, even though it may be difficult to completely dehydrate the extra-framework cations. Again, under the operating conditions applied in the present study, some remaining water molecules in the zeolite samples certainly prevent the solid adsorbents from reaching the theoretically expected heat upon adsorption. However what is finally important is the capacity of the solid to liberate enough energy upon adsorption for the following cycles. It can be noted that the adsorption energy release is about 65% of the primary adsorption one after a relatively strong activation able to remove almost all water molecules. The comparison with previous studies dealing with zeolites saturated with divalent cations [23] reveals that 65-70 % of the initial energy release is a good compromise for zeolites saturated with cerium, when compared with the case of pristine 13X saturated with Na cations (for which 70-75 % of the energy release for the first adsorption is obtained during water sorption cycling) or Mg- or Ca-exchanged zeolites (for which 30-50% of the energy release for the first adsorption is obtained during cycling as a function of the nature of the compensating cations).

Even if cerium-exchanged zeolites are difficult to dehydrate due to strong hydration energy for the cation, the molecules which are adsorbing during the following cycles provide enough energy to envisage the production of heat.

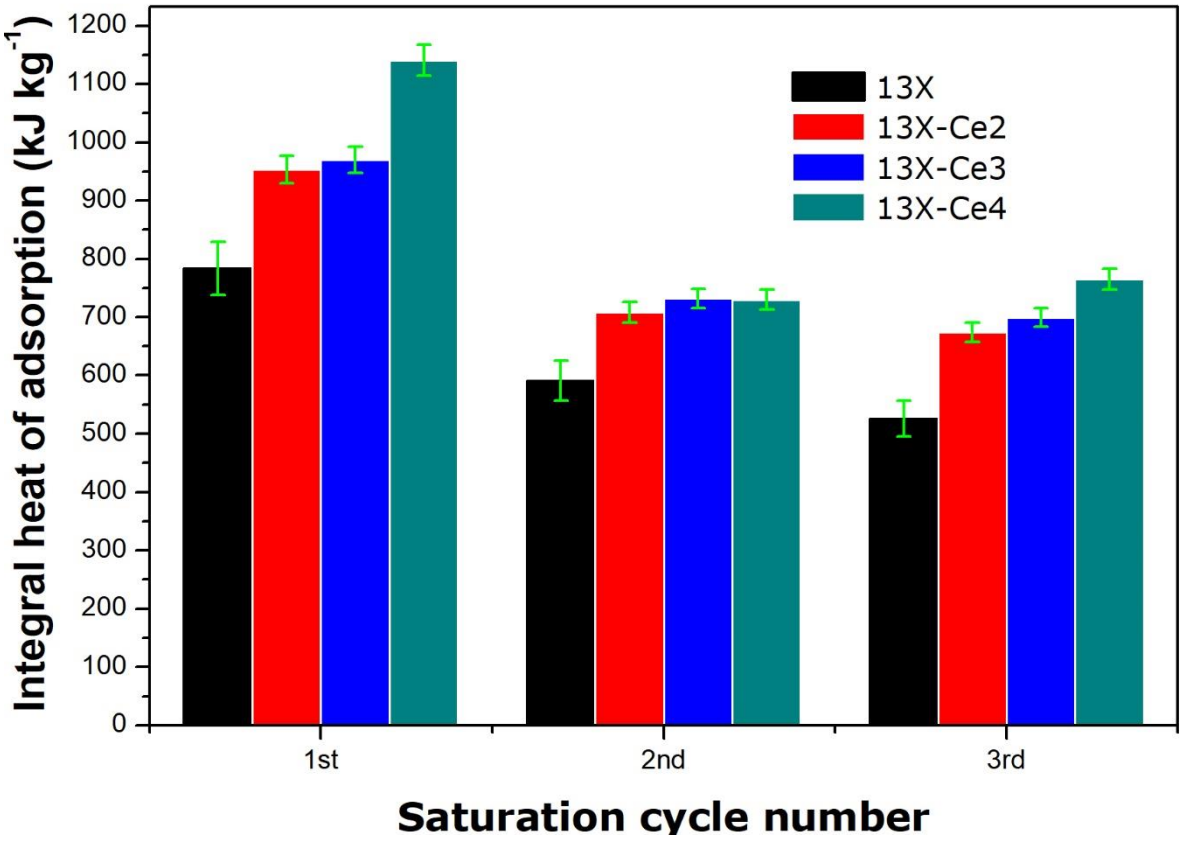

Figure 7. Results of the flow calorimetry measurements of the integral heat of adsorption for 3 successive hydration-dehydration cycles for different zeolite samples studied in the present work.

Conclusion

An alternative solution to store solar energy can be proposed using adsorption process occurring in natural porous adsorbent, thus allowing the cost of the storing materials to be greatly reduced. Within the framework of the present study, the potential use of commercially available zeolite samples exchanged with cations possessing high charges (i.e., Ce^{3+} and Ce^{4+}) was tested. For this purpose, an approach combining adequate experimental characterization methods with molecular simulations was proposed. It led to the identification of the main adsorption sites within the zeolite structures containing such compensating cations as a function of their oxidation state. Both the adsorption isotherms and the results of flow calorimetry measurements provided valuable information on the capacity of the corresponding solids to adsorb water and thus to release heat under conditions of mild regeneration. It was demonstrated that the

maximum heat values were much smaller than those expected from the theoretical calculation. In accordance with the results of thermogravimetric analysis of the samples, it was argued that the decrease in the performance was due to the presence of some water molecules remaining in the adsorbent at the end of the dehydration step. Nevertheless, the use of cerium-exchanged zeolites may be a reasonable solution for thermochemical storage applications if one wants to avoid the detrimental consequences of the drastic adsorbent regeneration. Such a drastic regeneration of the pristine 13X zeolite would be necessary to achieve the heat release level equal to that obtained with the cerium-exchanged analogues under less severe conditions of regeneration.

REFERENCES

[1] European Commission, Energy Efficiency: Buildings, (n.d.) https://ec.europa.eu/energy/en/topics/energy-effic.

[2] P. Tatsidjodoung, N. Le Pierrès, L. Luo, A review of potential materials for thermal energy storage in building applications, Renew. Sustain. Energy Rev. 18 (2013) 327–349. doi:10.1016/j.rser.2012.10.025.

[3] N. Yu, R.Z. Wang, L.W. Wang, Sorption thermal storage for solar energy, Prog. Energy Combust. Sci. 39 (2013) 489–514. doi:10.1016/j.pecs.2013.05.004 Review.

[4] K.E. N'Tsoukpoe, H. Liu, N. Le Pierrès, L. Luo, A review on long-term sorption solar energy storage, Renew. Sustain. Energy Rev. 13 (2009) 2385–2396. doi:10.1016/j.rser.2009.05.008.

[5] S. Kiyabu, J.S. Lowe, A. Ahmed, D.J. Siegel, Computational screening of hydration reactions for thermal energy storage: new materials and design rules, Chem. Mater. 30 (2018) 2006–2017. doi:10.1021/acs.chemmater.7b05230.

[6] H. Wu, F. Salles, J. Zajac, A critical review of solid materials for low-temperature thermochemical storage of solar energy based on solid-vapour adsorption in view of space heating uses, Molecules. 24 (2019) 945. doi:10.3390/molecules24050945.

[7] C. Bales, P. Gantenbein, A. Hauer, H.-M. Henning, D. Jaenig, H. Kerskes, et al., Thermal properties of materials for thermo-chemical storage of solar heat : Report B2 of subtask B, (2005).

[8] L. Navarro, A. de Gracia, S. Colclough, M. Browne, S.J. McCormack, P. Griffiths, et al., Thermal energy storage in building integrated thermal systems: A review. Part 1. active storage systems, 2015. doi:10.1016/j.renene.2015.11.040.

[9] H. Deshmukh, M.P. Maiya, S. Srinivasa Murthy, Study of sorption based energy storage system with silica gel for heating application, Appl. Therm. Eng. 111 (2017) 1640–1646. doi:10.1016/j.applthermaleng.2016.07.069.

[10] S. Mitra, N. Aswin, P. Dutta, Scaling analysis and numerical studies on water vapour adsorption in a columnar porous silica gel bed, Int. J. Heat Mass Transf. 95 (2016) 853–864. doi:10.1016/j.ijheatmasstransfer.2015.12.011.

[11] K. Szczodrowski, B. Prélot, S. Lantenois, J.-M. Douillard, J. Zajac, Effect of heteroatom doping on surface acidity and hydrophilicity of Al, Ti, Zr-doped mesoporous SBA-15, Microporous Mesoporous Mater. 124 (2009) 84–93. doi:10.1016/j.micromeso.2009.04.035.

[12] A. Jabbari-Hichri, S. Bennici, A. Auroux, Effect of aluminum sulfate addition on the thermal storage performance of mesoporous SBA-15 and MCM-41 materials, Sol. Energy Mater. Sol. Cells. 149 (2016) 232–241. doi:10.1016/j.solmat.2016.01.033.

[13] A. Khutia, H.U. Rammelberg, T. Schmidt, S. Henninger, C. Janiak, Water sorption cycle measurements on functionalized MIL-101Cr for heat transformation application, Chem. Mater. 25 (2013) 790–798. doi:10.1021/cm304055k.

[14] J. Canivet, A. Fateeva, Y. Guo, B. Coasne, D. Farrusseng, Water adsorption in MOFs: fundamentals and applications., Chem. Soc. Rev. (2014) 5594–5617. doi:10.1039/c4cs00078a.

[15] M.F. De Lange, K.J.F.M. Verouden, T.J.H. Vlugt, J. Gascon, F. Kapteijn, Adsorption-driven heat pumps: the potential of metal-organic frameworks, Chem. Rev. 115 (2015) 12205–12250. doi:10.1021/acs.chemrev.5b00059.

[16] S.K. Henninger, H.A. Habib, C. Janiak, MOFs as adsorbents for low temperature heating and cooling applications, J. Am. Chem. Soc. 131 (2009) 2776–2777. doi:10.1021/ja808444z.

[17] B. Mette, H. Kerskes, H. Drück, H. Müller-Steinhagen, Experimental and numerical investigations on the water vapor adsorption isotherms and kinetics of binderless zeolite 13X, Int. J. Heat Mass Transf. 71 (2014) 555–561. doi:10.1016/j.ijheatmasstransfer.2013.12.061.

[18] D. Lefebvre, F.H. Tezel, A review of energy storage technologies with a focus on adsorption thermal energy storage processes for heating applications, Renew. Sustain. Energy Rev. 67 (2017) 116–125. doi:10.1016/j.rser.2016.08.019.

[19] K.M. Kim, H.T. Oh, S.J. Lim, K. Ho, Y. Park, C.H. Lee, Adsorption equilibria of water vapor on zeolite 3A, zeolite 13X, and dealuminated Y zeolite, J. Chem. Eng. Data. 61 (2016) 1547–1554. doi:10.1021/acs.jced.5b00927.

[20] J.C. Moïse, J.P. Bellat, A. Méthivier, Adsorption of water vapor on X and Y zeolites exchanged with barium, Microporous Mesoporous Mater. 43 (2001) 91–101. doi:10.1016/S1387-1811(00)00352-8.

[21] D. Alby, F. Salles, J. Fullenwarth, J. Zajac, On the use of metal cation-exchanged zeolites in sorption thermochemical storage: Some practical aspects in reference to the mechanism of water vapor adsorption, Sol. Energy Mater. Sol. Cells. (2017) 0–1. doi:10.1016/j.solmat.2017.11.020.

[22] P. Aprea, B. de Gennaro, N. Gargiulo, A. Peluso, B. Liguori, F. Iucolano, et al., Sr-, Zn- and Cd-exchanged zeolitic materials as water vapor adsorbents for thermal energy storage applications, Appl. Therm. Eng. 106 (2016) 1217–1224. doi:10.1016/j.applthermaleng.2016.06.066.

[23] F. Salles, J.M. Douillard, O. Bildstein, C. Gaudin, B. Prelot, J. Zajac, et al., Driving force for the hydration of the swelling clays: Case of montmorillonites saturated with alkaline-earth cations, J. Colloid Interface Sci. 395 (2013) 269–276. doi:10.1016/j.jcis.2012.12.050.

[24] F. Salles, J.-M. Douillard, O. Bildstein, S. El Ghazi, B. Pr ́dot, J. Zajac, et al., Diffusion of interlayer cations in swelling clays as a function of water content: case of montmorillonites saturated with alkali cations, J. Phys. Chem. C. 119 (2015) 10370–10378. doi:https://doi.org/10.1021/jp512986d.

[25] Y. Marcus, A simple empirical model describing the thermodynamics of hydration of ions of widely varying charges, sizes, and shapes, Biophys. Chem. 51 (1994) 111–127. doi:10.1016/0301-4622(94)00051-4.

[26] D.W. Smith, Ionic hydration enthalpies, J. Chem. Educ. 54 (1977) 540. doi:10.1021/ed054p540.

[27] J.R. Fran ̧oise ROUQUEROL, Laurent LUCIANI, Philip LLEWELLYN, Renaud DENOYEL, Texture des matériaux pulvérulents ou poreux, Tech. l'Ingénieur. P1050 (2003) 1–24. http://cat.inist.fr/?aModele=afficheN&cpsidt=16521113.

[28] N. Tanchoux, P. Trens, D. Maldonado, F. Di Renzo, F. Fajula, The adsorption of hexane over MCM-41 type materials, Colloids Surfaces A Physicochem. Eng. Asp. 246 (2004) 1–8. doi:10.1016/j.colsurfa.2004.06.033.

[29] J. Zajac, R. Dutartre, D.J. Jones, J. Roziere, Determination of surface acidity of powdered porous materials based on ammonia chemisorption: comparison of flow-

microcalorimetry with batch volumetric method and temperature- programmed desorption, Thermochim. Acta. 379 (2001) 123–130. doi:10.1016/S0040-6031(01)00611-6.

[30] L. Palatinus, Superflip — A computer program for solution of crystal structures from x-ray diffraction data in arbitrary dimension., (2007).

[31] V. Petrícek, M. Dušek, L. Palatinus, Crystallographic computing system JANA2006: General features, Zeitschrift Fur Krist. 229 (2014) 345–352. doi:10.1515/zkri-2014-1737.

[32] G. Vitale, C.F. Mellot, L.M. Bull, A.K. Cheetham, Neutron diffraction and computational study of zeolite NaX: influence of SIII‘ cations on its complex with benzene, J. Phys. Chem. B. 101 (1997) 4559–4564. doi:10.1021/jp970393x.

[33] A. Sartbaeva, S.A. Wells, M.M.J. Treacy, M.F. Thorpe, The flexibility window in zeolites, Nat. Mater. 5 (2006) 962–965. doi:10.1038/nmat1784.

[34] C. Baerlocher, L.B. McCusker, Database of Zeolite Structures, (n.d.). http://www.iza-structure.org/databases/ (accessed September 11, 2018).

[35] D. H.Olson, The crystal-structure of dehydrated NaX, Zeolites. 15 (1995) 439–443. doi:https://doi.org/10.1016/0144-2449(95)00029-6.

[36] C. Abrioux, B. Coasne, G. Maurin, F. Henn, A. Boutin, A. Di Lella, et al., A molecular simulation study of the distribution of cation in zeolites, Adsorption. 14 (2008) 743–754. doi:10.1007/s10450-008-9123-z.

[37] M. Jeffroy, A. Boutin, A.H. Fuchs, Understanding the equilibrium ion exchange properties in faujasite zeolite from monte carlo simulations, J. Phys. Chem. B. 115 (2011) 15059–15066. doi:10.1021/jp209067n.

[38] M. Jeffroy, E. Borissenko, A. Boutin, A. Di Lella, F. Porcher, M. Souhassou, et al., Evidence of a framework induced cation redistribution upon water adsorption in cobalt exchanged X faujasite zeolite: A joint experimental and simulation study, Microporous Mesoporous Mater. 138 (2011) 45–50. doi:10.1016/j.micromeso.2010.09.031.

[39] M. Jeffroy, C.N. Draghi, A. Boutin, A new molecular simulation method to determine both aluminum and cation location in cationic zeolites, Chem. Mater. 29 (2017) 513–523.

[40] D.W. Smith, Ionic hydration enthalpies, J. Chem. Educ. 54 (1977) 540. doi:10.1021/ed054p540.

III.2. Conclusion

Given the possibility for enhanced heat release upon adsorption of water vapour within micropores of zeolites, as well as for higher enthalpy of hydration of multivalent compensating cations, Faujasite 13X-type zeolite sample has been tested as an adsorbent in view of potential uses in thermochemical storage of solar energy with the objective of avoiding the drastic adsorbent regeneration without greatly reducing the heat storage density. Three Ce-X samples with different ion exchange ratios (Ce2-13X, Ce3-13X and Ce4-13X) were obtained from the pristine 13X sample. The resulting Ce-X samples represented Faujasite X-type zeolite framework containing trivalent or tetravalent Ce^{3+} and Ce^{4+} ions as extra-framework compensating cations. By combining *in situ* XRD characterization and Rietveld refinement, it was possible to demonstrate that the compensating cations hardly moved away from their preferential sites I' and II of the 13X framework upon hydration process. The Monte Carlo simulations supported these observations, also revealing some extra cations located close to the supercages due to the higher energy of the hydration of sites. The model adsorption isotherms were also predicted on this basis and compared with experimental adsorption curves. The results of calorimetry measurements indicated a significant gain in terms of adsorption heat onto Ce-13X zeolites when compared with the commercial Na-13X sample. The hypothesis of incomplete adsorption regeneration under mild conditions (423 K, no vacuum treatment) was argued, thus leaving some water molecules adsorbed onto adsorbent after the end of the desorption step. A Ce-13X sample containing Ce^{4+} cations, i.e., Ce4-13X, was found to yield more than 1100 kJ per kg of the solid, whereas the adsorption onto 13X saturated with only Ce^{3+} produced around 950 kJ per kg of the solid. Compared to the pristine Na-13X zeolite, these values corresponded to a heat increase by 37.5% and 18.8%, respectively. However, after a regeneration step at a lower temperature of 353 K, only 700 kJ per kg of solid can be recovered upon the second and the third cycles for all Ce-13X zeolites. The measurements of water

adsorption under static conditions corroborated the findings that adsorption capacity of Ce-13X containing Ce^{4+} was lower than expected because of incomplete desorption due to the high affinity of water molecules towards Ce^{4+} cations.

In conclusion, zeolites will continue to attract significant interest as storage materials owing to the large amounts of heat released upon water adsorption. Nevertheless, the full thermal capacity of the material does not appear to be completely exploited due to strong activation conditions required to remove all water molecules. Consequently, a second type of material will be described in the next chapter, as being potentially more adequate to the mild regeneration conditions, in line with the goals of the present thesis.

References

[1] D. Alby, F. Salles, J. Fullenwarth, J. Zajac, On the use of metal cation-exchanged zeolites in sorption thermochemical storage: Some practical aspects in reference to the mechanism of water vapor adsorption, Sol. Energy Mater. Sol. Cells. (2017) 0–1. doi:10.1016/j.solmat.2017.11.020.

[2] L. Cindrella, A. Dyer, Ion-exchanged and salt hydrates-encapsulated zeolites for solar refrigeration, Sol. Energy Mater. Sol. Cells. 93 (2009) 161–166. doi:10.1016/j.solmat.2008.09.057.

[3] G.T. Whiting, D. Grondin, D. Stosic, S. Bennici, A. Auroux, Zeolite-MgCl2 composites as potential long-term heat storage materials: Influence of zeolite properties on heats of water sorption, Sol. Energy Mater. Sol. Cells. 128 (2014) 289–295. doi:10.1016/j.solmat.2014.05.016.

[4] G. Whiting, D. Grondin, S. Bennici, A. Auroux, Heats of water sorption studies on zeolite–MgSO4 composites as potential thermochemical heat storage materials, Sol. Energy Mater. Sol. Cells. 112 (2013) 112–119. doi:10.1016/j.solmat.2013.01.020.

[5] H. Wu, F. Salles, J. Zajac, A critical review of solid materials for low-temperature thermochemical storage of solar energy based on solid-vapour adsorption in view of space heating uses, Molecules. 24 (2019) 945. doi:10.3390/molecules24050945.

[6] N. Yu, R.Z. Wang, L.W. Wang, Sorption thermal storage for solar energy, Prog. Energy Combust. Sci. 39 (2013) 489–514. doi:10.1016/j.pecs.2013.05.004 Review.

[7] A. Haji Abedin, M.A. Rosen, Energy and exergy analyses of an open thermochemical energy storage system: methodology and illustrative application, Open Renew. Energy J. 5 (2012) 41–48. doi:10.2174/1876387101205010041.

[8] R. Gopal, B.R. Hollebone, C.H. Langford, R.A. Shigeishi, The rates of solar energy storage and retrieval in a zeolite-water system, Sol. Energy. 28 (1982) 421–424. doi:http://dx.doi.org/10.1016/0038-092X(82)90261-4.

[9] R.A. Shigeishi, C.H. Langford, B.R. Hollebone, Solar energy storage using chemical potential changes associated with drying of zeolites, Sol. Energy. 23 (1979) 489–495. doi:http://dx.doi.org/10.1016/0038-092X(79)90072-0.

[10] T. Schmidt, D. Mangold, H. Müller-Steinhagen, Central solar heating plants with seasonal storage in Germany, Sol. Energy. 76 (2004) 165–174. doi:https://doi.org/10.1016/j.solener.2003.07.025.

[11] G. Storch, G. Reichenauer, F. Scheffler, A. Hauer, Hydrothermal stability of pelletized zeolite 13X for energy storage applications, Adsorption. 14 (2008) 275–281. doi:10.1007/s10450-007-9092-7.

Chapter IV

Properties and mechanisms of water vapour adsorption onto ionosilica

Ionosilica materials are characterized by a significant adsorption of water vapour and good cycling capacities, as well as their tunable surface hydrophobic-hydrophilic balance due to the presence modular functional groups [1–4]. Despite these advantages, no specific research concerning the heat storage has been done up to date.

In the present chapter, we revealed the potential of ionosilicas as thermochemical storage materials, by examining the conditions of their activating/regenerating, their sorption properties towards water vapour, and their stability upon the sorption cycles. Furthermore, since no systematic study had been undertaken on the behaviour of these adsorbents, the intention of this study was to shed more light on the mechanisms by which water vapour adsorbed onto ionosilicas.

IV.1. Ionosilica samples used in the present study

The materials which have been considered for the purpose of the present study are ammonium-type ionosilicas DSM19, ISA8 and ISA100. Their chemical structures are shown in Figure IV.1. These ionosilicas have been functionalized by ammonium group as a cationic substructure compensated by different anions. The compensating anions have been proved to have tunable physicochemical properties in terms of polarity and hydrophilic-lipophilic character [4]. As detailed in Chapter II, the materials DSM19 and ISA100 are synthesized via hydrolysis-polycondensation process starting from the tris (3-(trimethoxysilyl)propyl)amine (**TrisN**) precursor. The subsequent protonation treatment with hydrochloric or sulfuric acid results in the introduction of such counter-ions as Cl^-, for DSM19 sample, and SO_4^{2-}, for ISA100 one. The ISA8 material, which contains both Cl^- and SO_4^{2-} as counter-ion, is obtained by following the ion exchange procedure. The anion exchange ratio is determined based on the chemical analysis by Wavelength Dispersive X-ray Fluorescence (WDXRF). After 5 different anion-exchange runs, a minimum of 47 % of the residual Cl^- is found in the final sample, which indicates the final exchange ratio of 53 %.

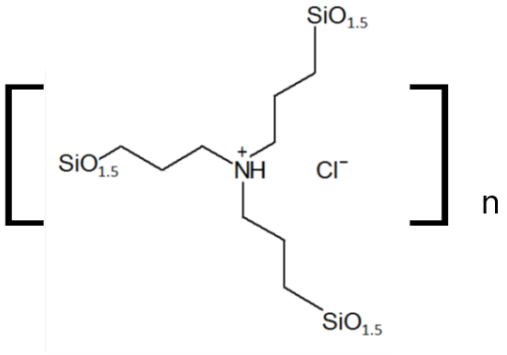

Ionosilica DSM19

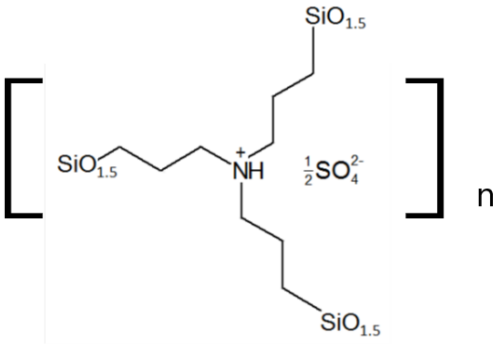

Ionosilica ISA100

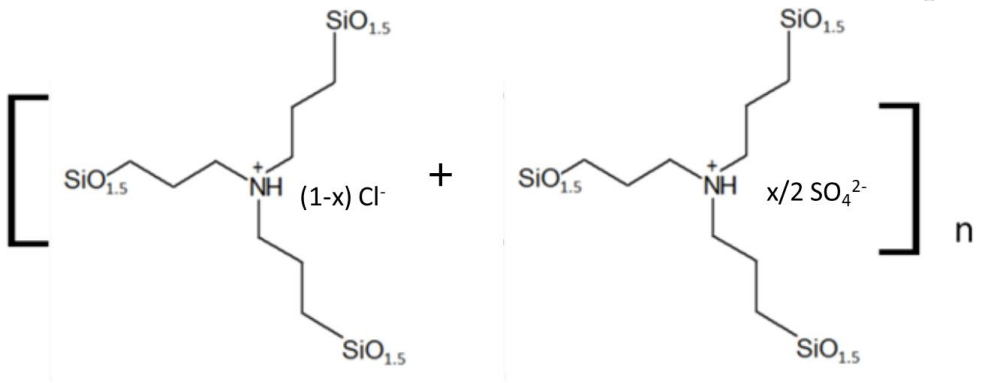

Ionosilica ISA8

Figure IV. 1*: Chemical structures of the ionosilica samples studied in the present work: DSM19, ISA100, and ISA8*

Prior to the synthesis of the ionosilica samples for the present study, it was necessary to decide upon using a surfactant template. Our synthesis strategy was guided by following two aspects. The first one was related to the chemical and thermal stability of the prepared materials. The surfactant-assisted synthesis, as described in several previous papers [1,4,5], would lead to a more ordered and uniformly sized pore architecture of the ionosilica samples, thus resulting in a high specific surface area. However this architecture presented some risk of fragility, as mentioned by Thach *et al.* who showed that the texture of the materials altered upon water adsorption was instable towards water [4]. Based on this information, the structural integrity of the samples submitted to repeated adsorption-desorption cycles could not be assured. Secondly,

from a practical point of view, a high-cost and rather complex surfactant-assisted synthesis was clearly not a suitable option when taking into account the upscaling of the thermochemical storage to an industrial level. Therefore, it was decided not to use any surfactant during the synthesis, although this gave the materials less regular organization at the mesoscopic level.

After the synthesis or ion exchange procedure, it was necessary to check the structural integrity and monitor the functionalization degree. As no surfactant was used in the synthesis of all ionosilica samples, the thermal and hydrothermal stability should be enhanced. At the same time, this rendered the ionosilica materials amorphous. Consequently, X-ray diffraction experiments could only provide very limited information about the structural integrity compared to the zeolite samples described in the previous chapter. Furthermore, FT-IR spectroscopy was used to get the first information about the efficiency of the functionalization procedure. The FT-IR spectra of DSM19, ISA8, and ISA100 are given in Figure IV.2.

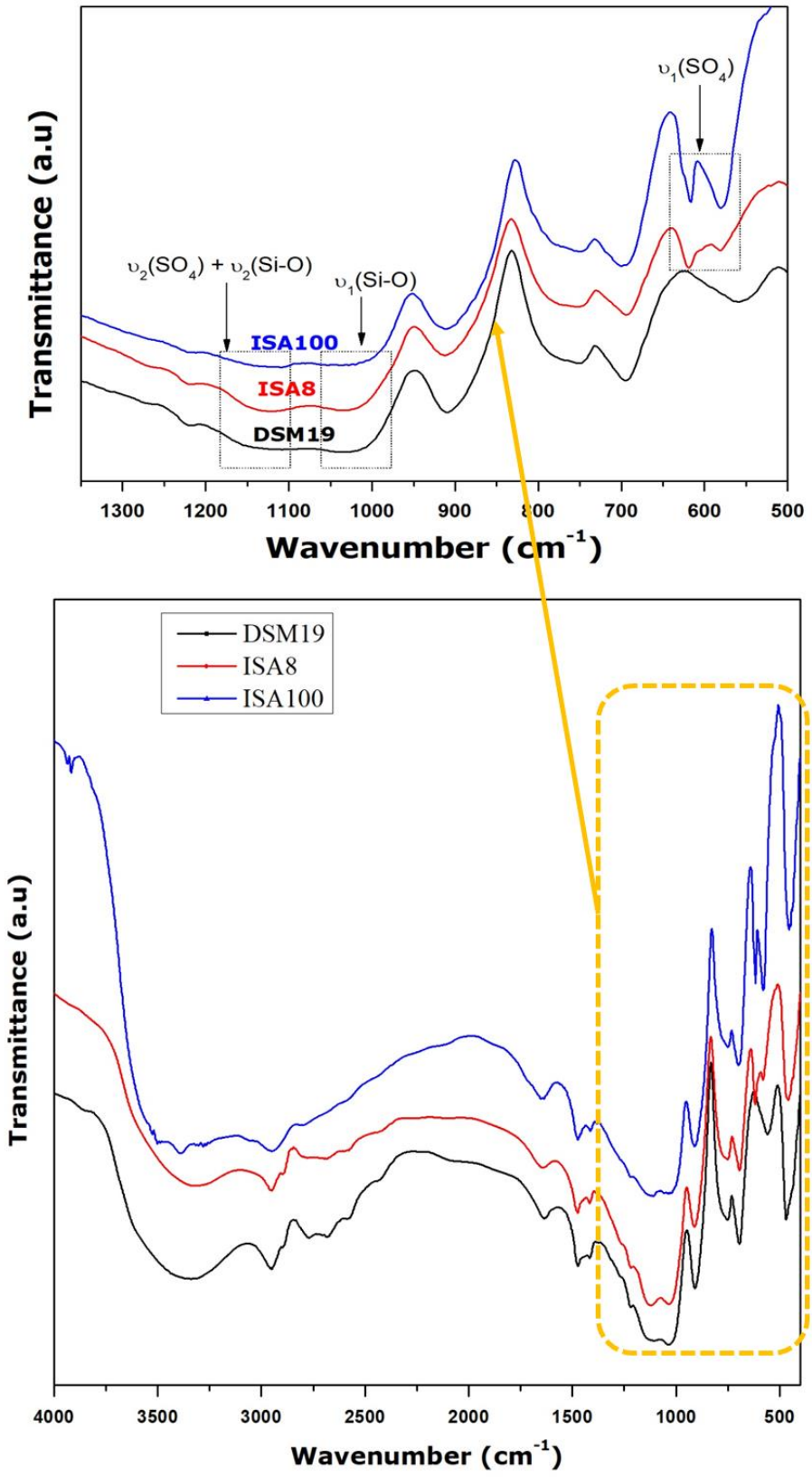

Figure IV. 2*: FTIR spectra of ionosilica materials: DSM19 (black), ISA8 (red) and ISA100 (blue).*

The three spectra exhibit broad absorption bands at 3300-3600 and around 1650 cm^{-1}, which correspond to the stretching and deformation vibrations of physisorbed water [6]. These bands indicating the presence of physisorbed water are still present in their spectra after 24 hours of drying at 353 K under air. This is also confirmed by the thermogravimetric analysis (TGA) presented later on (c.f.,Figure IV.3): at 353 K without vacuum treatment, 20-30 % of residual physisorbed water is still present in the samples which have been initially hydrated in ambient air for 2 days. Broad bands appeared from 1100 to 1000 cm^{-1} due to Si−O vibrations of the polycondensed siloxane [7]. CH_2 deformation vibrations can be identified at 1470 cm^{-1}. In the case of ISA8 and ISA100, extra absorption bands characteristic of the functional group can be also seen. The absorption band at 617 - 627 cm^{-1} can be attributed to the stretching vibration of the sulfate anion [7–9]. Another band of sulfate anion at 1120 cm^{-1} cannot clearly be identified because of overlapping with the total bulk absorption of Si-O vibrations. This gives an evidence of the successful functionalisation with sulfate groups in the as-synthesized and ion-exchanged ionosilica samples.

IV.2. Thermal behaviour of ionosilica samples and determination of the desorption-regeneration temperature

In order to obtain a high heat of adsorption during the discharging step required in view of the thermochemical storage uses, the solid adsorbent must undergo an appropriate thermal treatment to remove the retained water vapour from the surface without compromising the structural integrity. For this purpose, we have decided to perform firstly a thermogravimetric analysis (TGA) and record the thermograms from room temperature up to 573 K. Indeed, the previous work carried out by Thach *et al.* [10] on the ammonium-type ionosilica showed that the thermal stability went down when the thermal treatment exceeded 493 K. Beyond this value, a degradation due to the decomposition of amine groups took place.

The TGA curves from 298 K to 573 K are shown in Figure IV.3.

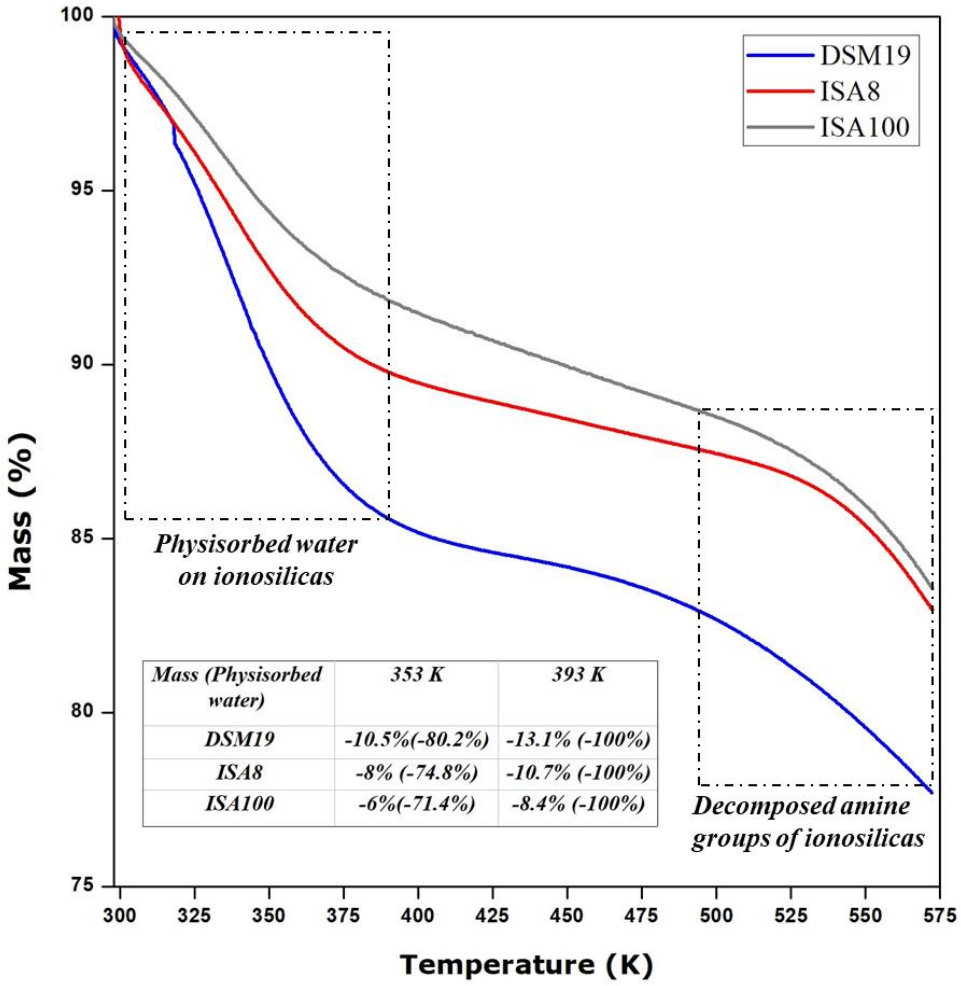

***Figure IV. 3**: TGA thermograms recorded on ionosilica samples DSM19, ISA8, and ISA100.*

At first sight, we observe a sharp mass drop around 483-523 K which corresponds to the amines decomposition, as mentioned by Thach *et al.* [10]. For DSM19, the amines decomposition starts at 483 K, and for ISA8 and ISA100, it starts at a relatively higher temperature around 523 K. This indicates that, with the modification of compensating counter-ions, the thermostability of ionosilica is enhanced probably due to the stronger interaction between sulfate anions and ionosilica framework. A careful analysis of these curves indicates that most of the physisorbed water is removed up to 393 K. Furthermore, the total water uptake by chloride functionalized ionosilica is higher than that by the sulfate analogue. During the

charging step of the thermochemical storage, higher charging temperatures are definitely not recommended: keeping heating the air flow at 393 K in a domestic space heating equipment will be difficult, as the cost of energy transfer and durability of the whole system have to be taken into consideration. If one tries to look at the weight loss at 353 K, which is a standard desorption temperature chosen for the silica gel material [11], DSM19, ISA8, and ISA100 have lost, respectively, 80.2%, 74.8%, and 71.4% of total physisorbed water. This temperature appears thus a good compromise for the thermal treatment of the samples when taking into account both the performance and the costs of the storage system. *Simultaneously, this is also the highest temperature acceptable in the flow calorimetry equipment*. Between the temperature of removal of physisorbed water (393 K) and decomposition of amines (483 K), the mass of the three samples continues to decrease but with a much slower rate. This suggests another mechanism to occur here, probably gradual dehydroxylation of the surface.

IV.3. Textural parameters of ionosilica materials

A series of gaseous N_2 adsorption was carried out on the three ionosilica samples in order to determine the specific surface area and pore size. These samples have been outgassed at 393 K under secondary vacuum for one night. The conditions of thermal treatment were determined based on the TGA analysis (c.f., Figure IV.3) and some previous work [4]. Unfortunately, only one of the three samples, namely ISA100, displays a non-negligible specific surface area of 85 $m^2 g^{-1}$. Compared with the specific surface areas in the range 390-860 $m^2 g^{-1}$ reported previously [1, 4,10], this result is greatly disappointing but not surprising if one takes into account that the porosity of the ionosilicas is mostly due to the use of structuring surfactant template during the synthesis. The isotherm for N_2 adsorption-desorption onto ISA100 shows a clear hysteresis loop (c.f., Figure II.8) of type H2 according to the IUPAC classification [12]. The pore diameter is calculated by using the BJH method applied to the

adsorption branch of the isotherm. The surface area and pore size parameters have been collected in Table IV.1. The pore size is about 3 nm which matches well with the result obtained from the TEM micrographs. The TEM observations also confirm non-porous aspect of the DSM19 and ISA8 samples.

Material	ISA100
BET Analysis	
S_{BET} ($m^2 g^{-1}$)	85.0
C_{BET}	109.8
BJH Distribution	
V_{pore} ($cm^3 g^{-1}$)	0.03
d_{pore} (nm)	3.0

Table IV. 1*: Surface area and pore size parameters obtained from appropriate BET and BJH processing of the gaseous N_2 adsorption isotherms for ISA100*

IV.4. Microscopic observation of the behaviour of the ionosilica samples in the presence of water vapour

A macroscopic scale visualization of the 'dynamic' behaviour of the three samples submitted to low pressures of water vapour from 200 Pa to 710 Pa has been done with the aid of an environmental scanning electron microscope (ESEM). As described in Chapter II, the relative humidity in the ESEM chamber is adjusted via the variation of the pressure inside, with a temperature fixed at 275 K in the present study [13]. It has been chosen to operate in this way in order to get an appropriate resolution of microscope images. Since the volume of the chamber is very large compared to that of the sample, operating under vapour pressures above 6 Torr (800 Pa) makes image optimization difficult. Moreover, it takes more time to arrive at the equilibrium state, according to several tests that have been performed. The images are shown in Figure IV.4.

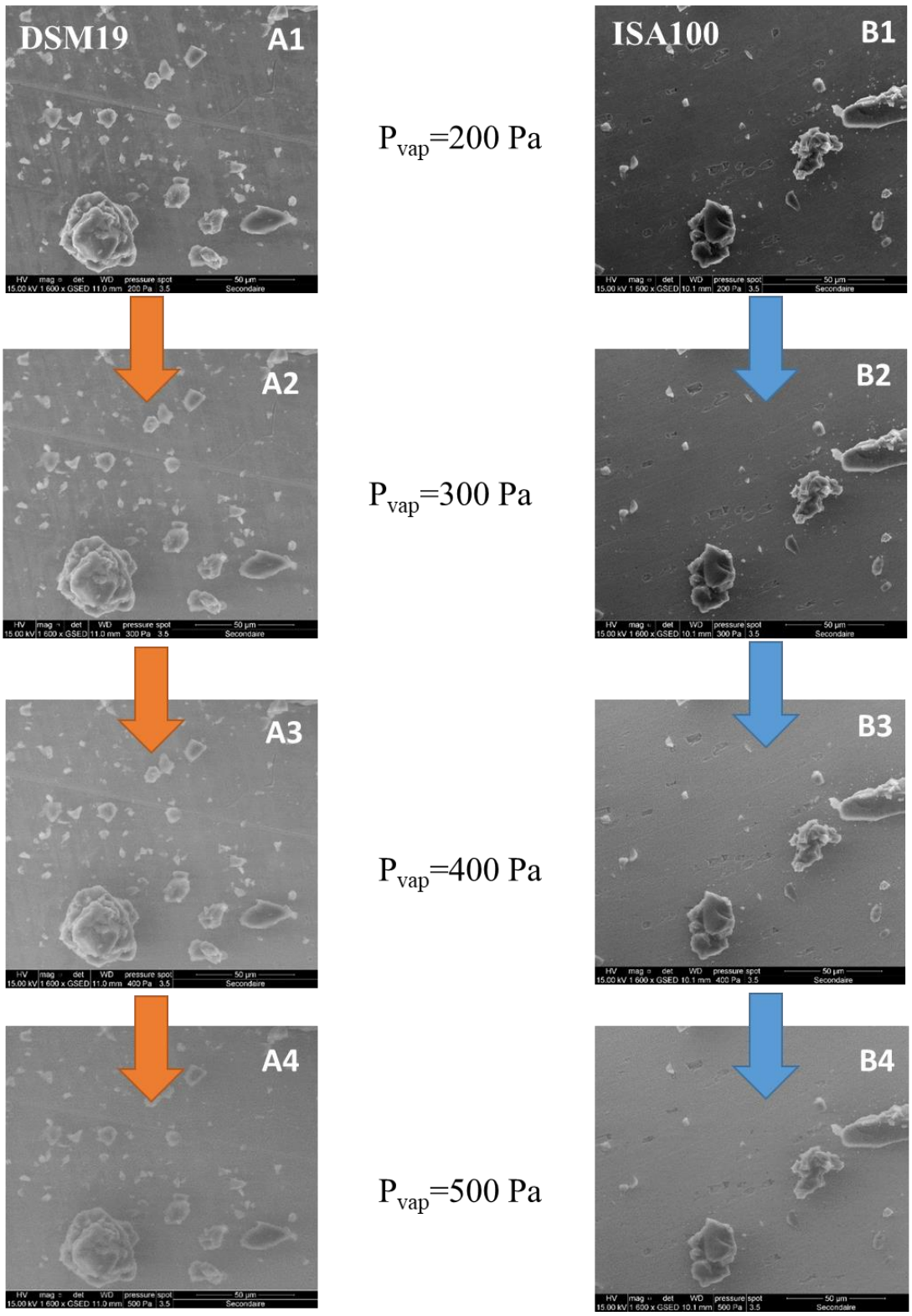
DSM19
A1
ISA100
B1
P_{vap}=200 Pa
A2
B2
P_{vap}=300 Pa
A3
B3
P_{vap}=400 Pa
A4
B4
P_{vap}=500 Pa

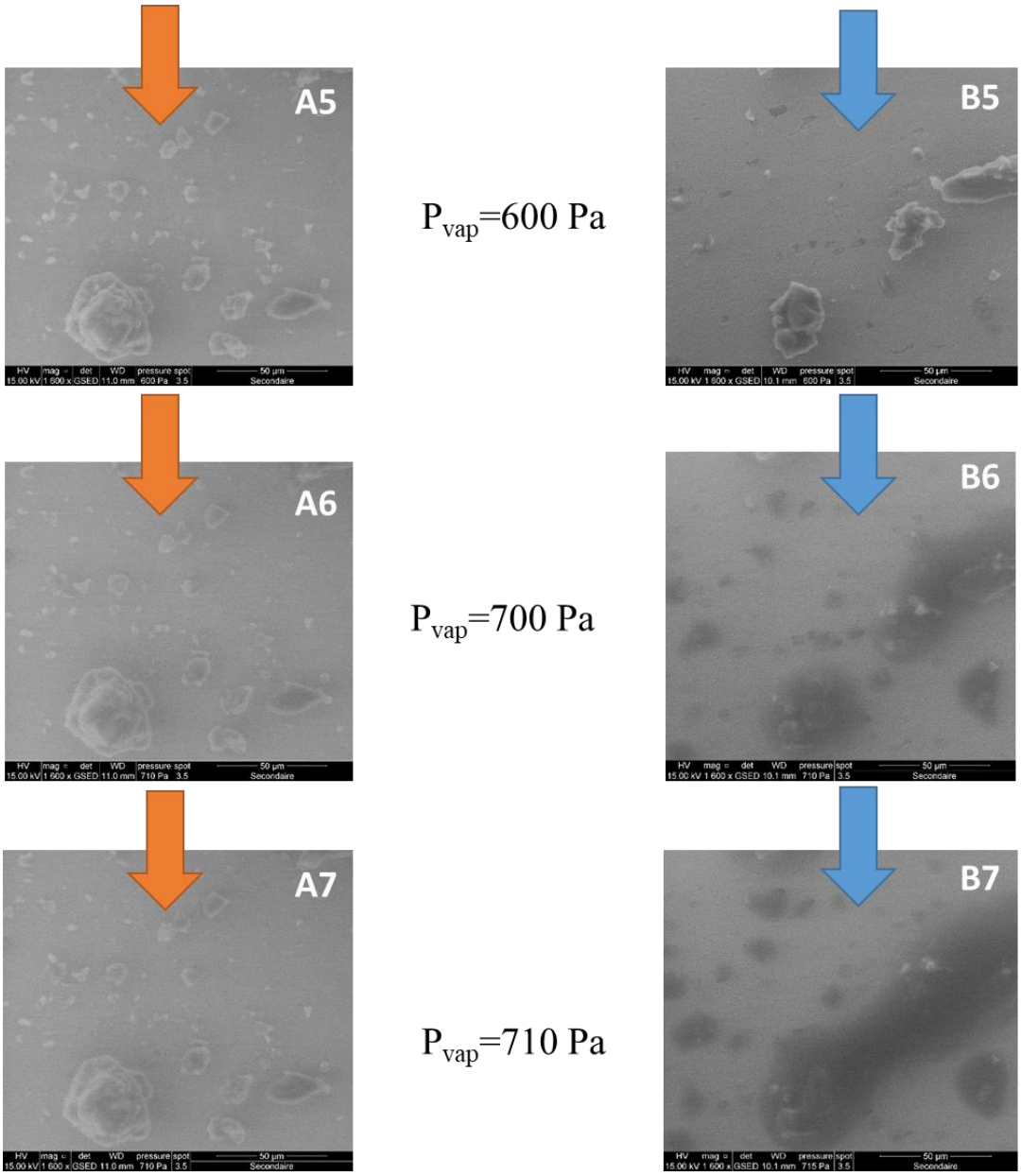

Figure IV. 4*: SEME images of ionosilices submitted to increasing pressure of water vapour (200 Pa, 300 Pa, 400 Pa, 500 Pa, 600 Pa, 700 Pa, and 710Pa). Left panels A1-A7: DSM19 with* Cl^- *counter-ions; right panels B1-B7: ISA100 with* SO_4^{2-} *counter-ions.*

A comparison of hydrophilic-hydrophobic behaviour at a microscopic scale is finally done for two ionosilicas having different compensating anions (Cl^- or SO_4^{2-}) by submitting them into the same water vapour environment under pressures varying from 200 Pa to 710 Pa. The dark shadow surrounding the particles shown in Fig.IV.4 corresponds to the water molecules which have been confined in the vicinity of the ionosilica surface. At lower pressures from 200-500 Pa, one can monitor the adsorption process by following the progressive loss of image

resolution on the edge of the particle images. This indicates that the adsorption of water vapour onto ionosilicas starts with a moderate rate when compared to the highly hydrophilic zeolite. As the pressure of water vapour increases, one can clearly observe different amounts of water molecules surrounding the ionosilica particles. The ISA100 particles attract significantly more water than the DSM19 ones. The same observations have been done twice on the same particles and the same dynamic behaviour is monitored each time. This points out the influence of the various counter-ions presented in the ionosilica samples on the adsorption process. It seems likely that the modification of the polarizability of silica groups has an effect on the adsorption of such polar molecules like water. The sulfate functionalized ionosilica is therefore more hydrophilic than the ionosilica with chloride counter-anions. It is important to notice that, above P_{vap} = 700 Pa, ISA100 appears completely saturated with water molecules, which may indicate that the overall water adsorption capacity of ISA100 is lower than that of DSM19.

It is worth noting that some decomposition of ISA100 particles is observed starting from P_{vap}=700 Pa. Therefore, some irreversible deformation occurs in the supersaturation region. Certainly, this may affect the cycling resistance of the sample, as has been observed in further sorption tests where the ISA100 sample gives a slightly reduced heat of water adsorption after each adsorption-desorption cycle.

IV.5. Adsorption properties of ionosilica materials towards water vapour

The adsorption–desorption isotherms for water vapour on the three ionosilica materials at 313 K are plotted in Figure IV.5. Activation of all three samples was carried out at 353 K during 8 h under a secondary vacuum.

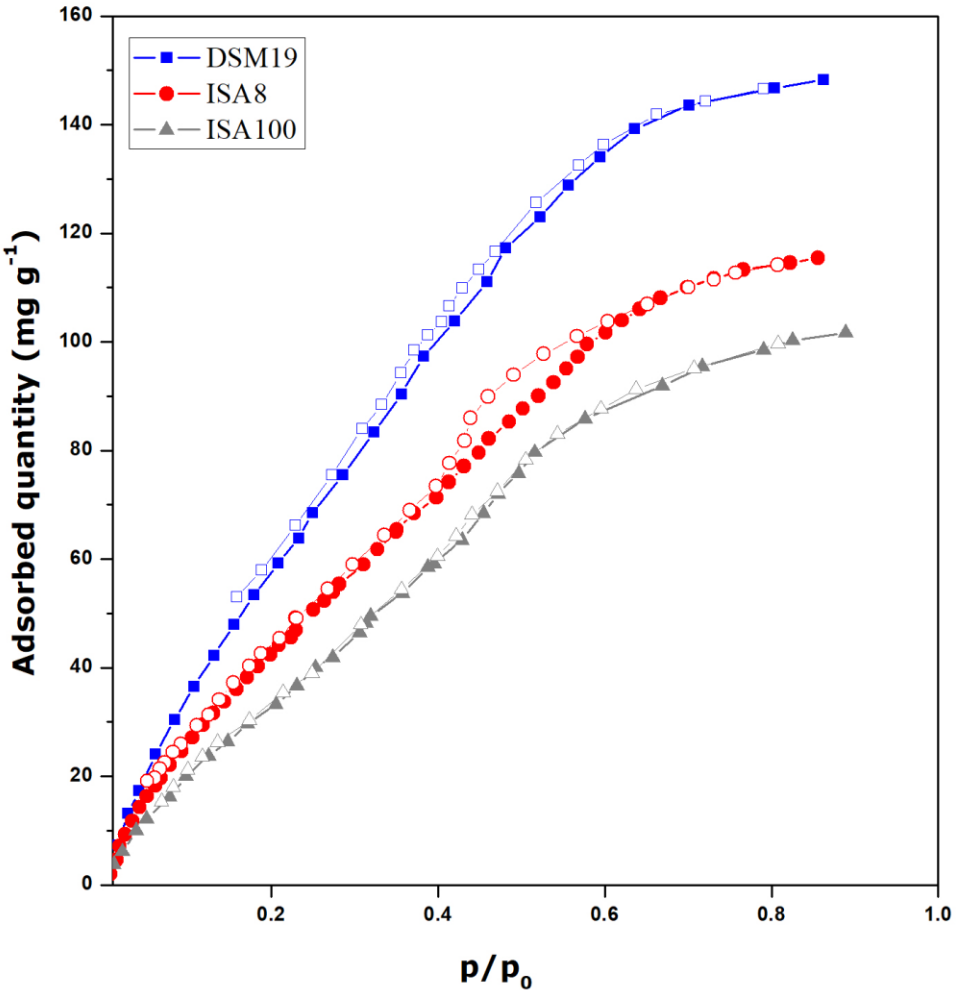

Figure IV. 5*: Adsorption-desorption isotherms for water vapour determined on DSM19, ISA8 and ISA100 at 313 K. The filled and empty symbols correspond to the adsorption and desorption data, respectively.*

The adsorption curves represent a mixture of Type II and Type IV isotherms according to the IUPAC classification [14,15] which suggests that the adsorption occurs in the form of a multilayer formation. No sharp increase in the water uptake is found on any isotherm curve until the surface saturation. This indicates that the ionosilica is characterised by a moderate water molecule-adsorbent interaction comparing to that of the zeolite. In the early stages of the adsorption process at low relative pressures, the three ionosilicas do not exhibit strong water uptake, which can be explained in two different ways: (i) the water molecule-adsorbent interaction on the ionosilica surface containing silanol-silane groups is weaker than the interaction of water molecules with compensating cations in the zeolite structure; (ii) the low

surface area of ionosilica is responsible for lower adsorption capacity. In the case of DSM19, the adsorption quantity increases almost linearly from the region of low relative pressures to higher pressure values of $p/p_0 = 0.6$. ISA8 and ISA100 exhibit a monolayer formation step at relative pressures lower than 0.05 but this feature does not show up very clearly. This indicates that the adsorption of water vapour onto DSM19 follows an unrestricted multilayer formation process due to its macroporosity and relatively weak adsorbate-adsorbent interaction. For ISA100, a slightly stepwise shape is observed after $p/p_0 = 0.4$, thereby suggesting a capillary condensation mechanism. For ISA8, capillary condensation occurs at around $p/p_0 = 0.4$-0.6, without showing a high adsorbate uptake. The hysteresis loops of type H2 indicate the existence of "ink bottle" type pores [14]. Surprisingly, no evident hysteresis loop is found on the isotherm curve for ISA100, whereas it appears on the gaseous N_2 adsorption-desorption isotherm.

The sorption capacity of the three ionosilica samples seems smaller than that of such zeolites as Ce-13X. In terms of total amount adsorbed, Ce2-13X can adsorb nearly 197 mg g^{-1} while DSM19, ISA8 and ISA100 adsorb 148 mg g^{-1}, 115 mg g^{-1} and 102 mg g^{-1}, respectively. Nevertheless, these differences become less significant if one takes into account the activation-regeneration temperatures of the samples: the ionosilicas may be activated at a lower temperature of 353 K, while a much higher temperature of 423 K is necessary to regenerate the Ce-13X sample.

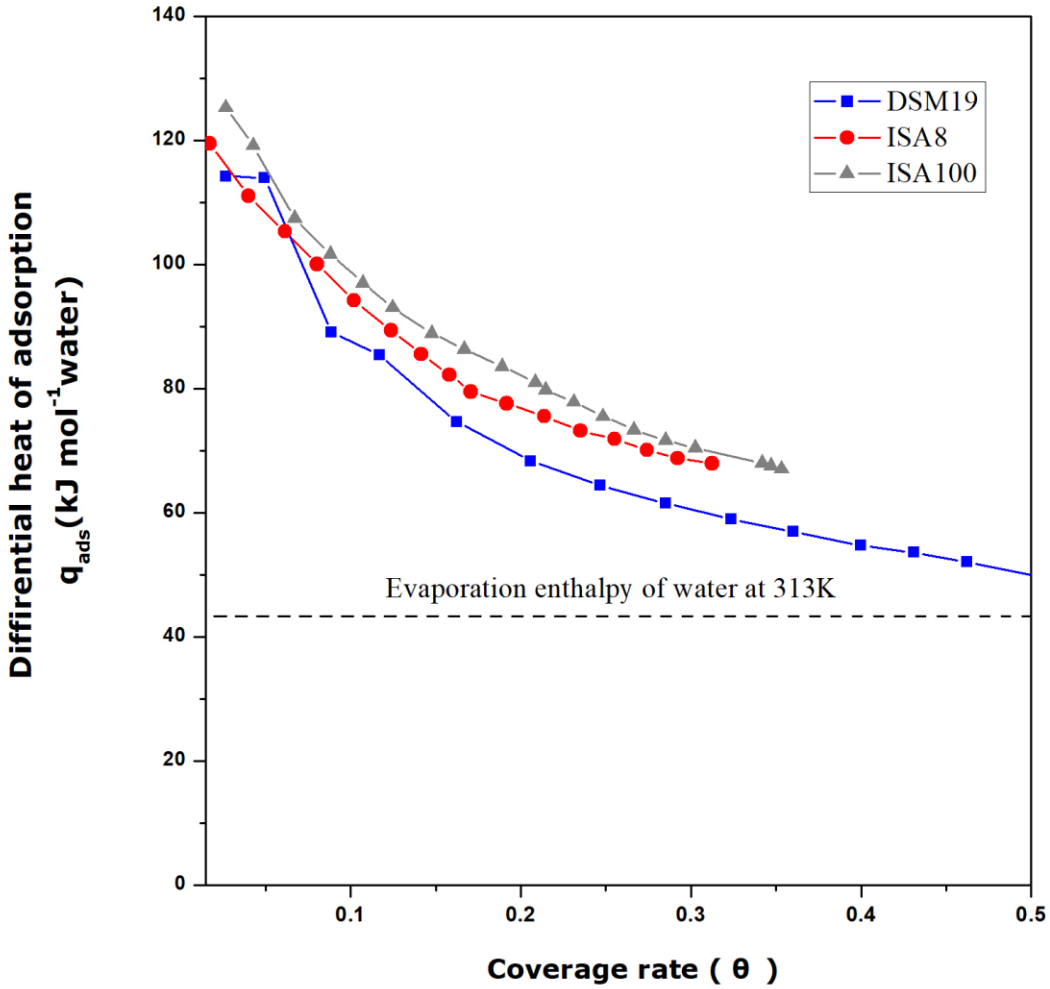

***Figure IV. 6**: Variations of the differential heat of adsorption for water vapour onto DSM19, ISA8, and ISA100 as a function of the surface coverage ratio at 313 K. The dashed line represents the evaporation enthalpy of water at 313 K.*

The differential heat of adsorption can be determined experimentally by coupling directly the calorimetry measurements with the adsorption measurements. The results are shown in Figure IV.6. As is mentioned in II.5 of previous chapter, the differential heat reflects the heat released upon adding an infinitesimal amount of the water vapour at a constant temperature. Although at zero surface coverage, the differential heat for the three samples is not as high as that obtained in the case of zeolite, the evolution of the heat release seems more kinetically suitable in view of the long-term heat storage. With increasing p/p_0 values, the differential heat of adsorption for ionosilica does not drop sharply like in the case of zeolite. Consequently, the heat release may be extended over longer time periods. A comparison of the

three heat curves leads to the following sequence of surface affinity towards water vapour at different surface coverage values: ISA100 >ISA8 >DSM19. This again reinforces our starting idea: sulfate anions possessing higher hydration enthalpy can yield higher heat values than those given by chloride anions during adsorption of water vapour.

Similar conclusions can be drawn from the calorimetry measurements of the integral heat of adsorption on the samples submitted to several cycles. The calorimetric studies have been carried out to test the sample performance in terms of heat release upon adsorption of water vapour at 296 K. Helium is used as a carrier gas to regenerate the samples, instead of vacuum pumping. Figure IV.7 shows the integral heat of adsorption recorded in three adsorption-desorption cycles. A significant improvement in the integral adsorption heat is observed after introducing sulfate anions into ionosilica sample. Indeed, the heat values increase in the following order: DSM19 < ISA8 < ISA100. Also a good cycling ability is found for the three ionosilica, although slight changes are observed in the case of ISA8 and ISA100. This can be caused by the decomposition of particles, as revealed before on the basis of ESEM observations.

Given the total energy released during the charging step of the thermochemical storage process, this weaker adsorbate-adsorbent interaction will lead to a smaller adsorption heat at low values of relative humidity. Theoretically, this could be a serious drawback for the utilization of ionosilica as THS materials. Nevertheless, this does not obviously mean that the ionosilica materials are not suitable THS materials or they are not as performant as zeolite materials. To understand this point, it is necessary to consider the materials in the context of the whole THS system by looking at this weaker adsorbate-adsorbent interaction from a technological viewpoint. During the charging step, a perfect control of drying and storage conditions is difficult to achieve, especially when an extra energy for pumping and/or the perfectly sealed equipment are needed. The drying of adsorbent requires a pre-heated air flow

with a low relative humidity. Then the dried adsorbent will be stored at ambient temperature from summer to winter under air containing a trace of water vapour. This means that the future discharging step starts at a relative pressure p/p_0 greater than 0. When taking into account only the real increase in the quantity of water adsorption during the discharging, the ionosilica materials appear more advantageous than the cation-exchanged zeolites. Indeed, the most exothermic adsorption of water vapour onto zeolite occurs at very low surface coverages that is before reaching the initial hydration stage of the discharging step.

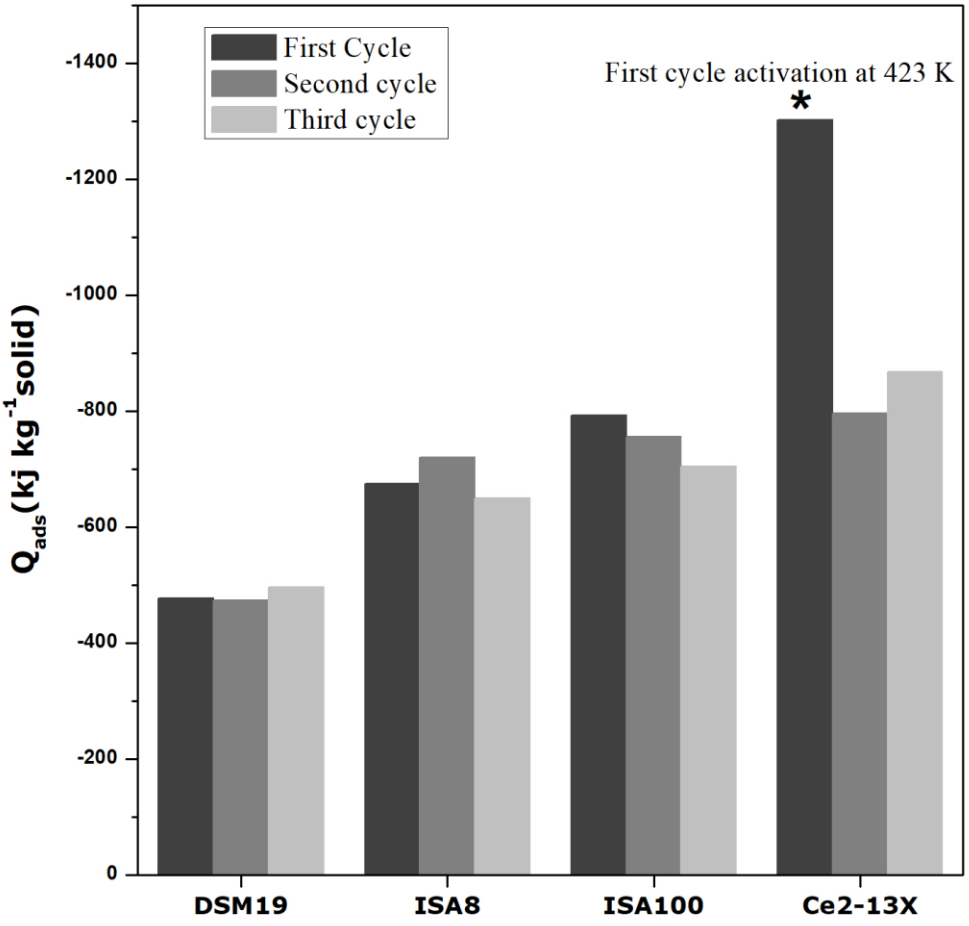

***Figure IV. 7**: Integral heats of adsorption for water vapour onto DSM19, ISA8, and ISA100 measured at 296 K under dynamic conditions during three consecutive cycles. Similar heat values obtained with Ce-exchanged FAU zeolite 13X are reported for comparison purposes.*

IV.6. Study of the mechanism of surface hydration for ionosilica

In order to investigate the adsorption mechanism for water vapour onto ionosilicas, a series of solid-state ^{29}Si NMR experiments has been performed. As mentioned in Chapter II, different signals of Q^n or T^m configurations can be recorded in the solid-state NMR experiments carried out on silica or functionalized silica materials. The main intention of the present study was to: (i) compare the contributions originating from different counter-ions to the hydration sequences on the surface of ionosilica, (ii) monitor the evolution at the microscopic level during the repeated hydration-dehydration cycles and verify their reversibility; (iii) propose a plausible hydration-dehydration mechanism for ionosilica.

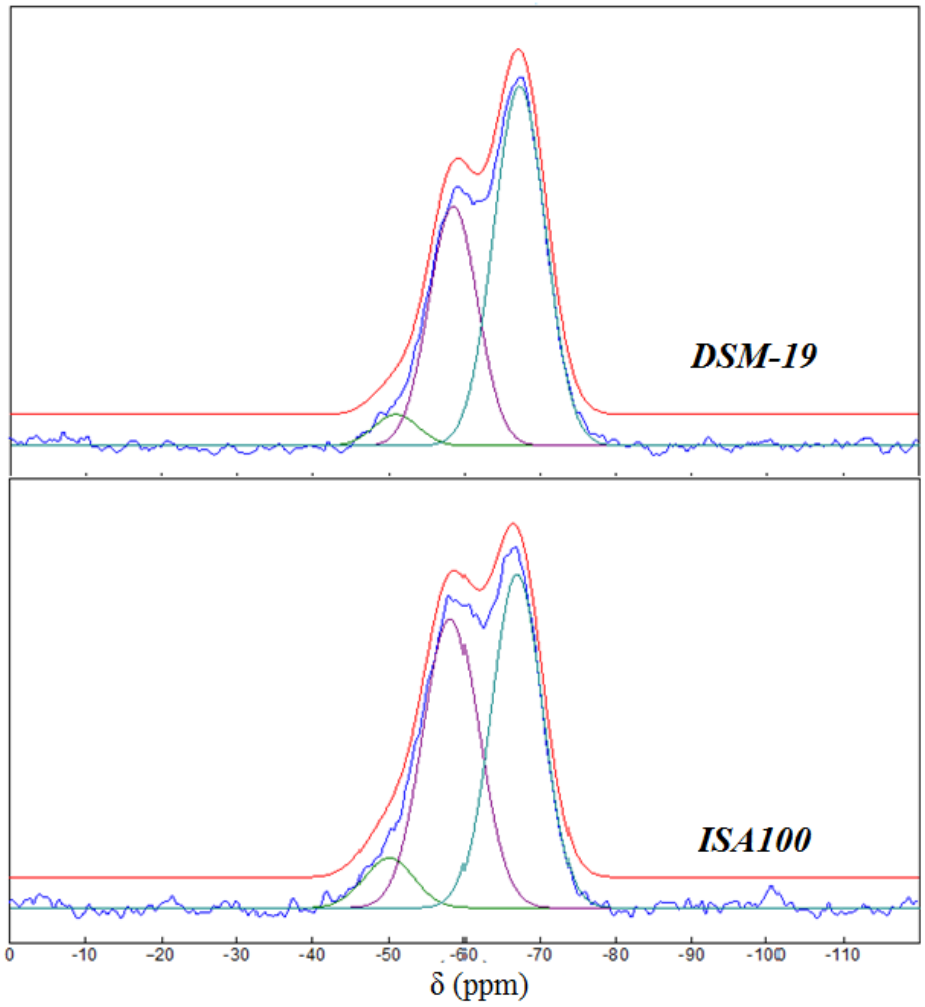

***Figure IV. 8**: ^{29}Si OP NMR spectra (blue) and their deconvolution (red) for DSM19 and ISA100 in the dry state*

Figure IV.8 shows the experimental ^{29}Si OP NMR spectra, as well as the simulated ones obtained by following the curve deconvolution procedure for DSM19 and ISA100 in the dry state. The ^{29}Si OP spectra have been recorded with 5 hours recycle delay which is sufficiently long for a quantitative analysis. The results of the curve deconvolution by using the Dmfit software (red lines) are also presented in Table IV.2. The curves associated with the T^1, T^2, and T^3 resonances at -50, -57, and about -67 ppm, respectively, are observed in both spectra. None of the Q^n resonances can be seen in the spectra which indicates that the ammonium groups remain within the bulk of the solid phase without being breaking down during the synthesis.

Attributions	DSM19			ISA100		
	Resonance position (ppm)	Relative integrals (%)	Resonance Width (ppm)	Resonance position (ppm)	Relative integrals (%)	Resonance Width (ppm)
T^1	-50.31	3.66	7.42	-50.12	7.04	7.76
T^2	-58.57	39.79	8.06	-58.25	44.72	8.56
T^3	-67.32	56.55	7.66	-66.90	48.25	8.00

***Table IV. 2**: Results of the deconvolution of the ^{29}Si OP NMR spectra for DSM19 and ISA100 in the dry state. The relative integrals represent the percentage of every peak intensity ($T^x/(T^1+T^2+T^3)$%), calculated from their decovoluted peak area; the resonance width is measured at half of maximum peak height which corresponds to the full width at half maximum, FWHM.*

The relative integrals corresponding to the initial samples are obtained by the spectra deconvolution for DSM19 and ISA100 dry samples, which have undergone the same outgassing procedure at 383 K under primary vacuum overnight. These results show clearly much difference between the proportions of various T units: more T^3 resonance is observed in DSM19, while the T^1 and T^2 resonances are visibly stronger in ISA100. This argues in favour of some intrinsic difference in the opening of the siloxane Si-O-Si bridge. The dry DSM19, which presents more T^3 units, has more rigorous Si-O-Si cross-linking. On the other hand, the dry ISA100 with a higher percentage of the T^1 and T^2 units, presents more germinal and isolated

silanol groups on the surface or within the bulk structure. Taking into account the hydrophobic character of a siloxane group and the hydrophilic character presented by the germinal and isolated silanol groups, as well as when comparing the percentage of T^m units in the two samples, one can suggest that the surface of ISA100 presents more hydrophilic character in the initial dry state.

The NMR OP spectra recorded on DSM19 and ISA100 after three consecutive hydration-dehydration cycles are shown in Figure IV.9. Firstly, there is much difference between the hydrated and dehydrated states in regards with the relative integrals and peak width. As can be seen from the results of the spectra deconvolution in Table IV.4, the T^3 resonance clearly decreases after sample hydration, while the T^1 and T^2 ones increase, which indicates that a transition from the T^3 substructure to the T^2 and T^1 silanol groups occurs during hydration. It is thus likely that the siloxane bridge of some highly condensed surface sites on ISA100 is opened by a hydroxylation mechanism, thus leading to the formation of Si-OH groups.

On the other hand, DSM19 sample does not appear to be much affected by hydration, especially with respect to the T^2 and T^3 configurations, which give the integrals being more or less the same before and after hydration. This is consistent with the previous conclusions drawn in the case of the dry samples: ISA100 ionosilica exhibits a more hydrophilic character. When it is surrounded by water molecules under a humid environment at 298 K, more siloxane bridges are opened and progressively form silanol groups, which results in a higher percentage of T^1 and T^2 signals than it is observed in the case of DSM19. Since the cross-linking of functionalized silicon chains is reduced on the surface, the chains being farther apart from one another, they gain greater freedom of movement, and thus greater mobility. DSM19 with a more crosslinked structure is more stable, and thus more resistant to water. Indeed, the detailed analysis of the OP NMR spectra recorded on the two ionosilica samples confirms this

conclusion: generally in the solid-state NMR experiment, the increase in the mobility of a nucleus implies a refinement of the peak width, which yields a better spectral resolution. That is why much refinement of the resonance peaks can be seen upon sample hydration. The deconvolution of the resulting spectra leads to the following conclusions:

- There is much variation among the T^1, T^2, and T^3 substructural units upon hydration.
- The resonance width of the T^3 unit decreases by 13-16 % (except for the third hydration cycle onto ISA100), which is the smallest change among those recorded for the three substructure units; this means that the T^3 substructural unit is the least sensible to water molecules, probably due to the strong cross-linking of the chains.
- The T^2 unit decreases by 19-28 %, thus indicating more sensitivity of T^2 upon hydration due to the increased chain mobility.
- The T^1 unit decreases by 21-35%, which means that it is the most sensitive among the three substructures to water molecules.
- The signal intensity, especially that for T^2 and T^3, remains almost unchanged before and after hydration, which may mean that the crosslinking structure of DSM19 is more stable, more resistant to water.

Furthermore, the cycling resistance of ionosilicas has been tested in the three consecutive hydration-dehydration cycles. In the case of DSM19, the three OP NMR spectra of the hydrated samples are quasi-superimposed and so are the three spectra of the dehydrated samples; no notable change is found which confirms a good cycling stability. This stability may be advantageous in the heat storage uses. ISA100 exhibits some undesired dynamics of changes upon three hydration-dehydration cycles, with the T^3 units increasing and the T^2 and T^1 units decreasing along the cycles. This evolution will slightly and progressively reduce the hydrophilic character of its surface, as supported by the results of calorimetric measurements of the integral heat of adsorption in Fig IV.7.

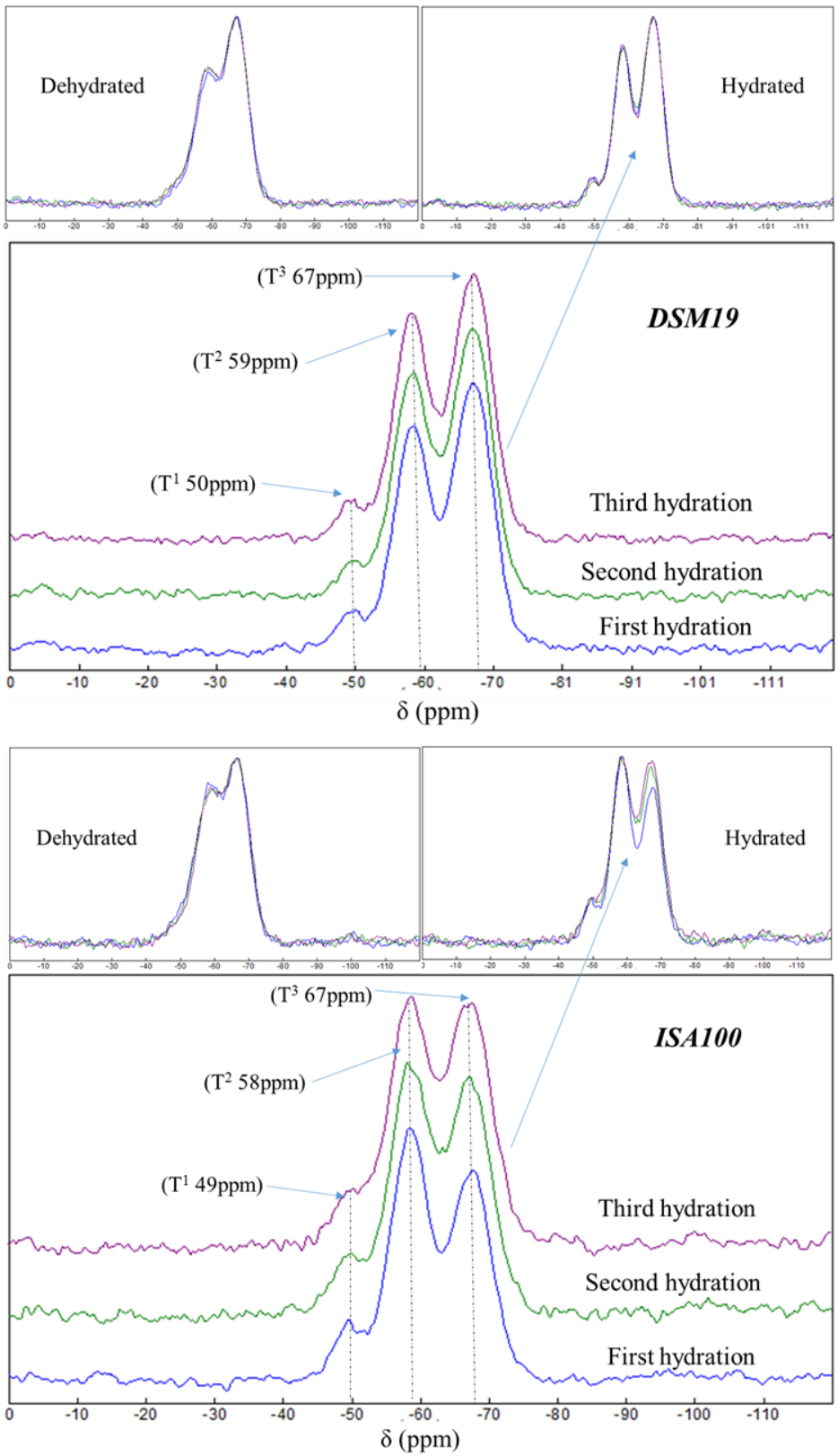

***Figure IV. 9**: [29]Si OP NMR spectra recorded on DSM19 and ISA100 submitted to three consecutive hydration-dehydration cycles.*

Sample	Attributions	Resonance position δ (ppm)	FWHM (ppm)	Relative intensity (%)
DSM19	T^1	-50.3	7.4	3.7
1st dehydration	T^2	-58.6	8.1	39.8
	T^3	-67.3	7.7	56.5
DSM19	T^1	-50.1	5.5 (-26%)	5.3
1st hydration	T^2	-58.5	6.1 (-25%)	40.7
	T^3	-67.4	6.7 (-13%)	54.0
DSM19	T^1	-50.3	8.0	5.8
2nd dehydration	T^2	-58.6	8.1	40.3
	T^3	-67.3	7.7	53.9
DSM19	T^1	-49.7	5.4 (-33%)	6.2
2nd hydration	T^2	-58.5	5.8 (-28%)	40.4
	T^3	-67.5	6.5 (-16%)	53.4
DSM19	T^1	-50.1	7.9	5.3
3rd dehydration	T^2	-58.5	8.0	40.2
	T^3	-67.3	7.7	54.5
DSM19	T^1	-49.9	5.4 (-32%)	5.9
3rd hydration	T^2	-58.5	6.1 (-24%)	40.2
	T^3	-67.4	6.7 (-14%)	53.9

Table IV. 3*: Results of the deconvolution of ^{29}Si OP NMR spectra recorded on DSM19 submitted to three consecutive hydration-dehydration cycles (percentage in the parenthesis corresponds to the decrease after sample hydration)*

Sample	Attributions	Resonance position δ (ppm)	FWHM (ppm)	Relative intensity (%)
ISA100	T^1	-50.1	7.8	7.0
1st dehydration	T^2	-58.3	8.6	44.7
	T^3	-66.9	8.0	48.3
ISA100	T^1	-49.3	5.4 (-31%)	8.4
1st hydration	T^2	-58.4	6.6 (-23%)	48.8
	T^3	-67.4	6.9 (-14%)	42.8
ISA100	T^1	-50.1	7.8	5.9
2nd dehydration	T^2	-58.3	8.6	43.9
	T^3	-66.9	8.0	50.2
ISA100	T^1	-49.6	5.4 (-31%)	9.0
2nd hydration	T^2	-58.5	6.6 (-23%)	45.9
	T^3	-67.3	6.9 (-14%)	45.1
ISA100	T^1	-50.1	7.8	4.5
3rd dehydration	T^2	-58.3	8.6	44.3
	T^3	-66.9	8.0	51.2
ISA100	T^1	-49.7	6.2 (-21%)	8.7
3rd hydration	T^2	-58.3	7.0 (-19%)	43.5
	T^3	-67.3	7.6 (-5%)	47.8

***Table IV. 4**: Results of the deconvolution of ^{29}Si OP NMR spectra recorded on ISA100 submitted to three consecutive hydration-dehydration cycles (percentage in the parenthesis corresponds to the decrease after sample hydration)*

Following the mechanism of surface dehydration on pure amorphous silicas proposed by Zhuravlev [16], this process can be divided into two different stages: (i) the removal of physisorbed water molecules which interact with the hydroxyl groups in the silica surface through two different hydrogen bonds, (ii) the surface dehydroxylation, thus resulting in the condensation of the neighbouring silanol groups and the formation of more stable siloxane bridges. Nevertheless, the present case is not completely consistent with this model because of the influence of the various functional groups and counter-ions, as evidenced by the results of

adsorption and NMR studies. In accordance with the discussion by Castillo *et al.* about the importance of the polarizability in the arrangement of adsorbed molecules in zeolites [17], and taking into account that the polarizability of SO_4^{2-} (average of 7 $Å^3$) is higher than that of Cl^- (average of 5.49 $Å^3$) [18,19], it seems quite plausible that the polarizability of the combination of amino-functional groups with different counter-ions is an important factor in adjusting the hydrophilic-hydrophobic surface character of ionosilica samples.

In light of the results of all experimental studies done on the ionosilica samples, the following hydration-dehydration sequences can be proposed; they are schematically presented in Fig.IV.10:

1) The surface of ionosilica at room temperature contains both silanol (isolated, germinal and vicinal) and siloxane groups.

2) During the first stage of adsorption process, water molecules start to adsorb on the OH groups via the H-bond and this exothermic process is accompanied by the heat release [20]; since this interaction is relatively weak and also because of the low surface area, water is retained to a moderate degree and with a quite slow kinetics; simultaneously, water molecules start to open the siloxane bridges by a hydroxylation reaction.

3) The so-opened hydrophobic siloxane bridges turn into hydrophilic silanol groups and they continue to adsorb water molecules, thereby enhancing the hydrophilic character of the surface.

4) When the dehydration begins, the physisorbed water leaves the surface as being retained by weak H-bonding.

5) The desorption is then followed by a surface dehydroxylation, which starts to take place at a lower temperature of around 353 K in comparison with other reported amorphous silicas [16,21]; the decreased dehydroxylation temperature, which finally depends on the nature of compensating counter-ions, is viewed as an advantage for the THS technology.

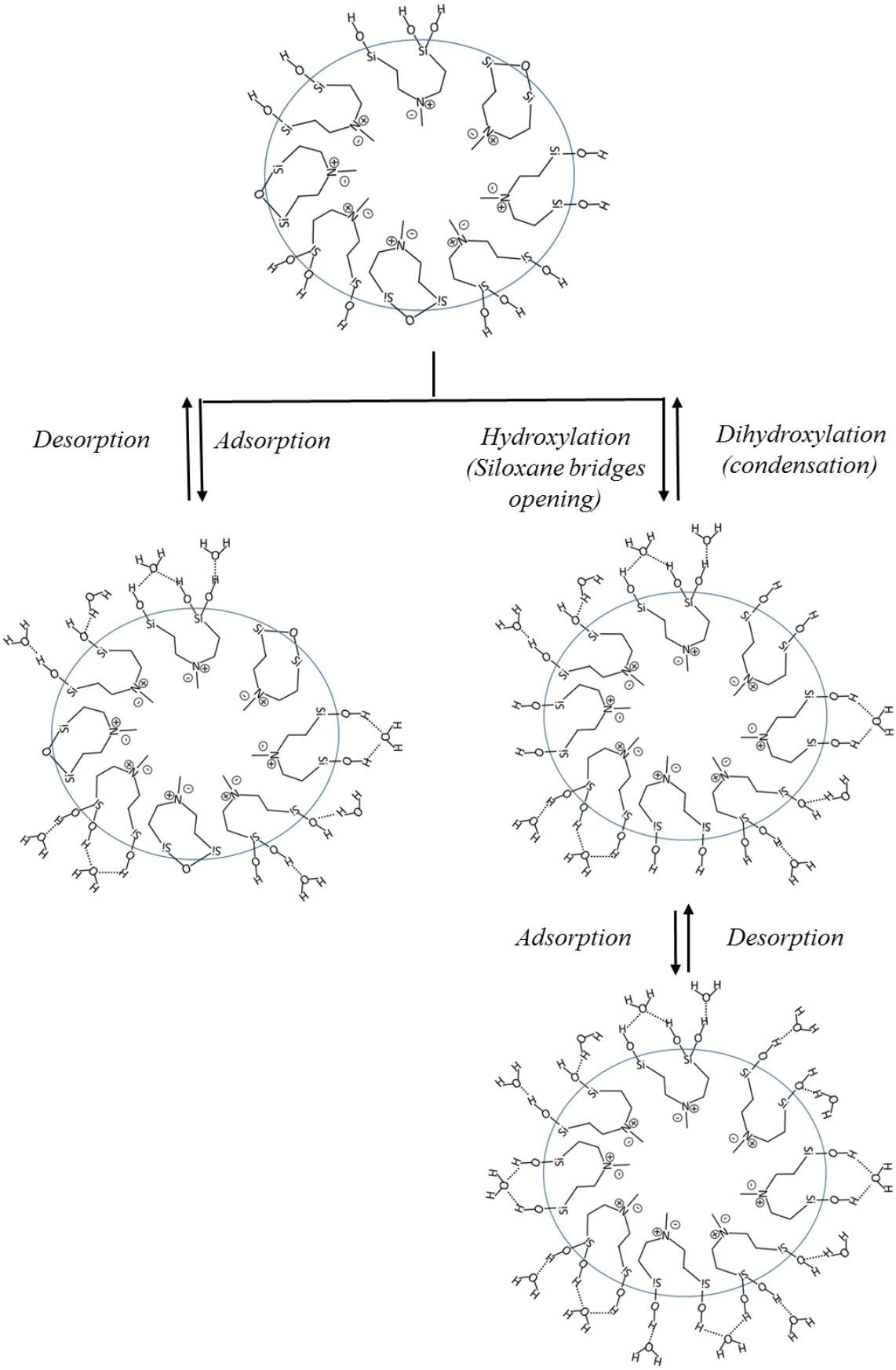

***Figure IV. 10**: Scheme showing the various stages of hydration-dehydration of ionosilica samples*

IV.7. Conclusions

In this chapter, the potential of ionosilica materials for the long term heat storage uses has been discussed. Three ionosilica samples containing ammonium moieties and different counter-ions (Cl^-, SO_4^2 as well as a mixture of Cl^- and SO_4^{2-}) obtained by functionalization via acid protonation or anion exchange were tested in adsorption experiments carried out under either static or dynamic conditions. The main conclusions drawn from these studies can be summarised as follows:

- Although possessing a weakly developed porous structure, ionosilica can provide heat of adsorption in the order of 700 to 800 kJ per kg of solid, and this heat may be obtained after a relatively mild regeneration, i.e., heating at 353 K under He flow, instead of vacuum treatment at 423 K.
- The ionosilica exhibits a good reversibility during a few repeated hydration-dehydration tests (at least up to 3 cycles) and the heat release is extended over several hours, which may be a great asset for thermochemical storage uses.
- The solid-state ^{29}Si NMR provides strong evidence that the siloxane bridges on the sulfate functionalized ionosilica ISA100 are easier to be opened and transformed into silanol groups, thereby imparting a more hydrophilic character to the surface; the polarizability of the counter-ion thus appears an import factor in adjusting the hydrophobic-hydrophilic surface balance; the higher hydration enthalpy of sulfate anions is also expected to enhance the heat released during the adsorption of water vapour and, consequently, the amount of energy stored per unit mass of the adsorbent.
- The hydration sequence of ionosilica includes one important step of reversible hydroxylation, which allows the adsorbent to adjust its adsorption properties when passing from the state of low relative pressures of water vapour to the state of high hydration values;

this switching between the hydrophobic and hydrophilic character of the surface is to be considered as being advantageous for the long term heat storage.

References

[1] Braun, M.; Thach, U.D.; Prelot, B.; Hesemann, P.; Esposito, D. Pd@ionosilica as heterogeneous hydrogenation catalyst for continuous flow reductive upgrade of cinnamaldehyde. J. Chem. Technol. Biotechnol. 2017, 92, 2229–2235 DOI:10.1002/jctb.5278.

[2] Bouchal, R.; Miletto, I.; Thach, U.D.; Prelot, B.; Berlier, G.; Hesemann, P. Ionosilicas as efficient adsorbents for the separation of diclofenac and sulindac from aqueous media. New J. Chem. 2016, 40, 7620–7626 DOI:10.1039/C6NJ01473A.

[3] Thach, U.D.; Prelot, B.; Pellet-Rostaing, S.; Zajac, J.; Hesemann, P. Surface properties and chemical constitution as crucial parameters for the sorption properties of ionosilicas: The case of chromate adsorption. ACS Appl. Nano Mater. 2018, 1, 2076–2087 DOI:10.1080/10668926.2011.567155.

[4] Thach, U.D.; Trens, P.; Prelot, B.; Zajac, J.; Hesemann, P. Tuning the interfacial properties of mesoporous ionosilicas: Effect of cationic precursor and counter anion. J. Phys. Chem. C 2016, 120, 27412–27421 DOI:10.1021/acs.jpcc.6b09457.

[5] Nguyen, T.P.; Hesemann, P.; Linh Tran, T.M.; Moreau, J.J.E. Nanostructured polysilsesquioxanes bearing amine and ammonium groups by micelle templating using anionic surfactants. J. Mater. Chem. 2010, 20, 3910 DOI:10.1039/b925352a.

[6] Chukin, G.D.; Malevich, V.I. Infrared spectra of silica. J. Appl. Spectrosc. 1977, 26, 223–229 DOI:https://doi.org/10.1007/BF00615613.

[7] Tsyganenko, A.A.; Storozheva, E.N.; Manoilova, O. V; Lesage, T.; Daturi, M.; Lavalley, J.C. Brønsted acidity of silica silanol groups induced by adsorption of acids. Catal. Lett. 2000, 70, 159–163 DOI:10.1023/A:1018845519727.

[8] Czuchajowski, L.; Duraj, S.; Kucharska, M. Vibrational studies of Na_2SO_4, K_2SO_4, $NaHSO_4$ and $KHSO_4$ crystals. Rasayan J. Chem. 2009, 2, 981–989 DOI:10.1016/0022-2860(76)82004-2.

[9] Database of ATR-FT-IR spectra of various materials : ATR-FT-IR spectra of Sodium sulphate (Na_2SO_4) http://lisa.chem.ut.ee/IR_spectra/paint/fillers/sodium-sulphate/ (accessed on Mar 9, 2018).

[10] Thach, U.D.; Hesemann, P.; Yang, G.; Geneste, A.; Le Caër, S.; Prelot, B. Ionosilicas as efficient sorbents for anionic contaminants: Radiolytic stability and ion capacity. J. Colloid Interface Sci. 2016, 482, 233–239 DOI:10.1016/j.jcis.2016.07.069.

[11] Sapienza, A.; Velte, A.; Girnik, I.; Frazzica, A.; Füldner, G.; Schnabel, L.; Aristov, Y. "Water - Silica Siogel" working pair for adsorption chillers: Adsorption equilibrium and dynamics. Renew. Energy 2017, 110, 40–46 DOI:10.1016/j.renene.2016.09.065.

[12] Stafford, K.; Sing, W. Physisorption hysteresis loops and the characterization of nanoporous physisorption hysteresis loops and the characterization of nanoporous materials. Adsorpt. Sci. Technol. 2004, 22 DOI:10.1260/0263617053499032.

[13] G. MONTES-HERNANDEZ, PhD thesis: Etude expérimentale de la sorption d'eau et du gonflement des argiles par microscopie électronique à balayage environnementale (ESEM) et analyse digitale d'images. Université Louis Pasteur de Strasbourg, 2002.

[14] Thommes, M.; Kaneko, K.; Neimark, A. V.; Olivier, J.P.; Rodriguez-Reinoso, F.; Rouquerol, J.; Sing, K.S.W. Physisorption of gases, with special reference to the evaluation of surface area and pore size distribution (IUPAC Technical Report). Pure Appl. Chem. 2015, 87, 1051–1069 DOI:10.1515/pac-2014-1117.

[15] Rouquerol, J.; Avnir, D.; Fairbridge, C.W.; Everett, D.H.; Haynes, J.M.; Pernicone, N.; Ramsay, J.D.F.; Sing, K.S.W.; Unger, K.K. Recommendations for the characterization of porous solids. Pure Appl. Chem. 1994, 66, 1739–1758

DOI:10.1351/pac199466081739.

[16] Zhuravlev, L.T. The surface chemistry of amorphous silica. Zhuravlev model. Colloids Surfaces A Physicochem. Eng. Asp. 2000, 173, 1–38 DOI:10.1016/S0927-7757(00)00556-2.

[17] Castillo, J.M.; Silvestre-Albero, J.; Rodriguez-Reinoso, F.; Vlugt, T.J.H.; Calero, S. Water adsorption in hydrophilic zeolites: Experiment and simulation. Phys. Chem. Chem. Phys. 2013, 15, 17374–17382 DOI:10.1039/c3cp52910j.

[18] Jungwirth, P.; Tobias, D.J. Chloride anion on aqueous clusters, at the air - Water interface, and in liquid water: Solvent effects on Cl- polarizability. J. Phys. Chem. A 2002, 106, 379–383 DOI:10.1021/jp012059d.

[19] Jungwirth, P.; Curtis, J.E.; Tobias, D.J. Polarizability and aqueous solvation of the sulfate dianion. Chem. Phys. Lett. 2003, 367, 704–710 DOI:10.1016/S0009-2614(02)01782-7.

[20] Mischler, C.; Horbach, J.; Kob, W.; Binder, K. Water adsorption on amorphous silica surfaces: A Car-Parrinello simulation study. J. Phys. Condens. Matter 2005, 17, 4005–4013 DOI:10.1088/0953-8984/17/26/001.

[21] Zhuravlev, L.T. Structurally bound water and surface characterization of amorphous silica. Pure Appl. Chem. 1989, 61, 1969–1976 DOI:10.1351/pac198961111969.

Chapter V

Towards testing the thermal performance of adsorbents under conditions close to those of their practical use in the thermochemical storage units

The selected materials for long-term thermochemical storage, namely ion-exchanged FAU zeolite (Ce-13X) and ionosilicas (DSM19, ISA8 and ISA100), have previously been analysed using various micro- and mesoscopic scale characterization techniques to evaluate their capacity to adsorb water vapour and to reversibly release heat when subjected to drying-hydration cycles. The objective of the present chapter is to describe a laboratory-scale test-rig, developed during the PhD thesis, which has been envisaged for evaluating the thermal performance of adsorbents under flow conditions. The results of the tests are reported and discussed with the aim of characterizing the heat storage materials under more realistic conditions of use, which may allow, in the future, the low-temperature thermochemical heat storage by sorption to be implemented into domestic space heating.

As discussed in the previous chapters, the two types of materials have promising properties as heat storage materials. In this chapter, the advantages of each material to progressively release heat are emphasised owing to appropriate kinetic studies of the heat evolution pattern during adsorption of water vapour. Afterwards, the results of a preliminary study of the temperature lift during adsorption of water vapour by commercial 13X zeolite under conditions of a gas flow are presented. Some physical factors crucial for the optimisation of the heat release process under real operating conditions are revealed. Due to delayed delivery of the equipment which, in turn, caused an important delay in the assembling of the test-rig, on the one hand, and unavailability of samples in quantities sufficient for laboratory-scale testing, on the other hand, it has been impossible to repeat the optimised experiments for ion-exchanged materials.

V.1. Different modes of heat transfer and modelling of the discharging step

In a thermochemical storage system based on water adsorption from the gas phase, the reactor is the site where charging (water vapour desorption) and discharging (water vapour sorption) stages are performed. Apart from the most important factor which is the adsorbing (i.e., storing) material, several other parameters can influence the thermal performance of the storing process. In order to ensure the complete transfer of the heat released during the adsorption step to the flowing carrier gas, and thus to maximally limit the heat loss, the thermal conductivity of the material used for the construction of the reactor and the rate of gas flow should be looked upon critically.

According to the literature of the subject, the following fundamental modes of thermal transfer may be encountered in different systems [1–3]:

i) **Thermal convection**: a heat transfer between a solid and a fluid (liquid, gas) phase; it is related to the movement of the fluid, and thus to a material transport:

$$q_{convection} = h \cdot A \cdot \Delta T \qquad (V.1)$$

Where

$q_{convection}$ is the heat flow in the direction of heat transfer by convection (W);

h is the coefficient of convection heat transfer (W m^{-2} K^{-1}) ;

A is the area through which heat flows (m^2);

ΔT is the temperature variation (K).

ii) **Thermal conduction**: a direct transfer within a material medium, which is done by propagation of heat; the thermal agitation movement (heat flow) always goes from hot to cold areas:

$$q_{conduction} = -k \cdot A \cdot \frac{\Delta T}{L} \quad (V.2)$$

Where

k is the thermal conductivity of the material medium (W m^{-2} K^{-1});

L is the length (m) of the reactor in the direction of a heat flow.

iii) **Thermal radiation**: an emission of electromagnetic radiation by a hot body; the electromagnetic energy received by the system is absorbed and converted into heat:

$$q_{radiation} = A \cdot \sigma(T_h^4 - T_c^4) \quad (V.3)$$

Where

σ is the Boltzmann constant, $5.669 \cdot 10^{-8}$ W m^{-2} K^{-4};

T_h and T_c are the hot and cold body temperatures respectively.

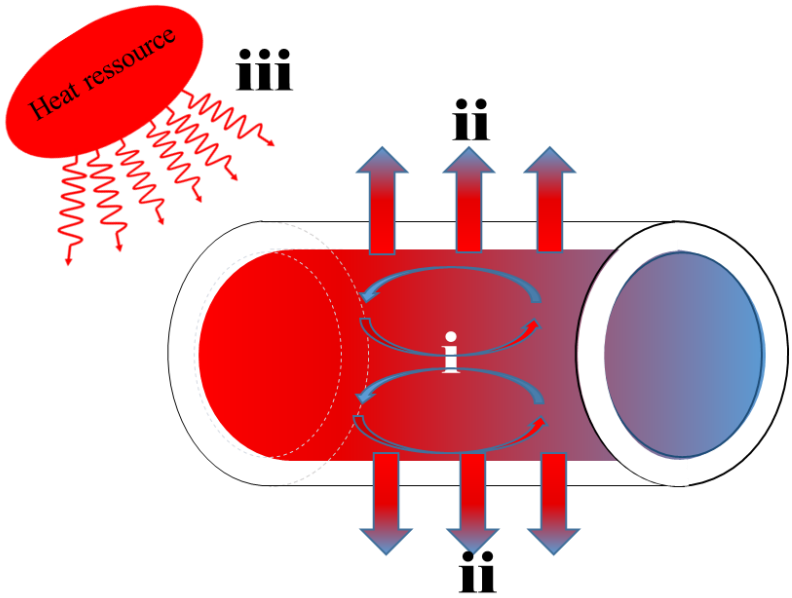

Figure V. 1*: Illustrative scheme of the principal mechanisms of heat transfer: i) thermal convection; ii) thermal conduction; iii) thermal radiation.*

In the case of the present adsorption tests in a storage reactor, there is no source for the emission of electromagnetic radiation. Therefore, this term may be neglected and only the convection and conduction ones should be taken into account, especially because they can occur simultaneously.

Using the thermal resistance approach [4], heat flow q can be written as follows:

$$q = \frac{T_i - T_e}{R_t} \qquad (V.4)$$

Where

T_i and T_e are the temperatures (K) of the gas inflowing to and outflowing from the reactor, respectively;

R_t is total thermal resistance (K W^{-1}) of the reactor.

The total thermal resistance R_t can be expressed in the following way:

$$R_t = (R_t)_{internal\ convection} + (R_t)_{conduction} + (R_t)_{external\ convection} \quad (V.5)$$

With the thermal resistances of internal and external convection:

$$(R_t)_{internal\ convection} = \frac{1}{h_i A_i} \quad (V.6)$$

$$(R_t)_{external\ convection} = \frac{1}{h_o A_o} \quad (V.7)$$

Where

h_i and h_o are convection heat transfer coefficients (W m^{-2} K^{-1}) of internal and external convection, respectively.

$$(R_t)_{conduction} = \frac{ln(\frac{r_o}{r_i})}{2\pi kL} \quad (V.8)$$

Where

k is the thermal conductivity (W m^{-2} K^{-1});

L is the length of the reactor (m);

r_i and r_o are inner and outer radius of the reactor, respectively.

The unknown parameters here are convection heat transfer coefficients h_i and h_o. The determination of the heat transfer coefficients due to convection is complicated because of the movement of water vapour. To solve the problem requiring the calculation of heat transfer coefficients for convection, the use of empirical correlations involving several dimensionless numbers (i.e., Reynolds number *Re*, Nusselt number *Nu*, and Prandtl number *Pr*) is proposed.

The Reynolds number provides an indication of the inertial and viscous forces present in a fluid. It is necessary to determine it if the gas flow inside the reactor is laminar, transitional

or turbulent. This information allows us to select an appropriate empirical correlation for Nusselt number, which represents the dimensionless form of convective heat transfer coefficient h.

$$Re = \frac{4\dot{m}}{\mu\pi D} \qquad (V.9)$$

Where

$\dot{m}$ is the mass flow of the gas;

D is the reactor diameter;

μ is the fluid viscosity.

Since the flow of gaseous nitrogen used as a carrier gas is controlled by a flowmeter, the internal convection is considered as a forced convection; therefore:

$$Nu = \frac{h_i L}{k} \qquad (V.10)$$

As far as air taken from the outside of the reactor is concerned, the convection is considered as a free one and, consequently:

$$Nu = \frac{h_o D}{k} \qquad (V.11)$$

- When *Re* < 2100, the mass flow is under laminar regime with a uniform heat flux on the surface [3] :

$$Nu = 4.36 \qquad (V.12)$$

- When 2100 < Re < 10000, the mass flow is under transitional regime, with

$$Nu = \frac{\left(f/8\right)(Re-1000)Pr}{1+12.7\left(f/8\right)^{1/2}(Pr^{2/3}-1)} \qquad (V.13)$$

Where the friction factor f and Prandtl number are calculated from the following expressions:

$$f = \frac{1}{(0.790 ln_{Re} - 1.64)^2} \quad (V.14)$$

$$Pr = \frac{\mu\, C_p}{k} \quad (V.15)$$

- When Re >10000, the mass flow is under turbulent regime, with:

$$Nu = 0.023 \times Re^{0.8} \times Pr^{0.33} \times (\frac{\mu_b}{\mu_w})^{0.14} \quad (V.16)$$

The careful analysis of the above models allows ***the dimension of the reactor*** (i.e. the length ***L*** and the radius of the reactor r_o, the thickness of its walls r_o-r_i), ***the thermal conductivity k of the construction material***, and ***the rate of a gas flow*** $\dot{m}$ to be identified as having a predominant impact on the overall heat transfer performance. In order to maximise the temperature lift of the dry gas flowing out of the reactor, it is thus necessary to reduce the heat loss via conductivity and enhance the heat convection process. It is important to note that these conclusions are inherent to the thermochemical process under particular operating conditions. For example, this is different from the measuring principle of the calorimetry device where the heat conduction through the adsorbent bed and the cell walls is a dominant transfer mode of the heat released upon adsorption. This is a reason why it will be always difficult to transpose the results obtained in the calorimetry measurements directly to the industrial practice. Nevertheless, by referring to simple modelling of the calorimetry results, it is possible to find certain indications on what should be considered important for the future implementation.

V.2. Impact of the gas flow rate as studied by gas flow calorimetry

With the use of DSM19 ionosilica sample, the calorimetry experiments were repeated 3 times by varying the flow rate of water vapour entering the calorimetric cell. The desorption step was performed at 353 K for 24 hours under different gas flows of helium, namely: 120, 210, and 300 mL h^{-1}, before being completely cooled down to the room temperature. The adsorption was done at 296 K making use of the same gas flow rate as upon the desorption step. The heat release was recorded in 10 successive cycles for each rate value. A fresh solid sample of about 120 mg was placed in the calorimetric cell after 10 cycles prior to the change of the flow rate. The resulting thermograms were plotted for the time slice intervals of 40 seconds considering the long duration of the experiments (c.f., Figure A.I.8 in Appendix I).

The results obtained are given in Figures V.2. In general, the three testing series reveal a good cyclability of the ionosilica sample compared to the Ce2-13X zeolite, whatever the gas flow of helium considered (c.f., Figure A.I.1-7 in Appendix I). Indeed, given the sensibility of the calorimetry measurement, no sharp drop of the adsorption heat can be observed. This indicates that no partial deactivation of the sample has occurred during the consecutive cycles.

The evolution of the heat released by ionosilica DSM19 sample at different flow rates shows that kinetics is more progressive with a lower flow rate. At 120 mL h^{-1}, the thermal effect lasts generally around 20 hours, with a maximum heat value being of 770 mJ g^{-1}. At 210 mL h^{-1}, the thermal effect lasts about 15 hours, with a maximum heat value being of 1091 mJ g^{-1}. When the flow rate increases to 300 mL h^{-1}, the duration of the thermal effect diminishes to 13 hours, with a maximum heat value exceeding 1384 mJ g^{-1}. Therefore, increasing the flow rate of the adsorbate makes the process more exothermic during shorter periods of time. Obviously, these observations are consistent with the conclusion drawn from the analysis of the model equations indicating the importance of the gas flow rate $\dot{m}$.

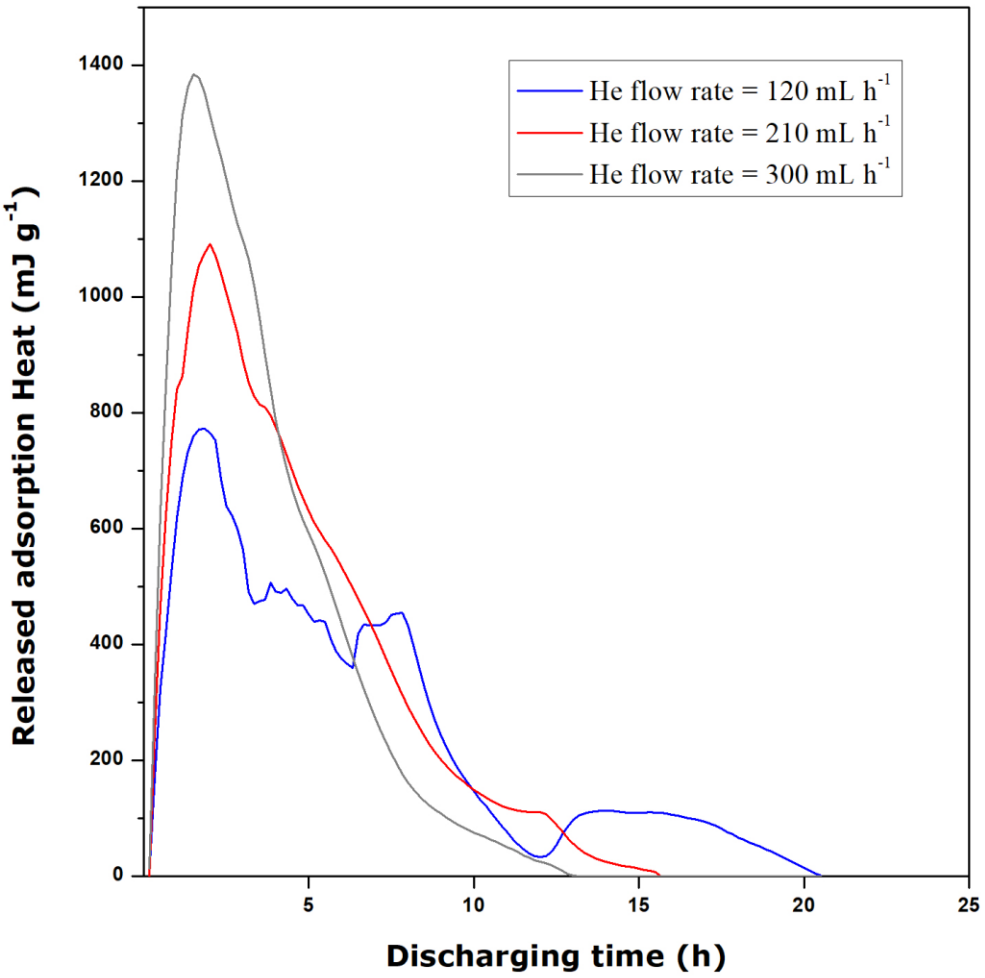

Figure V. 2*: Heat of adsorption released upon water vapour adsorption onto DSM19 at 296 K with Helium flow rates of 120 mL h^{-1}, 210 mL $h^{-1}$and 300 mL h^{-1}, respectively.*

V.3. Kinetics of the heat release during adsorption onto Ce2-13X and ion-exchanged ionosilicas

On the way towards the development of a bench-scale unit for testing greater amounts of sample, appropriate kinetic studies were made by means of the same calorimetry equipment to evaluate the maximum theoretical temperature of the carrying gas flowing out of the calorimetric cell. Each sample was first degassed at 353 K directly within the calorimetric cell through which the flow of helium was passed at a rate of 120 mL h^{-1}. The main purpose of this *in situ* activation was to avoid the mass loss and contamination during the sample transportation between the external drying rig and the calorimetric cell. After 24 hours of drying, the sample

was cooled down to the room temperature (the calorimeter was thermostated at 298 K). The adsorption was performed by flowing the carrier gas containing a constant amount of water vapour at a rate of 120 ml h^{-1}. The partial pressure of water vapour was controlled by using an on-line saturation vessel where the carried gas was saturated with water at 296 K. The thermal peak of adsorption was monitored until the complete saturation of the solid surface. The corresponding integral heat of adsorption was determined by integrating this peak. More details of the experimental procedures are given in Chapter II (c.f., section II.5.2).

To rationalize the resulting heat data, the thermogram representing the intensity of the thermal signal as a function of time was cut into small parts (slices) over short intervals of 40 sec each. Then, each part was integrated and transformed into a heat value, q'_{ads}. The following analytical equation was used to approximate the results obtained:

$$\frac{dq_{(He)}}{dt} \cdot C_p(He) \cdot T_i + \frac{dq_{(H2O)}}{dt} \cdot C_p(H_2O) \cdot T_i - \frac{dq_{(He)}}{dt} \cdot C_p(He) \cdot T_e = q'_{ads}$$

(V.17)

Where

$\frac{dq_{(He)}}{dt}$ and $\frac{dq_{(H2O)}}{dt}$ are the molar flow rate for the carrier gas and water vapour (mol h^{-1}), respectively;

$C_p(He)$ and $C_p(H_2O)$ are the heat capacities of the carrier gas and water vapour (kJ $mol^{-1}K^{-1}$), respectively;

T_i and T_e are the temperatures of the gas entering and leaving the calorimetric cell, respectively;

q'_{ads} is the heat value corresponding to a given 40 seconds large slice.

Hence, one of the most intuitive factor for a heating system, namely the temperature lift could be calculated as follows:

$$\Delta T = T_e - T_i \qquad (V.18)$$

In the above approximation, it was assumed that the whole heat release during each adsorption step was instantly given up to the flowing carrier gas without any heat loss. Furthermore, the adsorption was considered as being ideal and there was no more water vapour in the heated gas.

The results of the above-described modelling for different samples are shown in Figure V.2. Here, the temperature lift, ΔT, has been plotted as a function of the discharging time.

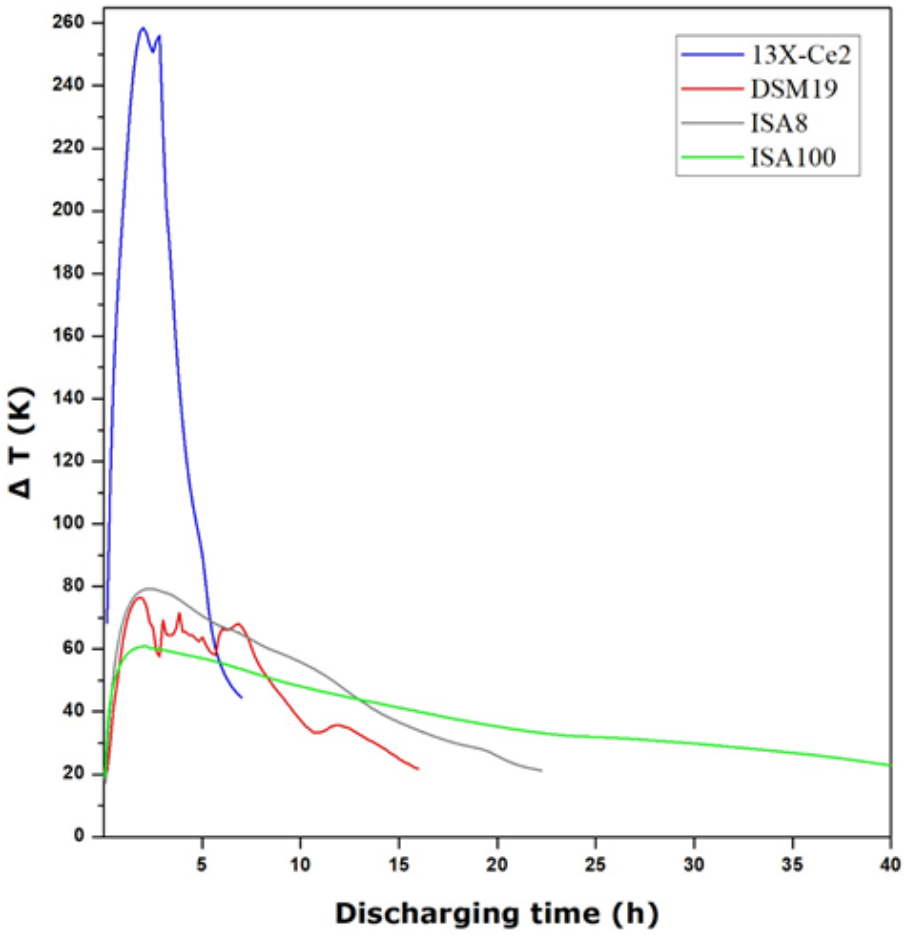

***Figure V. 3**: Temperature lift in the carrier gas flowing out of the calorimetric cell corresponding to the adsorption of water vapour onto Ce-13X, DSM19, IS8, and ISA100 at 298 K. The calculation was done by re-adapting the experimental data to 1 g of the solid sample.*

As can be seen in Fig. V.3, some significant differences can be observed between the zeolite and the three ionosilica samples in regards with the duration of the discharging step and the maximum temperature lift. In the case of ionosilicas, the rise in the theoretical temperature of the flowing gas is in the range of 60-80 K. This maximum temperature is attained considerably rapidly after about 1.5 hours of moist gas flow. Then the temperature lift starts to decrease progressively at a very low rate. Different duration periods of the discharging step are observed for DSM19, ISA8 and ISA100. The DSM19 sample containing compensating Cl^- ions shows a discharging time of 15 hours, while the ISA8 sample with a mixture of Cl^- and SO_4^{2-} is capable of releasing heat up to over 20 hours. Concerning ISA100 (solely SO_4^{2-} counter-ions), the discharging time extends to about 40 hours, showing a much more progressive temperature decrease. The maximum temperature lift for Ce2-13X can attain over 250 K owing to its highly hydrophilic nature which provides a greatly exothermic effect occurring for 2 hours. Afterwards, the heat effect diminishes sharply and the overall heat release extends only to 5 hours. This indicates, a very rapid saturation of the highly energetic surface sites and compensating cations.

These results derived from the calorimetry measurements were compared with those of the representative energy storage prototypes (Table V.1) performed as open systems. The ZAE installed a heating system in a school in Munich, applied T_{charge} = 403 K to get a temperature lift of 35 K for 14 hours [6,7]. The CETIL prototype applied T_{charge} = 413 K to get a temperature lift of 25 K for over 80 hours [5]. Our ionosilica samples showed a great potential as thermochemical storage materials: with a lower T_{charge} of 353 K, a theoretical temperature lift of 60-80 K was achieved for significantly longer periods. However, given the difference of the scale between our system and those prototypes, the present calorimetry results still remain very theoretical since several factors such as heat loss during transfer as well as non-utilisable sensible heat of storage material have not been taken into account in our simulation.

Project	Material	T_{charge} (K)	$T_{discharge}$ (K)	Air flow rate ($m^3 h^{-1}$)	ΔT_{max} (K)	Discharging duration (hours)
SolSpaces (2016) [11]	4.3 m^3 binderless 13X reactor of multi-segments	453	293	75	28	13
STAID (2015) [10]	2×40 kg 13X packed bed	393-453	293	120-180	37	8-10
ASIC (2014) [12]	50 kg 4A/13X rotating drum reactor	453-503	298	140	35	10
E-HUB (2014) [13]	2×75 kg 13X packed bed	453	313	80	30	25
CETHIL (2011) [5]	4.8 kg composite ZM15: 13X+15%MgSO4 packed bed	413	293	20	25	80
MONOSORP (2006) [14]	70 kg zeolite 4A honeycomb monoliths	443	293	100	22	20
ZAE Bayern (1997) [6,7]	7000 kg 13X packed bed	403	298-303	6000	35	14

Table V. 1: *Examples of open sorption THS prototypes with operating conditions and storage performances*

Taking into account the integral heats of adsorption reported in Fig. IV.7 in the previous chapter, it is easier to understand these two different patterns of heat evolution shown by the two types of materials. Under the same conditions of sample activation, ISA100 and Ce2-13X can yield the total heat amount around -800 kJ per kg of the sample. With a Helium flow at 353 K, this value of the total heat amount matches that obtained in the previous study as published by Alby *et al*. [8] for water vapour adsorption onto Mg-exchanged 13X sample with a cation-exchange ratio of 70 % under dynamic conditions of gas flow. Alby *et al*. reported a total heat amount of -810 kJ per kg with a vacuum pre-treatment at 473 K. This heat was demonstrated to sharply drop to around -200 kJ per kg when applied a vacuum pre-treatment at 298 K.

When the Ce2-13X presents a more progressive process of the heat release, the ISA100 generates the same heat amount in a more dynamic way. This information is of great importance for the design of the future storage systems. For a seasonal heat storage, ionosilica materials, and sulfate-functionalized ones in particular, have a great advantage when a slow release kinetics is required. The Ce-13X sample can be used if high instant values of the temperature are preferred. *An idea immediately emerging from these studies is to design a hybrid storage system, which could benefit from the advantages of both types of materials*. As is argued in the reference [9], the THS system alone cannot cover the total energy needs for space heating in homes, small businesses, and public buildings "if the quantity of the working materials employed should remain within reasonable limits". The design of a THS reactor should focus more on the compensating peak hours of the heat demand. Johannes *et al.* [10] showed that the critical peaks of the electricity demand in France during a typical winter day took place in the beginning (i.e. at 7:00 a.m.) and at the end (i.e. 6:00 p.m.) of the day, lasting about 2-3 hours. Based on the present study, it is reasonable to propose a hybrid system that, for instance, can utilise the segment of reactor containing Ce-13X to supply an instantaneous temperature lift throughout the peak hours, and will switch to the other segment with ionosilica materials in order to achieve a mild and continuous heat for the rest of required heating hours.

It should be emphasized here that the main difficulty in validating the above calculation lies in the lack of information about the real heat transfer between the adsorbent bed which produces the heat due to adsorption of water vapour and the flowing carrier gas which is progressively depleted in water vapour. To some extent, it is possible to justify the approximation when considering that the small flow rates used facilitate the attainment of the adsorption equilibrium and thus the complete drying of the carrier gas passing through the adsorbent bed. Nevertheless, the hypothesis of the zero heat loss by conduction within the adsorbent bed is difficult to accept. Of course, the use of well-isolated reactor is necessary to

decrease the heat loss. In light of this discussion, it is reasonable to admit that high temperature lifts inferred from the above-described calculation are unusually high and do not correspond to the reality of the storage process. With this truth in mind, it is interesting to make a comparison with the results obtained with the aid of a laboratory-scale test-rig for thermal performance evaluation of adsorbents under flow conditions.

V.4. Laboratory-scale test-rig for thermal performance evaluation of adsorbents under flow conditions

V.4.1. Description of the experimental set-up

The laboratory-scale test-rig developed within the framework of this thesis is devoted to test greater amounts of solid samples weighing up to 10 grams. This in turn will lead to an increase in the heat released during the adsorption of water vapour but, simultaneously, there may be a risk of enhanced heat loss. Hence, it is necessary to adjust the gas flow rate and to isolate the reactor from the surroundings. This equipment allows the real discharging step to be monitored by sensing the temperature changes of the carrier gas at different places inside and outside the reactor and thus can potentially provide important information on the storage process. Given the mass of solid sample necessary for each experiment, commercially available 13X zeolite was used first to optimise the operating conditions. 8 grams of 13X powder were introduced into the reactor for every test.

The experimental set-up is schematically depicted in Fig V.4; its photograph is presented in Fig V.5.

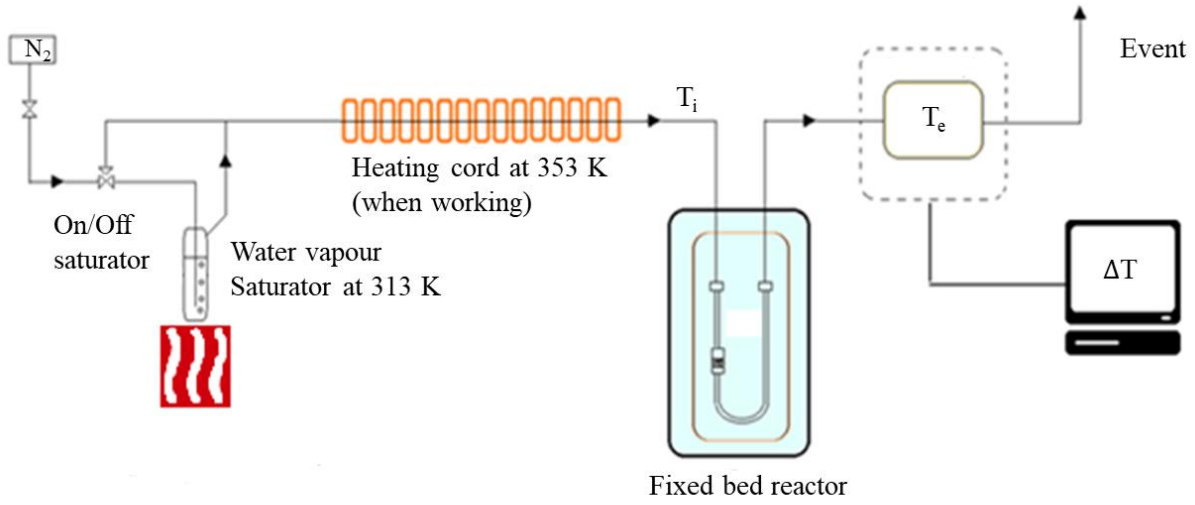

***Figure V. 4**: Schematic diagram of the laboratory-scale test-rig for thermal performance evaluation of adsorbents under flow conditions*

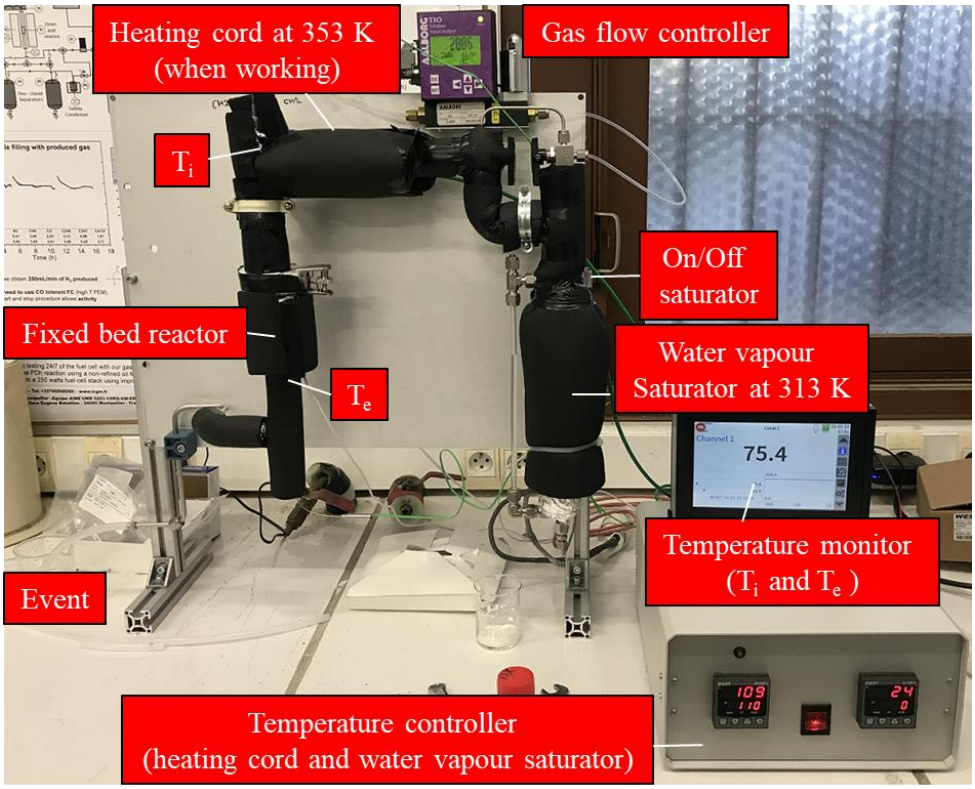

***Figure V. 5**: Photograph of the laboratory-scale test-rig for thermal performance evaluation of adsorbents under flow conditions*

In comparison with the previous performance tests carried out with the use of a gas flow calorimeter, the experimental procedures have been modified to approach more realistic conditions of use. Firstly, gaseous nitrogen was used as a carrier gas; it is the major composite of air. The first activation and the subsequent re-activation procedures were carried out *in situ* by heating the carrier gas to a given temperature before it entered the reactor. It was thus possible to gain an idea about the efficiency of the regeneration procedure.

In the microcalorimetry measurements, small rates of gas flow are usually used to reduce the heat loss with the gas flowing out of the calorimetric cell, thereby maximizing the heat conduction through the adsorbent bed and across the cell walls. In reality, this thermal conduction should be limited as much as possible so as to heat the outflowing gas as much as possible. In the present study, a reactor with larger diameter and length, as well as increased gas flows were applied (initially 2 L h^{-1}), and the T_i and T_e temperatures were taken inside the gas at the entrance and the exit of the reactor. The whole system was covered by the polyurethane foam to limit the heat exchange with the environment.

V.4.2. Some technical problems potentially faced when performing the THS process

- **Charging step**

In order to remove the traces of water from the zeolite structure, each cycle began with a desorption step which corresponded to the charging process. The carrier gas containing no humidity and flowing through the stainless steel tubing at a rate of 2 L h^{-1} was heated to a high target temperature set at 353 K. Given the thermal insulation of this home-made set-up, the temperature of incoming gas T_i could not reach 353 K because of heat loss, even with heating coil working at 393 K. This means that the efficiency of the charging procedure was below the initial expectation. In order to solve this problem, an extra layer of asbestos fibers was placed

outside the stainless steel tubing before covering it with the polyurethane foam. By doing this, the temperature of incoming gas was raised to 353 K, with heating coil working at 383 K.

Nevertheless, the efficiency of the heat transfer was still not sufficiently high, considering the heat loss during the long transporting distance travelled by hot air in a real building. To overcome this obstacle, the gas flow rate should be greatly increased. This parameter was considered as being more important for the discharging step.

- **Discharging step**

After about 24 hours of heating, the system cooled freely down to room temperature. At the end of the cooling phase, the carrier gas was directed to the water saturator where the saturation with water vapour occurred at 313 K. This resulted in a discharging step.

In the first series of tests, a reactor made of glass was used (Figure V.6).

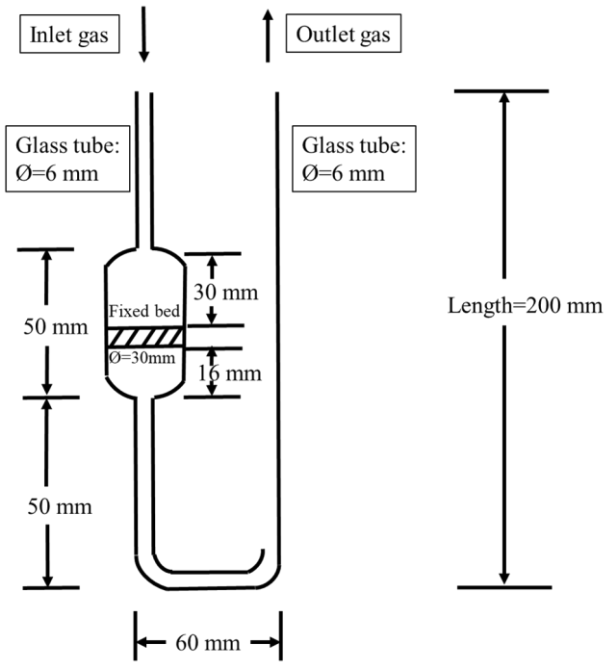

Figure V. 6*: The fixed-bed reactor made of glass, as used for the initial tests*

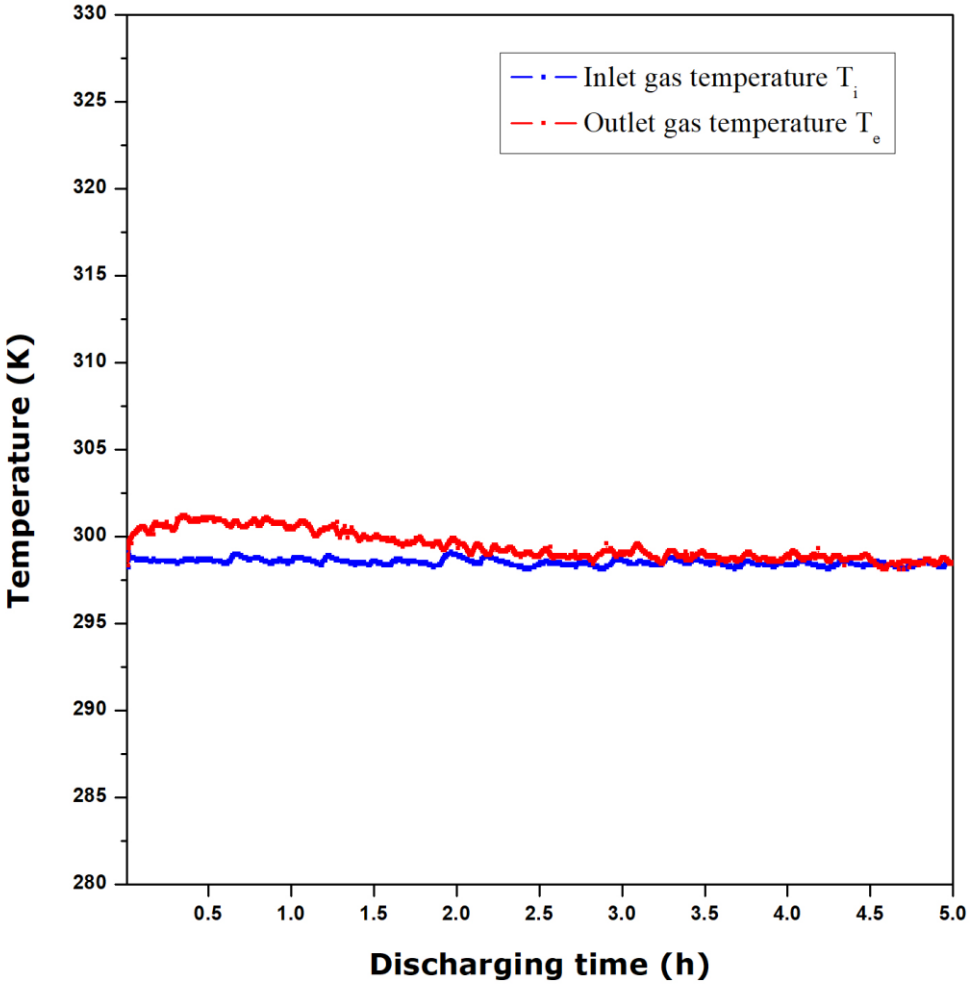

***Figure V. 7**: Temperature lift recorded for the discharging step making use of a glass reactor under a flow rate of 2 L h^{-1}*

The results of this initial test are shown in Figure V.7. With a glass reactor and at a flow rate of 2 L h^{-1}, the temperature lift ΔT was only about 3 K, then the heat effect disappeared after 3 hours. This is indeed disappointing, but not a surprising result, in light of the model consideration made in section V.1. The modification of two parameters was further regarded for the improvement of thermal performance: the thermal conductivity of construction material and the gas flow rate. Thermal conductivities of three types of construction materials envisaged for the present study are compared in Table V.2. Finally, the initial glass reactor was replaced by a rigid PVC one which has much lower thermal conductivity and at the same time has enough

thermal resistance for the temperature range of our experiments. Meanwhile, the gas flow rate was increased up to 30 L h^{-1}.

Materials	Thermal conductivity at 298 K ($W\ m^{-1}K^{-1}$)	Melting point (K)
Glass	1.1	1673-1873
Polytetrafluoroethylene (PTFE)	0.25	600
Polyvinyl chloride (PVC)	0.19	373-443

Table V. 2*: Thermal conductivity of several construction materials [15].*

The results of performance tests performed with this new configuration are given in Figure V.8. At first glance, a significant improvement of the temperature lift can be seen. A maximum $\Delta T = 35$ K is achieved after half an hour, and the total discharging time is around 3 hours. A fluctuation of the temperature lift can be observed right after it arrived its peak value, which can be explained by non-reactive material zone of our packed bed reactor. This has corroborated our hypothesis that the heat loss is closely related to the flow rate of the incoming gas and it may be reduced by increasing the gas velocity. The thermal conductivity of the material used for the construction of the reactor or even for the gas transporting tubing are also important to ensure the good thermal isolation of the system.

However, a temperature lift of 35 K may hardly be sufficient for the practical uses in heating systems, especially when integrated in a domestic ventilation system. Furthermore, this value is far below that expected on the basis of the heats of adsorption previously measured under flow conditions with the aid of the gas flow calorimetry equipment. Two reasons may be finally forwarded to explain this discrepancy: (1) heat loss through conduction within the bed of adsorbent and then passing across the reactor walls into the surroundings, (2) the sensible

heat of storage materials which is difficult to exploit. This part of energy was not taken into account when the kinetic models were established in V.3, as the quantity of the sample used was too small. However, when the reactor size of the lab-scale test-rig becomes bigger, this can no longer be negligible, which will surly affects the efficiency of the heat storage system.

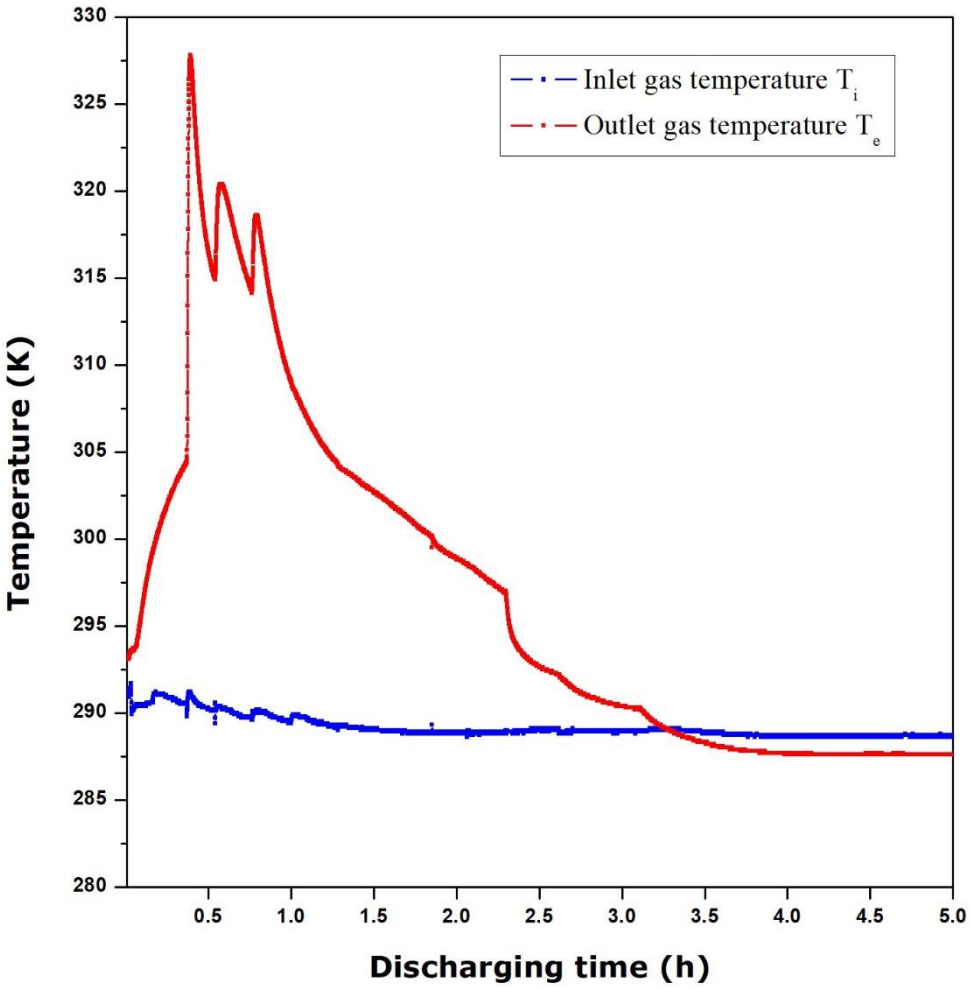

Figure V. 8*: Temperature lift recorded for discharging step making use of a PVC reactor at a flow rate of 30 L* h^{-1}

Apart from the present proposal of designing a hybrid storage system with the use of both types of materials, some projects described in the literature have provided other ideas to improve the THS performance and efficiency (c.f., Table V.1). Within the framework of the MONOSORP prototype, the storage material was introduced into the reactor with a honeycomb

monolith structure which had a large number of small straight channels that ensured a low pressure loss. The E-HUB and ZAE projects added an air-to-air heat recovery unit to increase the inlet temperature by using residual heat in the outflow, which allowed for higher outlet temperatures. The concept of multi-segments reactor presented in several prototypes was also an important concept allowing the modular control of heat release for the long term storage system. It could work in a parallel mode or a cascading mode, according to the heating requirements during peak hours. The ASIC design utilising a rotating drum reactor to avoid the formation of non-reactive material zones would certainly increase the efficiency of the system, although it also added extra cost to the equipment investment and energy consumption. For the purpose of further work on the industrial implementation of the thermochemical storage process, such ideas certainly deserve to be taken into consideration.

V.5. Conclusion

In this chapter, the focus has been placed on the kinetics of heat release during the adsorption of water vapour and the physical factors governing the thermal performance of the materials developed and characterized in the previous chapters. The objective was to approach the real operating conditions in view of potential applications in low-temperature thermochemical storage of energy. Based on the classical models for heat transfer in various media, the dimension of the reactor, the thermal conductivity of the construction material, and the rate of a gas flow were firstly identified as the key parameters with a predominant impact on the overall heat transfer performance. In order to maximise the temperature lift, it appeared necessary to reduce the heat loss via conductivity and enhance the heat convection process.

Changes in the heat release pattern caused by increasing the gas flow rate were first studied for DSM19 by gas flow calorimetry. In line with previous expectations, the kinetics of

heat evolution appeared faster with increased flow rates. The subsequent calorimetry tests carried out with the zeolite and ionosilica samples, subject to the same activation procedure, revealed a more progressive and regular heat release in the case of ionosilicas in compared with the Ce2-13X zeolite sample. This information is of importance to the future design of the storage units and argues in favour of the use of hybrid systems combining the two different behaviour patterns of zeolites and ionosilicas.

In the next step, a laboratory-scale test-rig was developed for thermal performance evaluation of adsorbents under flow conditions. The main objective of flow tests was to constantly monitor the temperature lift of gaseous nitrogen leaving the reactor and shed more light on the impact of the previously selected parameters on this thermal performance. The preliminary test performed with the use of 8 g of 13X placed in a glass reactor at a gas flow of 2 L h^{-1} yielded a very low temperature rise of 3 K. By switching to a PVC reactor and increasing the flow rate to 30 L h^{-1}, the temperature increase attained 35 K. This result again supported the hypothesis of the importance of thermal conductivity of the construction materials and the gas flow rate in a storage process.

References

[1] M. Kaviany, Principles of heat transfer in porous media, 2nd Ed., Springer, New York, 1995. doi:doi.org/10.1007/978-1-4612-4254-3.

[2] R.G. Carbonell, S. Whitaker, Heat and mass transfer in porous media, in: J. Bear, M. Yavuz Corapcioglu (Eds.), Fundam. Transp. Phenom. Porous Media, Springer, Dordrecht, 1984: pp. 121–198. doi:doi.org/10.1007/978-94-009-6175-3.

[3] R.P. Singh, D.R. Heldman, Heat transfer in food processing, in: S.L. Taylor (Ed.), Introd. to Food Eng., 4th Ed., Elsevier, 2009: pp. 247–399. doi:10.1073/pnas.0703993104.

[4] J.H. Lienhard IV, J.H. Lienhard V, A heat transfer textbook, 4th Ed., 2017. doi:978-04864793161.

[5] S. Hongois, PhD thesis: Stockage de chaleur inter-saisonnier par voie thermochimique pour le chauffage solaire de la maison individuelle, Institut National des Sciences Appliquées de Lyon, 2011.

[6] A. Hauer, Adsorption systems for TES—design and demonstration projects, in: H.Ö. Paksoy (Ed.), Therm. Energy Storage Sustain. Energy Consum. Fundam. Case Stud. Des., Springer, 2007: p. 409. doi:10.1007/978-1-4020-5290-3.

[7] A. Hauer, Thermal energy storage with zeolite for heating and cooling applications, Int. Sorption Heat Pump Conf. 2002. 1 (2002) 385–390. doi:WVH5H7WK1UX2HUP9 [pii].

[8] D. Alby, F. Salles, J. Fullenwarth, J. Zajac, On the use of metal cation-exchanged zeolites in sorption thermochemical storage: Some practical aspects in reference to the mechanism of water vapor adsorption, Sol. Energy Mater. Sol. Cells. 179 (2018) 223–230. doi:https://doi.org/10.1016/j.solmat.2017.11.020.

[9] H. Wu, F. Salles, J. Zajac, A critical review of solid materials for low-temperature thermochemical storage of solar energy based on solid-vapour adsorption in view of space heating uses, Molecules. 24 (2019) 945. doi:10.3390/molecules24050945.

[10] K. Johannes, F. Kuznik, J.L. Hubert, F. Durier, C. Obrecht, Design and characterisation of a high powered energy dense zeolite thermal energy storage

system for buildings, Appl. Energy. 159 (2015) 80–86. doi:10.1016/j.apenergy.2015.08.109.

[11] R. Weber, S. Asenbeck, H. Kerskes, H. Drück, SolSpaces – Testing and performance analysis of a segmented sorption store for solar thermal space heating, Energy Procedia. 91 (2016) 250–258. doi:10.1016/j.egypro.2016.06.214.

[12] B. Zettl, G. Englmair, G. Steinmaurer, Development of a revolving drum reactor for open-sorption heat storage processes, Appl. Therm. Eng. 70 (2014) 42–49. doi:10.1016/j.applthermaleng.2014.04.069.

[13] Energy-Hub for residential and commercial districts and transport (E-HUB),Report on a combination of thermal storage techniques and components, 2014. https://www.e-hub.org/pdf/D3.2_Thermal_storage_techniques_components.pdf.

[14] H. Kerskes, K. Sommer, Research report FZKA-BWPLUS: MonoSorp Integrales Konzept zur solarthermischen Gebäudeheizung mit MonoSorp, (2007).

[15] D.R. Lide, ed., CRC Handbook of chemistry and physics, 85th Ed., Taylor & Francis, 2004. doi:10.1021/ja906434c.

Chapter VI

General Conclusions and Future Outlook

VI.1. General Conclusions

Solar energy storage for space heating in the building sector is an important issue for the global policies to reduce Greenhouse Gas emissions and to better control the energy demand, as it can contribute alleviating the problem of intermittency of this renewable source. The present thesis has been thus devoted to the comprehensive analysis of a potential low-temperature thermochemical storage of solar energy based on the principles of vapour adsorption onto solid adsorbents in view of space heating uses. A critical review of the state of the art was first performed in order to assess the potential candidates as efficient adsorbents by referring strictly to the possible adsorption mechanism and practical aspects of their application under particular operating conditions. This has helped to orient the research towards open sorption systems operating in the moist-air flow with the use of water vapour, as being most suitable for realising the mild and environment-friendly operating conditions.

Within the framework of the present work, two types of innovative materials have been carefully considered, namely *Cerium-exchanged faujasite zeolites*, Ce-13X, and silica-based hybrid materials containing ionic groups, called *ionosilicas*. The Ce-13X zeolites were obtained through an ion-exchange process. The so-obtained samples contained trivalent or tetravalent Ce^{3+} and Ce^{4+} ions, as extra-framework cations thus compensating the negative charge of the zeolite framework. The expected increase in the energy storage density was related to the potential heat release upon physical adsorption of water molecules within the micropore structure and the phenomenon of cation hydration in line with the enhanced hydration energy due to the cation valence. The *in situ* XRD characterization and Rietveld refinement, revealed that the compensating cations hardly moved away from their preferential I' and II sites in the 13X framework during hydration process. Meanwhile, the introduction of Cerium cations modified the distribution of the compensating cations compared to the pristine zeolite sample. In addition, the presence of a large amount of water was argued to displace cations towards

larger cages (supercages and hexagonal prisms). The adsorption of water vapour onto selected samples was further tested under both static and dynamic conditions so as to improve the understanding of the adsorption phenomenon and the regeneration stage. It was demonstrated, among other things, that adsorbent regeneration carried out under mild conditions of Argon flow at 423 K (no vacuum treatment was applied) resulted in the inevitable presence of some water molecules remaining in the adsorbent at the end of the dehydration step. Despite this, the calorimetric measurements of the heat of adsorption revealed a significant gain in the heat released compared to the pristine Na-13X sample: for example, Ce4-13X (containing mainly Ce^{4+} cations) was able to yield more than 1100 kJ per kg of solid and 13X saturated with Ce^{3+} provided around 950 kJ per kg of solid; in comparison with the energy performances of Na-13X, these heat values corresponded to an increase by 37.5% and 18.8%, respectively. A lower-temperature regeneration under a flow of Helium at 353 K provided about 700 kJ per kg of solid for the second and third adsorption-dehydration cycles, irrespective of the Ce-13X sample.

In a second step, ionosilicas were functionalized by a complete or partial replacement of the initial Cl^- compensating ions with SO_4^{2-} anions. In spite of a weakly developed porous structure, ionosilicas could provide heats of adsorption in the order of 700 to 800 kJ per kg of solid for a longer duration of discharging (adsorption) stage compared to the zeolite samples studied previously. This time, the mild regeneration conditions of a flow of Helium at 353 K did not contribute to the reduction of energy performances. The solid-state ^{29}Si NMR provided evidence of presence of both silanol (isolated, germinal and vicinal) and siloxane groups on the surface of ionosilicas. The experimental results indicated the following sequence of the sensibility upon the hydration: T^1 (germinal silanol) > T^2 (isolated or vicinal silanol) > T^3 (siloxane). During the early stage of adsorption process, water molecules started to adsorb on the silanol groups via the H-bond, thus resulting in a heat release. Simultaneously, siloxane bridges began to be opened by a hydroxylation reaction and were transformed into hydrophilic

silanol groups. This allowed water molecules to be adsorbed during the next step, thereby enhancing the hydrophilic character of the surface. In particular, the siloxane bridges in the sulfate-functionalized ionosilica ISA100 appeared easier to be transformed into silanol groups, which enabled the hydrophilicity of surface to be tuned to a greater extent. This suggests that the counter-ions and their polarizability are significant factors in adjusting the surface hydrophobic-hydrophilic balance.

In order to better reproduce the potential operating conditions for the low-temperature thermochemical storage of energy, appropriate studies were undertaken on the kinetics of heat release during the adsorption of water vapour aiming at identifying the key parameters with a predominant impact on the overall heat transfer performance. The calorimetry tests carried out with the use of zeolite and ionosilica samples under the same activation/regeneration conditions, revealed a more progressive and regular heat release in the case of ionosilicas (13-20 hours) in comparison with the Ce2-13X zeolite sample (5-6 hours). This was regarded as an asset for the future use in the thermochemical storage. In order to maximise the temperature rise of the gas flowing out of the storage unit, the careful analysis of the fundamental equations for the heat and mass transfer in various media proved the necessity of reducing the heat loss via conductivity and enhancing the heat transfer through convection in the future storage installation. A laboratory-scale test-rig was developed for thermal performance evaluation of adsorbents under flow conditions, allowing to monitor the temperature lift of gaseous nitrogen leaving the reactor. The preliminary test performed with the use of 8 g of 13X placed in a glass reactor at a gas flow of 2 L h^{-1} yielded a very low temperature rise of 3 K. By switching to a PVC reactor and increasing the flow rate to 30 L h^{-1}, the temperature increase attained 35 K. Therefore, the importance of adjusting both the thermal conductivity of the construction materials and the gas flow rate in the overall storage process was corroborated by the results of these tests.

VI.2. Future outlook

With a view to exploring further ways to support the development of efficient units for low-temperature thermochemical storage of solar energy based on the principles of vapour adsorption onto solid adsorbents, it seems important to thoroughly consider the following items:

1) Deeper characterization work is necessary to quantify the proportion between the different oxidation states of Cerium (Ce^{3+} and Ce^{4+}) present at the extra-framework positions. In particular, the optimised preparation conditions to increase the percentage of Ce^{4+} cations should be determined as they yield higher adsorption heats in comparison with the Ce^{3+} ones. The use of such specific characterization techniques as X-ray photoelectron spectroscopy will contribute to improve the knowledge of the structure of this new material. Chemical dosing techniques could also be considered for quantifying the Cerium and determine the average charge of the ion.
2) The ionosilicas characterized in this work appear very promising as adsorbents for the heat storage. Nevertheless, some doubts remain to be dispelled about the precise structure of this material, and especially with regards to the porous structure and the fibre-form morphology observed by the transmission electron microscopy (c.f., Figure II.6). The reason for the formation of different layers deserves an in-depth understanding in order to confirm whether this is due to the presence of double-charged sulfate ions. Chemisorption with the use of such probe molecules as NH_3 could also bring useful information concerning the bonding forces on the ionosilica surface, in order to shed more light on the creation-deletion procedure for bonds involving silanols. Such information will surely be helpful for the future simulation work aiming to propose a reactive force-field able to reproduce by Molecular Dynamics simulation the hydration-dehydration mechanism occurring in ionosilicas and the strong interaction between the framework and the counter-ions. Besides, it would be also appropriate to carry out several comparative studies for some other factors such as the

quantity of SO_4^{2-} or the drying method (e.g., oven heating or lyophilisation) and their impact on the structuration/texture of ionosilica.

To go further, it would be preferable to consider a form of material maximising the ratio of the surface area to the volume, so as to benefit from a larger contact area between the adsorbent and the adsorbate. In light of the promising adsorption properties exhibited by the weakly porous ionosilica samples considered here, the possibility of shaping these materials to get more surface area, with the aid of such *shaping procedures as sintering or pelletizing into monolithic* bodies with well-defined homogeneous porosity, may be a breakthrough in enhancing the energy storage density.

3) The laboratory-scale test-rig developed for thermal performance evaluation of adsorbents under flow conditions has proven its usefulness. Nevertheless, the tests have been performed only with the commercial Na-13X sample available at the time required in sufficient quantities. It is clear that a comparative study of the sorption kinetics and the temperature lift should be carried out when acquiring at least similar quantities of Ce-exchanged zeolites and ionosilicas. Furthermore, the comprehension of the behaviour of zeolites containing Ce^{3+} or Ce^{4+} at the lab scale should also be determined.

4) As mentioned in section V.4.2, the sensible heat of storage materials is difficult to exploit. When the reactor size of the lab-scale test-rig becomes bigger, this can no longer be negligible, which will surely affect the efficiency of the heat storage unit. Therefore, it is necessary to use specific characterization techniques to measure the thermal conductivity and heat capacity for each material in order to get a more precise estimate of the thermal performance.

5) As far as the future transfer of technology from laboratory to industry is concerned, more factors influencing the overall performance of the working system have to be considered in

the designing process. Besides the thermal conductivity of the construction materials and the gas flow rate, the choice of the reactor type is to be included. As an example, the use of packed-bed or multi-segment reactors should be regarded as a function of the real requirements for space heating. Moreover, the appropriate shaping of the storage material is necessary to limit the pressure drop through the adsorbent bed. Given the sorption behaviour of the zeolite and ionosilica samples studied in the present work, it is highly suggested that a hybrid storage system may benefit from the advantages of each type of materials. As already discussed in section V.3, a multi-segment reactor can use a Ce-13X sample to obtain an instantaneous temperature lift, in combination with ionosilica to achieve a more steady heating.

Résumé étendu de la thèse en français

Introduction générale

Avec la perspective d'une augmentation considérable de l'énergie mondiale, de la raréfaction des sources d'énergie fossile et du changement climatique, il devient urgent d'augmenter l'efficacité énergétique des procédés existants et de mettre en œuvre la diversification des sources d'énergie. L'Union Européenne a lancé la "Stratégie Europe 2020" affichant des objectifs ambitieux, tels que des réductions de 20% des émissions de gaz à effet de serre par rapport aux niveaux de 1990, la production de 20% de la consommation d'énergie provenant d'énergies renouvelables et une augmentation de 20% de l'efficacité énergétique d'ici 2020.

Le secteur résidentiel reste l'une des catégories les plus consommatrices d'énergie. En effet, en 2016, ce secteur représentait plus de 25 % de la consommation totale en Europe, ce qui le classait parmi les trois principaux consommateurs d'énergie après les transports et l'industrie. En outre, la majeure partie de cette consommation d'énergie dans ce secteur reste liée au chauffage de l'espace (par exemple 62% en 2017 selon le fournisseur d'électricité français EDF).

Dans ce contexte, le développement des énergies propres et renouvelables est devenu un impératif stratégique pour le développement durable et constitue sans aucun doute un moyen efficace d'améliorer l'efficacité énergétique et de réduire les gaz à effet de serre. Les recherches scientifiques se sont de plus en plus axées vers les énergies renouvelables, telles que les énergies solaire, éolienne et hydraulique. Parmi celles-ci, l'énergie solaire apparaît actuellement comme l'une des alternatives les plus prometteuses aux sources d'énergie conventionnelles. Cependant, son principal inconvénient vient de l'intermittence entre l'approvisionnement et la demande du fait du cycle du soleil. Par conséquent, un système de stockage d'énergie doit être développé, afin de capter et stocker l'énergie thermique disponible pendant les périodes d'ensoleillement et

de la restaurer ensuite en fonction des besoins. Grâce à cela, il sera alors possible de faire correspondre l'offre et la demande au fil du temps.

Actuellement, différents types de systèmes de stockage d'énergie existent: électrochimiques (batteries rechargeables classiques), mécaniques (stockage hydroélectrique pompé), électriques (supercondensateurs), chimiques (piles à hydrogène) et thermiques (en utilisant les stockages de chaleur sensible ou latente). Ces systèmes se trouvent encore à différentes phases de développement. Parmi ces technologies existantes, celle basée sur l'énergie thermique gagne de plus en plus en crédibilité, comme une option prometteuse pour le stockage de l'énergie solaire, notamment dans le cadre des applications pour les systèmes de chauffage domestique dans les bâtiments.

Deux technologies existent pour le stockage d'énergie thermique à court terme et ont déjà été mises en œuvre industriellement à grande échelle, dans les applications de bâtiment: le stockage de chaleur sensible et latente. Le stockage de chaleur sensible est lié à la capacité thermique des matériaux de stockage tandis que le stockage de chaleur latente implique des effets thermiques associés à un changement de phase d'un matériau. Néanmoins, ces procédés peuvent s'accompagner d'une perte d'énergie non négligeable, d'une instabilité thermique et d'investissements très coûteux en termes d'isolation thermique, ce qui soulève un problème énorme lorsqu'il s'agit d'un système de stockage saisonnier. Plus récemment, le stockage thermochimique utilisant des modifications du potentiel chimique résultant de réactions chimiques réversibles ou de phénomènes de sorption appropriés est considéré comme une alternative prometteuse pour le stockage de chaleur à long terme. En effet, dans ce système, l'énergie solaire peut théoriquement être stockée en séparant le couple réactif pendant un temps arbitraire sans aucune perte de chaleur. Cependant, malgré les avantages présentés par le système de stockage thermochimique, certaines restrictions relatives au fonctionnement des réacteurs thermochimiques, telles que la température de régénération élevée, le cycle de

stockage complexe, peuvent contribuer à un coût élevé et à la complexité de la conception du matériau.

Objectif de la thèse et la structure du manuscrit

L'objectif général de cette thèse est de proposer, d'étudier et de caractériser un système de stockage d'énergie solaire thermique utilisant un processus de sorption pour le chauffage des locaux dans l'application des bâtiments. Pour cela, la mise en place de moyens de stockage appropriés, suffisamment efficaces, viables sur les plans écologique et économique est nécessaire. À cette fin, nous avons choisi d'appliquer nos stratégies de recherche classiques aux étapes suivantes: (i) concevoir et élaborer un système de stockage approprié pour une utilisation pour un stockage à long terme de l'énergie de sorption, comprenant une étape de synthèse et une étape de modification des matériaux de stockage, afin de déterminer les conditions de fonctionnement appropriées et d'améliorer les performances des matériaux existants; (ii) développer les outils thermodynamiques requis pour l'analyse et l'optimisation des performances d'adsorption, (iii) comprendre le comportement de l'eau à l'échelle microscopique dans les matériaux choisis (zéolithes et ionosilices) en suivant les aspects mécanistiques et énergétiques de l'hydratation de ces solides. Cette dernière étape apparait comme très importante, puisque les mesures macroscopiques résultent généralement des processus se produisant aux échelles inférieures. Afin de déterminer la relation entre structure et performances d'adsorption d'eau pour ces matériaux, ainsi que les mécanismes moléculaires, différentes techniques expérimentales ont été couplées: mesures des isothermes d'adsorption de vapeur d'eau, mesures de calorimétrie en flux de gaz et caractérisation par RMN du solide (^{29}Si). Ces résultats expérimentaux ont ensuite été confrontés aux simulations moléculaires pour tenter de déterminer les mécanismes d'hydratation notamment dans les zéolites. Finalement, un banc d'essai d'adsorption simulant les conditions réelles de stockage thermochimique a été développé

et testé, avant d'être ensuite utilisé pour élucider les paramètres essentiels et envisager une utilisation à l'échelle industrielle.

Dans cette thèse, deux types d'absorbants poreux ont été considérés pour les applications au stockage de l'énergie: la zéolite X (faujasite) à échange d'ions de cérium (sous différents degrés d'oxydation) et de nouveaux matériaux (ionosilices) hybrides et amorphes possédant également des ions compensateurs de charge au sein de la structure.

Le manuscrit de thèse se décompose en une introduction générale, cinq chapitres, une conclusion et des perspectives.

Le chapitre 1 présente tout d'abord les généralités sur le stockage de l'énergie thermique et, plus concrètement, une étude bibliographique sur l'état de l'art du stockage thermochimique à basse température principalement basé sur l'adsorption de la vapeur d'eau contenue dans l'air humide par des adsorbants poreux dans le cadre de systèmes de sorption ouverts. Ce chapitre nous oriente vers les deux types d'adsorbants poreux choisis (zéolites et ionosilices), qui possèdent les propriétés requises, et se prépare à révéler leur potentiel en tant que matériaux de stockage thermochimiques.

Au cours du chapitre 2, nous détaillons nos stratégies pour la synthèse et la modification des matériaux. L'idée générale vise à exploiter l'énergie d'hydratation élevée des espèces ioniques compensatrices de charge, afin d'améliorer leurs performances en tant qu'adsorbants de vapeur d'eau. Les méthodes de caractérisation structurale, texturale et thermodynamique sont décrites ainsi que nos stratégies d'étude des mécanismes d'adsorption de la vapeur d'eau dans les deux types de matériaux.

Les chapitres 3 et 4 présentent les résultats de la caractérisation des deux adsorbants sélectionnés. Diverses techniques ont été appliquées pour caractériser les propriétés texturales et structurales des adsorbants, ainsi que leur affinité pour la vapeur d'eau, afin de mieux comprendre le mécanisme d'adsorption d'eau et l'évolution des échantillons solides lors de la

sorption. Les échantillons ont également été soumis à plusieurs cycles d'hydratation-déshydratation dans un calorimètre à flux de gaz et les effets thermiques correspondants accompagnant les étapes d'hydratation ultérieures ont été mesurés. Le but de cette caractérisation est de comparer les deux types de systèmes de sorption et notamment les performances thermiques globales et la stabilité du cycle. L'effet de la nature des ions compensateurs sera particulièrement souligné dans la présentation des résultats.

Dans le dernier chapitre 5, certains paramètres clés du processus de stockage à grande échelle du stockage thermochimique sont détaillés et discutés, grâce au travail de caractérisation effectué sur un montage à l'échelle du laboratoire, en utilisant plusieurs grammes de solide dans les conditions réelles de fonctionnement utile.

Enfin, dans une conclusion générale, les principaux résultats de ce travail de thèse sont rappelés et les perspectives et expérimentations complémentaires à mener pour aller plus loin dans la thématique sont présentées.

Chapitre I

Le chapitre 1 est essentiellement présenté sous la forme d'une revue. Dans cette revue, nous avons montré que le stockage thermochimique à basse température (température d'activation des solides inférieure à 150 °C) basé sur l'adsorption de la vapeur d'eau, issue de l'air humide, par des adsorbants poreux dans des systèmes de sorption ouverts, constitue une alternative prometteuse. Cette conclusion tient compte de l'utilisation croissante des énergies renouvelables, l'amélioration de l'efficacité énergétique et la réduction des effets de serre, parmi les différentes technologies de stockage thermique détaillées dans la littérature scientifique et technique. Outre l'avantage d'utiliser un adsorbat «vert» et économique à faible coût, comme la vapeur d'eau, la densité de stockage d'énergie dépend beaucoup moins de la température de décharge (adsorption), ce qui permet de régler plus facilement l'étape de charge en fonction des besoins de la régénération complète de l'adsorbant, son intégrité structurale ou texturale et sa

stabilité vis-à-vis de l'eau. Plus particulièrement, les systèmes de sorption ouverts fonctionnant dans le mode de flux d'air humide, c'est-à-dire en adsorbant la vapeur d'eau de l'air extérieur, offrent l'avantage de fonctionner à pression atmosphérique et température ambiante. Ce type de fonctionnement évite ainsi des conditions potentiellement néfastes de fortes pressions partielles d'adsorbat combinées à des températures élevées. Néanmoins, cette technologie de stockage thermochimique est encore peu développée et le principal défi reste que le couple adsorbant-vapeur d'eau actif assure une densité énergétique et une efficacité élevées tout en réduisant les coûts d'investissement et d'exploitation. Il est également nécessaire que les risques et les problèmes environnementaux encourus soient minimisés au maximum. Pour cela, le choix des matériaux doit être soigneusement adapté aux conditions réelles d'utilisation.

Chapitre II

Comme indiqué dans la revue, les matériaux synthétiques possédant une porosité uniformément structurée avec des surfaces spécifiques élevées et un caractère de surface (caractère hydrophile-hydrophobe notamment) ajustable semblent répondre à ces exigences et constitueront certainement les adsorbants du futur. En comparant les différents types de matériaux, deux familles d'adsorbants poreux apparaissent comme prometteurs et sont sélectionnés pour le présent travail: la zéolite de type faujasite et l'ionosilice. La zéolite de type faujasite a déjà fait ses preuves comme adsorbant de vapeur d'eau prometteur grâce à sa porosité élevée, à son affinité et à sa sélectivité vis-à-vis de l'adsorbat en faveur de l'eau et à sa résistance à long terme aux cycles répétés de chargement et de déchargement. Contrairement aux zéolithes qui ont été bien étudiées, les ionosilices constituent une famille de nouveaux matériaux hybrides et amorphes à base de silice qui n'a jamais été étudiée pour l'application de stockage de chaleur. Le seul travail relatif à leur aptitude à l'adsorption de vapeur d'eau a mis en évidence un potentiel intéressant : la mesure d'une isotherme d'adsorption d'eau de forme progressive permettant d'absorber de petites quantités de vapeur d'eau aux basses pressions de vapeur et de

grandes quantités de vapeur d'eau à des pressions plus élevées. Ce comportement peut être particulièrement intéressant dans le cas du stockage thermochimique à basse température afin d'éviter des problèmes lors de la régénération de l'adsorbant ou du stockage à long terme puisque l'adsorbant entre les étapes de chargement et de déchargement n'aura pas de perte d'activité. D'autres modifications de ces matériaux, tels que l'échange d'ions et la fonctionnalisation de groupe, visent à améliorer les performances de stockage de la chaleur en exploitant l'énergie élevée d'hydratation des espèces ioniques compensatrices portant des charges électriques élevées et présentes dans les matériaux. C'est également une partie de l'idée principale développée pour la présente étude.

Chapitre III

L'accroissement de la densité de stockage de la chaleur par diverses structures à base de zéolites par rapport à d'autres matériaux de stockage a fourni des arguments solides dans le but de leur utilisation potentielle comme adsorbants dans le cadre du stockage thermochimique de l'énergie solaire par adsorption de vapeur d'eau ou réfrigération solaire. La zéolite 13X a été un des premiers adsorbants appliqué pratiquement pour le stockage thermochimique à court terme et à basse température dans le but de proposer un chauffage quotidien des locaux. Néanmoins, certains inconvénients peuvent sérieusement limiter l'action des zéolithes en tant qu'adsorbants efficaces de la vapeur d'eau. En effet, afin de garantir la régénération complète de l'adsorbant, après chaque étape de décharge (adsorption de vapeur d'eau), des conditions de séchage difficiles sont nécessaires. Sans cela, le dégagement de chaleur lors de l'adsorption sera fortement réduit, compromettant ainsi la réversibilité des phénomènes de sorption impliqués et la cyclabilité du processus de stockage. Lorsqu'elles sont soumises à un grand nombre de cycles de séchage-hydratation répétés, les zéolithes de type 13X semblent subir une amorphisation progressive et l'évolution concomitante de la structure des pores. De plus, la migration de cations extra-charpentes entre divers sites cristallographiques accompagnant les séquences

d'hydratation et de déshydratation peut être difficiles à contrôler ou même à gérer. C'est l'idée de base développée dans le cadre de cette thèse, qui cherchait à améliorer la préparation de zéolithes par échange cationique, pour permettre la régénération de l'adsorbant dans des conditions douces et en utilisant des cations compensateurs de charge possédant de fortes enthalpies d'hydratation. La diminution inévitable de la quantité de chaleur libérée lors de l'étape ultérieure d'adsorption pourrait être compensée par la chaleur intégrale accrue de l'adsorption due à une hydratation plus exothermique des cations de compensation extra-charpente.

Grâce aux études expérimentales couplées à la modélisation du mécanisme d'hydratation des zéolithes à échange, l'évolution des profils d'hydratation pour des échantillons échangés de cations contenant des cations trivalents et quadrivalents de cérium (c'est-à-dire Ce^{3+}, Ce^{4+}) est comparée à celle observée pour l'échantillon 13X initial contenant des ions compensateurs Na^{+}. Les propriétés d'adsorption des matériaux sont déterminées sur la base des mesures des isothermes d'adsorption à l'équilibre pour la vapeur d'eau et des chaleurs d'adsorption différentielles et intégrales correspondantes, obtenues dans des conditions statiques et dynamiques. L'analyse de raffinement de Rietveld des diagrammes de diffraction des rayons X et les simulations Monte Carlo dans l'ensemble Grand Canonical sont également exploitées dans le but d'améliorer la compréhension du mécanisme d'hydratation au niveau moléculaire et notamment comprendre l'impact des molécules d'eau sur la mobilité des cations compensateurs. Le but de cette approche est de vérifier dans quelle mesure les cycles de séchage-hydratation peuvent être contrôlés avec de tels adsorbants, et donc de fournir les informations précises quant à la possibilité d'éviter une régénération drastique de l'adsorbant, sans réduire considérablement la densité de stockage de chaleur. Ces résultats et la discussion connexe sont également présentés sous forme de manuscrit écrit qui sera soumis au journal *Microporous and Mesoporous Materials*.

Inspirée de l'idée de profiter de la chaleur dégagée par l'adsorption physique de vapeur d'eau dans les micropores des zéolites, ainsi que de l'enthalpie supérieure d'hydratation des cations multivalents, la zéolite de type Faujasite 13X a été testée comme adsorbant à la vapeur d'eau en vue d'utilisations potentielles, dans le stockage thermochimique de l'énergie solaire. Trois zéolithes Ce-X (Ce2-13X, Ce3-13X et Ce4-13X) ont ainsi été préparées par échange d'ions. Les échantillons résultants consistent en une armature de zéolite 13X et en des cations compensateurs de charge extra-réseau trivalents ou tétravalents (Ce^{3+} et Ce^{4+}). En combinant la caractérisation DRX in situ et l'affinement Rietveld, nous avons démontré que les cations compensateurs migrent faiblement de leurs sites préférentiels I' et II du réseau de la zéolite 13X au cours du processus d'hydratation. Les simulations Monte Carlo réalisées sur les structures comparables aux Ce-X confirment ces observations, puisque seulement quelques cations se localisent près des supercages, du fait de la plus grande énergie d'hydratation des sites. Les mesures calorimétriques traduisent un gain significatif en chaleur d'adsorption sur les zéolites Ce-13X par rapport au système commercial, malgré la présence résiduelle de certaines molécules d'eau dans l'adsorbant à la suite de l'étape de déshydratation sous vide. Ce4-13X est capable de libérer plus de 1100 kJ par kg de solide, tandis que 13X saturé en Ce^{3+} fournit environ 950 kJ par kg de solide. Comparées à une zéolithe 13X saturée par des cations Na^{+}, ces valeurs correspondent à une augmentation de 37,5% et 18,8%, respectivement. Cependant, après une régénération plus basse de la température de désorption (sans traitement sous vide et à 353 K), seuls 700 kJ par kg de solide peuvent être récupérés aux deuxième et troisième cycles pour toutes les zéolithes Ce-X. Les tests statiques d'adsorption de vapeur d'eau montrent également que les performances d'adsorption de Ce-X contenant Ce^{4+} sont inférieures aux prévisions en raison d'une désorption incomplète due à la très forte affinité de Ce^{4+} pour les molécules d'eau. Par conséquent, un matériau plus adapté aux conditions de régénération

douces est ensuite envisagé, à des fins de stockage thermochimique et pour une activation à basse température.

Chapitre IV

Les matériaux amorphes ionosilices se caractérisent par une adsorption importante de vapeur d'eau et de bonnes capacités de cyclage (vis-à-vis de l'adsorption d'eau), ainsi que par leur caractère hydrophobe-hydrophile de surface ajustable, du fait de la présence de groupes fonctionnels modulaires. Malgré ces avantages, aucune recherche spécifique concernant le stockage de chaleur n'a été effectuée à ce jour sur ces matériaux.

Nous avons alors révélé, dans ces travaux de thèse, le potentiel des ionosilices en tant que matériaux de stockage thermochimique, en examinant les conditions de leur activation/régénération, leurs propriétés de sorption vis-à-vis de la vapeur d'eau et leur stabilité aux cycles de sorption. En outre, comme aucune étude systématique n'avait été entreprise sur le comportement de ces adsorbants, nous avons essayé d'éclairer davantage la caractérisation sur la compréhension des mécanismes par lesquels la vapeur d'eau s'absorbe sur les ionosilices. Nous avons ainsi montré clairement le potentiel de ces matériaux pour l'utilisation de stockage de chaleur à long terme. Trois échantillons d'ionosilices contenant des fractions d'ammonium et différents contre-ions (Cl^-, SO_4^{2-} ainsi qu'un mélange de Cl^- et de SO_4^{2-}) obtenus par fonctionnalisation grâce à une protonation acide ou un échange d'anions ont été testés dans des expériences d'adsorption effectuées en conditions statique ou dynamique. Les principales conclusions tirées de ces études peuvent être résumées comme suit:

• Bien que possédant une structure poreuse faiblement développée, les ionosilices peuvent fournir une chaleur d'adsorption de l'ordre de 700 à 800 kJ par kg de solide, cette chaleur pouvant être obtenue après une régénération relativement douce, c'est-à-dire un chauffage à 353 K sous un flux de He, au lieu d'un traitement sous vide à 423 K.

• Les ionosilices présentent une bonne réversibilité lors de quelques tests d'hydratation-déshydratation répétés (au moins jusqu'à 3 cycles) et le dégagement de chaleur s'étale sur plusieurs heures, ce qui peut constituer un atout majeur pour les applications de stockage thermochimique.

• La RMN du ^{29}Si à l'état solide fournit une preuve que les ponts siloxane sur l'ionosilice ISA100 échangée sulfate sont plus faciles à ouvrir et à transformer en groupes silanol, conférant ainsi un caractère plus hydrophile à la surface. La polarisabilité du contre-ion apparaît donc comme un facteur important pour ajuster l'équilibre de surface hydrophobe-hydrophile et l'enthalpie d'hydratation plus élevée des anions sulfates devrait également permettre d'augmenter la chaleur dégagée lors de l'adsorption de la vapeur d'eau et, par conséquent, la quantité d'énergie stockée par unité de masse de l'adsorbant.

• La séquence d'hydratation obtenue dans les ionosilices comprend une étape importante d'hydroxylation réversible, qui permet à l'adsorbant d'ajuster ses propriétés d'adsorption lorsqu'il passe de l'état de basses pressions relatives de vapeur d'eau à l'état d'hydratation élevée. Cette transition entre le caractère hydrophobe et hydrophile de la surface doit être considérée comme avantageuse pour le stockage de chaleur à long terme.

Chapitre V

Les matériaux sélectionnés pour le stockage thermochimique à long terme, à savoir les zéolithes FAU (Ce-13X) et les ionosilices (DSM19, ISA8 et ISA100) à échange d'ions, ont déjà été analysés à l'aide de diverses techniques de caractérisation à l'échelle micro et mésoscopique, afin d'évaluer leur capacité d'absorption de la vapeur d’eau et celle de dégager, de manière réversible, de la chaleur lorsqu’il est soumis à des cycles de séchage-hydratation. L’objectif suivant était de développer un banc d’essai à l’échelle du laboratoire, envisagé pour évaluer les performances thermiques des adsorbants dans des conditions d’écoulement. Les résultats des tests sont consignés et discutés dans le but de caractériser les matériaux de stockage de la

chaleur dans des conditions d'utilisation plus réalistes, ce qui pourrait permettre, à l'avenir, de stocker la chaleur thermochimique à basse température par sorption dans le chauffage domestique.

L'accent a été mis sur la cinétique de dégagement de chaleur lors de l'adsorption de vapeur d'eau et sur les facteurs physiques qui régissent la performance thermique des matériaux développés et caractérisés dans les chapitres précédents. Notre volonté était de réaliser une expérimentation proche des conditions réelles de fonctionnement en vue d'applications potentielles dans le stockage thermochimique de l'énergie à basse température. Sur la base des modèles classiques de transfert de chaleur dans divers milieux, la dimension du réacteur, la conductivité thermique du matériau de construction et le débit d'un flux de gaz ont d'abord été identifiés comme les paramètres clés ayant un impact prédominant sur les performances globales de transfert de chaleur. Afin de maximiser l'élévation de température, il est apparu nécessaire de réduire les pertes de chaleur par conductivité et d'améliorer le processus de convection de chaleur.

Les modifications du schéma de dégagement de chaleur provoquées par l'augmentation du débit de gaz ont d'abord été étudiées pour DSM19 par calorimétrie à écoulement de gaz. Conformément aux attentes précédentes, la cinétique de dégagement de chaleur est apparue plus rapidement avec l'augmentation des débits. Les tests de calorimétrie ultérieurs effectués avec les échantillons de zéolite et d'ionosilice, soumis à la même procédure d'activation, ont révélé un dégagement de chaleur plus progressif et régulier dans le cas d'ionosilices par rapport à l'échantillon de zéolite Ce2-13X. Cette information est importante pour la conception future des unités de stockage et plaide en faveur de l'utilisation de systèmes hybrides combinant les deux types de comportement différents des zéolithes et des ionosilices.

À l'étape suivante, un banc d'essai à l'échelle du laboratoire a été mis au point pour évaluer les performances thermiques des adsorbants dans des conditions d'écoulement.

L'objectif principal des tests de débit était de surveiller en permanence l'élévation de la température de l'azote gazeux sortant du réacteur et de mieux comprendre l'impact des paramètres précédemment sélectionnés sur cette performance thermique. L'essai préliminaire réalisé avec l'utilisation de 8 g de 13X placés dans un réacteur en verre à un débit de gaz de 2 L h^{-1} a donné une très basse augmentation de température de 3 K. En passant à un réacteur en PVC et en augmentant le débit de 30 L h^{-1}, l'augmentation de température atteinte à 35 K. Ce résultat confirme encore l'hypothèse de l'importance de la conductivité thermique des matériaux de construction et du débit de gaz dans un processus de stockage.

Conclusions générales et perspectives

Pour conclure, il apparait que le stockage de l'énergie solaire pour le chauffage des bâtiments dans le secteur du bâtiment est un élément important des politiques mondiales visant à réduire les émissions de gaz à effet de serre et à mieux contrôler la demande en énergie, car il peut contribuer à atténuer le problème de l'intermittence de cette source d'énergie renouvelable. La présente thèse a donc été consacrée à l'analyse complète d'un potentiel de stockage thermochimique de l'énergie solaire à basse température, basée sur les principes de l'adsorption de vapeur sur des adsorbants solides en vue des utilisations de chauffage des locaux. Un examen critique de l'état de la technique a d'abord été effectué afin d'évaluer les candidats potentiels comme des adsorbants efficaces en se référant strictement au mécanisme d'adsorption possible et aux aspects pratiques de leur application dans des conditions de fonctionnement particulières. Cela a permis d'orienter les recherches vers des systèmes de sorption ouverts fonctionnant dans le flux d'air humide utilisant de la vapeur d'eau, car ils conviennent le mieux à la réalisation de conditions de fonctionnement douces et respectueuses de l'environnement.

L'adsorption de vapeur d'eau sur des échantillons de zéolites sélectionnés a ensuite été testée dans des conditions statiques et dynamiques afin d'améliorer la compréhension du

phénomène d'adsorption et de l'étape de régénération. Il a été démontré, entre autres choses, que la régénération de l'adsorbant effectuée dans des conditions douces de flux d'argon à 423 K (aucun traitement sous vide n'était appliqué) entraînait la présence inévitable de certaines molécules d'eau dans l'adsorbant à la fin de l'étape de déshydratation. Malgré cela, les mesures colorimétriques de la chaleur d'adsorption ont révélé un gain significatif de la chaleur dégagée par rapport à l'échantillon vierge de Na-13X.

Dans un deuxième temps, les échantillons d'ionosilices ont ensuite été fonctionnalisés. Malgré une structure poreuse faiblement développée, les ionosilices pourraient fournir des chaleurs d'adsorption de l'ordre de 700 à 800 kJ par kg de solide pendant une plus longue période de décharge (adsorption) par rapport aux échantillons de zéolite étudiés précédemment. La RMN du ^{29}Si à l'état solide a mis en évidence la présence de groupes silanol (isolés, germinaux et vicinaux) et siloxane à la surface des ionosilices. Les résultats expérimentaux indiquent la séquence suivante de la sensibilité à l'hydratation: T1 (silanol germinal) > T2 (silanol isolé ou vicinal) > T3 (siloxane). Au début du processus d'adsorption, les molécules d'eau ont commencé à s'adsorber sur les groupes silanol via la liaison H, entraînant ainsi un dégagement de chaleur.

Les tests de calorimétrie effectués avec l'utilisation d'échantillons de zéolithe et d'ionosilice dans les mêmes conditions d'activation / régénération ont révélé un dégagement de chaleur plus progressif et régulier dans le cas d'ionosilices (13 à 20 heures) par rapport à l'échantillon de zéolite Ce2-13X (5-6 heures).

En vue d'explorer d'autres moyens de soutenir la mise au point d'unités efficaces pour le stockage thermochimique de l'énergie solaire à basse température, reposant sur les principes d'adsorption en phase vapeur sur des adsorbants solides, il semble important d'examiner attentivement les points suivants:

1) Des travaux de caractérisation plus approfondis sont nécessaires pour quantifier la proportion entre les différents états d'oxydation du cérium (Ce^{3+} et Ce^{4+}) présents aux positions extra-cadre. En particulier, les conditions de préparation optimisées pour augmenter le pourcentage de cations Ce^{4+} doivent être déterminées, car elles produisent des chaleurs d'adsorption plus élevées par rapport aux cations Ce^{3+}. L'utilisation de techniques de caractérisation telles que la spectroscopie photoélectronique à rayons X (XPS) contribuera à améliorer la connaissance de la structure de ce nouveau matériau. Des techniques de dosage chimiques pourraient également être envisagées pour quantifier le cérium et déterminer la charge moyenne de l'ion.

2) Les ionosilices caractérisées dans ce travail semblent très prometteuses comme adsorbants pour le stockage de chaleur. Néanmoins, des doutes subsistent quant à la structure précise de ces matériaux, en particulier en ce qui concerne la structure poreuse et la morphologie de la forme de la fibre observée par microscopie électronique à transmission. La raison de la formation de différentes couches mérite une compréhension approfondie afin de confirmer si cela est dû à la présence d'ions sulfate à double charge. La chimisorption associée à l'utilisation de molécules sondes telles que NH_3 pourrait également apporter des informations utiles sur les forces de liaison à la surface de l'ionosilice, afin de mieux comprendre le processus de création-suppression des liaisons impliquant des silanols.

Ces informations seront sûrement utiles pour les futurs travaux de simulation visant à proposer un champ de force réactif capable de reproduire le mécanisme d'hydratation-déshydratation se produisant dans les ionosilices et la forte interaction entre les cadres. En outre, il conviendrait également de mener plusieurs études comparatives pour d'autres facteurs tels que la quantité de SO_4^{2-} ou la méthode de séchage (par exemple, chauffage au four ou lyophilisation) et leur impact sur la structuration / texture de l'ionosilice.

Pour aller plus loin, il serait préférable d'envisager une forme de matériau maximisant le rapport surface / volume, de manière à bénéficier d'une surface de contact plus grande entre

l'adsorbant et l'adsorbat. À la lumière des propriétés d'adsorption prometteuses présentées par les échantillons d'ionosilice faiblement poreux considérés ici, la possibilité de mettre en forme ces matériaux pour obtenir une plus grande surface, à l'aide de procédures de mise en forme telles que le frittage ou la formation de corps monolithiques à porosité homogène bien définie, peut être une avancée dans l'amélioration de la densité de stockage d'énergie.

3) Le banc d'essai mis au point à l'échelle du laboratoire pour l'évaluation de la performance thermique des adsorbants dans des conditions d'écoulement a prouvé son utilité. Néanmoins, les tests ont été effectués uniquement avec l'échantillon commercial de Na-13X disponible au moment requis en quantités suffisantes. Il est clair qu'une étude comparative de la cinétique de sorption et de l'élévation de température doit être réalisée lors de l'acquisition de quantités au moins similaires de zéolithes et d'ionosilices échangés par du cérium. De plus, la compréhension du comportement des zéolithes contenant Ce^{3+} ou Ce^{4+} à l'échelle du laboratoire devrait également être déterminée.

4) La chaleur sensible des matériaux de stockage est difficile à exploiter. Lorsque la taille du réacteur de l'appareil d'essai à l'échelle du laboratoire devient plus grande, cela ne peut plus être négligeable, ce qui affectera sûrement l'efficacité de l'unité de stockage de chaleur. Par conséquent, il est nécessaire d'utiliser des techniques de caractérisation spécifiques pour mesurer la conductivité thermique et la capacité thermique de chaque matériau afin d'obtenir une estimation plus précise de la performance thermique.

5) En ce qui concerne le futur transfert de technologie d'un laboratoire à un autre, il faut prendre en compte davantage de facteurs influant sur les performances globales du système en fonctionnement lors de la conception. Outre la conductivité thermique des matériaux de construction et le débit de gaz, le choix du type de réacteur doit également être inclus. À titre d'exemple, l'utilisation de réacteurs à lit compacté ou à segments multiples devrait être considérée comme une fonction des besoins réels en chauffage. De plus, la mise en forme

appropriée du matériau de stockage est nécessaire pour limiter la perte de charge à travers le lit d'adsorbant. Compte tenu du comportement à la sorption des échantillons de zéolite et d'ionosilice étudiés dans le présent travail, il est fortement suggéré qu'un système de stockage hybride puisse bénéficier des avantages de chaque type de matériaux. D'après la littérature, un réacteur multi-segments peut utiliser un échantillon de Ce-13X pour obtenir une élévation instantanée de la température, en association avec de l'ionosilice pour obtenir un chauffage plus régulier.

Appendix I

Figure A.I.1. Heat of adsorption released upon adsorption of water vapour onto DSM19 at 296 K with a Helium flow rate of 120 mL h^{-1} in 10 consecutive dehydration-adsorption cycles.

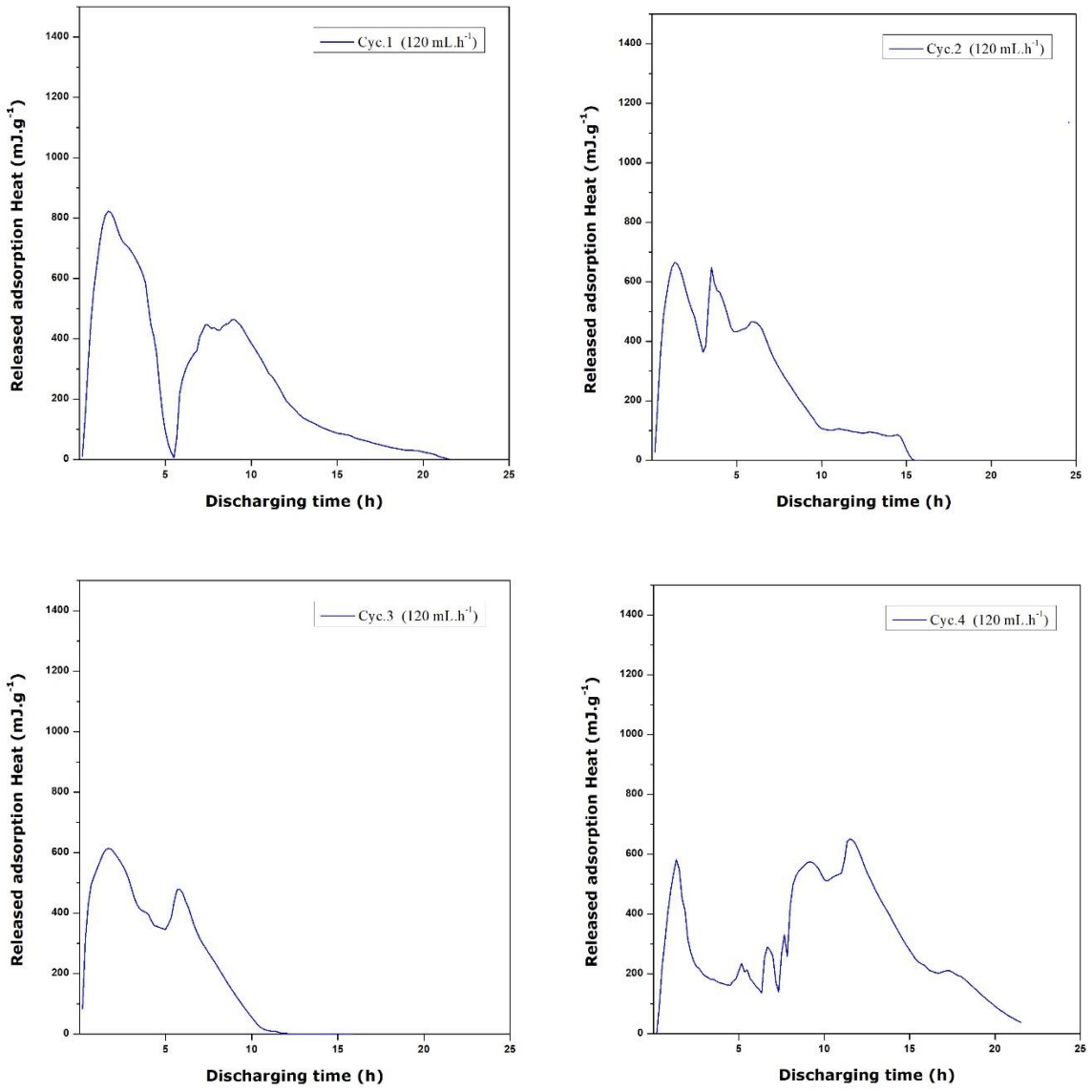

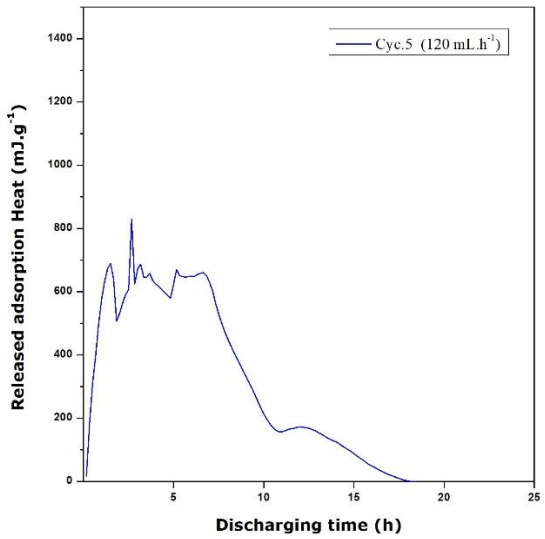
Cyc.5 (120 mL.h-1)
Released adsorption Heat (mJ.g-1)
Discharging time (h)

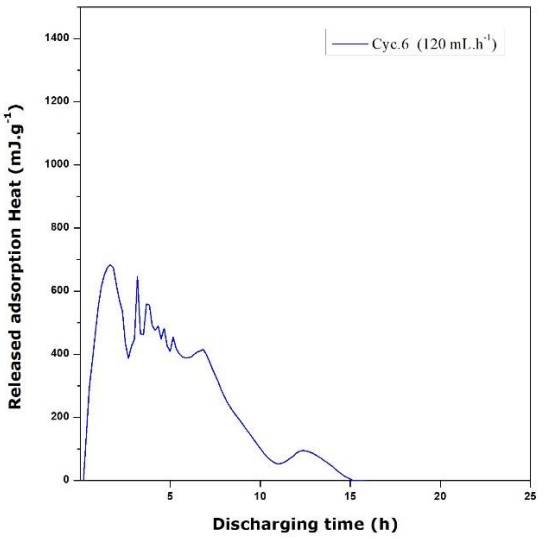
Cyc.6 (120 mL.h-1)
Released adsorption Heat (mJ.g-1)
Discharging time (h)

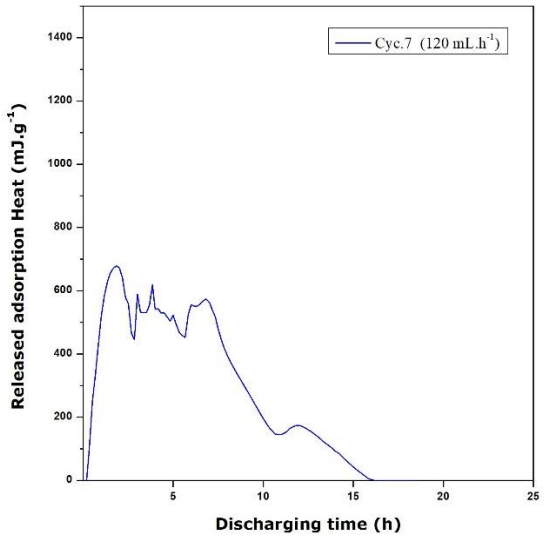
Cyc.7 (120 mL.h-1)
Released adsorption Heat (mJ.g-1)
Discharging time (h)

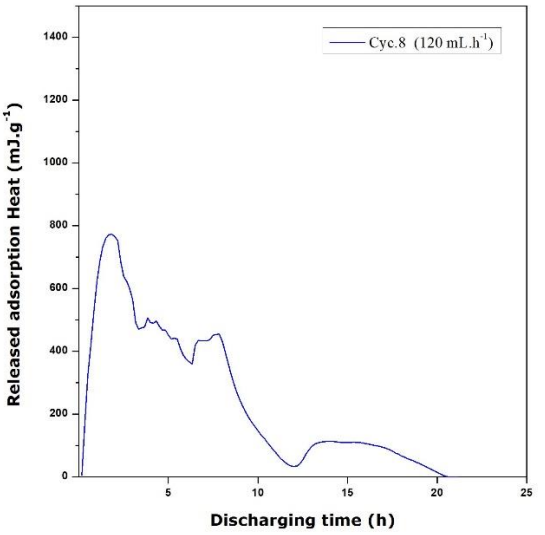
Cyc.8 (120 mL.h-1)
Released adsorption Heat (mJ.g-1)
Discharging time (h)

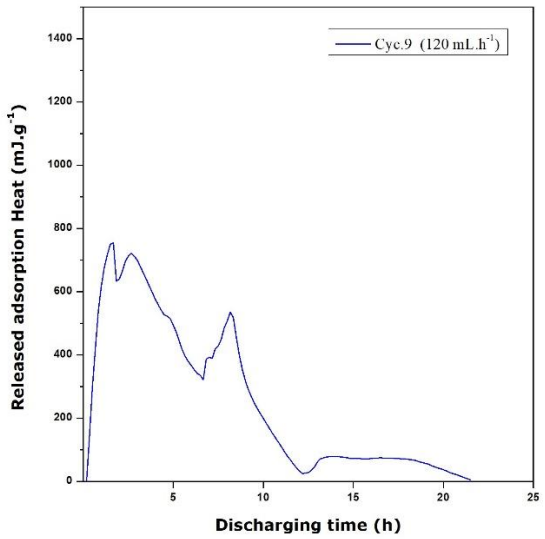
Cyc.9 (120 mL.h-1)
Released adsorption Heat (mJ.g-1)
Discharging time (h)

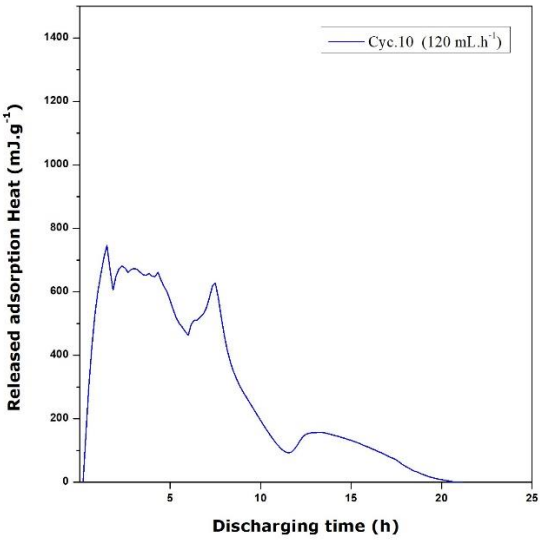
Cyc.10 (120 mL.h-1)
Released adsorption Heat (mJ.g-1)
Discharging time (h)

Figure A.I.2. Heat of adsorption released upon adsorption of water vapour onto DSM19 at 296 K with a Helium flow rate of 210 mL h^{-1} in 10 consecutive dehydration-adsorption cycles.

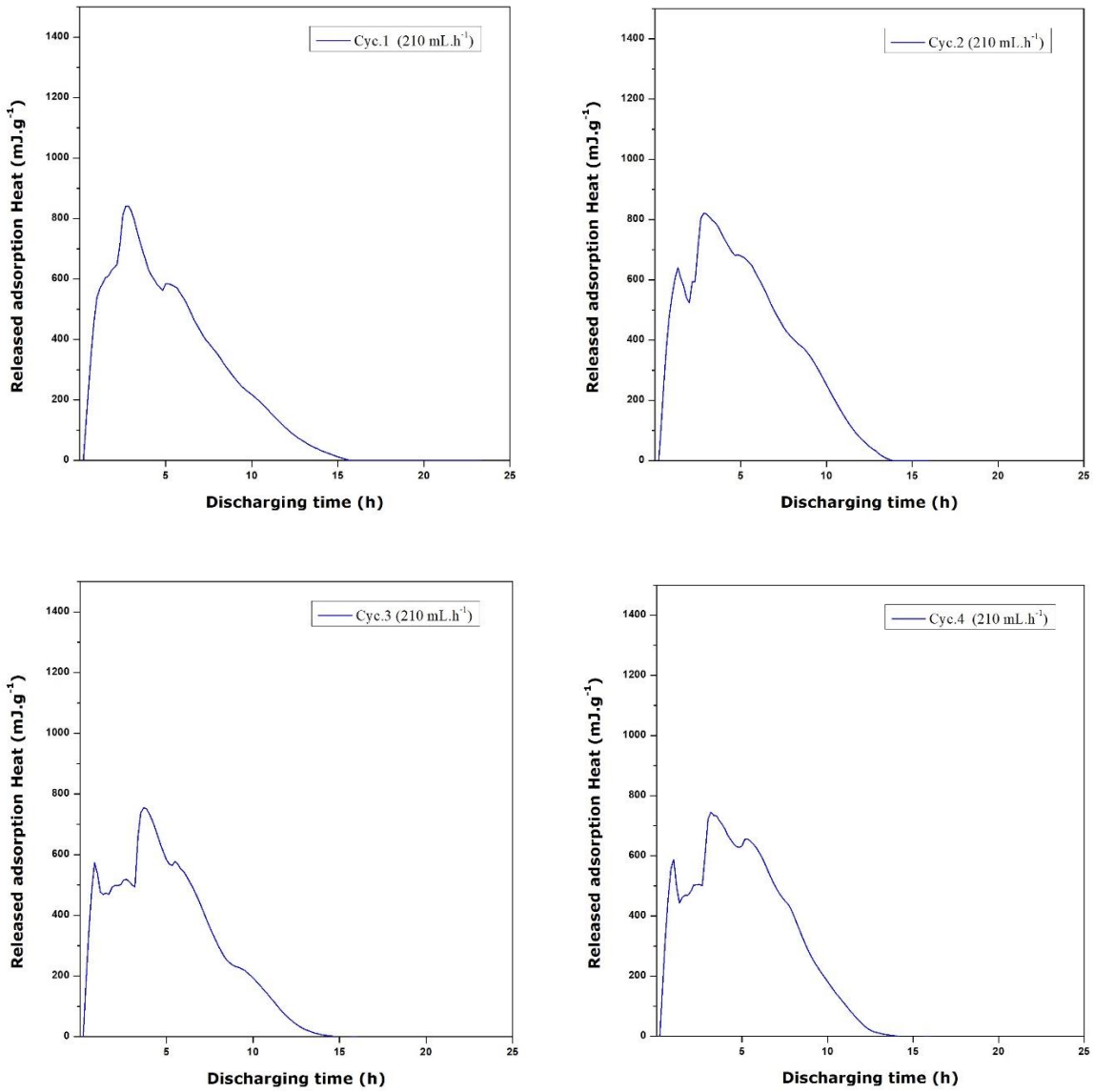

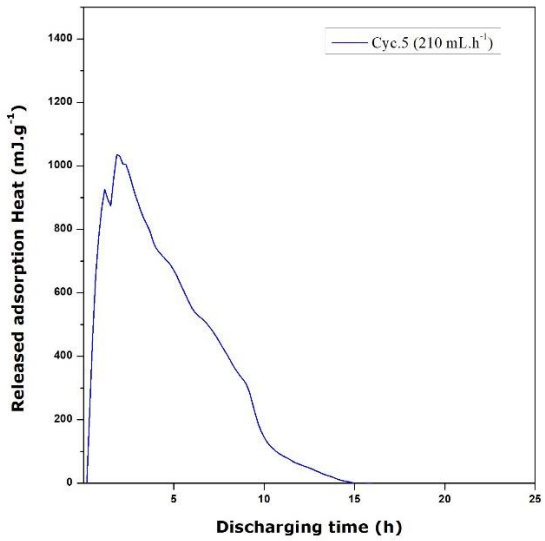
Cyc.5 (210 mL.h-1)
Released adsorption Heat (mJ.g-1)
Discharging time (h)

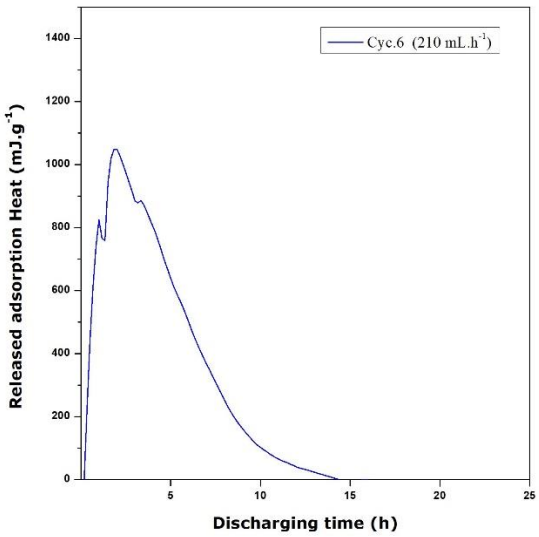
Cyc.6 (210 mL.h-1)
Released adsorption Heat (mJ.g-1)
Discharging time (h)

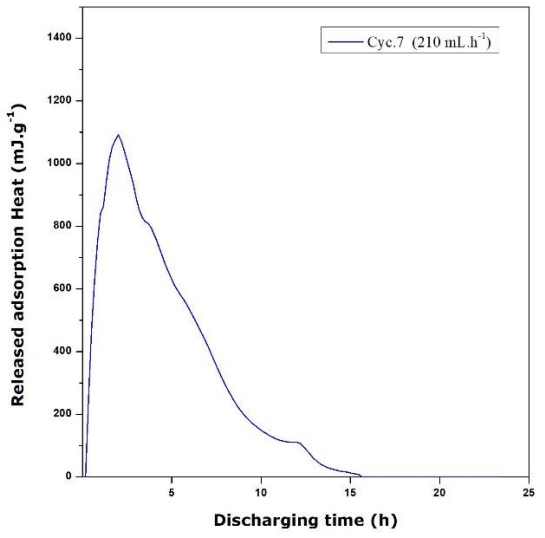
Cyc.7 (210 mL.h-1)
Released adsorption Heat (mJ.g-1)
Discharging time (h)

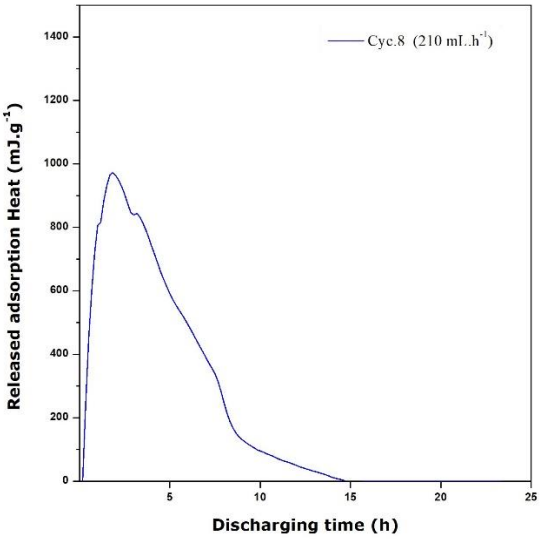
Cyc.8 (210 mL.h-1)
Released adsorption Heat (mJ.g-1)
Discharging time (h)

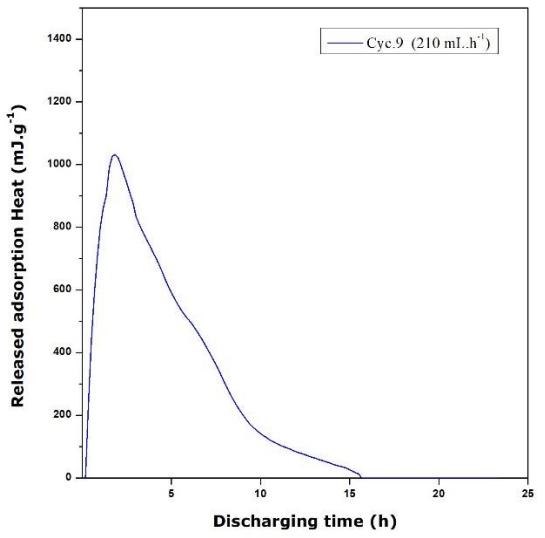
Cyc.9 (210 mL.h-1)
Released adsorption Heat (mJ.g-1)
Discharging time (h)

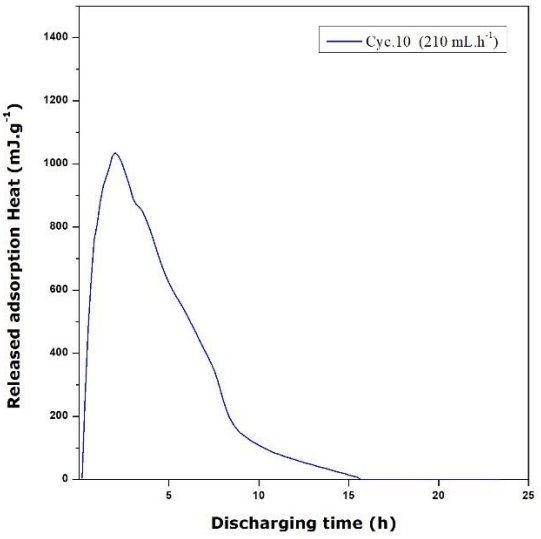
Cyc.10 (210 mL.h-1)
Released adsorption Heat (mJ.g-1)
Discharging time (h)

Figure A.I.3. Heat of adsorption released upon adsorption of water vapour onto DSM19 at 296 K with a Helium flow rate of 300 mL h^{-1} in 10 consecutive dehydration-adsorption cycles.

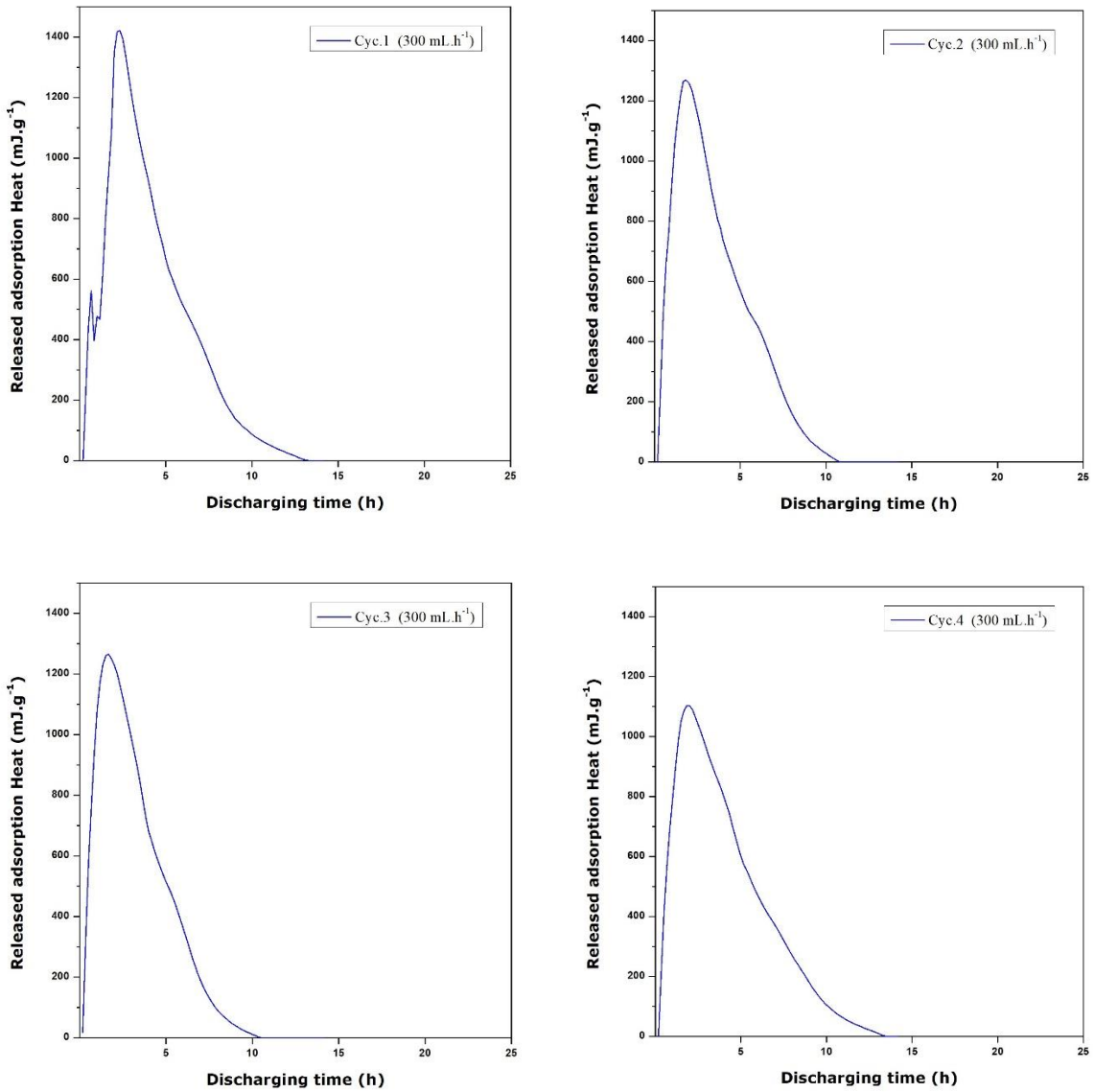

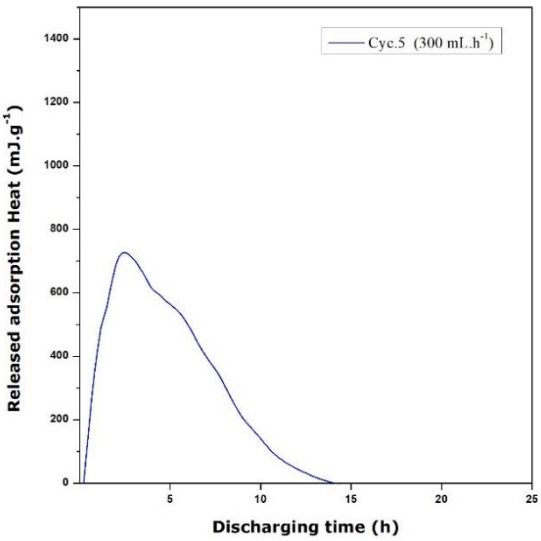
Cyc.5 (300 mL.h-1)
Released adsorption Heat (mJ.g-1)
Discharging time (h)

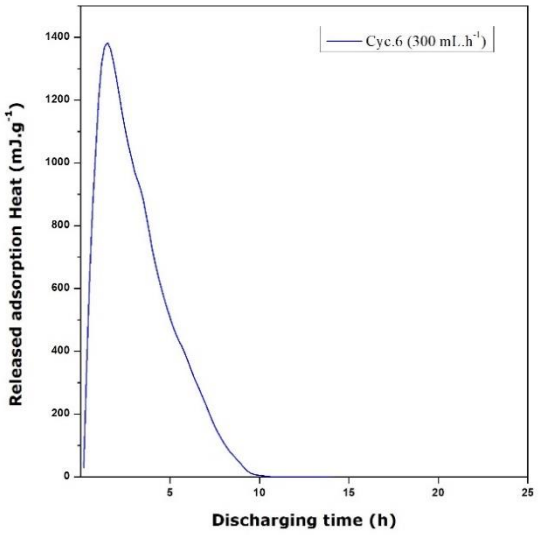
Cyc.6 (300 mL.h-1)
Released adsorption Heat (mJ.g-1)
Discharging time (h)

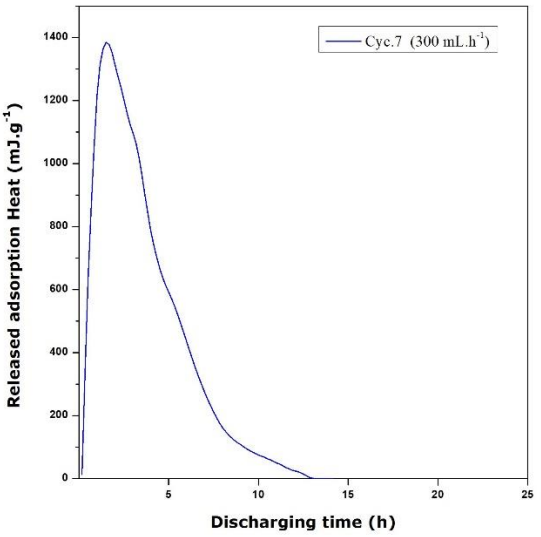
Cyc.7 (300 mL.h-1)
Released adsorption Heat (mJ.g-1)
Discharging time (h)

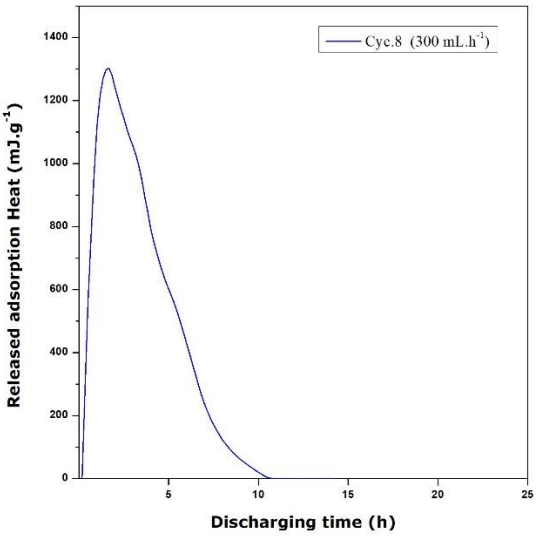
Cyc.8 (300 mL.h-1)
Released adsorption Heat (mJ.g-1)
Discharging time (h)

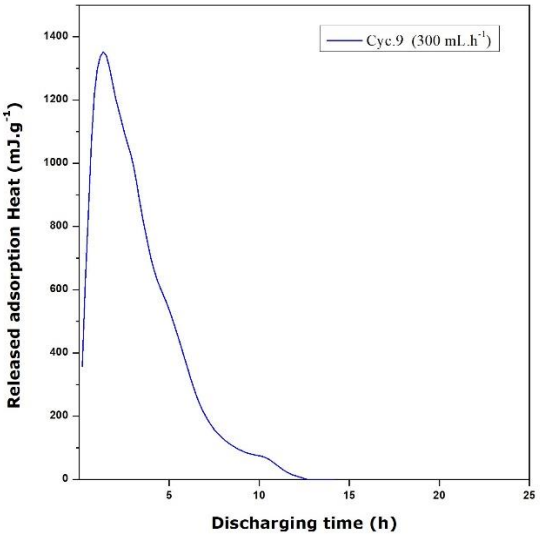
Cyc.9 (300 mL.h-1)
Released adsorption Heat (mJ.g-1)
Discharging time (h)

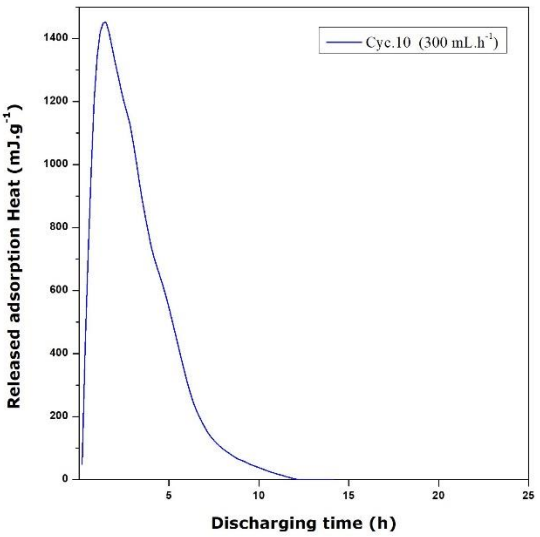
Cyc.10 (300 mL.h-1)
Released adsorption Heat (mJ.g-1)
Discharging time (h)

Figure A.I.4. Heat of adsorption released upon adsorption of water vapour onto Ce2-13X at 296 K with a Helium flow rate of 120 mL h^{-1} in 5 consecutive dehydration-adsorption cycles.

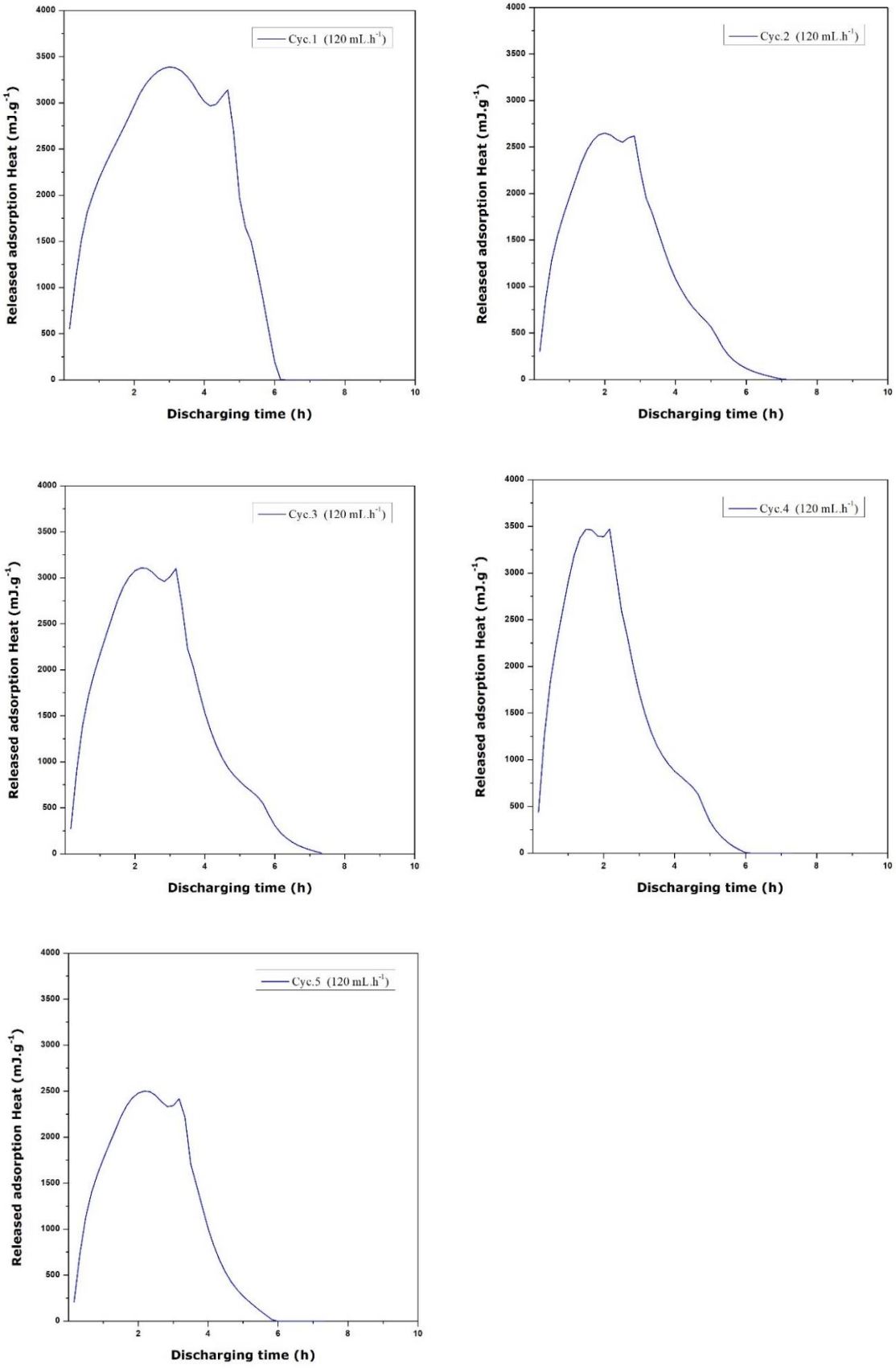

Figure A.I.5. Heat of adsorption released upon adsorption of water vapour onto ISA8 at 296 K with a Helium flow rate of 120 mL h^{-1} in 5 consecutive dehydration-adsorption cycles.

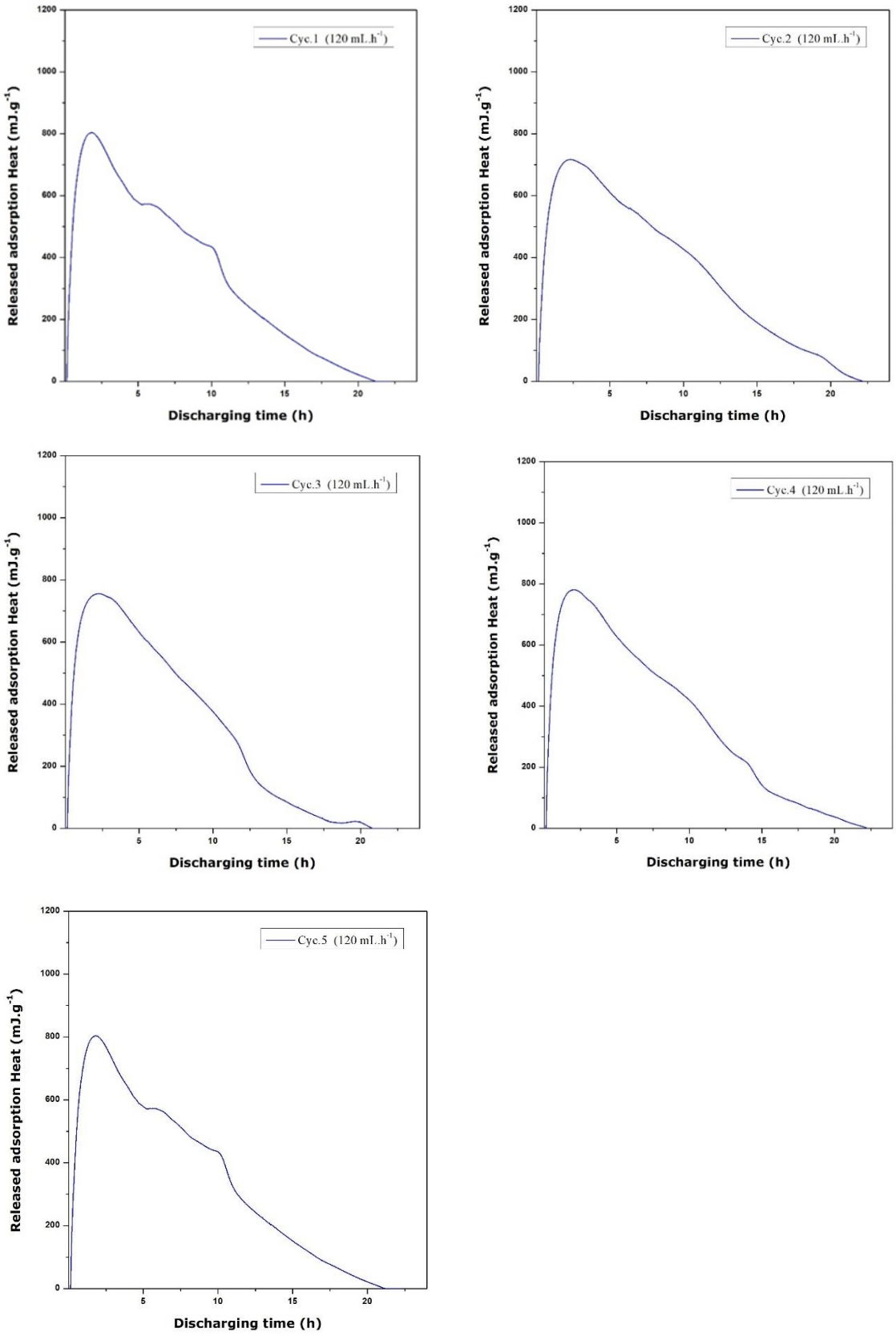

Figure A.I.6. Integral heats of adsorption of water vapour onto DSM19 at 296 K with Helium flow rates of 120 mL h^{-1} , 210 mL h^{-1} and 300 mL h^{-1} in 10 consecutive dehydration-adsorption cycles.

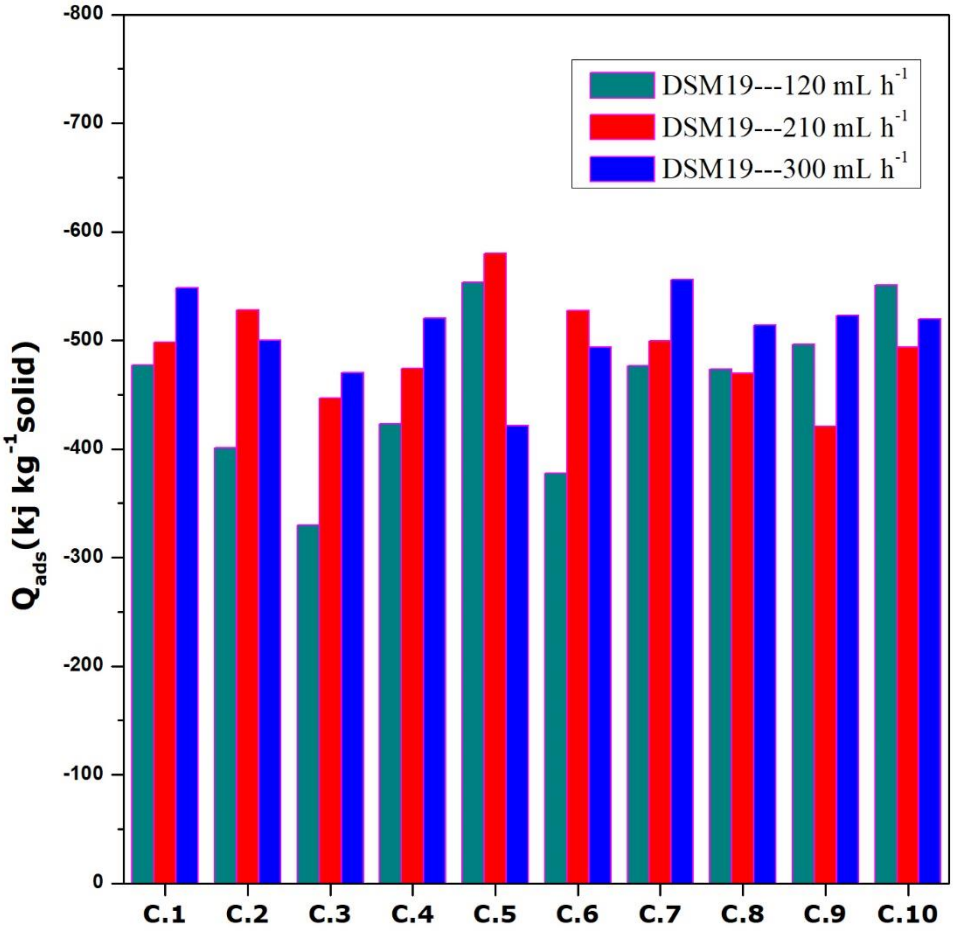

Figure A.I.7. Integral heats of adsorption of water vapour onto ISA8 and Ce2-13X at 296 K with a Helium flow rate of 120 mL h^{-1} in 5 consecutive dehydration-adsorption cycles.

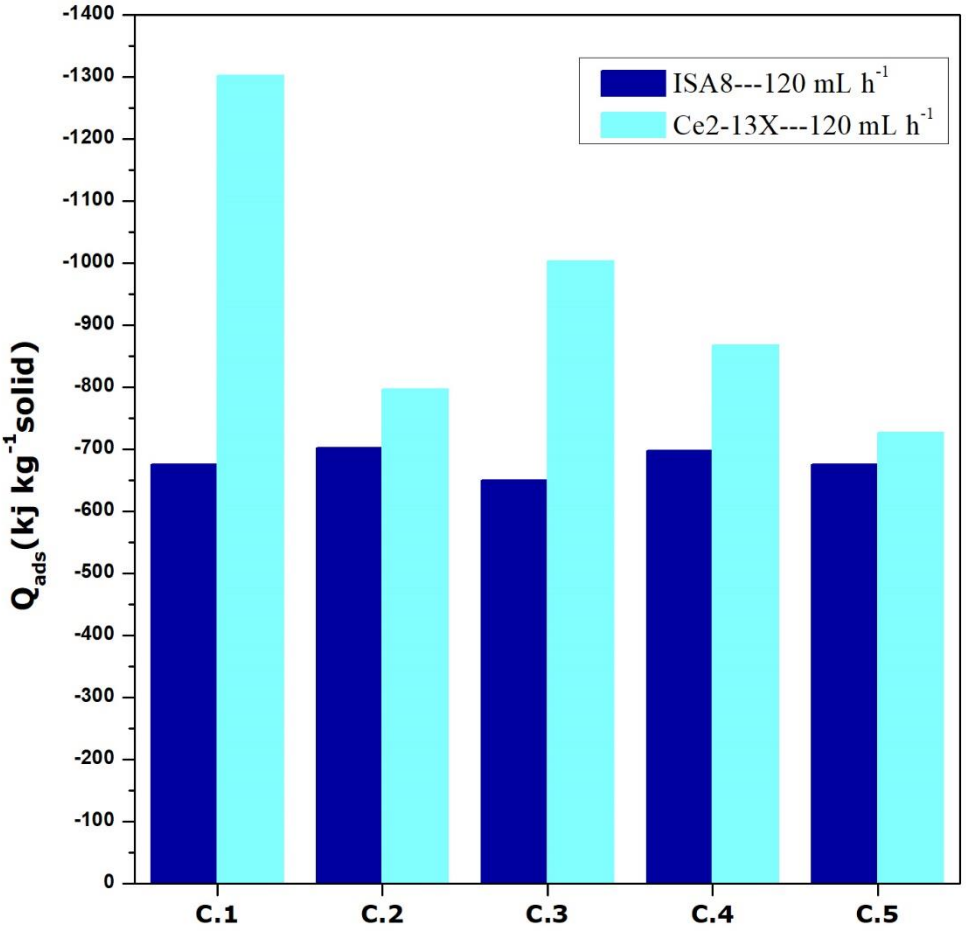

Figure A.I.8. Diagram explaining the processing of the thermal signal generated by the gas flow calorimeter to obtain a thermogram over a reduced time scale.

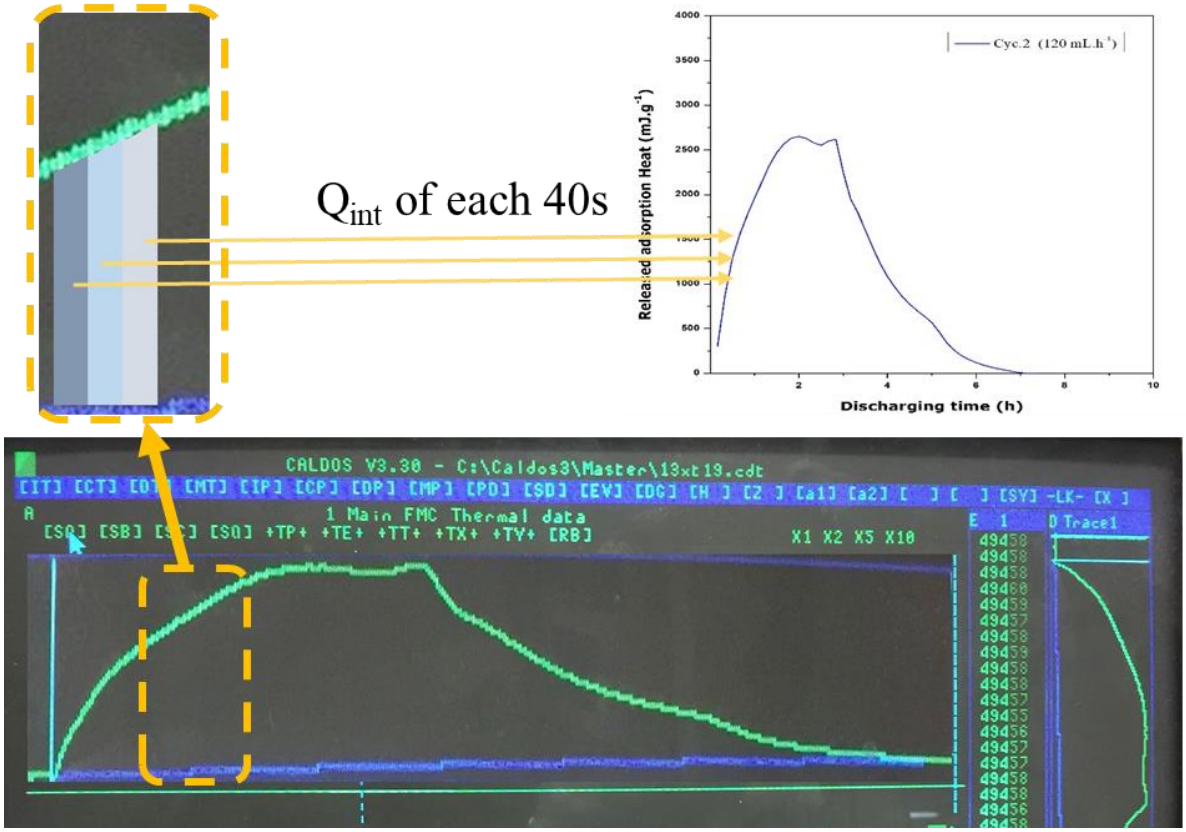

Given the long duration of each calorimetry experiment against reduced recording capacity of the CALDOS software (Microscal Ltd), the thermal signal profiles were processed in a way to obtain reduced thermograms plotted over a reduced time scale. For the purpose of data presentation and further model calculation, the signal profile was divided into time slice intervals of 40 sec each. Then the corresponding profile fragments were integrated, thus resulting in cumulative heat values for successive time slice intervals. These cumulative heat values were subsequently plotted as single points corresponding to the discharging time values taken every 40 seconds.

Appendix II

Supporting Information

for

Comprehensive description of the hydration mechanism in Ce-exchanged zeolites in view of potential uses in low-temperature thermochemical storage of energy

Hao Wu, Philippe Trens, Bernard Fraisse, Fabrice Salles*, Jerzy Zajac*

Institut Charles Gerhardt (ICGM), Université de Montpellier, CNRS, ENSCM. Place Eugène Bataillon, 34095 Montpellier Cedex 5, France,

E-mail: fabrice.salles@umontpellier.fr, jerzy.zajac@umontpellier.fr

Table S1: Partial charges of the zeolite framework atoms, as used in Monte Carlo calculations.

Atom label	Partial charge
Si	2.4
Al	1.4
O	-1.2

Figure S1: DRX diffraction pattern recorded with bulk $Ce(NO_3)_3.4H_2O$ taken from: Milinski, N., Radivojevic, P., Djuric, S., Ribar, B., Crystal Structure Communications, 11, 1241 - 1244, (1982)

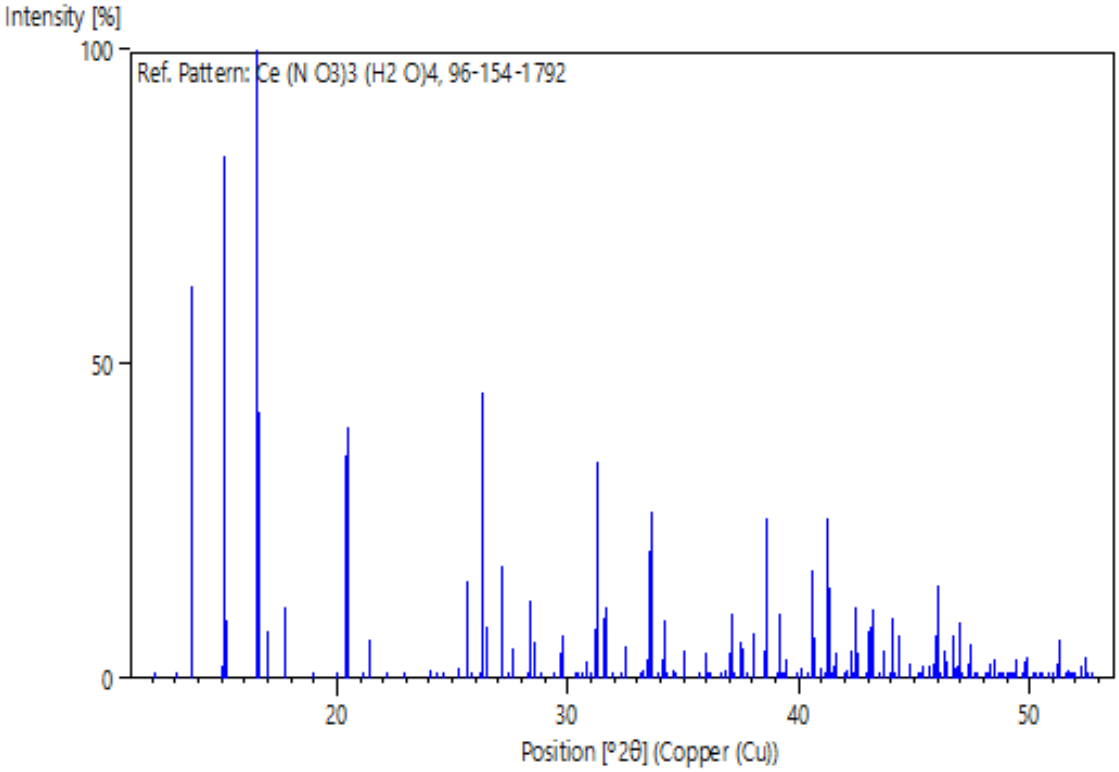

Figure S2: Crystallographic positions of various framework and extra-framework atoms in the Ce-exchanged 13X zeolite, as inferred from the structure refinement procedures on the basis of *in situ* XRD measurements at different temperatures. (x,y,z are the Fractional coordinates; Occ. is the atom site occupancy; U is the atomic displacement parameter; Site is multiplicity of sites; Sym. is the site symmetry)

(a) A typical snapshot of the unit cell at 30 ℃ (view along the c axis)

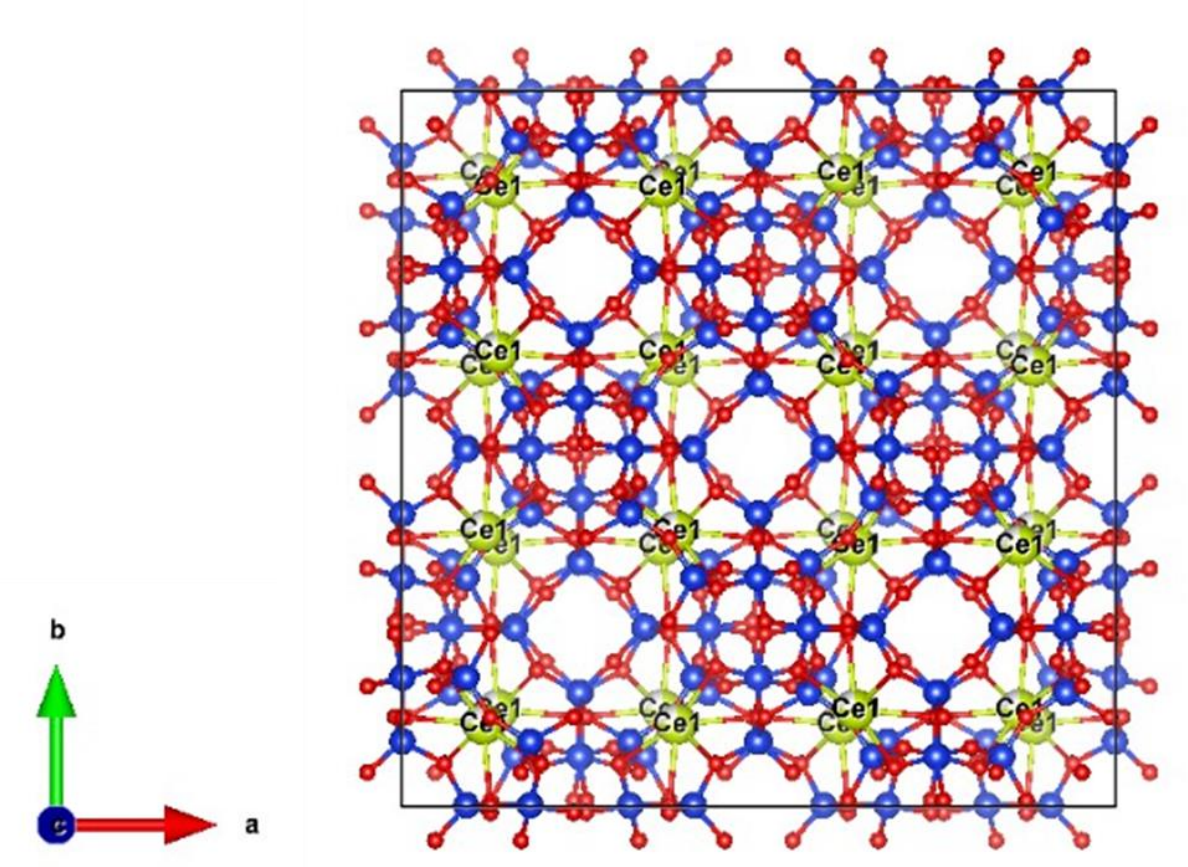

a = 25.06855 Å

			x	y	z	Occ.	U	Site	Sym.
1	Ce	Ce1	0.88569	0.11431	0.11431	1	0.038	32e	.3m
2	Si	Si1	0.99773	0.1787	0.0865	0.57	0.038	192i	1
3	Al	Al1’	0.99773	0.1787	0.0865	0.43	0.038	192i	1
3	O	O4	0.99811	0.12711	0.12711	1	0.038	96g	..m
4	O	O1	0.9425	0.19667	0.0575	1	0.038	96g	..m
5	O	O2	0.24225	0.125	0.00776	1	0.038	96h	..2
6	O	O3	1.04722	0.16779	0.04722	1	0.038	96g	..m

(b) A typical snapshot of the unit cell at 80 ℃ (view along the c axis)

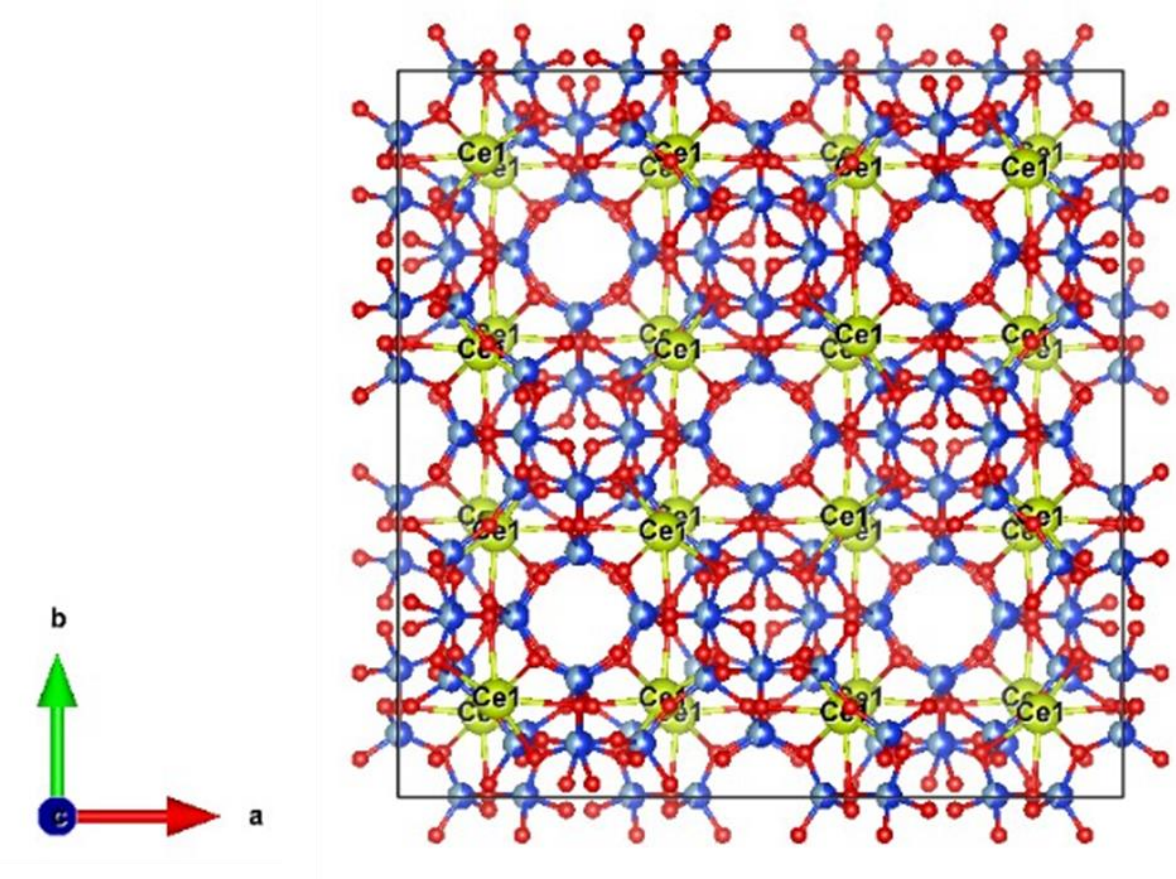

a = 25.02986 Å

			x	y	z	Occ.	U	Site	Sym.
1	Ce	Ce1	0.88502	0.11498	0.11498	1	0.038	32e	.3m
2	Si	Si1	0.8238	0.08777	0.00399	0.57	0.038	192i	1
2	Al	Al1’	0.8238	0.08777	0.00399	0.43	0.038	192i	1
3	O	O1	0.06144	0.06144	0.06144	1	0.038	32e	.3m
4	O	O2	0.87427	0.12573	0.00157	1	0.038	96g	..m
5	O	O3	0.80493	0.06113	0.06113	1	0.038	96g	..m
6	O	O4	0.83583	0.0455	-0.0455	1	0.038	96g	..m
7	O	O5	0.24037	0.125	0.00963	1	0.038	96h	..2
8	Na	X1	0	0	0.5	1	0.038	8b	-43m

(c) A typical snapshot of the unit cell at 150 ℃ (view along the c axis)

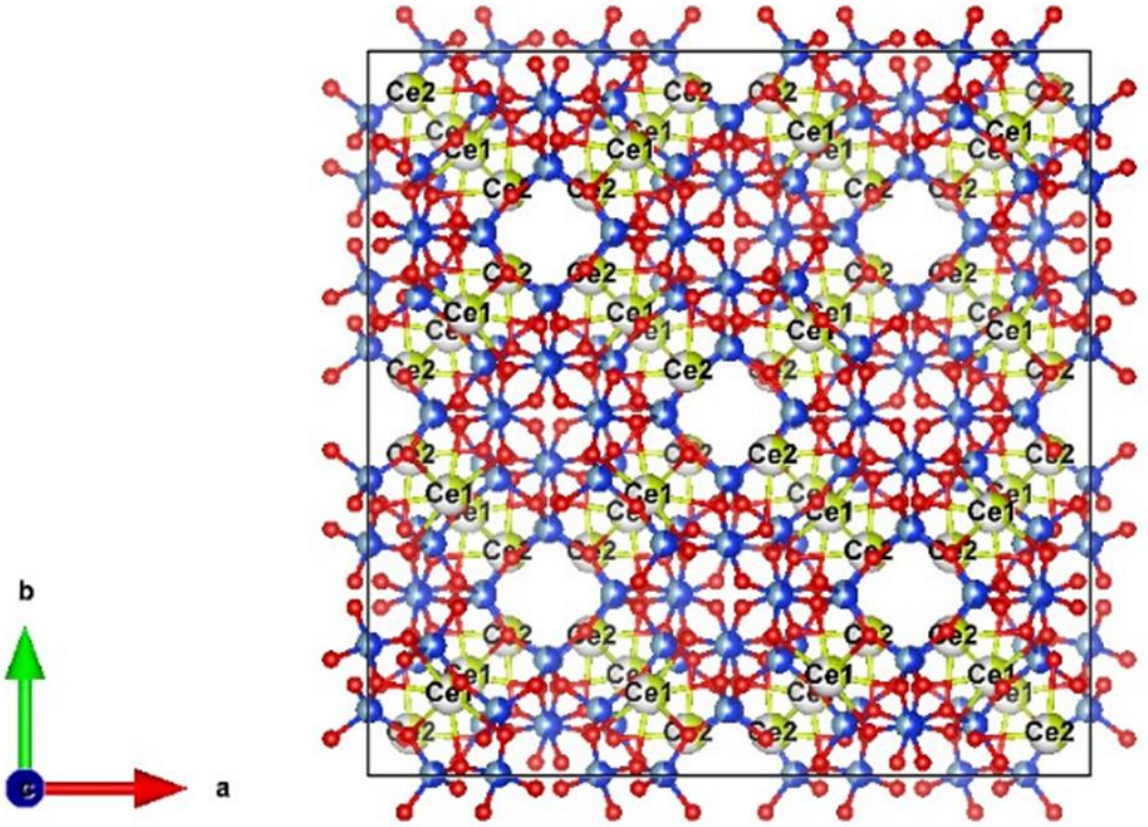

a = 25.06855 Å

			x	y	z	Occ.	U	Site	Sym.
1	Ce	Ce1	0.88745	0.11255	0.11255	0.344	0.044	32e	.3m
2	Si	Si1	0.90979	0.18015	0.00202	0.57	0.038	192i	1
3	Al	Al1'	0.90979	0.18015	0.00202	0.43	0.038	192i	1
4	O	O1	0.94382	0.18922	0.05618	1	0.038	96g	..m
5	O	O2	0.87163	0.12837	0.01207	1	0.038	96g	..m
6	O	O3	0.94925	0.16011	-0.05075	1	0.038	96g	..m
7	O	Ow1	0.03876	0.03876	-0.03876	1.003	0.073	32e	.3m
8	O	O4	0.23214	0.125	0.01786	1	0.038	96h	..2
9	Ce	Ce2	0.44175	0.44175	0.05825	0.399	0.044	32e	.3m
10	O	Ow2	0.90321	0.09679	0.09679	1.065	0.044	32e	.3m
11	O	Ow3	0.665	0.6653	0.1633	0.073	0.044	192i	1

(d) A typical snapshot of the unit cell at 300 ℃ (view along the c axis)

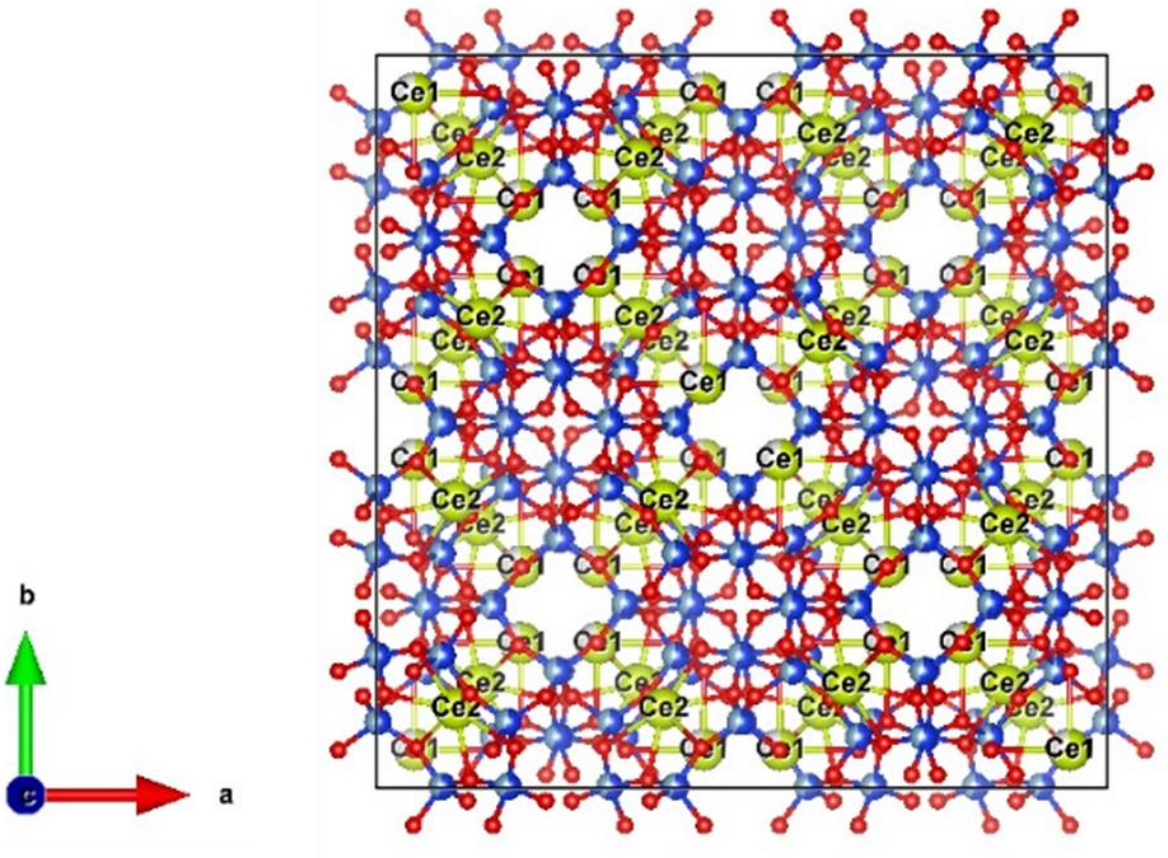

a = 25.08053 Å

			x	y	z	Occ.	U S	ite	Sym.
1	Si	Si1	0.90974	0.18053	0.00221	0.57	0.038	192i	1
2	Al	Al1'	0.90974	0.18053	0.00221	0.43	0.038	192i	1
3	O	O1	0.94473	0.18917	0.05527	1	0.038	96g	..m
4	O	O2	0.87158	0.12842	0.0109	1	0.038	96g	..m
5	O	O3	0.94854	0.15931	-0.05146	1	0.038	96g	..m
6	O	O4	0.23211	0.125	0.01789	1	0.038	96h	..2
7	Ce	Ce1	0.19767	0.30233	0.30233	0.69	0.093	32e	.3m
8	Ce	Ce2	0.14164	0.14164	0.35836	0.135	0.093	32e	.3m

(e) A typical snapshot of the unit cell at 450 ℃ (view along the c axis)

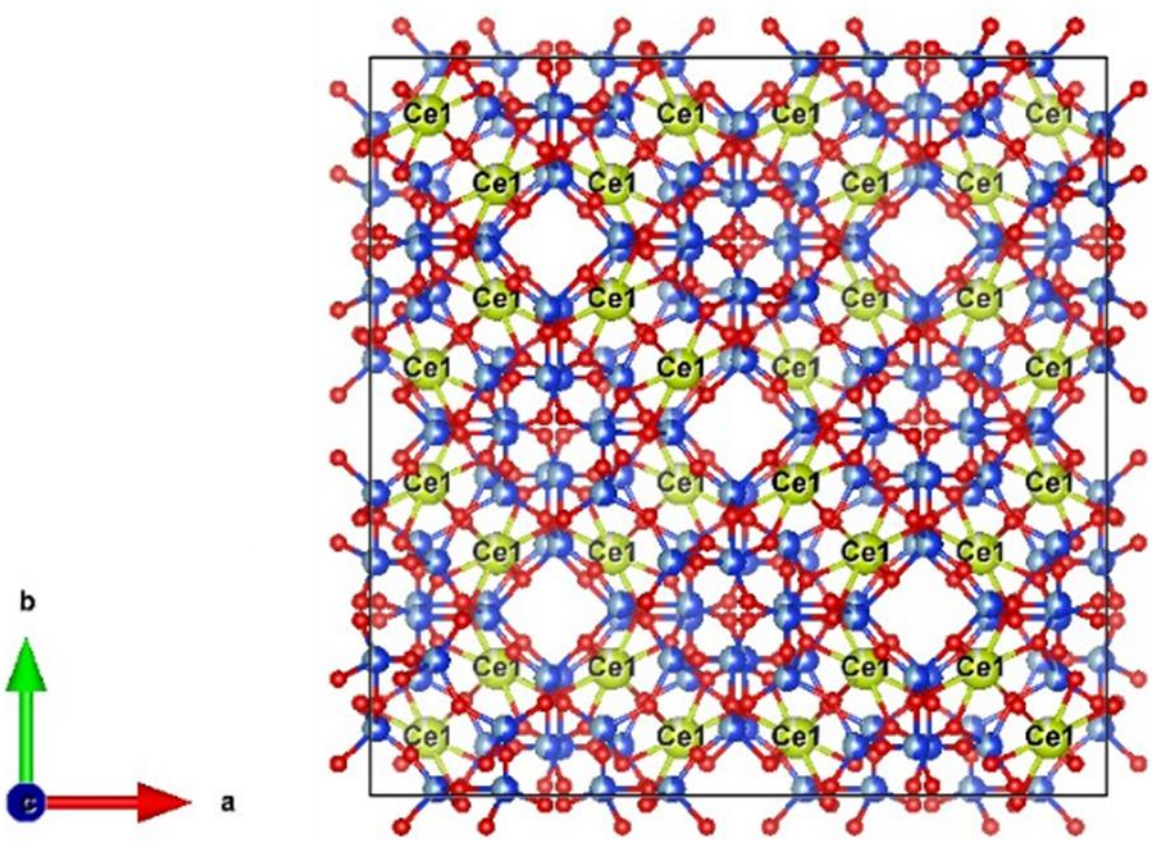

a = 25.11228 Å

			x	y	z	Occ.	U	Site	Sym.
1	Si	Si1	0.90953	0.18357	0.00844	0.57	0.025	192i	1
2	Al	Al1'	0.90953	0.18357	0.00844	0.43	0.025	192i	1
3	O	O1	0.94451	0.18436	0.05549	1	0.025	96g	..m
4	O	O2	0.87876	0.12124	0.00872	1	0.025	96g	..m
5	O	O3	0.95727	0.15759	-0.04273	1	0.025	96g	..m
6	O	O4	0.23741	0.125	0.01259	1	0.025	96h	..2
7	Ce	Ce1	0.92204	0.07796	-0.07796	0.946	0.103	32e	.3m
8	Na	Na1	0.625	0.125	0.125	0.656	0.103	16d	.-3m
9	O	Ow1	0.83111	0.33111	0.33111	0.409	0.103	32e	.3m

(f) A typical snapshot of the unit cell for the sample cooled down to 30 ℃

(View along the c axis)

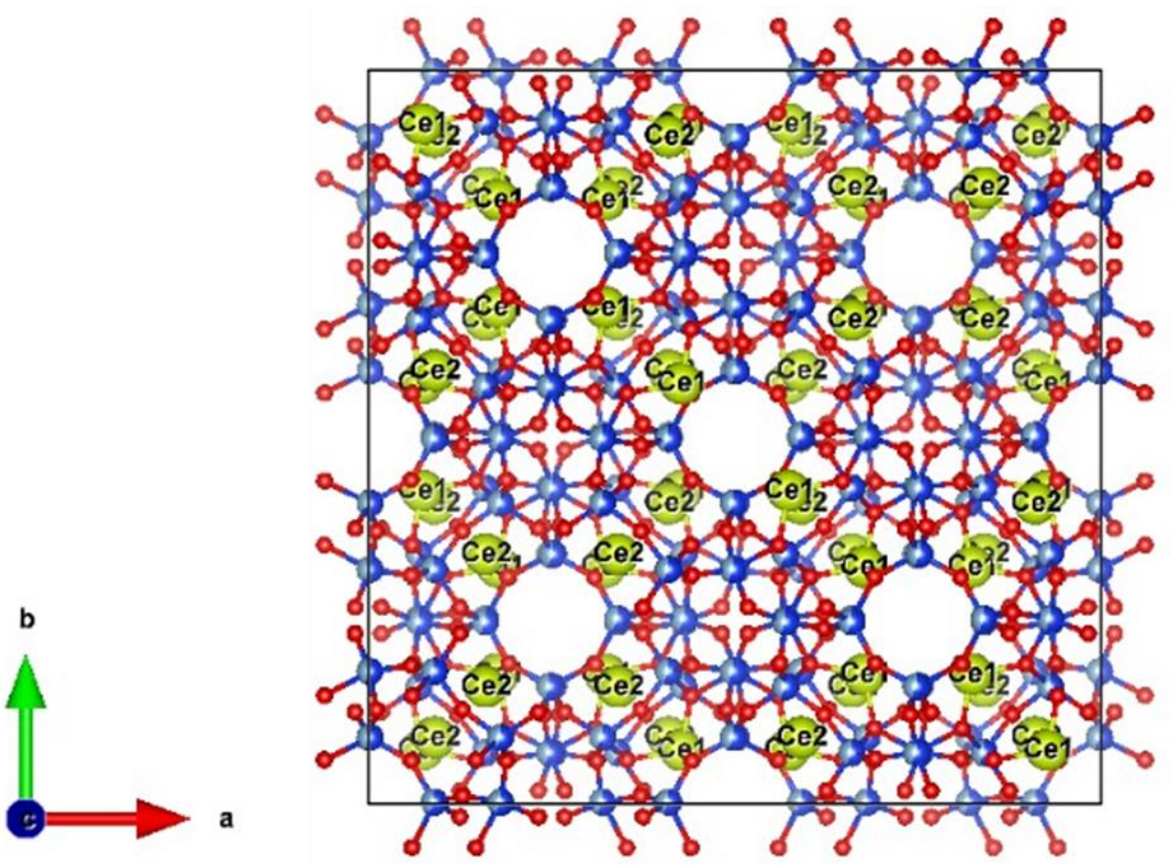

a = 24.97398 Å

			x	y	z	Occ.	U	Site	Sym.
1	Si	Si1	0.90974	0.18053	0.00221	0.57	0.038	192i	1
2	Al	Al1'	0.90974	0.18053	0.00221	0.43	0.038	192i	1
3	O	O2	0.87158	0.12842	0.0109	1	0.038	96g	..m
4	O	O4	0.23211	0.125	0.01789	1	0.038	96h	..2
5	Ce	Ce1	0.92673	0.07327	-0.07327	1.096	0.072	32e	.3m
6	O	O3	0.94023	-0.14716	0.05977	1	0.038	96g	..m
7	O	O1	0.94153	0.18846	0.05847	1	0.038	96g	..m
8	Ce	Ce2	1.1596	0.1596	-0.1596	0.031	0.038	32e	.3m

Appendix III

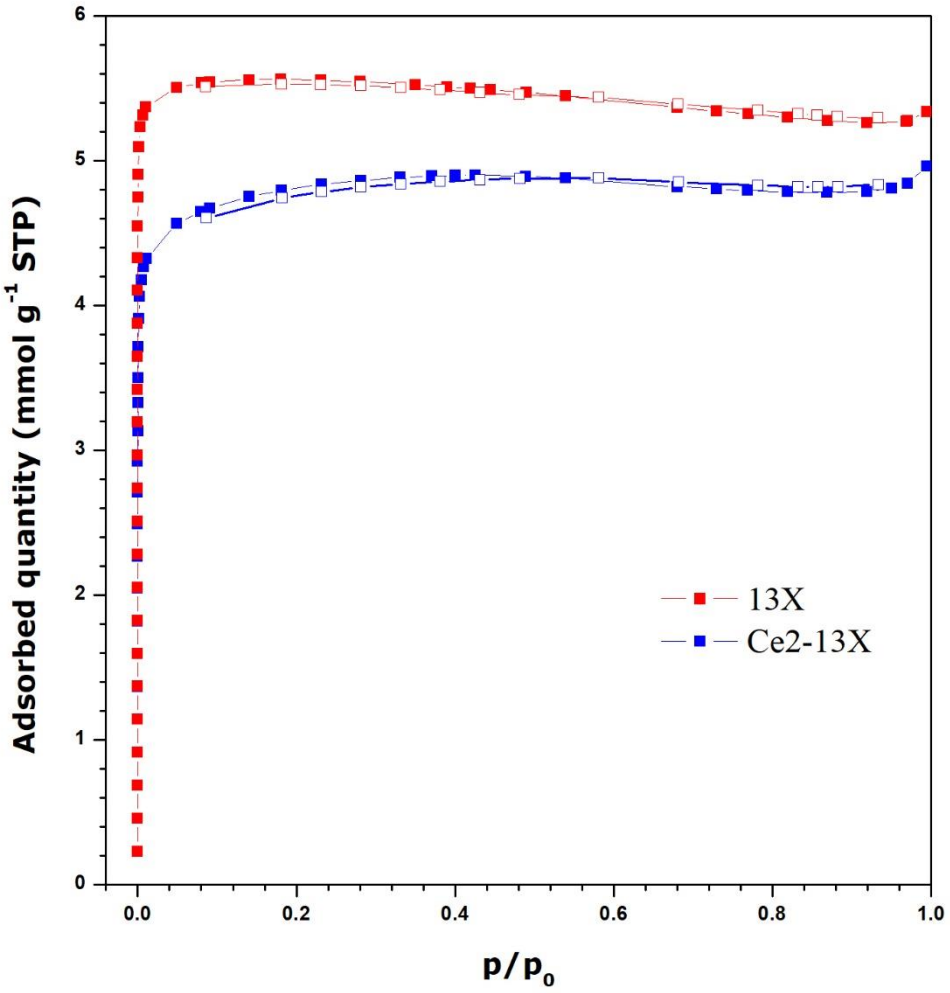

Figure A.III.1: Experimental N_2 adsorption-desorption isotherm for commercial 13X and Ce2-13X outgassed at 473 K overnight under secondary vacuum. The filled and empty symbols correspond to the adsorption and desorption isotherms, respectively.

Table A.III.1: Apparent surface area obtained from gaseous N_2 adsorption isotherms, respectively, for 13X and Ce2-13X, as inferred from the data processing based on appropriate B.E.T. model.

Material	13X	Ce2-13X
S_{BET} ($m^2 g^{-1}$)	427.4	372.1